University of Southampton Research Repository
ePrints Soton

Copyright © and Moral Rights for this thesis are retained by the author and/or other copyright owners. A copy can be downloaded for personal non-commercial research or study, without prior permission or charge. This thesis cannot be reproduced or quoted extensively from without first obtaining permission in writing from the copyright holder/s. The content must not be changed in any way or sold commercially in any format or medium without the formal permission of the copyright holders.

When referring to this work, full bibliographic details including the author, title, awarding institution and date of the thesis must be given e.g.

AUTHOR (year of submission) "Full thesis title", University of Southampton, name of the University School or Department, PhD Thesis, pagination

http://eprints.soton.ac.uk

University of Southampton

Faculty of Engineering and the Environment

Aquatic Flight Inspired Propulsion for Autonomous Underwater Vehicles

Sain-Gee Keith Man

Thesis for the degree of Doctor of Philosophy

March 2015

Page intentionally left blank

University of Southampton

Abstract

Faculty of Engineering and the Environment

Doctor of Philosophy

Aquatic Flight Inspired Propulsion for Autonomous Underwater Vehicles

By Sain-Gee Keith Man

Modern Autonomous Underwater Vehicle (AUV) technology has a number of limitations and one of these is vehicle manoeuvrability. Conventional flight style AUVs generally have turning circle diameters of five or more vehicle lengths, but most marine animals can turn in under one body length. This shows there is merit in looking at marine animals for inspiration to improve the manoeuvrability of AUVs. Aquatic flight propulsion is one marine animal propulsion strategy that was identified early in the research as having the potential to full fill this role.

Aquatic flight propulsion has been studied experimentally in the past, but most of the past research focused in one or two axis aquatic flight (foil pitch and dorsoventral roll). However, marine animal literatures show animal aquatic flight is a three axis problem and there is an additional motion component in anteroposterior yaw. The effect of this yaw motion is not well understood and this will be the focus of this thesis's research.

The effect of aquatic flight yaw motion is investigated using a combination of computation modelling and experimental studies. It found two-axis aquatic flight is better for producing propulsive thrust for most scenarios, but three-axis aquatic flight is useful for producing additional off axis force. In particular, the three axis slanted foil actuation path can produce a sizeable vertical force with very little change to the horizontal thrust coefficient, which would be very useful for a positively buoyant AUV to control its depth.

The experiment verified the model's results and many of the experiment data points were within 30% of the model prediction. The experiment has a relatively large uncertainty due to turbulences in the recirculating water channel, so 30% is a reasonably good fit. Whilst there is room for improvement for both the model and the experiment, the current model is sufficient to produce provisional estimates for actuator and control system design as well as identification of various cases of interest for further in depth analysis.

Page intentionally left blank

I. Table of Contents

Chapter 4: Asymmetric Stroke..131

Chapter 5: NIMBLE Experiment Design 171

Page intentionally left blank

II. List of Figures

III. Academic Thesis: Declaration of Authorship

I, Sain-Gee Keith Man

declare that this thesis and the work presented in it are my own and has been generated by me as the result of my own original research.

Aquatic Flight Inspired Propulsion for Autonomous Underwater Vehicles

I confirm that:

1. This work was done wholly or mainly while in candidature for a research degree at this University;
2. Where any part of this thesis has previously been submitted for a degree or any other qualification at this University or any other institution, this has been clearly stated;
3. Where I have consulted the published work of others, this is always clearly attributed;
4. Where I have quoted from the work of others, the source is always given. With the exception of such quotations, this thesis is entirely my own work;
5. I have acknowledged all main sources of help;
6. Where the thesis is based on work done by myself jointly with others, I have made clear exactly what was done by others and what I have contributed myself;
7. Part of this work have been published as: (Man et al., 2012)

Signed: …

Date: 3rd March 2015

Page intentionally left blank

IV. Acknowledgement

I would like to thank my supervisory team, Dr J.I.R. Blake, Dr S.W. Boyd, and Dr A.B. Philips for their help throughout this research and their assistance on the writing of this report. With the oversight of my main supervisor, editorial advice has been sought. No changes of intellectual content were made as a result of this advice.

I'd also like say thank you to the staffs at University of Southampton's EDMC workshop for the construction of the experiment test rig, and K. Scammell for his help at the University of Southampton, Chilworth Hydraulics Laboratory. I must thank Dr A. J. Murphy, Dr M. Haroutunian, and staffs at the Wind Wave Current Tank at Newcastle University for their help at various stages of the research project. I am especially grateful for them to grant me access of their facility when the Chilworth Internal Flume at University of Southampton broke down. Dr M. Haroutunian also contributed greatly to the preliminary database analysis which identified of manoeuvrability as one of the major performance gap between animal and AUV performance.

Finally I need to thank my family for their supports throughout the course of this PhD research, particularly during the very difficult period towards the end.

Page intentionally left blank

V. Nomenclature

A	Area of foil, m^2
A_{surf}	Surface Area, m^2
a_n	Total foil acceleration at Blade element, ms^{-2}
BL	Body length, m
C_D	Drag Coefficient
C_L	Lift Coefficient
C_T	Horizontal Thrust Coefficient
C_{VF}	Vertical Force (lift/down force) Coefficient
F_T	Horizontal Thrust, N
F_{DF}	Vertical Thrust (down force), N
F_L	Lift, N
F_D	Drag, N
f	Stroke frequency, Hz
g	Gravity, ms^{-2}
L	Characteristic length, m
L_D	Hull equatorial diameter, m
L_p	Hull polar diameter, m
L_S	Foil Span, m
L_C	Foil Chord, m
m	Mass, kg
P	Pressure, Nm^{-3}
Q	Torque, Nm^{-1}
R	Total foil span, m
r	Element distance from actuation axis, m
r_0	Distance from foil root to actuation axis, m
Re	Reynolds number
St	Strouhal number
T	Stroke cycle period, s
U	Global inflow velocity, ms^{-1}
V	Vehicle velocity, ms^{-1}
V_{in}	Foil local inflow velocity, ms^{-1}
V_{vol}	Volume, m^3

α	Angle of attack, rad (unless specified otherwise)
β	Inflow angle, rad
ε	Angle between acceleration vector and vertical roll, rad
ρ	Sea water density, ($1024.75 kgm^{-3}$)
ν	Kinematic viscosity ($1.044 \text{x} 10^{-6} m^2 s^{-1}$ at 25°C)
θ	Pitch angle, rad
θ_0	Pitch angle amplitude, rad
ϕ	Roll angle, rad
ϕ_0	Roll angle amplitude, rad
ψ	Yaw angle, rad
ψ_0	Yaw angle amplitude, rad
ω	Angular frequency, $rad\ s^{-1}$

Chapter 1: Introduction

1.1 Motivation

The world's oceans contain a vast amount of resources, most of which are located at great depths or under the ocean floor and they are very difficult to access. The pressure and remoteness of the location due to depth is too much for human divers, so exploration must be done with manned submersible and robotic vehicles. In the mid-20th century, Autonomous Underwater Vehicles (AUVs) began to emerge from various research laboratories around the world. Unlike Remotely Operated Vehicles (ROVs), AUVs are designed to operate independently and without human operator input or connection to a mother ship. Since their inception, there has been a rapid evolution of AUVs from novel research interest into serious tools for the marine and maritime industry.

Up until the 1980's, AUVs were limited to very simple missions. However, the computer revolution in the late 20th and early 21st century produced computer systems compact and powerful enough to make autonomous operation a reality. This breakthrough led to an expansion in the number of missions that can be carried out using AUVs and an explosion in the number of new vehicle designs. These new capabilities are opening new applications of AUV that traditionally utilise survey ships, ROV and human divers.

One of the emerging markets of AUV is offshore inspections where an AUV has to transverse a long distance to reach an inspection site and then perform tight manoeuvre in confined environment to perform the inspection. Another emerging market is wildlife documentary filming where an unmanned vehicle will be deployed to follow a group of animals in their natural environment, such as filing a pod of dolphins as they swim. These missions require a new class of vehicle that is both fast and manoeuvrable, which used to be a mutually exclusive requirement.

This thesis research identified a paired-fin propulsion strategy know as aquatic flight propulsion, which is used by animals such as penguins, seals and sea turtle, as a potential locomotion strategy that can full fill the goal of a fast and manoeuvrable AUV. Animals that utilise this propulsion strategy are known to be good long distance swimmer, some with annual migration that is known to be thousands of kilometres in length, and yet they also have great manoeuvrability to enable them to hunt and navigate complex costal and coral reef environment that allow them feed and come ashore to rest and breed.

Furthermore, most aquatic flight propelled animals have relatively rigid bodies and this also lends itself well for adaptation in a manmade platform which must have a rigid pressure vessel to protect the sensitive equipment from sea water. This is an important advantage of aquatic flight propelled AUV over more commonly researched fish style body-and-caudal fin propelled AUV, which must sacrifice a portion of their vehicle length and payload space for its flexible tail.

There are still a lot of unknown regarding aquatic flight propulsion, chief among which is the three axis propulsion gait that is observed to be used by many of aquatic flight propelled animals. This thesis research will focused on the effect of the anteroposterior yaw component in a single aquatic flight propulsor, and this will lay the ground work for a future paired or quad fin aquatic flight propelled AUV like the concept drawing in Figure 1-1.

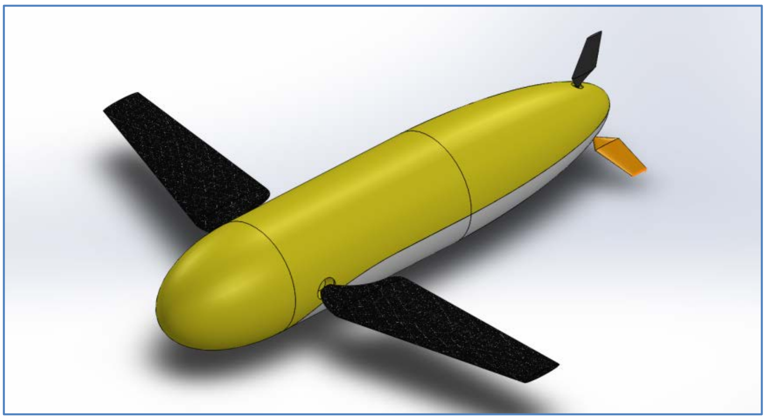

Figure 1-1 - Concept aquatic flight propelled AUV that is similar in size and displacement to seal, large penguins and small AUV. The main foils acts as the primary propulsor and primary direction.

1.2 Background

1.2.1 The AUV Market

The depth of the world’s ocean is an environment hostile to human life. Although work in shallow water can be performed by human diver in scuba gear, deep water operation can only be carried out by manned submersibles or robotic vehicles. There are two classes of robotic vehicles, the Remotely Operated Vehicle (ROV) and the Autonomous Underwater Vehicle (AUV). The former is tether to a mothership and remotely piloted by a human operator. This type of vehicle generally used in operations that require significant human input such as detailed study of a site of interest, underwater salvage or underwater construction. This class of vehicle are often very manoeuvrable, but they have very limited range that is confined by the length of the tether that connects the ROV to the mothership. In comparison, AUVs are controlled by onboard computers and this class of vehicle is designed to operate autonomously without any human input once the mission begins. As such the AUV must be self-contained and carried all equipment and power source required to complete its mission. Due to lack of physical connection to the mothership, an AUV can perform long range missions that can cover hundreds if not thousands of kilometres.

Until recently, the lack of human input means AUV are generally confined to mission with relatively simple mission profiles, but this changed with recent advancement in microcomputers and artificial intelligence. This opened up new possibilities and allowed AUV to be used in certain mission that was once restricted to manned submersible, ROV and human divers. This in turn led to a rapid expansion of the AUV market. By 2010, there were over 90 different models of AUV in service with various navies, survey companies and research institutions around the world, and 76% of these vehicles were introduced in the period between 2000 and 2005 (Westwood, 2010), some examples are shown in Figure 1.

The rapid advancement of the AUVs allowed them to replace expensive survey ships for many missions, such as mapping and hydrographical surveys. An AUV can potentially operate 24 hours a day and only return to base for recharging its batteries, thus freeing up human resources for other tasks. In one study, a surveying mission between Iceland and Scotland would cost an estimated €245k for a manned vessel, whereas performing the same mission with an AUV would cost less than €98k (Griffiths and Edwards, 2003). In another study, an AUV can save a surveying company approximately £150k and 50 operation hours for a 10kmx10km block survey compared to a survey ship (Danson, 2002). In addition to the cost advantages, AUVs also opened up access to some global regions that were previously inaccessible to ships.

Figure 1-2 - Different types of AUVs. Slocum glider (left), Remus 100 (centre), Autosub 6000 (right). Image source: AUVAC

In a survey carried out by Douglas-Westwood (2010), of the 629 AUVs surveyed, 145 were operated by the military (23%), 220 by research institutes (35%), 256 by various survey companies (41%) and 8 by others (1%). In terms of AUV market values, which were estimated to be worth $2.3 billion in 2010, 49% was spent by the military, 31% by research institutions, 8% by oils and gas industry, 7% by hydrographic sectors and 5% telecommunication industries.

1.2.2 AUV Classification

Different mission generally require vehicle with different capabilities and no single vehicle can perform every type of mission. The mission requirements generally determine the optimum vehicle for the task. For example, large survey class AUVs can operate multi-day missions in open-ocean and use power hungry instruments, but they are ill suited for mapping a river or a lake due to their manoeuvrability constraints. At the other end of the spectrum, small AUVs that can manoeuvre well in confined coastal and inland waters would often lack the endurance to perform long range missions in the high sea.

AUV can be categorised by their size and displacement into three groups – Large, Medium, and Small (Newman, 2010). Large AUVs usually operate in open-ocean and generally have displacement between 500-5000kg and lengths of 3-6m. Their large capacity batteries can power a sophisticated suite of instruments and allow them to travel long distances of over several hundred kilometres. These advanced capabilities come at a cost and a typical large AUV costs between $1 and $5 million. These vehicles often require specialist handling equipment, which can further increase the logistic and operating costs. Large AUVs included models such as Kongsberg’s Hugin series, Hydroid’s Remus6000, and NOC’s AutoSub series (Westwood, 2010; McPhail, 2007).

Sometimes smaller vehicles can be a more economical alternative for missions that do not require the full capabilities and endurance offered by large AUVs. Medium sized AUVs typically weigh between 50kg and 500kg, but some are modular and can be broken down into air transportable packages. These vehicles are typically between 2-3 metres long, cost between $250k and $1 million, and can also support reasonably sophisticated sensor suites. AUVs belonging to this class included Hafmynd’s Gavia, Bluefin Robotics’ Bluefin 9 and 21, and MIT’s Odyssey series.

Often even medium sized AUV can still be too expensive or cumbersome for many missions, so there is a significant market for an even smaller sub-50kg class of AUV. These small AUVs often have limited range (up to 40km) and shallow depth ratings (up to 100m). Their small size restrict the amount of payload and batteries these vehicles can carry, so most have reduced capability compared to the larger platforms. However, small size and low weight means many of these AUVs can be manually handled (picked up by hand instead of specialist crane), thus significantly reducing the logistic and operational costs. The typical unit cost of a small AUV is around $250k (Westwood, 2010), and this makes the small AUV very popular. The small AUV accounts for over 66% of all AUVs in operation and most of these are Remus100 and Iver2 (Newman, 2010).

In addition to classification based on size there is also another other groups of notable AUVs, known as the glider. Whilst most AUVs and ROVs relied on propeller for propulsive thrust, gliders rely on a novel propulsion method that uses a pair of ‘wings’ and a buoyancy engine instead of propeller. The buoyancy engine pumps water in and out of the vehicle to change the glider’s buoyancy, and the vertical force from sinking and floating is converted into horizontal motions using a set of gliding wings. Gliders generally have very long range and the range of small gliders often exceeds the range of large AUVs. In 2009, a 50kg Slocum Electric Glider made a 7408km journey from America to Spain, this is well in excess of the range of most conventional AUV that weight two orders of magnitude more (Newman, 2010). A further development of the Slocum glider that is known as the Slocum Thermal Glider is designed to extract energy from natural variation in ocean temperature to power its buoyancy engine, which effectively gives this glider unlimited range. The vehicle’s operation is only limited by the hotel load drain on its batteries (Davis et al., 2003).

Sinking and floating is a fundamental part of glider application, so they cannot take part in missions that require operating at a constant depth or shallow water. The buoyancy propulsion method also makes gliders the least manoeuvrable AUV and this restricts gliders to missions with fairly simple mission profiles. However, these are the trade-offs most gliders make in exchange for their extreme range.

One reason for glider being of particular interest to this research is the vehicle’s similarity to an aquatic flight AUV. In theory, installation of a buoyancy engine in an aquatic flight AUV will allow the aquatic flight AUV to operate in ‘glider mode’ during its long transit to the mission area by using its hydrofoils as glider wings. Once the vehicle arrived at the mission area, it can switch over to aquatic flight mode, which would increase its speed, manoeuvrability and agility and allow it to perform its mission. After that it will return to the energy efficient glider mode for its return to base.

1.2.3 The AUV Missions

Traditionally AUVs were used for environmental survey and mapping in open water, where the vehicle sets off on a predetermined course and collects data as it travels. The vehicle would rely on simple sensors that measure speed, depth, and direction for navigation. The vehicle would travel on a predetermined path but it would not be able to react to unexpected obstacles such as an unmarked reef or seamount. Recent advancements allowed AUVs to make decisions based on input from more advanced sensors, which allowed the AUV to react to unexpected situations and undertake more complex missions. These newer missions include inspection of offshore assets such as oil pipelines and platforms, where the vehicle may need to travel over a long distance to reach the mission area, and then carry out detailed localised survey once it arrived.

Whilst advanced artificial intelligence will allow AUVs to perform some underwater inspection missions by replacing the human decision making process with computer, the hydrodynamic modern flight styled AUVs are ill suited for many of these mission. Missions such as off shore assets inspection requires the vehicle to hover and remain in a fixed position over the target of interest. This requires good low speed control and manoeuvrability especially when complex ocean current is taken into account. Whilst conventional control surfaces are good at cruise speed, they become inefficient at low speed or and ineffective at hover. As such, an alternative direction control solution is needed for AUV undertaking inspection missions. The ROV manoeuver at low speed using multiple lateral thrusters, but these create extra drag when the vehicle is cruising, thereby reducing vehicle endurance. The reduced hydrodynamic efficiency is not a big concern for ROVs because they receive power from a mother ship and have limited range. In contrast AUVs must rely on the limited power stored on-board the vehicle to travel from base to the mission area, perform the mission and return, and the increased drag from the lateral thrusters can be problematic. As such there is a market for a manoeuvring system that is effective at both cruise and hover.

In addition to low speed manoeuvrability, there is also a performance gap between AUV and animal's manoeuvrability at high speed. A recent BBC documentary – Dolphins: Spy in the pod, showed there is a market for vehicle with good high speed manoeuvrability. The documentary used cameras mounted in robotic submersibles to film dolphin pods as they travelled but the vehicles had difficulty keeping up with the dolphin pods. Creating an AUV that can travel and keep up with marine animals will require further advancement in artificial intelligence, propulsion and vehicle hydrodynamics.

1.2.4 Nature's solution

Today's unmanned submersibles are either optimised for long range operation and as a result have limited manoeuvrability, or optimised for low speed manoeuvrability but have poor range. Range and manoeuvrability appeared to be mutually exclusive in manmade vehicles, but this is not the case for marine animals. Many long range swimmers, such as dolphin, seals, and penguins, are also very manoeuvrable. Therefore, marine animals can provide a source of inspiration for improving the manoeuvrability of high speed, long endurance AUVs.

Furthermore, the day-to-day activities of many marine animals exhibit similar patterns to the mission profiles of some AUVs. A survey and mapping AUV's mission profile is very similar to that of large filter feeding whales and sharks, since these animals have to cruise over a long distance during migration between feeding and breeding grounds. An AUV performing inspection missions would need to travel from base to the mission area, navigating around the submerged structures of offshore installations in search of defects. This is not dissimilar to a sea turtle traveling from its breeding ground beach to the feeding ground, and then navigates around a coral reef in search of food. These similarities suggest there are lessons that can be learned from nature.

Traditionally animal locomotion research has focused on improving propulsion efficiency, because animal swimming was believed to be more efficient than manmade propulsion methods. However, the original hypothesis that claimed animals was significantly more efficient than manmade vehicles were disproven by later research. The Gray's Paradox, as it was known, was the result of a paper published in the 1930's concerning dolphins swimming performance. This is discussed in detail by Fish and Rohr (1999), but in summary Gray's research measured the speed of swimming dolphins from a moving ship, but his calculation found dolphins did not possess enough muscles to achieve the speed measured. In fact it estimated dolphins were underpowered by a factor of seven, so Gray concluded the animals must be using some novel drag reduction mechanism. This lead to various theories such as boundary layer acceleration, compliant surfaces based on flexible skin, and secretion of a drag reduction fluid from tears. However, the author of the original paper did not take into account the dolphin's wave riding behaviours and anaerobic muscles that can provide much higher power output over a short period of time compared to normal aerobic muscles. While the Gray's Paradox has now been disproven, it sparked the research interest in marine animal hydrodynamics.

Many modern researchers found oscillating foil swimming was more efficient than that of a manmade propeller (Lindsey, 1979; Fish and Hui, 1991; Fish, 1993; Fish and Rohr, 1999). However, the improvement in efficiency is limited to a few percent rather than a few hundreds. Whilst dolphin and tuna's oscillating foils may be more efficient than manmade propellers, the linear actuators required to drive them are very inefficient. Most shape memory alloy (SMA) actuators are less than 2% efficient and their theoretical maximum efficiency is less than 10% (Van Humbeeck, 2001). Biological muscle has better efficiency than SMA, but it is still limited to 40% at best (Bangsbo et al., 2001). In comparison, the efficiency of a well-designed brushless DC motor and its drive train can have a combined efficiency in excess of 90%. A simple calculation will show a 90% efficient bio-inspired propulsor coupled to a 10% efficient drive train will perform worse than a 50% efficient propeller coupled to a 90% efficient drive train. Therefore any efficiency gained from having an oscillating foil propulsor is usually lost by having poor internal power transmission. As such this research will not be concerned with the propulsor efficiency at this stage.

Whilst biomimetic propulsion may not provide any gain in propulsion efficiency, it can provide improvement in manoeuvrability. Traditional non hover flight style AUVs and gliders have turning circles several times the vehicle's lengths. In comparison, many fish species can turn within one body length and reverse its heading using only half a tail beat. This manoeuvrability advantage is also reported in several bio-inspired autonomous underwater vehicles. The tuna inspired biomimetic VCUUV from the Draper Laboratory was able to perform a complete reversal of direction at low speed in less than one body length and could make a turn at high speed with virtually no loss of velocity (Anderson and Chhabra, 2002).

From these results, it is clear an AUV equipped with a biomimetic locomotion system may be able to achieve manoeuvrability not achievable using conventional engineering designs. While vehicles equipped with lateral thrusters may match the low speed performance of median paired fin (MPF) propelled fish (Sub Dimension Engineering's Orion work class ROV's turn rate is approximately 120°/s while stationary), they are unable to match the performance at high speed because lateral thrusters become less effective in cross flow (Healey et al., 1994; Saunders and Nahon, 2002; Palmer et al., 2008).

1.3 Aim

The aim of this investigation is to investigate propulsion and manoeuvrability of animals through computational modelling and experimentation. The analysis will specifically target aquatic flight style swimming. The results of the investigation will provide understanding of the thrust producing mechanisms of this swimming mode, which can be used in the future development of propulsors for advanced manoeuvrable AUVs.

1.4 Research and Methodology

The aim will be achieved through the following objectives:

1. Review literature and other sources of information for details about animals and AUV to identify gaps in their limitations and gaps in their performance. This goal is to identify the propulsion mechanism and locomotion strategy that can close this gap and the result of this would be further investigated. The result of this study found aquatic flight to be a candidate that can full fill the goal of improving AUV manoeuvrability.

2. In depth literature analysis of the identified propulsion mechanism know as aquatic flight. A computation model would be built to help develop an understanding of the underlying mechanisms behind aquatic flight style propulsion

3. Extension of the model to investigate three-axis aquatic flight, and study the effect of the anteroposterior yaw motion in the aquatic flight stroke. The model will simulate operation under different conditions to gain an understanding of the optimum operating conditions.

4. Design and develop an experimental platform to provide data to validate the computational models of aquatic flight style propulsion. This will involve design and construction of an experimental actuator for testing in a controlled environment, which may be a recirculating water channel or a towing tank.

5. Examination of the aspects of aquatic flight style propulsion through modelling and experiment. Aspects not previously investigated in the literature such as changing gait patterns and off axis strokes are explored.

1.5 The NEMO Project

This research forms part of the EPSRC funded Nature in Engineering for Monitoring of the Oceans (NEMO) project. This project is a collaboration between the University of Southampton, Newcastle University and the National Oceanography Centre, Southampton. The project aims to improve autonomous underwater vehicle (AUV) performance using nature inspired technologies. This involved analysing current AUV technologies and identifying their limitations, and then studying marine animals to identify whether any animals possessed features that could be used to solve the limitations identified in AUVs.

The NEMO project was divided into two work packages. Work Package 1 (WP1) investigated diving capabilities and Work Package 2 (WP2) investigated locomotion. The NEMO project database was created at the beginning of the project to collect, process, and analyse information about AUVs and animals. It was used to identify performance gaps between animals and manmade vehicles.

Manoeuvrability was identified as one of the major performance gaps identified and changed the focus of WP2 from propulsion to manoeuvrability. The NIMBLE subproject was created with in WP2 to investigate propulsion and manoeuvring mechanics of the aquatic flight mechanism and is the subject of the present research.

1.6 Thesis Outline

This thesis is separated into seven chapters. Chapter 1 is the introduction. Chapter 2 is literature review chapters that will look at traditional manmade technology as well as animal swimming mechanics. It identified the performance gaps in manoeuvrability between animals and AUVs, and showed aquatic flight propulsion can be the solution that can reduce this gap.

It will also provide an overview of the existing research in biological propulsion and bio-inspired AUV.

Chapter 3 cover aquatic flight propulsion and the Blade Element Theory model designed to study it. In particular the chapter will focus on symmetrical three-axis aquatic flight with an actuation component in yaw in additional to pitch and roll. The existing studies in aquatic flight focused on two-axis actuation, namely foil pitch and roll, but biological aquatic flight always contains a third actuation component in yaw. The effect of this component is not known and this chapter is dedicated to the study of the effect of this component on thrust coefficient.

Chapter 4 investigate asymmetric stroke and its uses as a mean to produce off axis thrust for manoeuvring. The asymmetric stroke can be applied through inducing an angle bias or a slanted actuation path through the addition of the yaw component. The main focus of this chapter will be the vertical force coefficient each type of asymmetric stroke produce and its effect on the horizontal thrust coefficient.

Chapter 5 is a chapter about the design and construction of an experiment that is used to verify the model prediction. It covers the design of the mechanical, electrical, control and measurement systems, including the design concept, inspirations, ideas and specifications. The chapter also covers measurement, calibration and data processing.

Chapter 6 contains the result analysis of the experiment that was designed to verify the BET model. The experiment analysed the forces and thrust coefficient from the two-axis and the three-axis figure-of-eight actuation path and examine its agreement with the modelling results. There are a number of interesting findings in the experiment that was not initially expected, including the significance of the tip loss effect on the thrust coefficient.

Chapter 7 is the final chapter and the conclusion of this thesis. It provides a conclusion of the research and summarise the findings. It also discusses the findings and short coming of the current research and a present a plan for the future.

Chapter 2: Literature Review

2.1 Introduction

Recent advances in automation and artificial intelligence opened up a lot of potential application for AUVs, but the hydrodynamics of the vehicles are slow to keep up with these advances. As such many of today's AUV platforms will struggle with many new missions enabled by advances in other fields. Whilst AUV development had been going on for half a century, marine animals had evolved continuously for over half a billion years and the solution to overcome the current AUV's limitation may already exist in nature. Therefore, there is merit in looking at nature for inspiration to improve the performance of current generation of AUV.

This thesis research began with the creation of an AUV and marine animal database that collect various data from the two groups, including physical data, such as weight and length, kinematics data, speed, turning circle, diving depth, energetics data, such as fuel capacity and power consumption, etc… and perform correlation analysis on the results. The database was then used to identify gaps in the performance between AUV and animals, and then uses this data to identify a potential animal solution for further investigation.

The study identified platform manoeuvrability as a major performance gap between animals and AUV. It also identified aquatic flight as an animal propulsion mechanism with the potential to close this performance gap.

After identification of aquatic flight and manoeuvrability as the research target, it is important to know the existing work on aquatic flight and the related propulsion gait before embarking on the research. The second part of this literature review will examine the theories and existing research regarding animal propulsion and aquatic flight from both the biological and the engineering perspective. The literature review will also briefly cover the theories on AUV propulsion and manoeuvring.

2.2 Comparison of AUV and Animal Performance

At the early stages of the research, the performance data of over a hundred AUVs and animals were collected from various sources such as marine animal journals and manufacturer specifications and sorted into a database. The aim was to identify deficiency in existing AUV technologies and to identify an animal inspired solution that can overcome that limitation. The collected data included physical dimension and displacement, kinematic data such as cruise and max speed, range, diving depth, as well as other data energy capacity, instrument load out, energy expenditure etc…. These data would be analysed against each other to discover any correlation between various data sets. The comparisons included the turning circle diameters vs speed, body length, mass, Cost of Transport vs Speed, range and operational endurance, Mass vs speed, diving depth, endurance, etc….

Among numerous findings, the database analysis identified a performance gap between animal and AUV manoeuvrability and a group of animals that utilised aquatic flight as their main propulsion mechanism stood out as a possible solution to overcome the manoeuvrability constraint of AUVs.

2.2.1 Comparison between Animals and Manmade Vehicles Manoeuvrability

Since manoeuvrability, acceleration and efficiency are parameters that depend on a number of variables, they are more difficult to measure and quantify than linear data such as speed, length and mass. Both the turning circle and the turning rate of a vehicle and animal often depend on its travel speed when the turn is executed. As such manoeuvrability data is rarely stated and when it is stated it is usually in the form of minimum turning circle diameter/radius and maximum turn rate. Since the number of the data point for maximum turn rate was insufficient for a meaningful analysis, the investigation will focus on the turning circle diameter of animal and AUV.

Whilst absolute turning circle is important in deciding whether a vehicle is suitable for a particular mission, it is less useful for comparing propulsion and manoeuvring strategy because larger vehicles will generally require more space to turn. Therefore comparison between vehicles of different size will be made with non-dimensional parameters. This can be achieved through normalising the turning circle diameter against the vehicle length to account for the variation in size.

2.2.1.1 *Normalised Turning Circle Diameter vs. Body Length*

After the turning circle diameters were normalised against the vehicles' length, the investigation plotted the normalised turning circle against the vehicle hull length or animal body length (Figure 2-1). It was found that most conventional flight style AUVs can turn 180° with in about 5 body lengths (BL) which roughly equates to around 10m in absolute term for smaller vehicle to approximately 40m larger vehicles. This is better than most survey ships and is sufficient for most open water survey missions, but it is still relatively large and can limit the vehicle's ability to perform missions that requires close up manoeuvring (e.g. an inspection mission). Gliders have the poorest manoeuvrability compared to other vehicles and animals in the survey. The three gliders in the survey have turning circle diameters between 25-35 BL, which roughly equates to 40-60m in absolute terms. This is almost an order of magnitude larger than conventional AUVs of similar size.

On the other side of the manoeuverability spectrum for manmade vehicles are AUVs equiped with lateral thrusters or bioinspired propulsion system, both of which performed better than traditional AUV platforms of a simiar size. Draper Laboratory's tuna-inspired Vorticity Control Unmanned Undersea Vehicle (VCUUV) has a turning diameter of 2.2BL, which is a significant improvement over the traditional flight style AUV. The similar sized aquatic flight propelled Finnegan has a even smaller turning diameter of 0.77BL which is an improvement over the VCUUV. The VCUUV and Finnegan represent the two major swimming styles used by marine animals. VCUUV was modelled on a tuna fish which uses Body and Caudal Fin (BCF) locomotion for propulsion, while Finnegan was modelled on sea turtles and utilise Median and Paired Fin (MPF) locomotion for propulsion. Details descriptions of BCF and MPF swimming can be found in later sections.

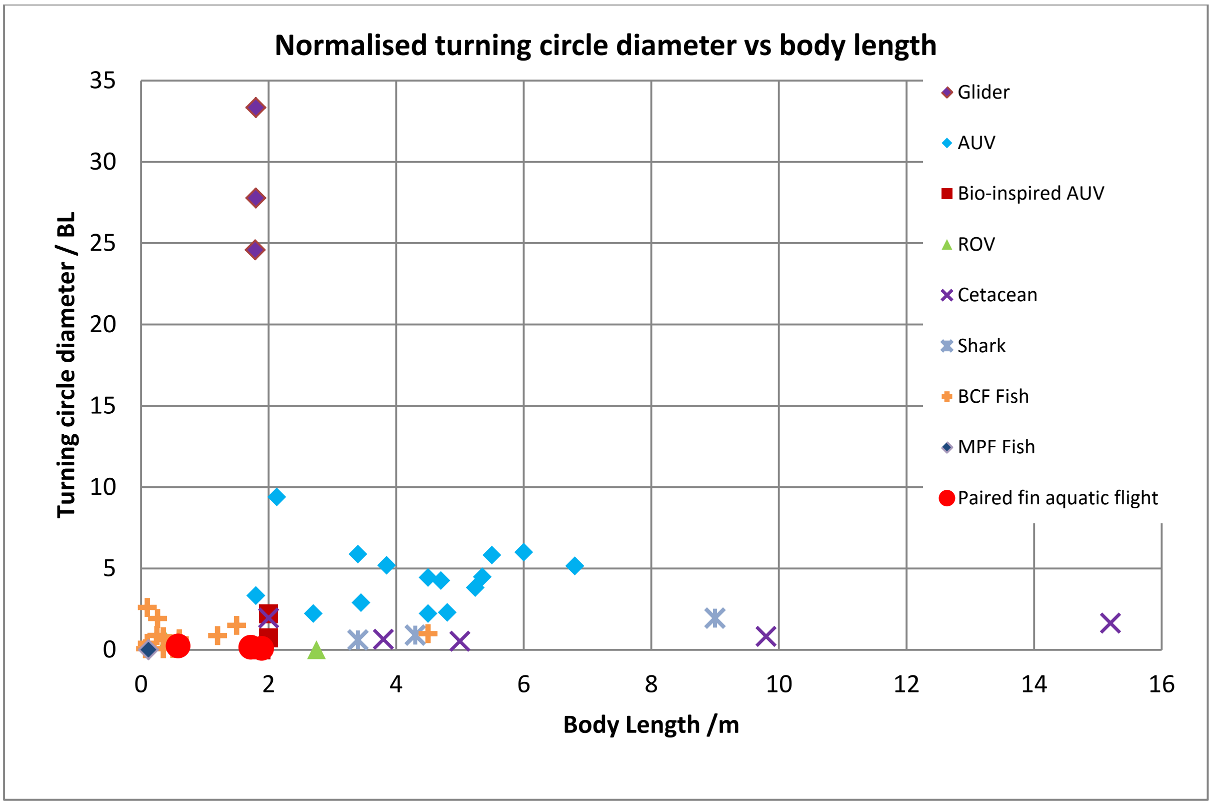

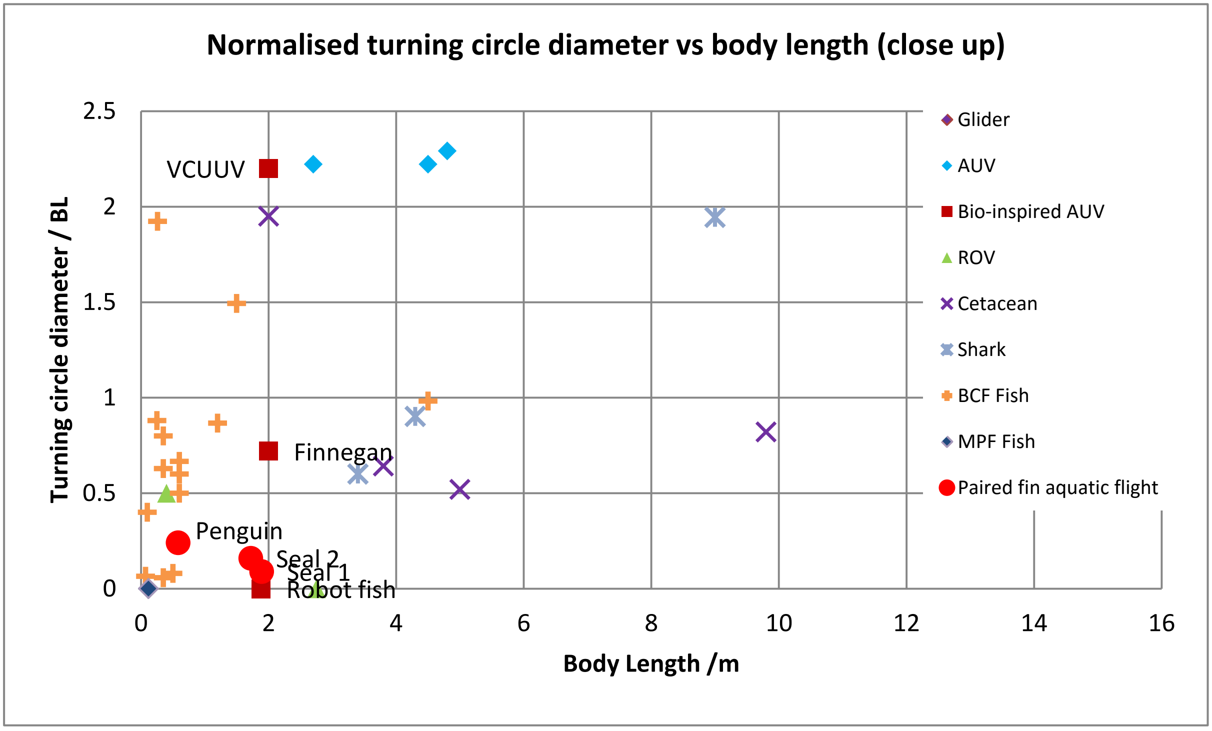

Figure 2-1 Non dimensionalised turning circle vs body length. The diagram showed AUV had inferior turning performance when compared to animals, the performance of gliders were a lot worse than the AUVs

In addition to AUV turning circle, the plot also features animal turning circles diameters from dozens of marine animals. It demonstrates that many animals have turning circle diameter less than 1.0BL, which means most can turn within the length of its body. The plot further divided the animals into five groups, namely cetacean (whales and dolphins), sharks, fish that utilised BCF locomotion, fish that utilised MPF locomotion, and animals that utilised a special form of MPF locomotion know as aquatic flight.

The plot shows most BCF propelled animals, such as cetaceans, sharks and many BCF fish, have turning circle diameter between 0.5 and 1.0BL, whereas fish and animals that utilise MPF locomotion can turn much tighter. Penguins and seals were found to be able to turn within a quarter of their body length, which shows there may be some advantage to MPF locomotion for manoeuvring. As such, further investigation should be carried out to analyse their locomotion.

2.2.1.2 *Normalised Turning Circle Diameter vs. Normalised Speed*

The second part of the investigation analysed the relationship between a vehicle's manoeuvrability and its cruising speed. A body optimised for high speed and long range cruising generally have a relatively slender body with a large length to diameter (L/D) ratio. A high L/D ratio vehicle would experience less form drag when moving through water when compared to a low L/D ratio one, but the opposite is true for skin friction. Published literature suggests the optimum L/D ratio for AUV is between 6 and 8 (Ferguson, 2003). In addition to vehicle drag, vehicles with L/D ratio longer than 8 can become difficult to stabilise in pitch, while vehicles with L/D ratio shorter than 6 can become unstable in yaw (Ferguson, 2003). A vehicle designed for long range high speed operation should have a slender hull form to reduce drag and increase stability, but increase stability also means reduced manoeuvrability so this vehicle should have a greater difficulty making a turn and thus have a larger turning circle. Therefore it is reasonable to hypothesise a body designed for higher maximum speed should be less manoeuvrable than one optimised for a lower speed.

Figure 2-2 shows a plot between normalised turning circle diameter and normalised speed, where both variables were normalised by body length. The diagram suggests that AUV speed were unrelated to their turning performance and their turning performance is generally very poor when compared to animals. The typical AUV has a cruise speed of 0.4BL s^{-1} and a turning circle diameter of between 4-5BL. Most animals can swim much faster, yet able to turn much tighter. Most animals can turn in less than 2BL and a significant proportion of those are able to do it in less than 1BL.

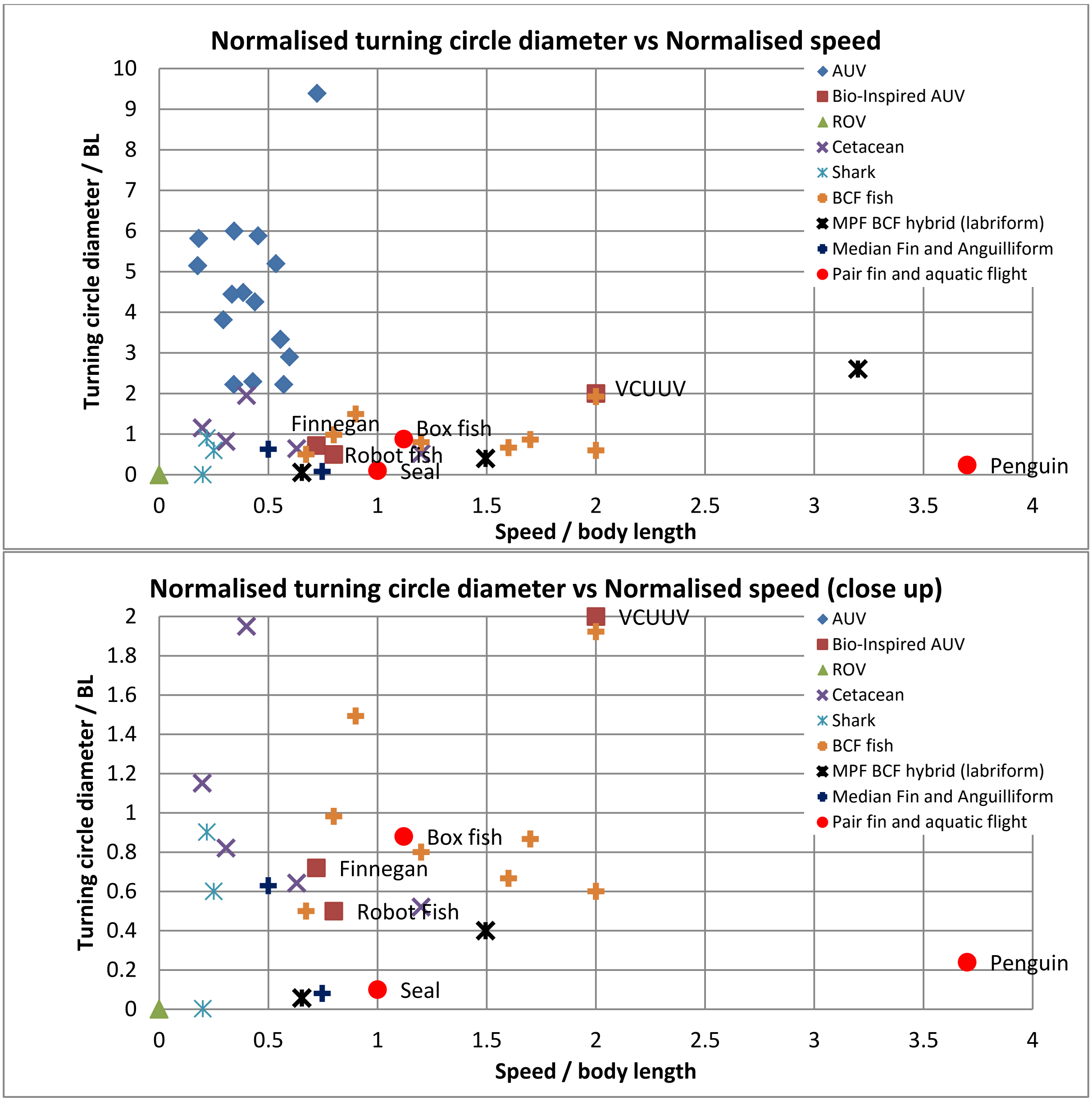

Figure 2-2 – Normalised turning circle diameters vs normalised speed. Note the improved manoeuvrability of the bio-inspired AUVs such as Finnegan and VCUUV (brown squares). Also note the high speed and small turning circle of the penguins and seals

As such, the original hypothesis of faster bodies should have larger turning circle were not supported by results from the plot. This suggested animal may have very efficient turning mechanism, so they can maintain good manoeuvrability even with a body that is optimised for high speed swimming. It also suggests most AUVs are not optimised for turning since the turning performance and speed appears independent.

The MPF animals again show superior manoeuvrability compared to animals using BCF. The category average for cetacean and sharks turning diameter is 0.82BL, while BCF fish is 0.98BL. By comparison, MPF animals averaged turning diameter of 0.62BL. Looking at the plot, it can be seen the MPF animals tends to have tighter turning circle when compared to others at the same normalised speed. Seals can maintain a tight turning circle diameter of 0.1BL and be able to swim at 1BL s^{-1}. The penguin example is even more extreme, as it is able to travel at 3.7BL s^{-1} and still maintain a tight turning circle of 0.24BL. The turn rate data not shown here also suggested MPF has superior agility. A penguin can turn at a rate in excess of 550° s^{-1} and a seal can turn at a rate of 690°s^{-1}. In comparison, a bottle nose dolphin turn rate is only 220° s^{-1}. A typical man made AUV such as the Remus 100 has a turn rate of 3-5° s^{-1} (Anderson and Chhabra, 2002), while an ROV such as an Odyssey ROV can turn at up to 120° s^{-1}. The bio-inspired VCUUV has a maximum turn rate of 75° s^{-1}, but a turn rate of 17° s^{-1} is more typical. VCUUV can also maintain constant forward speed with turn rate up to 30°s^{-1} (Anderson and Chhabra, 2002).

2.2.2 Summary

The results of the animal and AUV comparison demonstrated marine animals generally have better manoeuvrability than AUVs. Among animal locomotion, MPF propulsion appeared to show better manoeuvrability than BCF propulsion. Whilst a typical AUV can complete a turn within five times its body length, the turning circle for BCF fish is just under 1.0BL. The MPF animals were shown to have some of the tightest turning circle, with both penguins and seals being able to complete a turn in less than one quarter of their body length. If an AUV needs to be both fast and manoeuvrable, then a MPF propulsion mechanism may be able to deliver the required performance improvement. Special interest should be paid to the propulsion mechanism of seals and penguins, namely aquatic flight, because they were shown to be very manoeuvrable and also very fast. Furthermore they are similar in size to a typical small AUV so their propulsion mechanism would be less affected by scaling.

2.3 Manoeuvring

Since the database analysis of various animal and AUV data shows manoeuvrability is a major performance gap between animal and AUVs, it is important to know the fundamentals of underwater manoeuvring. This section will present an overview of the basics of underwater manoeuvring such as the coordinate systems, name of various degrees of freedoms and what factors and forces affects the manoeuvrability of a vehicle underwater.

Underwater locomotion has six degrees of freedom (DOF). The three translational DOF are surge, heave and sway (X, Y, Z), and the three rotational DOF are pitch, roll and yaw (θ, ϕ, ψ) (Figure 2-3). Surge is aligned to the principle direction of travel and most vehicle and animal are optimised to reduce drag in this direction.

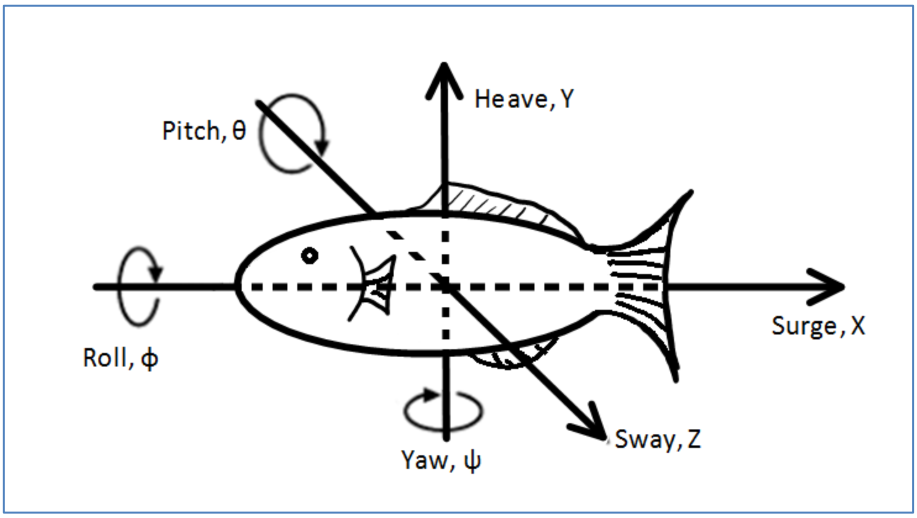

Figure 2-3 – The six degrees of freedom that is used to describe marine animal locomotion. Coordinate is centred on the animal. (adapted from Fish (2004))

Apart from surge, the freedom of movement in the other five DOFs depends on the design of individual animals and vehicles. Yaw and pitch control are important for steering the vehicle and for depth control. Depth can also be controlled through heave motion by using adjustable ballast or vertically aligned thruster. Roll is less important for manmade vehicles and is usually passively corrected by the relative positioning of the vehicle centre of mass and centre of buoyancy. Sway is only controllable if the vehicle has lateral thrusters.

Most modern flight style AUVs are designed for efficient long distance cruising, where manoeuvrability is not a major concern. In fact an AUV that can reverse its direction within a few minutes and within a few body lengths is considerably more manoeuvrable than a conventional survey ship with a deep water tow that can take hours and many kilometres to make a turn.

For the few vehicles that require good manoeuvrability for its mission, most would be equipped with lateral thrusters for low speed manoeuvers. Examples included ECA's ALISTAR 3000 and University of Southampton's Delphin2 (Phillips et al., 2013), both of which are equipped with lateral thrusters that provide off axis thrust for steering and depth controls. These hover capable AUVs often have extremely small turning circles and many can turn on the spot with an effective turning circle diameter of zero. However, effectiveness of lateral thrusters is reduced when the AUV speed increases, so these torpedo shaped AUVs would revert to conventional control surfaces for directional control when travelling at speed (Palmer et al., 2008).

Many marine animals swim using oscillating or undulating foil propulsor for propulsion and manoeuvring, the propulsor's alignment has a significant effect on the animals' manoeuvrability in certain axes. Most fish species are very manoeuvrable in yaw due to their vertically aligned tail, but many of their predators, such as dolphins and penguins, have horizontally aligned propulsors which are less effective for steering yaw but more effective in pitch.

Some predators overcome this limitation by changing their pattern of movement by introducing roll into their turn. Penguins and seals roll their body during a turn to take advantage of their superior turning ability in pitch, and they have been recorded to turn at a rate of 550°/s and 690°/s respectively (Fish, 2004).

Regardless of the propulsion methods or gaits, an animal or vehicle needs to produce force and torque to propel and steer itself and to overcome various types of resistance such as mass inertia and hydrodynamic drag. The linear translational motion of a vehicle or animal is governed by the Newton's second law of motion (2-1), while the rotational motion is governed by the Euler equation (2-2) (Nahon, 1996).

$$F = ma \qquad (2\text{-}1)$$

$$M = I\dot{\omega} + \omega \times I\omega \qquad (2\text{-}2)$$

There are three components to consider when analysing manoeuvring dynamics of animals and vehicles – the body/hull, the control surfaces, and the propulsor. A simple model for analysing underwater vehicle manoeuvring dynamics has been proposed in Nahon (1996). It is based on ships and submarine manoeuvring models, and analysed the effects of each vehicle component individually and then recombined them to produce the final results.

The five key forces and moments components contributing to the vehicle manoeuvring dynamics are:

- Gravitational forces, (F_g, M_g)
- Buoyancy, (F_b, M_b)
- Propulsive, $(F_p,\ M_p)$
- Control, (F_c, M_c)
- Hydrodynamic , (F_h, M_h)

A detailed description on how these forces are incorporated into equations (2-1) and (2-2) can be found in Nahon (1996). In summary, each vehicle component (hull, control surfaces, propulsor …) would produce a certain amount of each of these five forces. All of these would contribute to the resultant force and moment acting on the vehicle. Since each component produces force differently, the resultant force of each vehicle component would be calculated separately around the component’s centre of pressure. The total vehicle resultant force and torque would be calculated from the total force produced by each component, and the distance between the vehicle centre of mass and the component’s centre of pressure. As such, certain components such as control surfaces perform best when placed away from the vehicle centre to maximise steering torque, but centre of buoyancy and gravity should be close together horizontally to avoid introducing unwanted pitch moment on the vehicle.

Since a vehicle’s manoeuvring model can be broken down into contributions from various components, it is possible to take out individual components and research it and make improvement. The improvement should carry over when it is reintegrated into the whole vehicle. As such, this research on improving manoeuvrability will concentrate on one component of the platform, namely the aquatic flight propulsor on the animal.

2.4 Limitation of AUV Propulsion and Manoeuvring

When a vehicle travels in water, it needs to produce a constant thrust to overcome the hydrodynamic drag acting on the body. Drag is proportional to the square of velocity, so the quicker a vehicle travels, the greater thrust would be required to overcome the resistance. If the vehicle needs to accelerate, it needs to produce more thrust than drag. Otherwise the vehicle would slow down if drag is greater than thrust. Likewise, when a vehicle needs to change direction, it needs to apply a force to induce a moment in order to make the turn.

Of the five forces acting on an underwater vehicle, gravitational force (weight) and buoyancy are usually fixed. The hydrodynamic forces acting on the hull (included lift and drag) depend on the vehicle velocity and are not directly controllable. Therefore, the two forces the vehicle can control are the control force and the propulsion forces. Control forces are applied by control surfaces and lateral thrusters, while propulsion forces are produced by the propulsor.

This section gives a brief overview of the two main sources of control and propulsion force for manmade AUV, namely control surfaces and propellers.

2.4.1 Control Surfaces

The control surfaces in an AUV are hydrofoil. When a hydrofoil moves through a fluid medium at an angle, it deflects the fluid stream and generates a side force perpendicular to the foil motion (lift) which can be used for various purposes such as maintaining depth and direction control. The lift force generated by the hydrofoil is determined by the angle of attack and the square of the foil velocity. Generally the foil velocity is determined by the vehicle speed, so the only control variable is the angle of attack which is determined by the foil's pitch angle. Foils with controllable pitch are used in many steering applications such as ship's rudder and aircraft elevators. Details of its operation can be found in many fluid mechanics books such as Molland and Turnock (2007)

In a brief summary, the control surface steer the vehicle by producing a steering torque that acts on the vehicle’s centre of the resultant force. The steering torque on the vehicle depends on the total force produced by the control surface and the distance between the control surface and the vehicle’s centre. The effective steering torque can be increase or decrease by changing the placement of the control surfaces. A smaller surfaces placed further away from the centre can generate the same amount of steering torque as larger surfaces placed nearer the centre. Since smaller control surfaces produce less drag during cruise and it can improve a vehicle’s efficiency while cruising. On the other hand, if a vehicle needs a control surface to apply a constant force for depth control, it will benefit from a larger surface placed closer to the vehicle’s centre as less energy will need to be expended to counteract the unwanted torque produced.

Control surface produces force when the hydrofoil intercepts the fluid flow at an angle and deflects the fluid flow. The angle between the foil chord line and the inflow direction is known as the angle of attack, α. The forces generated perpendicular to the flow is known as lift, F_L, and forces generated along the direction of the flow is known as drag, F_D. The foil forces are functions of the fluid density (ρ), inflow velocity (V_{in}), and foil area (A), as well as the non-dimensional lift and drag coefficients (C_L, C_D). The formula for calculating foil lift and drag forces are given by equation (2-3) and (2-4).

$$F_L = \frac{1}{2}\,\rho\, {V_{in}}^2 C_L A_{foil} \qquad (2\text{-}3)$$

$$F_D = \frac{1}{2}\,\rho\, {V_{in}}^2 C_D A_{foil} \qquad (2\text{-}4)$$

The values of lift and drag coefficients depend on the foil’s angle of attack, but their relationships are not straight forward, because lift and drag coefficients are also dependent on variables such as foil shape and Reynolds number. The lift and drag coefficients of some common foil profiles are available in published data tables, but the coefficient of less common foil profiles often have to be measured experimentally or find through detailed computer modelling.

Whilst a hydrofoil's lift force is controlled by the pitch angle, which in turn determines the angle of attack and the lift coefficient, there is another important variable to consider – the inflow velocity. The foil force is proportional to the square of the inflow velocity and the inflow velocity of a control surface is determined by the vehicle's speed, or in the case of a control surface mounted aft of the propeller, the outflow velocity of the propeller.

It can be seen from equation (2-3) and (2-4) that the control surface have a potential to produce a large steering force when the vehicle is moving at speed, but it will become less effective when the vehicle is travelling slowly and will stop producing any steering force when the vehicle becomes stationary, such as when the vehicle is at hover. As such for a vehicle designed for mission with a slow speed or hover phase must have an alternative direction control system, such as a lateral thruster, to steer the vehicle at these speed.

2.4.2 Propellers and Thrusters

The propeller is the most common aquatic propulsor in manmade systems, and it is consists of a number of hydrofoils rotating around a hub. The rotational motion of a propeller increases the inflow velocity into the propeller blades, changes the inflow angle, and adds energy and momentum to the flow.

The mechanics of propeller is well developed and can be modelled by one of the following three theories: the momentum theory, blade element theory, and circulation theory (Prandtl and Betz, 1927; Seddon, 1990; Healey et al., 1994; Abu Sharkh et al., 2003; Lewis, 1988). Adaptations of these methods were also used in the for studying animal swimming and flying (Blake, 1979; Lighthill, 1971; Sfakiotakis et al., 1999; Forng-Chen et al., 2004; Sane and Dickinson, 2002; Dickinson et al., 1999).

In summary, the momentum theory treats the propeller as a black box that changes momentum of the flow and does not consider how thrust is produced. A more advanced model is needed to study the mechanism behind the thrust production. The Blade Element Theory (BET) is based on theory of aerodynamics and was adapted to study propeller design by Prandtl and Betz (1927). This method divides the propeller blade radially into a number of individual blade elements. Each element is analysed as a separate hydrofoil and then their results are integrated to calculate the total force produced by the propeller blade. Detail description of blade element theory for propellers can be found in Molland and Turnock (2007).

2.4.2.1 *Off Axis and Transient Thrusters*

Whilst the steady state operation of a propeller is fairly easy to calculate using the models described in the previous sections, additional complication exists when the propeller operates in transient mode or operates at an angle to the inflow current such as when the propeller is used in a steering thruster. A model for a propeller operating in transient mode will need to account for effects such as added mass of the fluid and potential foil stall when the blades' angle of attack exceed the stall angle. A propeller operating at an oblique angle also has to account for flow difference on the advancing half of the propeller and the receding half. This section will outline some of the limitation associated with propeller operating in off axis and transient modes.

During steady state operation, a propeller thrust is proportional to the square of the propeller's rotation speed (Cody, 1992; McLean, 1991), but an additional term is needed to account for the added mass when the propeller accelerates or decelerates (Healey et al., 1994). Details of a transient model can be found in (Healey et al., 1994) but in a brief summary an added mass force term is added to the thrust calculation and this term is described by equation (2-5).

$$F_{AM} = (\rho A L \gamma)\dot{U}_a \qquad (2\text{-}5)$$

The added mass force is dependent on the acceleration that is described by $\dot{U}_a$. γ is the effective added mass ratio. The added mass force causes a delay in the propeller's transient response such that the propeller will take longer to build up speed.

In addition to propulsion, propellers based thrusters are used by many vehicles for direction control and require more advanced model to analyse their operation during manoeuvring. As previously mentioned control surfaces are ineffective at low or zero vehicle velocity, so propeller based thrusters are required for steering a vehicle at low speed. Some vehicles use fixed thruster mounted in external pods, some use internal thrusters mounted inside through hull tunnels, and some use steerable thrusters.

External thrusters are usually self-contained unit that can be fitted to vehicle with minimal impact to the vehicle internal design. However these thrusters can be a significant cause of drag during cruising so they can reduce the overall propulsive efficiency. The thruster drag can be reduced by internalising the lateral thruster. An internal thruster with a well-designed tunnel thruster entrance can minimise the interference with external flow and reduce the impact of the thruster. However internal thrusters do require hull penetration and can use up valuable space in a vehicle. (Palmer, 2009)

The varying performance of thrusters at different speeds is related to the way the thruster jet interacts with the ambient flow. A thruster is most efficient when the jet velocity is significantly higher than the ambient flow velocity. As ambient flow speed is increased, the speed ratio between ambient flow velocity and jet velocity is increased and this leads to a reduction in the thruster's effective force. At very low speed of advance (low speed ratio), the thruster force are very close to the thrust produced predicted by conventional propeller model. However, when the vehicle starts to move, the thruster jet is deflected and its effectiveness is reduced. The relationship between the thruster effective force and the speed ratio between the jet velocity and ambient flow velocity is shown in Figure 2-4. Further details of tunnel thruster dynamics and thruster-hull interaction can be found in Palmer (2009).

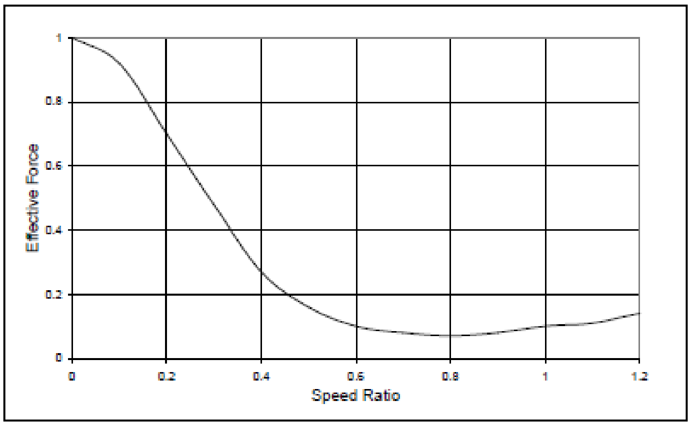

Figure 2-4 – Tunnel thruster effective force vs ambient flow velocity-jet velocity ratio (Palmer et al., 2008)

When a propeller operates at an angle to the incoming flow, conventional wisdom may suggest the propulsive force generated by the propeller could be calculated by multiplying the thrust with the cosine of the angle. However, experiments performed by Kim and Chung (2006) and others showed this is not true and suggested there are other forces and effects at work. Kim and Chung’s thruster model investigated the effect of angled inflow. The model is based on the momentum theory and divided the thruster flow into three regimes based on their inflow angle and reaction from ambient flow, namely the Equi-directional, anti-directional, and the vague-directional state. Each of these states exhibit different behaviour and have different effects on the thrust coefficient. The three states are separated by the Critical Incoming Angles, θ_1^* and θ_2^*. Further details on this can be found in Kim and Chung (Kim and Chung, 2006).

2.4.3 Summary

Conventional AUVs and other manmade vehicle relied on two type of propulsor for direction control – the control surface and the propeller. Both systems have the merits and limitation.

The force produced by a control surface depends on the square of the inflow velocity, foil angle of attack, and the inflow angle. As such control surfaces are most effective when the vehicle is cursing at high speed, but loses their effectiveness when the vehicle slows down. Control surfaces cease to function when the vehicle is stationary and the vehicle must switch to propeller based lateral thruster for manoeuvring.

Most AUVs use propeller for propulsion and some also utilise propeller in lateral thrusters for steering. A propeller’s thrust is normally proportional to the square of the rotation rate when the propeller is mounted in line with the flow and rotating at a constant velocity. However, when the propeller accelerate or decelerate, added mass effect from the surrounding fluid would delay the propeller’s transient respond. As such the transient effect from added mass should be considered when analysing animals’ propulsor.

Additional complication occurs when the thruster is mounted at an angle to the flow. In a tunnel thruster, the thruster jet could be deflected by the ambient flow, which would reduce the jet’s effectiveness. The thrust reduction depends on the ratio between the thruster jet velocity and the ambient flow velocity. Thruster efficiency decreases as the ambient flow velocity (vehicle travel velocity) increases. If the propeller is un-ducted or have a short duct, the interaction between the rotating propeller disk and the angled inflow can become very complicated.

Since control surfaces and lateral thruster performance are affected by vehicle speed, a vehicle designed to operate at a range of speed needs both manoeuvring system. This could increase the vehicle’s drag and complexity of the design. Therefore a novel biologically inspired propulsion and manoeuvring system that is effective at both speed regimes would be very useful for the future AUV.

2.5 Animal inspirations

Marine animal locomotion is extremely diverse as a result of billions of years of evolution. This continuous development along multiple independent routes has led to dozens of distinct propulsion strategies in modern marine animals. Occasionally, unrelated animals would independently evolve very similar solutions to a problem in a process known as convergent evolution. These converged solutions often represent an optimum solution to the given problem.

Current theories suggested life began in the depth of the ocean around 3.5 billion years ago during the Archean era as simple single cell organisms that drift passively in the ocean current. Gradually these organism evolved locomotion and those that can move to find food and mate has a selective advantage over those that are immobile. The evolution process continued over the billions of years and produced the diverse variety of life seen on earth today.

Animals such as fish, cephalopods (e.g. squid, octopus), and arthropods (e.g. shrimp, crab) represents a continuous non-stop optimisation for oceanic life (Figure 2-5). However, they are not the only animals that live in the sea. There is another class of animals known as the secondary marine animals that evolved from land animals that returned to live in the sea. Most of the terrestrial ancestors for these secondary marine animals lost their original aquatic propulsor when they evolved to live on land, so the secondary marine animals must revolved new means of propulsion for swimming at sea. While some re-evolved a fish like body, others developed locomotion systems that were unique to them and shared very little in common with their fish ancestors (Figure 2-6). In some cases, unrelated secondary marine animals may independently evolve very similar non-fish solutions. This means these new secondary marine animal solutions may represent an alternative optimum.

Figure 2-5 - Examples of various types of marine animals that uses different type of propulsion. Left – Cuttlefish (cephalopods) – uses both jet propulsion and undulating fin for locomotion, Centre - shark (fish) – uses swimming propulsion and manoeuvres, Right – shrimp (arthropods) – swam using its legs in drag base paddling, and uses tail flick for high speed escape manoeuvres. Image Source: Wikipedia 2010 – public domain materials

Figure 2-6 - Various marine animals with terrestrial ancestors. Each of these evolved independently with their unique style of propulsion. Left – Orca (Cetacean) – BCF swimming, Centre – Humboldt penguin, evolved for limb under water flight, Right – Plesiosaurs, Artist impression, four flippers propulsion. Image Source: Wikipedia 2010– public domain materials

One notable convergent evolution is the fusiform body shape used by pelagic fish, such as sharks and tunas, ichthyosaur, mosasaur, cetacean, and sirenia (Figure 5). The fusiform body is wide in the middle and tapered towards the head and tail, with a rounded cross section. Shark and tuna are fish and their fusiform bodies represent the result of millions years of continuous evolution to optimise a fish body for high speed swimming, but many secondary marine animals also independently evolved this body shape from unrelated terrestrial ancestors in different geological periods that are separated by millions of years. Both cetacean and sirenia are mammals, but cetaceans descended from an extinct ungulate carnivore distantly related to the hippopotamus, and sirenia evolved from an herbivorous ancestor related to the elephant. The Ichthyosaurs were Triassic and Jurassic era (250-145Ma) marine reptiles that evolved from a yet to be discovered land reptile. All three groups also evolved their front legs into small flippers for direction control, slowly lost their hind limbs, and developed their tail into flukes. The end results are bodies that looked very similar to each other and also to sharks. (Massare, 1994; Lindgren et al., 2010; Fish, 2004). This suggests the fusiform body shape has a significant advantage over other types of propulsion strategies and there is a strong selective pressure towards this body form.

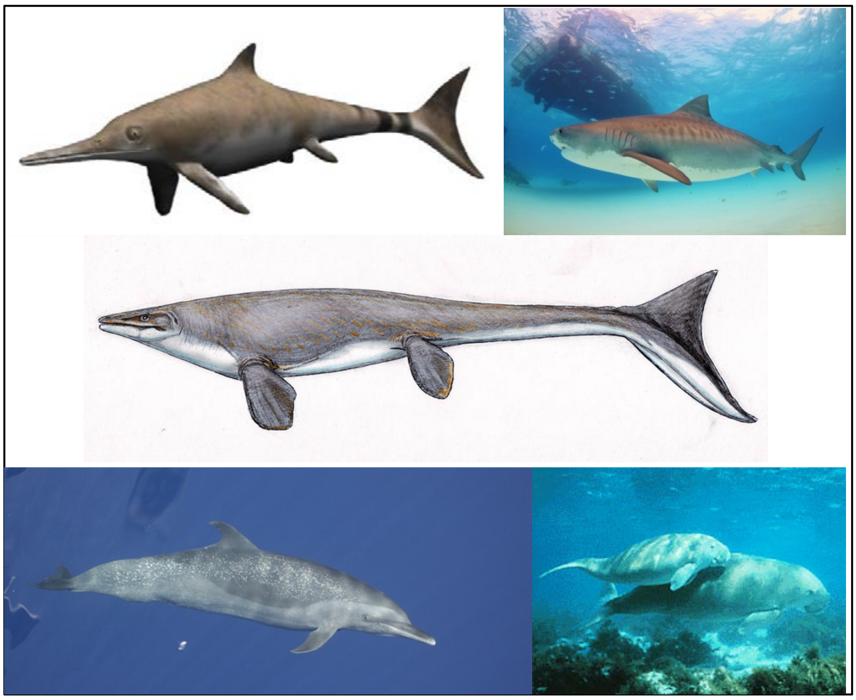

Figure 2-7 - Example of convergent evolution – different animals with different ancestor evolving independently towards the same solution. Top left – Ichthyosaurus - early Jurassic marine reptile with a yet to be discovered terrestrial ancestor. Top right– Tiger shark, a fish. Middle – Platecarpus – a Cretaceous mosasaur – a pre-historic marine monitor lizard. Bottom left – spotted dolphin. Bottom right – Dugong

Another example of convergent evolution is aquatic flight propulsion used by numerous secondary marine animals such as eared seals (Otariidae), penguins, turtle, and plesiosaurs. These animals processed enlarged and elongated high aspect ratio wing shaped flipper that is optimised to lift based propulsion as opposed to the more common fan shaped webbed feet that are optimised for drag based propulsion. The wing-shaped flippers allowed these animal to use the more efficient lift based propulsion that is estimated to be around 80% as opposed to the 33% for drag based propulsion (Fish, 1996; Walker and Westneat, 1997). For comparison an AUV propeller is around 40% efficient (Triantafyllou and Triantafyllou, 1995). Generally animals that utilise aquatic flight relied on their flippers as the main propulsor and direction control. Particularly, the fore-flippers of eared seals (Otariidae) and sea turtles produced most of the thrust when these animals are swimming and act as control surfaces when the animals turn. This case of convergent evolution into aquatic flight propulsion shows aquatic flight is an optimum solution for underwater propulsion and it can serve as an inspiration for a novel propulsion and manoeuvring system for AUV.

2.6 Biological Locomotion

There are many methods of aquatic propulsion and the optimum propulsion method often depends on the Reynolds number (Re) associated with the animal's normal life style. The Reynolds number, as stated in equation (2-6), describes the ratio of viscos forces to inertial forces and a propulsor's efficiency often depend on this number. Inertia forces dominate when the Reynolds number is high and viscous forces dominates when the Reynolds number is small.

$$\mathrm{Re} = \frac{\mathrm{UL}}{\nu} \qquad (2\text{-}6)$$

An animal can be an efficient swimmer in one flow regime but inefficient at another. Generally, foil base propulsion is efficient over the widest range of Reynolds number, while jet propulsion is only efficient at large Re, and flagellum/ciliary propulsion is only effective at very low Re (10^{-3}) (Lighthill, 1969). Most adult fish tends to swim in the inertia dominated region of $10^3 < Re < 10^6$ using fin based propulsion methods (Sfakiotakis et al., 1999). The Reynolds number for the larger animals is not dissimilar to that of AUV, which means the propulsion strategy used by these animals can be carried over to the manmade vehicles.

Fin based propulsion can be separated into two groups based on the appendages used in propulsion. Name of various appendages in a marine animal can be seen in Figure 2-8. The body and caudal fin locomotion (BCF) uses the animal's body and the caudal (tail) fin as the propulsor. This type of propulsion is most commonly associated with fish and cetacean. The other group of fin propulsion is known as median paired fin locomotion (MPF). This group uses either fin pairs (Left-right pectoral fins or dorsal-anal fins pairs) or long elongated fin across the centre line of the fish. BCF and MPF can be further divided into several subgroups based on the fins involved, their shape, and whether the dominant motion is undulatory or oscillatory. The names of various fins on a fish are shown in Figure 2-8 and the various swimming modes and the corresponding active fins are shown in Figure 2-9.

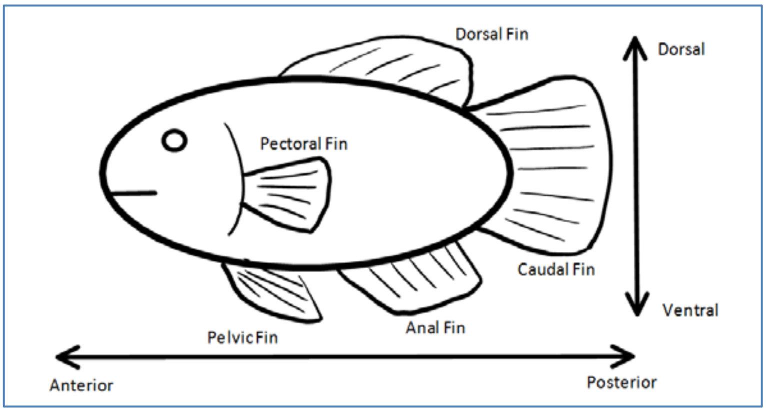

Figure 2-8 – Name of various fins on a fish, and various anatomical directions on animals. (Directions omitted include the lateral directions (left and right) and proximal–distal which describes different ends of a limb/fin (Proximal - towards to body, Distal - away from the body))

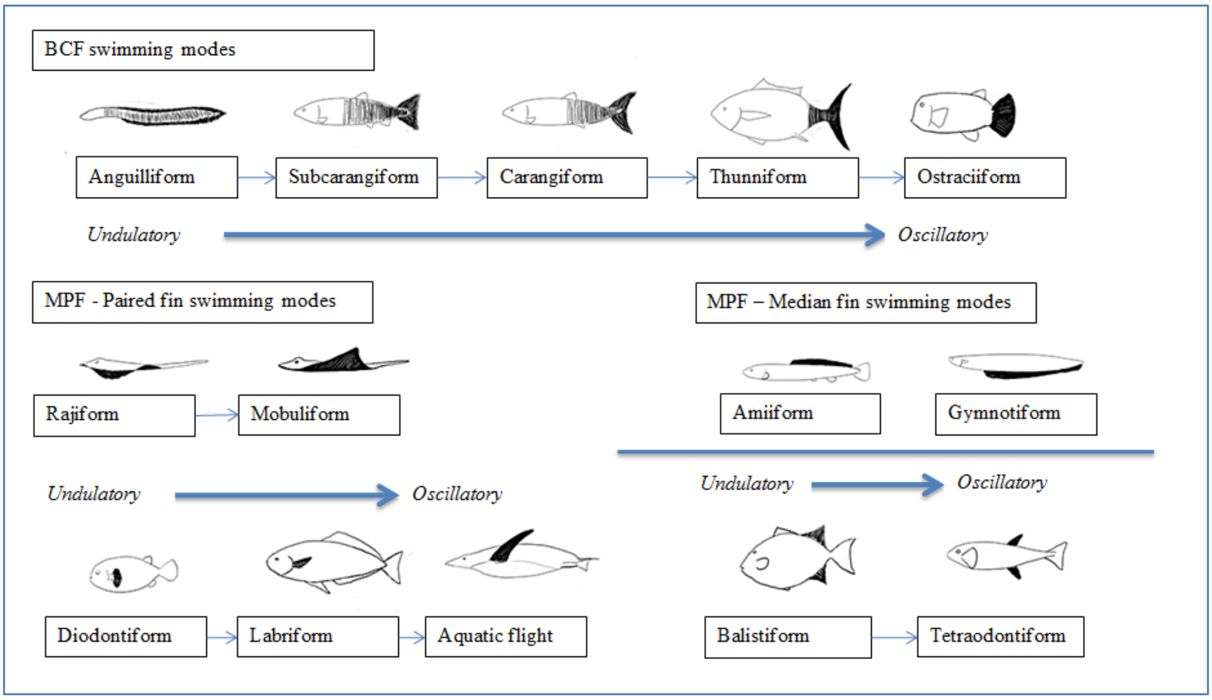

Figure 2-9 – General classification of fish swimming modes (Adapted from(Sfakiotakis et al., 1999; Lindsey, 1979)) Blacken areas denote the fins and parts of the body involved in the swimming mode

In general, most animals that swim using oscillatory lift based propulsion possess wing shaped fins that taper towards the tip. As such, lift based swimming mechanisms (e.g. thunniform, aquatic flight) can be studied using models derived from those that were originally designed for studying aerofoils and hydrofoils (Wu, 1961; Lighthill, 1970; Lighthill, 1971; Read et al., 2003).

Animals swimming using undulatory drag-based propulsion (e.g. anguilliform) are less straight forward, but it can be model using a finite element approach that involves dividing the animal's body into individual segments and then analysing the force and momentum produced by each segment before integrating the segments' results to produce the final results for the whole animal. Details the most well-known of these finite element models - the elongated body theory (EBT) was developed by Lighthill in the 1960's. This is beyond the scope of this research, but details can be found in (Lighthill, 1969; Lighthill, 1971).

Aquatic flight belongs to the oscillatory lift based MPF group and is closely related the other pair fin lift based propulsion such as labriform and mobuliform propulsion. In the case of the fish and rays, their pectoral fins are equivalent to the secondary marine animal's forelimbs. Many fish can switch between MPF and BCF swimming to suit their swimming speed (Webb, 1994; Walker and Westneat, 1997; Walker and Westneat, 2002), but aquatic flight and mobuliform swimmer relied exclusively on their pair fin for propulsion.

Mobuliform and Rajiform are swimming styles used by batoid fish (rays) and some cephalopod species such as cuttlefish and squid. These swimming styles utilise paired elongated pectoral fins (or swimming skirt in the case of cephalopods) that are almost as long as the animal's body. Mobuliform is a lift base mechanism used by pelagic species, such as manta rays, and it is characterised by the oscillatory beating of the large elongated pectoral fin for propulsion (Jun et al., 2007; Clark and Smits, 2006; Rosenberger and Westneat, 1999). Rajiform is a related drag based propulsion mechanism that produce thrust by generating a locomotory wave along the elongated pectoral fins, and it can produce very precise movement at low speed (Aitken and O'Dor, 2004). The transition from one to the other is gradual and some species are able to switch between the two modes of propulsion.

Labriform and Diodontiform locomotion are MPF swimming styles used by most fish, and both mechanisms use the fish's pectoral fins for producing thrust. Labriform is a lift based oscillatory mechanism that produces thrust with a dorsoventral motion (up-down), whereas diodontiform is predominantly a drag based mechanism that produces thrust using an anteroposterior (forward-backward) rowing motion with powered and recovery stroke. Labriform is more efficient and produce more thrust than diodontiform at higher velocity, but diodontiform can produce more thrust at lower velocity (Walker and Westneat, 1997).

Due to the closely related hydrodynamics between aquatic flight, mobuliform and labriform propulsion, techniques designed to study one of these mechanism can be readily applied to study the others.

2.6.1 Overview of Aquatic Flight Locomotion

Aquatic flight is a propulsion strategy used by a large numbers of secondary marine animals past and present, with sea turtle, penguins and the extinct plesiosaurs being the most well-known. The fore-limbs of sea turtle, otariidae seals (eared seals) and plesiosaurs evolved into wing shaped flippers from ancestors with paddle type limbs. Unlike the flippers on cetacean and ichthyosaurs which act as control surfaces, aquatic flight animals use their front flippers as their main propulsor and they generate thrust for propulsion as well as manoeuvring. Whilst paired fin propulsion is generally believed to be less efficient than body and caudal fin propulsion, lift based aquatic flight propulsion mechanism were found to have efficiencies up to 80% (Feldkamp, 1987b). While this may be slightly less efficient than body and caudal fin mechanism used by fish and cetaceans, it gives the animal better manoeuvrability in water and some mobility on land.

Flippers used in aquatic flight often have locked joints, flattened bones, and minimal muscle mass. The elbow joints in some species are locked by connective tissue to enhance the flipper stiffness, while muscle and other unnecessary tissues were lost to reduce the cross sectional area of these flippers to minimise drag. The foil takes on a wing shape that narrow towards the tip, which is opposite to the typical fan shape fin used by animals optimised for drag based diodontiform propulsion.

The aquatic flight propulsors generate thrust almost continuously over a stroke cycle using hydrodynamic lift. The foil typically oscillates in a dorsoventral manner (up and down) and produce thrust in both strokes. Ideally, the up and down strokes should be symmetrical and produce the same force, but some species may not be able to achieve this due to physiological limitations or have the need to generate a vertical force for depth control. The propulsion cycle only produces net drag at the apex of each stroke where the foil reverses direction. This ‘recovery’ phase only account for a small percentage of the stroke cycle compared to the much longer recovery stroke in drag based propulsion cycle. The foil propulsor’s angle of attack has an intermediate value of up to 60°, which is less than the angle typically seen in drag based propulsion. Similar to some fish that is able to switch between labriform and diodontiform locomotion depending on the situation, animals using aquatic flight propulsion can also switch between the lift-based aquatic flight stroke and a drag based rowing stroke should the need arise. For example, the penguins and sea turtles propel themselves using lift based synchronised dorsoventral flapping almost exclusively while cruising, but both switch to drag based asynchronous paddling whilst manoeuvring at low speed.

Compared to the lift base propulsion cycle, the drag based paired fin propulsion, such as diodontiform locomotion, has two distinct phases signified by two very different strokes, the power stroke and the recovery stroke. In the power stroke, thrust is generated by first orientating the fin in the plane perpendicular to the foil movement ($\alpha \sim 90°$) and maximising the fin area by expanding (adducting) it. This is followed by the stroke that pushes against the water and generates thrust. The power stroke is follow by a recovery stroke where the fish re-orientate the fins into a plane parallel to the actuation motion ($\alpha \sim 0°$), contract (abducting) them and feather them forward and return them to the initial starting positions. The recovery stroke aims to minimise drag during the return to the starting position, but the recovery stroke is a significant net drag phase nevertheless. In addition to the drag forces produced by the strokes, the rotational motions of the fin can also have a small contribution to total force (Walker and Westneat, 1997). Fins optimised for drag based propulsion typically have large paddle shaped fin that expands towards distal end (Blake, 1981; Walker and Westneat, 2002). This shape maximised area in the thrust production region near the tip.

Detailed mathematical models of pectoral fin swimming can be found in a series of papers by Blake, Kato, Walker and Westneat (Kato and Furushima, 1996; Walker and Westneat, 1997; Kato, 2000; Walker and Westneat, 2002; Forng-Chen et al., 2004; Blake, 1979). A blade element theory description of labriform propulsion is discussed in detail in this thesis.

When investigating aquatic flight it is important to remember the process of evolution towards aquatic flight faces many limitations and these often directly affect an animal’s swimming pattern. As such the aquatic flight used by certain animals may not be the optimum form of aquatic flight as the animal need to form a compromise between their swimming performances with other priorities such as mobility on land. For example, skeletal analyses show neither seals nor plesiosaurs could lift their humerus above horizontal, which prevented them from using a full aquatic flight motion, instead their actuation cycle is a hybrid cycle that contains a powered and recovery phase found in drag based strokes (Massare, 1994). Penguins on the other hand, can lift their flipper above horizontal by as much as 45° and can swim using a pure lift based cycle (Bannasch, 1994; Watanuki et al., 2006; Fish, 2004; Massare, 1994). Seal and plesiosaur need to use all four limbs for walking on land whereas penguin is bipedal, and this suggests the seal's stroke may be a compromise between hydrodynamics and terrestrial mobility whereas the penguin's stoke may be more representative of an optimum aquatic flight stroke.

All living aquatic flyer (e.g. penguins, sea lions, sea turtles etc…) evolved their front limb into highly developed wing shaped flippers for propulsion, but their hind limbs are less developed and are only used for steering and walking on land. During normal swimming, their hind limbs trail passively behind the body and have no significant contribution to propulsion. However, the fossils of the extinct plesiosaurs show there is an alternative type of aquatic flight that uses four flippers. Fossil analysis show plesiosaurs' hind flippers were as well developed as their fore-limb which suggests plesiosaur hind limbs were actively used in propulsion.

Since no living animals use four flippers propulsion strategy similar to one used by the plesiosaurs, it lead to the question, how did the plesiosaurs swim with four flippers? Skeletal analysis showed plesiosaurs flippers structure resemble that of living sea lions, which suggest they may have a similar stroke pattern (Massare, 1994). Experiments by Long et al (2006) suggested a four flipper mechanism provides superior acceleration to that of a two flipper system, but had a significant penalty for cruising. Their experiment also show differences in efficiency based on gait pattern. This effect was expected as the rear flippers operate in the wake of the front flippers, if the rear flipper interacted destructively with the wake of the front flippers, it would reduce efficiency. On the other hand, if the flippers interact constructively the motion of the rear flipper would contribute to propulsion.

Plesiosaurs were ambush predator, where short distance burst speed would be more important to the animals' survival than long distance cruise efficiency. It is possible the four flippers strategy came about when the animal cannot enlarge a single pair of flipper further due to structural limitations, as such the number of flipper must increase to give the plesiosaur additional thrust needed for hunting. Since seal's hybrid stroke cycle can produce more thrust than a pure lift based cycle, it also supports this hypothesis.

Since aquatic flight propelled animals utilise two or four mostly identical propulsors, only one flipper needs to be modelled and its results can be applied to the other flipper units. A number of different models have been proposed to study aquatic flight and labriform propulsion, including a kinematic model which describes the aquatic flight propulsor's motion through two sinusoidal equations (Licht et al., 2004b; Techet, 2008). In addition to models for aquatic flight, models for aerial flights are also relevant to this study. A blade element approach was used to studying insect flight (Ansari et al., 2006) and drag based diodontiform locomotion (Blake referred to as labriform) (Blake, 1979), and this method can be adapted to study aquatic flight. Vortex interactions between flippers have been studied by Long et al. (2006) but is beyond the scope of this research.

2.6.2 Studies of the hydrodynamic of aquatic flight

Whilst there are many existing research in MPF propulsion such as diodontiform, labriform, rajiform and mobuliform, studies that focuses in aquatic flight as a propulsion mechanism is less common. The most extensive hydrodynamics studies to date are those performed by a research group in Massachusetts Institute of Technology (MIT) through experimentation (Licht et al., 2004a; Licht et al., 2004b; Flores, 2003; Techet, 2008). Their research was based on previous work on a pure heave foil which simulated the hydrodynamics of a tuna tail (Read et al., 2003; Hover et al., 2004; Anderson et al., 1998; Anderson and Chhabra, 2002). The pure heave foil work eventually gave rise to Robotuna and VCUUV, while the flapping foil work lead to the Finnegan AUV.

The flapping foil experiments consist of two parts, the first part tested a number of two-axis (pitch and roll) flapping foil actuators in a water tunnel and towing tank, while the second part mounted four of these actuators in a free swimming AUV – Finnegan (Figure 2-10).

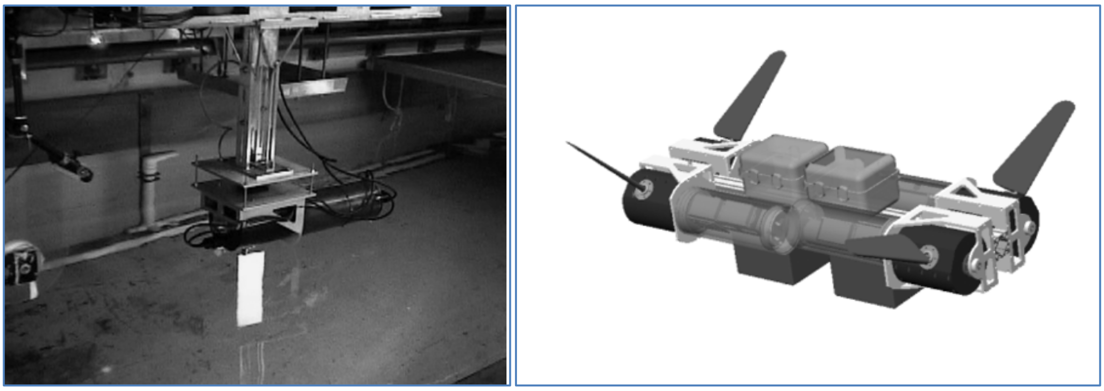

Figure 2-10 – (Left) MIT's flapping foil towing tank experiment. (Right) Illustration of the Biomimetic flapping foil autonomous underwater vehicle (BFFAUV) (which eventually became Finnegan) (Licht et al., 2004b)

The kinematic model describing two axis (pitch and roll) aquatic flight motion use two sinusoidal equations ((2-7), (2-8)).

$$\phi(t) = \phi_o \, sin\left(\omega_\phi t + \beta_\phi\right) + \phi_{bias} \qquad (2\text{-}7)$$

$$\theta(t) = \theta_0 \, sin(\omega_\theta t) + \theta_{bias} \qquad (2\text{-}8)$$

The towing tank experiment examined the thrust and 'lift' force of the flapping cycle, with and without pitch bias, by testing at a range of Strouhal number from 0.2 to 1.0 and an angle of attack between 20° and 60°. The thrust coefficients were between 0 and 5 in the range examined. The follow up experiment with the Finnegan AUV found the four wing propelled vehicle have exceptional manoeuvrability and capable of doing a turn in less than one body length. Further details of their results can be found in a number of paper and thesis published by the group (Licht et al., 2004a; Licht et al., 2004b; Flores, 2003; Techet, 2008).

2.6.2.1 *Blade Element Method for Studying Flapping Wing Propulsion*

Aquatic flight locomotion involves a flapping foil rotating around a pivot at the root end of the foil. This rotational motion causes different parts of the foil to move at different velocities depending on the distance from the pivot. As such, the foil sections near the tip of the foil will experience greater inflow and flapping velocity than the foil root. This span-wise variation in flow and the periodic oscillation of the foil makes it difficult to simplify the aquatic flight problem into a form that can be solved by either a two-dimensional or steady state model. The aquatic flight propulsion problem is inherently three dimensional and transient and such problem is difficult to model.

Licht's studies simplified the problem into a two dimensional form by making calculations at 70% of the span. Assessing the foil at 0.7span is the norm for propeller blades analysis as it is believed this is the point where the larger force generated at the tip is balanced by the smaller force at the root. However, while this 0.7span assumption is sufficient for modelling a propeller rotating at constant speed, it is unknown whether this assumption remains valid for a flapping foil whose speed changes constantly throughout a propulsion cycle. Therefore a more complete modelling approached would be to divide the foil into smaller blade elements and analyse them separately.

The Blade Element Theory (BET) method is a simple type of finite element method that divides a foil span-wise into small segments which are to be analysed independently. This method is commonly used in engineering, but has not been used for modelling aquatic flight. Nevertheless, it has been used for studying aerial flight and Blake R.W. (1979) used it to analyse the mechanics of the drag-based power stroke of an angelfish. While the angel fish stroke pattern is closer to the drag based diodontiform, the methods can be adapted to study lift based flapping foil propulsion.

The original Blake's BET model uses 4 blade elements from tip to root. The foil is swept along an anteroposterior path in yaw, rather than the dorsoventral path in lift based labriform locomotion. Equations (2-9) and (2-10) give the normal (v_r) and spanwise (v_s) velocity component.

$$v_n = \omega r - V \sin\psi \tag{2-9}$$

$$v_s = V \cos\psi \tag{2-10}$$

As the foil moves through the water, it generates lift and drag. The force acting normal to each blade element is given by equation (2-11), where ρ is the density of water, A is the area of the blade element, and C_n is the normal force coefficient (roughly equates to the drag coefficient).

$$dF_n = \frac{1}{2}\rho v^2 dA C_n \tag{2-11}$$

Blake's model used the force coefficient for a flat plate at a high angle of attack to simulate the fin on the fish. The foil is expected to operate at a Reynolds number between 10^3 and 10^4 for most of the power stroke with an angle of attack between 40° and 90°. At these angles of attack and Reynolds number, the C_n is approximately 1.1 (Blake, 1979). This simple force coefficient can be applied because of the diodontiform locomotion, where the foil alternates between very high and very low angle of attack. By comparison, aquatic flight foil operates at much lower angles of attack throughout most of the propulsion cycle and this will require a more complex model to be created for calculating the foil's lift and drag coefficient.

The foil force that was calculated for each element would be summed together to produce the total foil force. This foil force can then be used for calculating various parameters such as thrust, energy expenditure and efficiency. Blake's BET model and Licht's kinematic model would form the bases for the blade element aquatic flight model used in the current research. There are many differences between aquatic flight locomotion and the diodontiform locomotion motion and the underlying mechanics, so new components and sub-models will need to be developed in order to overcome the aforementioned shortcomings and accurately model aquatic flight.

2.6.3 Aquatic Flight Foil Path

Existing studies of the hydrodynamic of aquatic flight (e.g. (Licht et al., 2004b; Flores, 2003; Techet, 2008)) modelled wing actuation in two axis – pitch and roll. However, published zoological literature suggests that most aquatic flight foil actuation paths have an additional component in yaw, whose effect is unknown.

Aerial flights performed by birds and insects contain a significant yaw component. Most aerial flight foils also follow an asymmetric path where the upstroke takes a different path to the downstroke. The asymmetry is needed because the wing has to generate lift to support the animal's weight in air (Ansari et al., 2006; Sane, 2003). In comparison, most marine animals are neutrally or nearly neutrally buoyant, so they do not need to generate significant lift force or down force. Nevertheless, stroke asymmetry has also been observed in marine animals using aquatic flight and the related labriform propulsion.

The foil motion of labriform propulsion in fish has been studied extensively by Walker and Westneat (1997) using video motion capture on a negatively buoyant tropical coral fish known as bird wrasse (*Gomphosus varius*). The fish was filmed swimming between 1-6BLs^{-1} at 60Hz using two cameras, one recorded the dorsal view and the other recorded the lateral view. The study found the fin tip of this fish moved in a thin figure-of-eight with a 20° incline angle. Figure 2-11 shows the mean fin tip displacement for the fish. Angle of attack is mostly positive during the down stroke and negative in the up stroke. Likewise, the distal fin chord has a negative pitch angle during the down stroke and a positive pitch angle during the upstroke. However, the stroke is asymmetric, such that the down stroke produced more vertical lift force than horizontal thrust, but the up stroke produced mostly horizontal thrust.

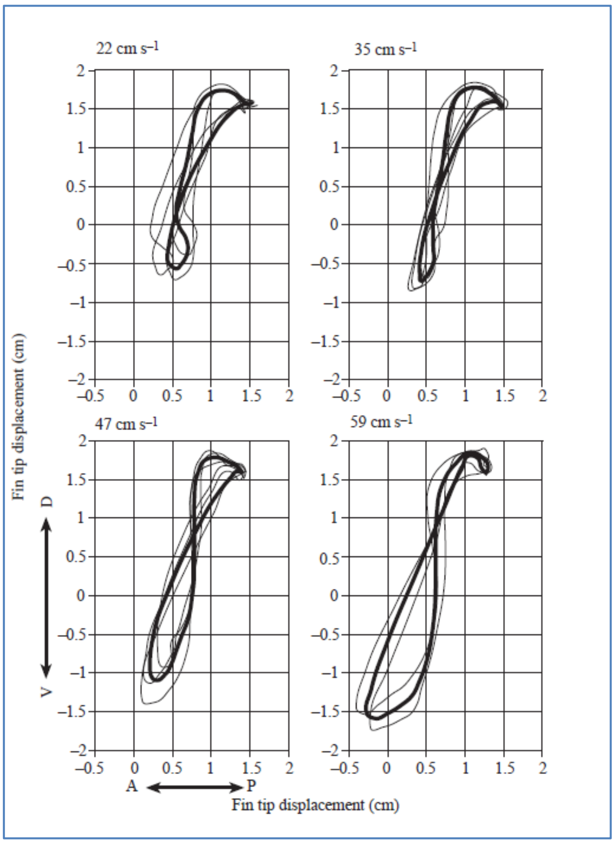

Figure 2-11 – Fin tip displacement recorded by Walker and Westneat for a fish (*Gomphosus varius*) swimming using labriform locomotion (Walker and Westneat, 1997)

In addition to mechanics of aerial flight and labriform propulsion, a number of studies of aquatic flight animal propulsion also show motion in the third axis (Clark and Bemis, 1979; Davenport et al., 1984; Feldkamp, 1987a; Massare, 1994; Rivera et al., 2013). Figure 2-12 shows the results from Clark and Bemis’s (1979) study of penguin swimming motion in a zoo. The plots suggested there may be a yaw component in the motion, but the results are inconclusive. It is not clear if this is caused by physiological limitations of the animal, measurement error or real hydrodynamic benefits that motivated evolution toward three-axis propulsion. Nevertheless it demonstrated that aquatic flight dorsoventral flapping may not be a straight forward combination of pitch and roll of the flapping foil, but a more complex interaction of pitch, roll and yaw.

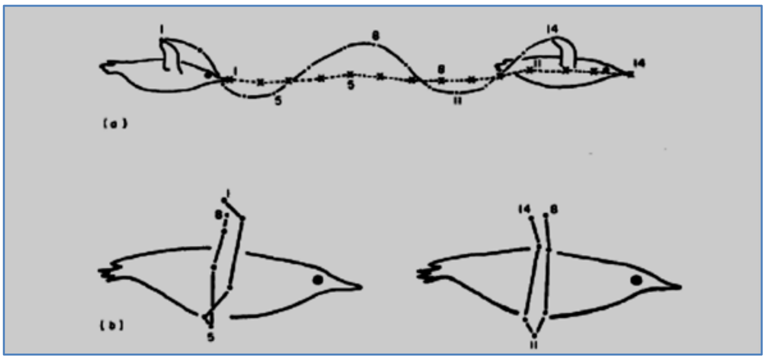

Figure 2-12 – Path followed by penguin wing during aquatic flight propulsion (Clark and Bemis, 1979)

Sea turtles are another animal group that utilise aquatic flight for underwater propulsion. Sea turtles and the pig-nose turtle (a fresh water species) have high aspect ratio wing shaped foreflippers optimised for lift based propulsion. The sea turtle utilises synchronised dorsoventral flapping at normal swimming speeds, like that of penguin, but switches to asynchronous alternating flapping at low speeds, similar to the gait used by fresh water species (Walker, 1971; Davenport et al., 1984; Rivera et al., 2013).

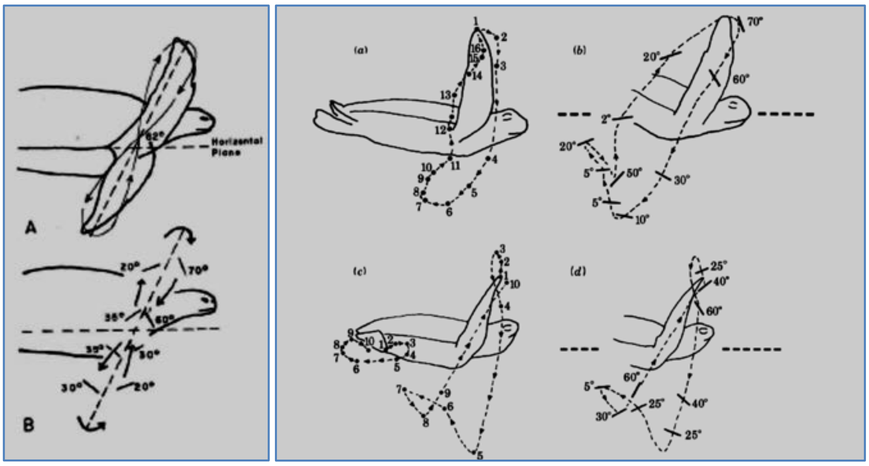

Figure 2-13 – Sea turtle flipper actuation path. Left: Early observation carried out by Walker WF on free swimming turtle. It suggested the foreflipper followed a figure of eight path (Walker, 1971). Right: (a) Blade tip position in normal swimming. (b) Blade pitch angle in normal swimming. (c) Blade tip position in high speed swimming. (d) Blade pitch angle in high speed swimming. (Davenport et al., 1984)

Early studies suggest the foreflipper of the turtle follows a figure-of-eight path (Walker, 1971). The study filmed several species of sea turtles, free swimming, in an aquarium through a pot hole at 32Hz. The study analysed the swimming style of four species and found their swimming style to be very similar. The four species studied were the green turtle (*Chelonia mydas*), Hawksbill (*Eretmochelys imbricata*), Ridley (*Lepidochelys kempii*), and loggerhead (*Caretta caretta*). Figure 2-13 (Left) shows the path described in the study. The actuation path takes the shape of an inclined figure-of-eight with an inclination between 40° and 70° from horizontal. The flipper moved posteriorly (backwards) during the down stroke and anteriorly (forward) during the upstroke. The distal end of the flipper has a maximum pitch angle of 80° during the down stroke and 35° during the up stroke.

However, more recent analysis of sea turtle swimming showed their actuation paths do not intersect mid-stroke, but follow a more oval shaped path (Figure 2-13 (Right)) (Davenport et al., 1984; Rivera et al., 2013). Davenport's (1984) study investigated the flipper actuation of juvenile green turtle (*Chlelonia mydas*) using TV cameras. It found the up stroke and down stroke followed a different path, and each stroke cycle showed a secondary peak. A very similar stroke pattern was also observed for the loggerhead sea turtle (*Caretta caretta*) (Rivera et al., 2011).

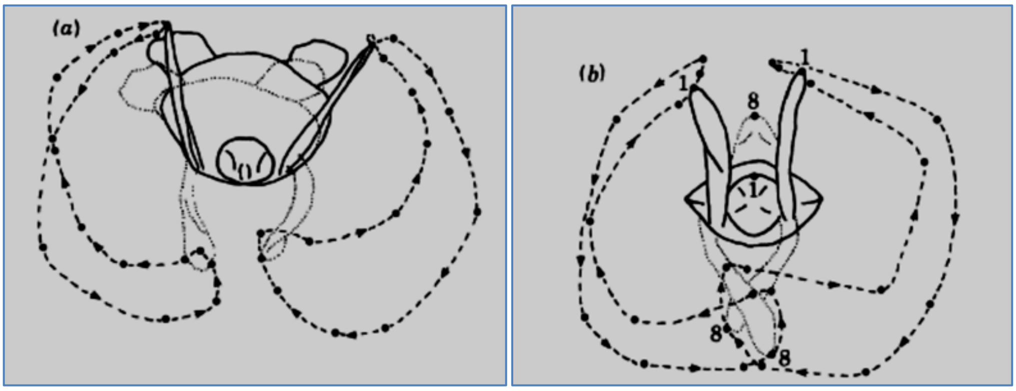

Figure 2-14 – Frontal view of the path traced by the tip of green sea turtle's front flipper during (a) normal swimming and (b) high speed swimming (Davenport et al., 1984)

This second loop in the transition between the down stroke and the up stoke is caused by the flipper's flexibility. The sea turtle flipper is not completely rigid, so there is a lag between the action at the root of the flipper and that at the tip. The effect is most visible at the end of the down stroke where the humerus (upper arm bone) begins to move upwards but the tip continues to move downwards (Figure 2-14 (Left)). At higher swimming speed the sea turtle’s left and right flippers can overlap (Davenport et al., 1984) (Figure 2-14 (Right))

A similar study of turtle limb motions was carried out by Rivera et al., (2013) which investigated the propulsion gait of the pig-nosed turtle (*Carettochelys insculpta*). The study also compared it with three other turtle species, the Florida softshell turtle (*Apalone ferox*), the pond slider turtle (*Trachemys scripta*), and the loggerhead sea turtle (*Caretta caretta*). The pig-nosed turtle is the only fresh water species to possess a highly modified wing shaped forelimb that superficially resembled that of the sea turtles. This wing shape suggests the pig-nosed turtle also utilised a lift based mechanism for propulsion. The pig nosed turtle is a very distant relative of the sea turtle and is more closely related to the soft shell turtles, which uses pure rowing locomotion with paddled like webbed feet. The loggerhead sea turtle uses pure flapping locomotion with high aspect ratio wing shaped forelimbs but is more closely related to the paddling pond slider turtle. The stroke patterns of the pond slider and pig-nosed turtles are believed to be intermediates between the pure rower and pure flapper. Figure 2-15 shows the mean foil path of these animals. Since the sea turtle and the pig-nosed turtle wing shaped flipper evolved independently, their similarities are the results of convergent evolution.

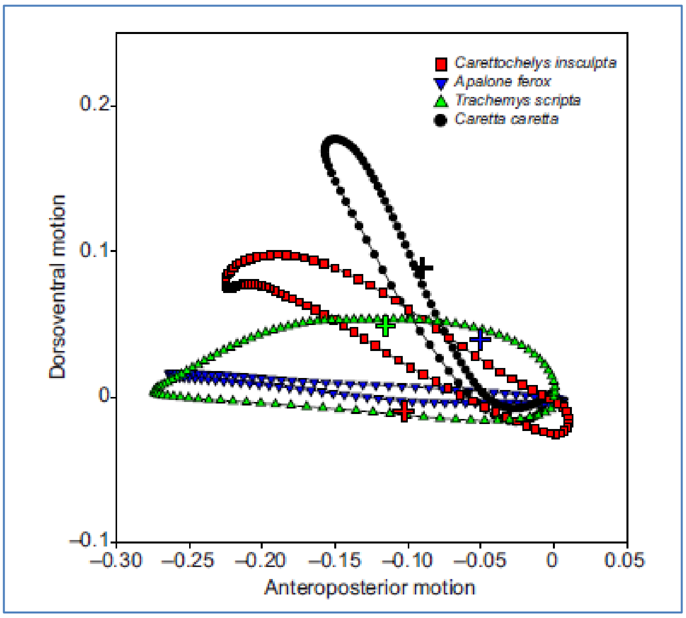

Figure 2-15 – Normalised wing tip displacement for four species of turtle. *Caretta caretta* is a sea turtle and *Caretochelys insculpta* is pig-nosed turtle. Both have high aspect ratio wing shaped flippers. The other two are freshwater rower with paddle like legs and swim using a crawling stroke. (Rivera et al., 2013)

The Rivera study filmed the lateral and ventral side of the animal at 100Hz whilst swimming in a custom built recirculating flume and a glass aquarium. The study found whilst the pig-nosed turtle resembled the sea turtle, its actuation mechanism was significantly different. The inclination angle of the pig-nosed turtle’s actuation path is less than 45°, the angle which determines whether an animal’s stroke should be classified as rowing or flapping.

The low stroke inclination angle of the pig nosed turtle is caused by the flipper actuation mechanism at the musculoskeletal level. Whilst penguin and sea turtle fore flippers generate their dorsoventral motion (roll) through actions of the humerus bone, close examination of the pig-nosed turtle humerus bone was found to move with an anteroposterior motion in yaw similar to the rowing turtles. The observed dorsoventral motion was generated by the twisting of the elbow joint instead. As such, the dominant motion remained anteroposterior. This shallow actuation path affected the hydrodynamics of the stroke and resulted in a hybrid stroke cycle, where the ‘up’ stroke generated thrust using lift based mechanism with moderate angle of attack, and the ‘down’ stroke generated thrust using a drag based mechanism with a very high angle of attack.

A hybrid lift-drag stroke is also used by sea lions (Feldkamp, 1987a). Feldkamp’s study of California sea lion’s propulsion mechanism found the sea lion uses a hybrid aquatic flight stroke cycle with three phases (Figure 2-16). The study named the three phases as power phase, paddle phase and recovery phase. The power phase and recovery phases are lift based strokes, and they are equivalent to down stroke and up stroke in normal aquatic flight. The paddle phase takes place in between the transition from down stroke to up stoke. This phase uses a drag based stroke with a very high angle of attack, and it is equivalent to the power stroke in drag based paddling. In order to avoid confusion with strokes in other propulsion gaits, these three phases will be referred to as the down stroke, paddle stroke and up stroke. The advantage of this hybrid cycle is it allows the animal to generate more thrust than a pure lift based cycle by introducing the paddle stroke, while being more efficient than a pure drag based cycle because the lift based up and down strokes replaced the inefficient recovery stroke. The study believed the hybrid stroke arises from the need to walk on land, where the anteroposterior motion found in the paddle phase is essential.

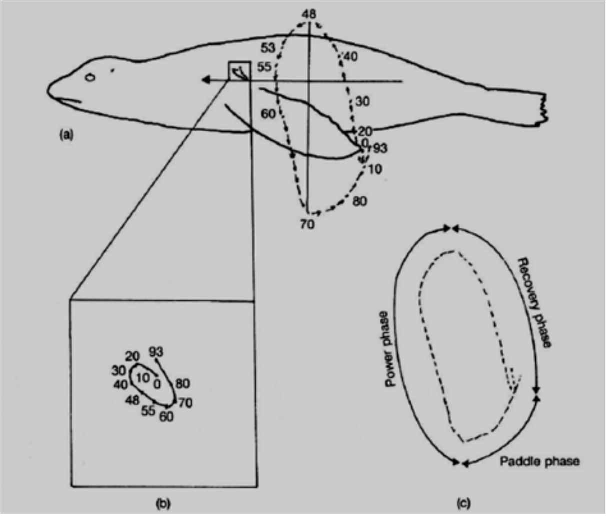

Figure 2-16 – Seal flipper foil path (Feldkamp, 1987a)

Skeletal analysis of the plesiosaurs found it has a similar restriction to seals, therefore it is believed to swim in a somewhat similar manner (Figure 2-17)(Massare, 1994). This can be expected as seals and plesiosaurs occupied the same ecological niche, and both have to crawl onto land to reproduce. The biggest difference between the two animals is the plesiosaurs swam using all four limb flippers, while sea lions only swim with the two fore flippers.

After reviewing the literature concerning the stroke paths of aquatic flight animals, it is clear all of animals examined exhibited three axis motion in their swimming strokes. While the effect of two-axis aquatic flight has been studied by various research groups, the effect of three axis stroke path is unclear. Therefore there is a need to further investigate the three axis swimming stroke and see whether it has any benefit on manoeuvrability.

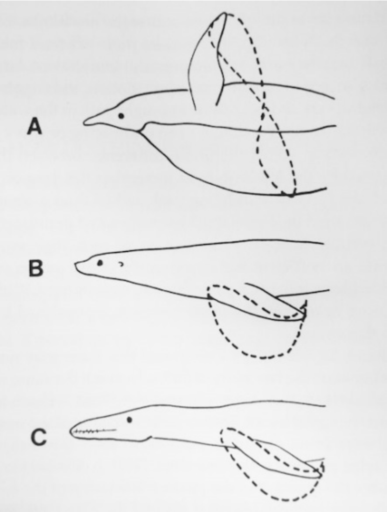

Figure 2-17 – Stroke pattern of penguins, seals and plesiosaurs (Massare, 1994)

2.6.4 Summary of aquatic flight and related propulsion strategy

Whilst AUV and other manmade vehicle locomotion can be summarised into propeller for propulsion, and control surface and thruster for manoeuvring, marine animal locomotion has been shown to be far more complex. Animals can swim using fins, legs, flagellum, and jet propulsion etc.…, and each type can be further divided into dozens of different sub-types. Fin based swimming is used by most marine vertebrates and a number of invertebrates and has been shown to be one of the most efficient propulsion strategies used by marine animals. Among them the median and paired fin (MPF) locomotion are more manoeuvrable while the body and caudal fin (BCF) propulsion is more efficient.

Among the MPF swimming modes is a lift-based propulsion strategy known as aquatic flight. This propulsion strategy is used by many secondary marine animals, such as penguin and sea turtle, and it has been shown to be capable of propelling the animal at high speed whilst maintaining very good manoeuvrability. The efficiency of this lift based MPF swimming is only slightly less efficient than lift based BCF swimming, which makes it a good compromise between the need for efficient open water cursing and manoeuvrability in confined environment.

There have been a number of studies on aquatic flight, but most were either one or two axis based. These studies analysed the lift and drag force produced by a flapping foil actuating in pitch and roll. However, the review of literature on aquatic flight animal locomotion showed the animal stroke path contains an additional component in yaw, and the effect of this third actuation axis is unknown and requires further investigation.

2.7 Summary

This thesis research began by using a database approach to collect data about manmade vehicle and marine animal performance. The aim of the database analysis was to objectively identify performance gaps between animals and AUVs, and develop a bio-inspired solution that will allow manmade vehicles to overcome this performance gap. This analysis eventually identified manoeuvrability as one of the biggest gaps between the performance of marine animals and manmade vehicles. It also identified animal aquatic flight may be a solution that can overcome this performance gap.

The investigation then reviewed the key factors affecting manoeuvrability. The hull design, vehicle mass, and propulsor thrust are important in determining the vehicle's acceleration. Meanwhile, the control surface and thruster designs and their relative placement within the vehicle are important factors that will have significant effect on the vehicle's turning performance. Review of existing literature showed both the control surface and the thruster have a fundamental limitation relating to the vehicle speed. Control surfaces are very efficient at high speed, but become ineffective at low speed and will cease to function when the vehicle is stationary. Thrusters have the opposite problem in that they are very effective when the vehicle is stationary or moving slowly, but they become less efficient as the vehicle speed increases. Therefore a vehicle designed for operation at a range of speed will require both mechanism.

In comparison, marine animals do not appear to suffer this limitation and their fin based propulsion systems were shown to be fairly effective at both high speed and low speed. Aquatic flight is one of the animal propulsion strategies that are shown to be a good compromise between speed, efficiency and manoeuvrability, and it is used by many secondary marine animals such as seals and penguins.

Aquatic flight propulsion consists of a pair of high aspect ratio wing shape fins flapping with a dorsoventral oscillatory motion. This flapping motion increases the inflow velocity into the foil and adds energy and momentum to the flow. The foil pitch motion adjusts the angle of attack and rotates the lift and drag force vector such that a component of the lift force become the propulsion thrust. Existing models of aquatic flight analysed it as a two-axis problem (pitch and roll), but the literature review of animal aquatic flight stoke paths show most animal aquatic flight are actuated in three axes. The effect of yaw motion in aquatic flight propulsion is unknown and requires further investigation.

For the purpose of bio-inspired vehicles, MPF has another advantage over BCF swimming modes because MPF relies on fins for propulsion instead of the body. As such the body of most MPF swimmer are relatively rigid. In the case of the sea turtles (MPF aquatic flight), it would not be incorrect to describe them as having a rigid hull (shell). This trait would be very useful for AUVs because manmade submersibles need to have a rigid pressure vessel to protect the electronics and other sensitive components from sea water. A BCF inspired vehicle would need to sacrifice a significant proportion of the vehicle length for the flexible tail, but a MPF inspired vehicle can have a rigid hull like many existing AUVs. This means a MPF inspired vehicle will have greater capacity than a BCF inspired vehicle, while maintaining a manoeuvrability advantage over conventional vehicle.

The literature review of AUVs and animals identified aquatic flight to be the best candidate for improving AUV manoeuvrability and reduce the gap between AUVs and animals. Therefore the study concluded the main focus of this research should be an investigation into aquatic flight.

Chapter 3: Aquatic Flight Modelling

3.1 Introduction

The literature review and analysis showed animals that utilise aquatic flight propulsion can be both fast and manoeuvrable – two properties that are normally mutually exclusive in manmade platforms. Before aquatic flight propulsion can be used in autonomous underwater vehicle, further investigations must be carried out to study the mechanism behind this method of propulsion. The Nature Inspired Manoeuvrable Bio-Locomotion Experiment (NIMBLE) was created to study aquatic flight through a combination computer modelling and experimentation.

The review of biological literature of animal aquatic flight showed the foil stroke path in animals are combinations of pitch, roll, and yaw, rather than simple pitch and roll that was assumed by previous hydrodynamic research. This means animal aquatic flight is actuated in three axes, and the effect of this yaw component is largely unknown. It may produce additional thrust, it may produce additional lift force, or it may be a limitation caused by physiological limitations. It may also be a combination of all of these. Since the third axis motion is likely affect the performance of aquatic flight, it is necessary further investigate its effect. The results of this research will add to the knowledge base of aquatic flight propulsion and will aid future design of an aquatic flight propulsor for AUV.

The computational modelling part of this research utilises a quasi-steady method based on blade element theory. Unlike many three dimensional fluid flow problems, such as fish tail and rotating propeller, it is difficult to simplify aquatic flight locomotion into a two dimensional steady state problem. During the aquatic flight propulsion cycle, the flapping foil moves around a pivot and the roll and pitch velocities changes constantly. This means the model must capture the two dimensional movement of the foil in the tangential plane, as well as account for the variation of flow along the foil span. To further complicate this problem, the flapping motion creates a constant change in the inflow angle, angle of attack, and inflow velocity. All of these combine to make the aquatic flight problem three dimensional and transient. Since three dimensional transient problems are difficult and expensive to compute, using a quasi-steady method can speed up the analysis and reduce computational time.

However, quasi-steady methods are often less accurate than computational fluid dynamics (CFD) approaches based on Reynolds averaged Navier-Stokes (RANS), so the results will be a need to verified experimentally.

When aquatic flight is broken down into its simplest form, it is basically a hydrofoil rotating around an axis. This is not dissimilar to a propeller blade rotating around its hub, except the aquatic foil blade has a constantly changing pitch angle, and it oscillates between two angular positions instead of making a full rotation. The aquatic flight foils periodically reverse direction during a propulsion cycle and the blade pitch angle follows it to keep the thrust pointing in the forward direction regardless of whether the cycle is in the up stroke phase or the down stroke phase. The fact that the flapping foil shares some similarities with propellers suggested models designed to study propellers may be adapted to study aquatic flight. In propeller analysis, it is usual practice to make the measurement velocity at 0.7 span (Healey et al., 1994). This approach was also taken by the MIT researchers when they defined the kinematic model for aquatic flight (Techet, 2008; Licht et al., 2004b). 70% of the span is often chosen for analysis because it is approximately the point where the increased forces produced near the faster foil tip would cancel out the effect from reduced forces produced near the slower foil root. The centre of pressure can be affected by foil design as well as operating condition, and it is unknown whether the 0.7span assumption remains valid for a flapping foil where the foil radial velocity changes constantly. The blade element theory aquatic flight model was developed to overcome this uncertainty and produce a model that is more representative of the hydrodynamics of a flapping foil.

3.2 Preliminary Video Investigation

Whilst there are lots of literature covering the stroke patterns of sea lions and turtles, there are surprisingly few covering the stroke pattern of penguins. Clack and Bemis (1979) study is one of the earliest study to include video analysis of aquatic flight strokes, but the exact path of the stoke was unclear (Figure 2-12). The penguins' stroke may followed either a figure-of-eight shaped path or an oval shaped one, with sources supporting one (Massare, 1994) or the other (Clark and Bemis, 1979). Nevertheless, these figures show the penguin wing did not followed the same path in the up stroke and the down stroke, and there is a difference in the yaw position between these two paths. Therefore it was decided it is necessary to carry out a preliminary analysis of penguin's stroke pattern and permission was acquired from Paulton's Park, Southampton (a theme park with a zoo) to film their Humboldt penguins swimming in the penguin pool.

The park's penguin pool is approximately 1.5m deep and has two large viewing windows approximately 2m across (Figure 3-1), and cameras used for this study would look through these windows. The filming was non-invasive and do not interfere with the penguins normal routine. However, arrangements have been made with the park's keepers to throw fish in such a way that would encourage the penguins to swim across the viewing windows during feeding time.

Paultons Park's penguin pool housed around 30 Humboldt penguins. Humboldt penguin (*Spheniscus humboldti*) is a medium sized penguin specie. They feed on small schooling fish and squids, so they need to be fast, agile and manoeuvrable to catch their prey. The species weights an average of 6.6kg with a body length of 0.68m. Photographic analysis of an individual in Paultons park pool allowed calculation of various body dimensions with respect to body length (BL). The flipper wing span was 0.41BL with a chord of 0.1BL. This corresponded to a span of 0.28m and a chord of 0.072m (See Figure 3-2).

Figure 3-1 - Paultons Park Penguin Pool. The photo on the left show the two viewing windows along the wall

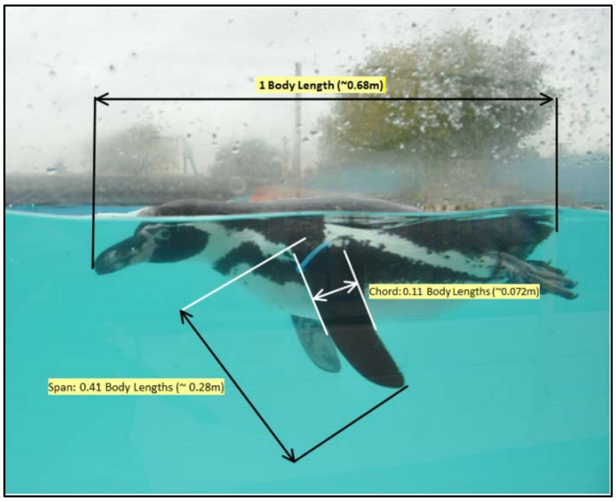

Figure 3-2 - Body Plan of a Humboldt Penguin at Paultons Park

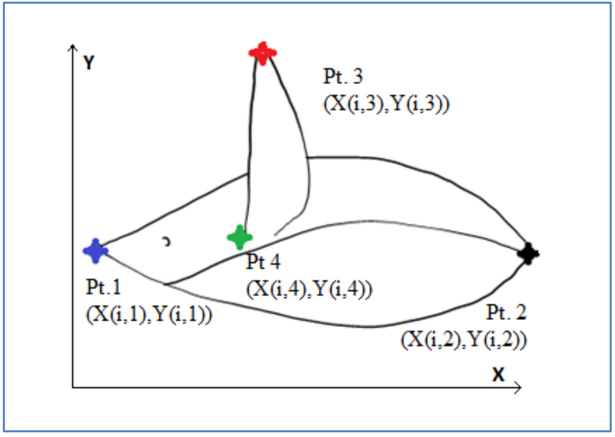

Figure 3-3 – The four reference point on the penguin

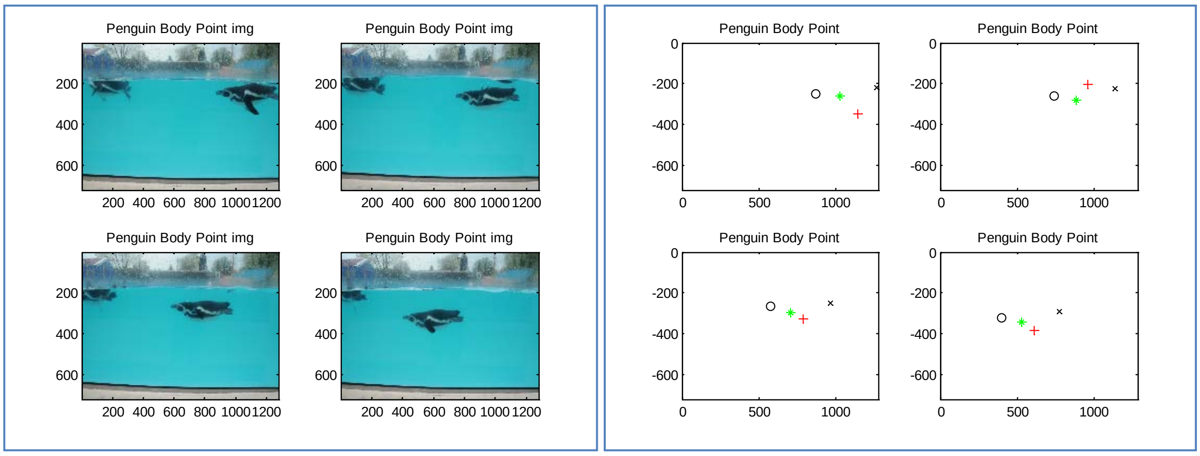

Figure 3-4 – Frame by frame swimming of the penguins. Four of these frames (Frame 1, 6, 12, 18) and their associated reference points are shown.

A video camera was used to capture footages of penguins as they swam across a viewing screen. The video was recorded at 24 frames per second at a resolution of 1280x720 pixels. The video clip was cropped and played back frame by frame. Four reference points were selected manually from images of the animal, namely beak, tail, wing tip and wing root (

Figure 3-3). Four of these frames and their associated reference points are shown in Figure 3-4.

The beak and tail points were used to define a coordinate for the analysis. The beak point defined the origin and the line connecting the beak point to the tail point was defined as the X axis. The wing tip and wing root points would be plotted in this coordinate to show the stroke of the bird during aquatic flight. An example of this is shown in Figure 3-5. The plot show the foil wing tip movement appears to have a significant yaw component, even when compared to the spread of the wing root point and tail point. The same pattern of spread is also observed in the other video shown, but the uncertainty is quite high so it cannot be concluded with certainty that the yaw component exists. Nevertheless, couple these results with stroke patterns mentioned in the literature, it would be reasonable to assume penguin aquatic flight is actuated in three-axis. Therefore further investigation should be carried out to investigate the effect of yaw actuation.

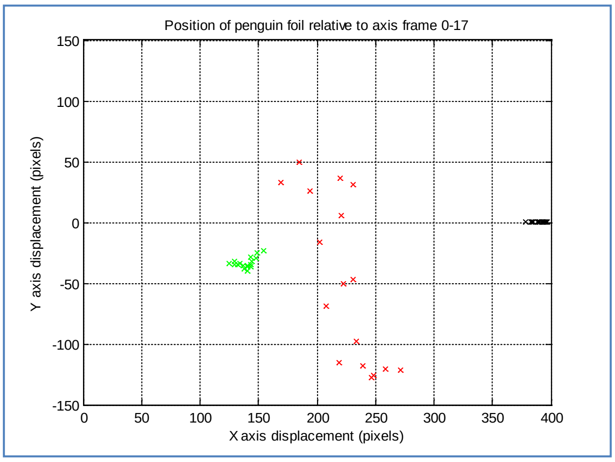

Figure 3-5 – A plot of the penguin wing tip and wing root position for one of the video clip

Aside from investigating the penguin’s stroke path, the video investigation also looked at other parameters of penguin swimming. The penguins were observed to swim in a straight line at speed between 1.8 and 3.5 BL/s. The Strouhal number varied between 0.28 and 0.50, and the flapping frequency was between 2.4 and 2.8Hz. The video analysis also showed penguins were able to turn at rate of up to 206°/s and interestingly the animal turn with their back pointing away from the centre of the turn (pitch down). This is the opposite of how flying birds and aircraft turn (back toward centre, pitch up) but it is consistent with observations reported in literature (Clark and Bemis, 1979). The investigation also looked at the relationship between the foil roll position and time, and found troll motion of penguin’ stroke followed a sine wave (Figure 3-6). This supports the use of sinusoidal equations in the model to describe the motion of aquatic flight.

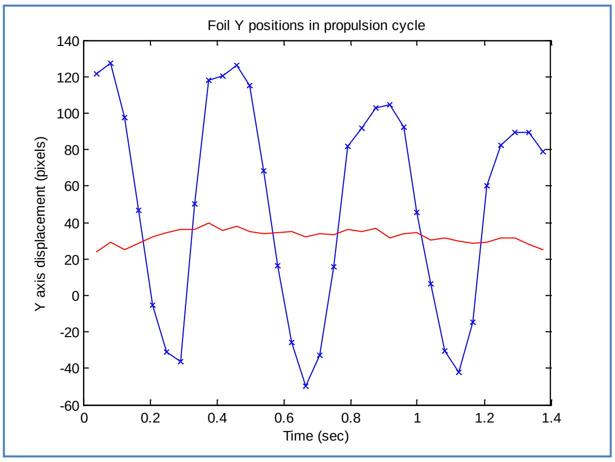

Figure 3-6 –A plot of the penguin’s wing tip and wing root Y position against time. Blue – wing tip, Red – wing root

3.2.1 Summary of Preliminary Video Motion Analysis

The preliminary video motion analysis on penguin’s aquatic flight aimed to find the stroke pattern of used by this bird. The investigation filmed a number of Humboldt penguins swimming freely across a glass viewing screen located on the side of their pool. The results show significant amount of scatter, but strongly suggest there is a yaw component in a penguin’s aquatic flight. The results also suggest penguins utilised a figure-of-eight stroke path instead of an oval path, because the horizontal spread in the wing tip position is highest at both ends of the strokes. If the animal used an oval stroke path, then one would expect a more significant spread in the middle of the stroke instead of the end.

In addition to penguin’s stroke path, the video analysis also agreed with the literature regarding penguin’s manoeuvrability. While the maximum observed turn rate is not as fast as some reported in the literature, the 206°/s turn rate that was measured is still extremely fast. Furthermore, the animal was not under any pressure to turn at its maximum rate (e.g. appearance of a predator), so this observed turn rate may not represent the limit of what the animal can do. The other parameters such as swimming speed, and Strouhal numbers also mostly agree with those reported in the literature.

Since the video analysis’s results and information in published literature suggesting penguins use a 3-axis figure-of-eight propulsion path instead of the two axis dorsoventral path, it is necessary to carry out further investigation of three axis aquatic flight propulsion. Furthermore, the figure-of-eight path should be the main focus of this investigation.

3.3 Single Element Simple Quasi-Steady Model (SQS)

Before performing a full analysis with the blade element model, it is necessary to test the model against results from published literature. The kinematics model of the aquatic flight locomotion will be based on the model used by Licht et al. (2004a). However, Licht's model is mostly used for describing the foil's motion rather than to estimate forces involved in aquatic flight. Their force model was very basic and will only give an estimate on the maximum force, torque and power requirement. The detailed analysis of aquatic flight was performed through experiments in a water tunnel and towing tank.

As such, Licht's model needs to be modified and extended before it can be used for simulating aquatic flight. The first step was to add an aerofoil model to calculate the forces involved. The foil used in this simulation is a NACA 0012 foil, the dimensions of which are listed in Table 1. The foil is actuated in pitch (θ) and roll (ϕ) and the flapping motion can be described by two sinusoidal equations ((3-1), (3-2)).

$$\theta(t) = \theta_0 \, sin(\omega_\theta t) + \theta_{bias} \tag{3-1}$$

$$\phi(t) = \phi_o \, sin\left(\omega_\phi t + \alpha\right) + \phi_{bias} \tag{3-2}$$

A hydrofoil generates lift and drag when it moves through the water. The lift and drag forces (F_L, F_D) depends on factors such as foil design, inflow velocity and angle of attack. These forces can be calculated using equations (3-3) and (3-4).

$$F_L = \frac{1}{2}\rho V_{in}^2 A_{foil} C_L \tag{3-3}$$

$$F_D = \frac{1}{2}\rho V_{in}^2 A_{foil} C_D \tag{3-4}$$

The lift and drag coefficients (C_L, C_D) are functions of the angle of attack, and could be found through interpolation of the foil lift and drag coefficient tables. Values in the lift and drag coefficient tables can be obtained through experiments, calculated using CFD methods, or looked up in existing data tables if the foil cross section is one of the common aerofoil section (e.g. NACA). Initially, the investigation experimented with acquiring foil thrust coefficient through the Xfoil program and using the lift and thrust coefficients for a flat plate, but later it was found the Sheldhal and Klimas's (1981) lift and drag coefficients produced the best result due to the high angles of attack involved (see later section for detail).

The angle of attack of the foil is the difference between the inflow angle and the pitch angle, and it can be calculated using equation (3-5) (Licht et al., 2004b). The first term of the equation represented the inflow angle of the fluid entering the foil (β), while the second and third terms are the formula for calculating pitch angle as seen in equation (3-1).

$$\alpha = -\,arctan\left(\frac{\omega r_{0.7}\phi_0\, cos(\omega t)}{U}\right) + \theta_0\, cos(\omega t) + \theta_{bias} \qquad (3\text{-}5)$$

Figure 3-7 shows the various forces and motion acting on the flapping foil. Since the lift and drag forces are aligned with the inflow direction, a transformation is required to calculate the vertical and horizontal forces from the results. The transformation used for these are shown in equation (3-6) and (3-7).

$$F_x = F_L\, sin(\beta) + F_D cos(\beta) \qquad (3\text{-}6)$$

$$F_y = F_L\, cos(\beta) - F_D sin(\beta) \qquad (3\text{-}7)$$

The combination of Licht's kinematic model and the aerofoil force model produced the single element quasi-steady model (SQS), which is implemented in Matlab. It evaluated the thrust coefficients for a range of angles of attack and Strouhal numbers at various flapping amplitudes (ϕ_0). The model used Sheldahl and Klimas's (1981) lift and drag coefficient data for a NACA0012 foil operating at a Reynolds number of 160,000.

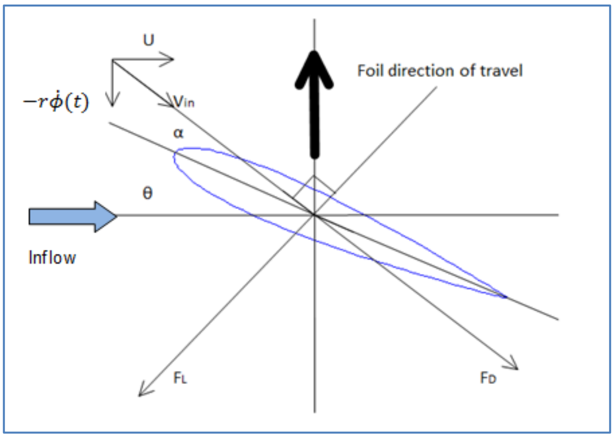

Figure 3-7 - Lift generation by an aerofoil

Foil Span	0.4m	**Foil Chord**	0.25*Span
Foil Sections	NACA0012	h_0/L_C	0.29
ϕ_0	20°	r_0 (estimated)	0.2m
Reynolds number	160,000	**Strouhal number**	0.2 – 0.8

Table 1 - SQS model analysis parameters

Since the results of the SQS model will be compared against Licht’s experimental results, the analysis parameters would be kept as closed to Licht’s set up as possible (Licht et al., 2004b). The parameters used in the model are listed in Table 1. Some of these parameters will be different to the parameters used for the BET aquatic flight analysis which is designed to be compared against results from the NIMBLE experiment.

3.3.1 Results

The model examined the thrust coefficient produced by four different roll amplitudes (5^o, 10^o, 20^o and 60^o) (Figure 3-8). The thrust coefficient is relatively high when the angle of attack was below 5°, but it started to fall when the angle of attack increased above 5°. This is because the foil began to stall. The minimum thrust coefficient was produced at angle of attack of approximately 10°. However, as the angle of attack increases, the thrust coefficient recovered and reached another maximum between 20° and 30°. As the angle of attack rose above 30°, the thrust coefficients gradually fall back to zero and then becoming negative.

All four contour plots show almost identical results and imply the thrust coefficient is not affected by roll amplitude. This insensitivity to roll amplitude is also reported in the MIT dataset (Licht et al., 2004b). This is caused by the non-dimensionalisation of the frequency and amplitude into the Strouhal number, where variations in the flapping amplitude are compensated by changes in the flapping frequency. Figure 3-9 compares cross sections of the thrust coefficient plot at four chosen angles of attack. These thrust coefficients are plotted against the Strouhal number at different flapping amplitudes. The plot show the thrust coefficient is very low at angle of attack of 10°, but it gradually increased as angle of attack increased. The thrust coefficient reached its maximum between 20° and 40°. After that the thrust coefficient began to fall. When the maximum angle of attack reached 60°, the flapping cycle was unable to generate any thrust below a Strouhal number of 0.5.

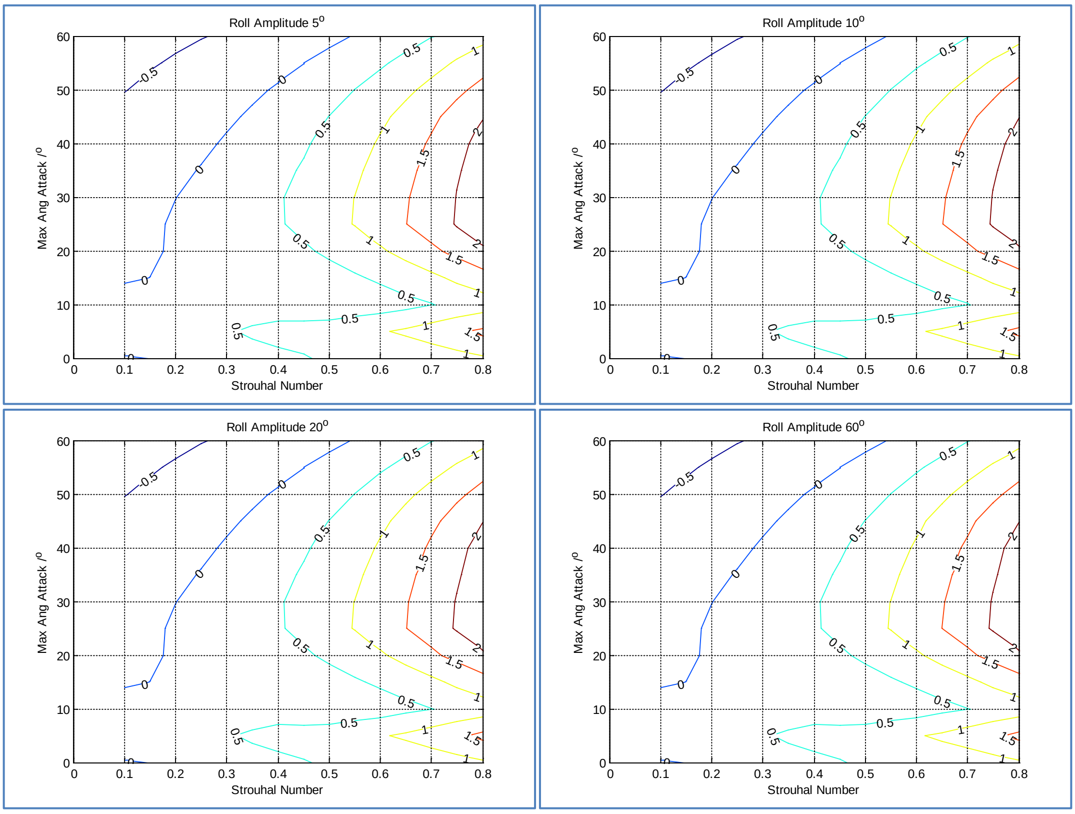

Figure 3-8 – Thrust coefficients for a range of Strouhal number and angle of attack for different roll amplitudes

In addition to Licht’s result, Read et al.’s experiment on a pure heave foil also showed the thrust coefficient is unaffected by variation in heave amplitude (Read et al., 2003). However, the same investigation found, given the same Strouhal number and angle of attack, cycles with lower oscillation amplitudes and higher frequencies have better propulsive efficiencies at lower Strouhal number than cycles with higher amplitudes but lower frequencies. The opposite occurs at higher Strouhal numbers where cycles with greater heave amplitudes are more efficient. The differences in efficiencies should be noted when the foil is used for steady state propulsion, but it is less important when the goal is to improve manoeuvrability.

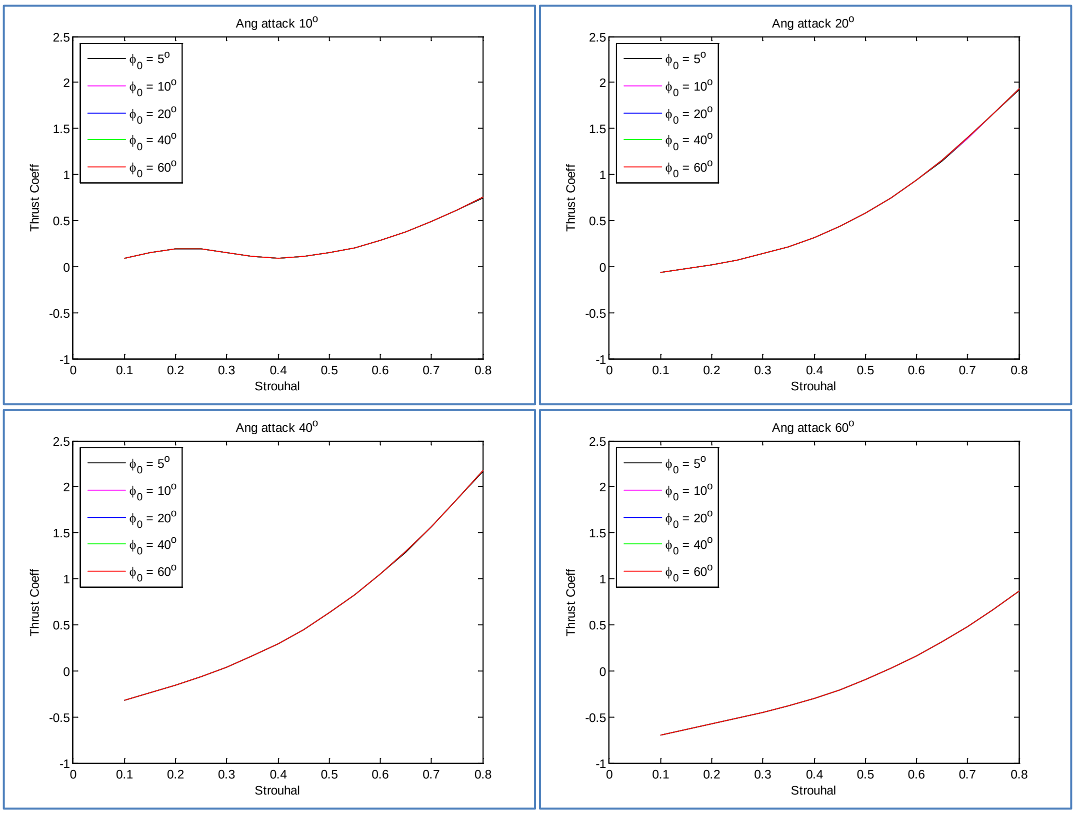

Figure 3-9 – Comparison between thrust coefficients for max angle of attack of 10°, 20°, 40° and 60° with roll amplitude of 5°, 10°, 20°, 40°, and 60°.

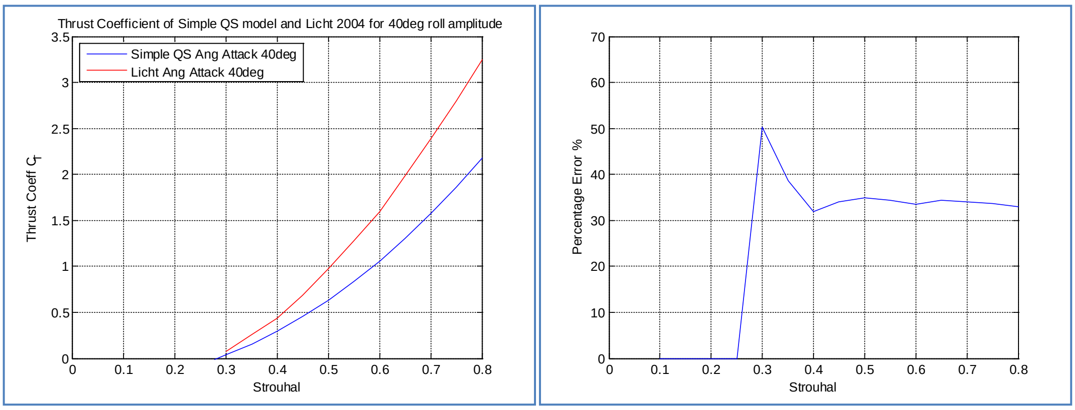

Figure 3-10 – (Left) Plot comparing the thrust coefficient of Licht's experimental results and SQS model for roll amplitude of 20° and maximum angle of attack of 40°. (Right) Percentage difference between Licht's experimental results and the SQS model

Figure 3-10 shows a comparison between the result of the single element SQS model and Licht's experimental results. It shows the thrust coefficient prediction was in the same order of magnitude as the experimental results, but this model under estimated the thrust coefficient by around 30% to 35%. This is a reasonable match given the SQS model used a different foil design and only accounted for the hydrodynamic forces associated with hydrofoil lift and drag. It did not account for variation in flow along the span of the foil nor other hydrodynamic forces such as added mass and rotational flow.

3.3.2 Summary

The single element simple quasi steady (SQS) model attempted to model aquatic flight locomotion by adding a hydrofoil model onto Licht’s kinematic model. Whilst the results this model produced showed a similar trend to Licht’s experimental results, it produces an estimate that is approximately 25% lower. This difference could be attributed to differences in the foil design and limitation in the single element model in analysing aquatic flight which has varying inflow conditions along the span. As such there is a need to improve on this model using Blade Element Theory.

In addition to the differences in the model and experiment thrust coefficient, this investigation also found the Strouhal number can correct for variation in roll amplitude by changing the flapping frequency, which agreed with the experimental results published by Licht and Read (Read et al., 2003; Licht et al., 2004b).

3.4 Modelling Methods – Blade Element Theory

3.4.1 Blade Element Theory Model

The single element simple quasi-steady model demonstrated that the model is robust as it shows a similar trend to results published in the literature, so the next step would be to apply blade element theory to the flapping foil model to improve its accuracy as well as investigate the effect of three axis aquatic flight. Blade element theory was developed to study propeller blades by William Froude in 1878 and David Taylor in 1893. This method was adapted by Blake to study diodontiform drag based paddling and by Lighthill to study BCF locomotion in fish (Blake, 1979; Lighthill, 1971). The blade element method divides the foil span into a number of blade elements and evaluated each element separately. The results of the calculations for individual elements were combined at the end to produce a sum of forces for the whole foil.

So far, the existing models for aquatic flight simulate the foil motion using two sinusoidal equations, one for roll and one for pitch. The additional motion component in yaw required some additional changes to the model to allow it to evaluate the foil forces in three axis aquatic flight. Foil lift and drag forces are calculated either perpendicular or parallel to the inflow. In a pure heave foil, the forces would be in line with the horizontal and vertical (X and Y) direction, but the forces acts tangential to the foil span in a flapping foil, which changes depending on the foil orientation. The two tangential directions in two-axis actuation are X and ϕ, but the forwards-backwards yaw component of three-axis actuation changes the tangential directions to ψ and ϕ. The layout of the three-axis aquatic flight BET model is shown in Figure 3-11.

The foil motion in the three-axis actuation cycle followed simple sinusoidal patterns like the two-axis kinematic model, but with an additional third equation that describes the yaw motion. Pitch angle, $\theta(t)$, roll angle, $\phi(t)$,and yaw angle $\psi(t)$, are defined by equation (3-8), (3-9), and (3-10) respectively.

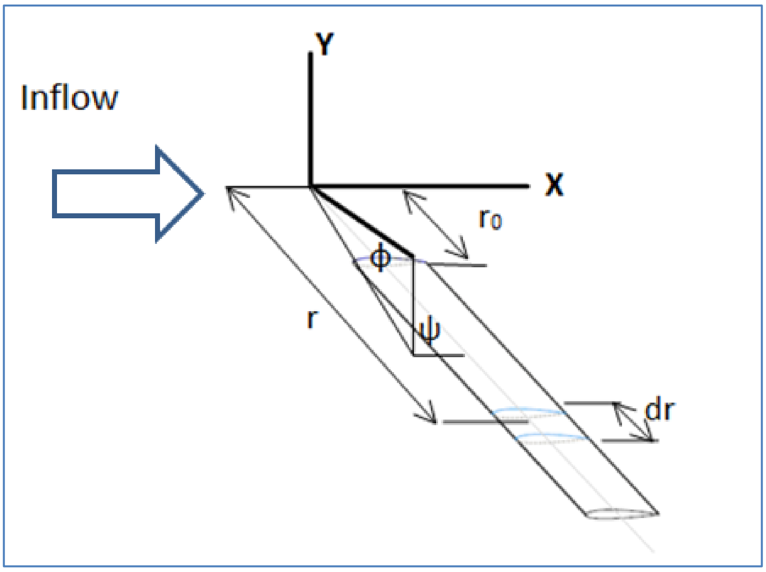

Figure 3-11 – Analysis of three axis flapping foil using blade element theory

$$\theta(t) = \theta_0 \sin(\omega_\theta t) + \theta_{bias} \tag{3-8}$$

$$\phi(t) = \phi_o \sin\left(\omega_\phi t + \omega_{\phi 0}\right) + \phi_{bias} \tag{3-9}$$

$$\psi(t) = \psi_0 \sin\left(\omega_\psi t + \omega_{\psi 0}\right) + \psi_{bias} \tag{3-10}$$

The new yaw component changes the foil's local inflow. The inflow velocity, V_{in}, of a foil actuated in three axes is given by equation (3-11), where U is the vehicle velocity (or the global inflow velocity), $r\dot{\psi}$ is the yaw velocity which is a multiple of the radius and the yaw angular velocity. Heave velocity $\dot{h}$ is equalled to the multiple of the radius and the angular velocity in roll, $r\dot{\phi}$.

$$V_{in} = \sqrt{\left(U + r\dot{\psi}\right)^2 + \left(r\dot{\phi}\right)^2} \tag{3-11}$$

The direction of various forces and motion on a flapping foil element is shown in Figure 3-12. It showed the inflow velocity is a now dependent on inflow, roll velocity and yaw velocity. The foil lift and drag forces would be perpendicular and parallel to the inflow angle respectively.

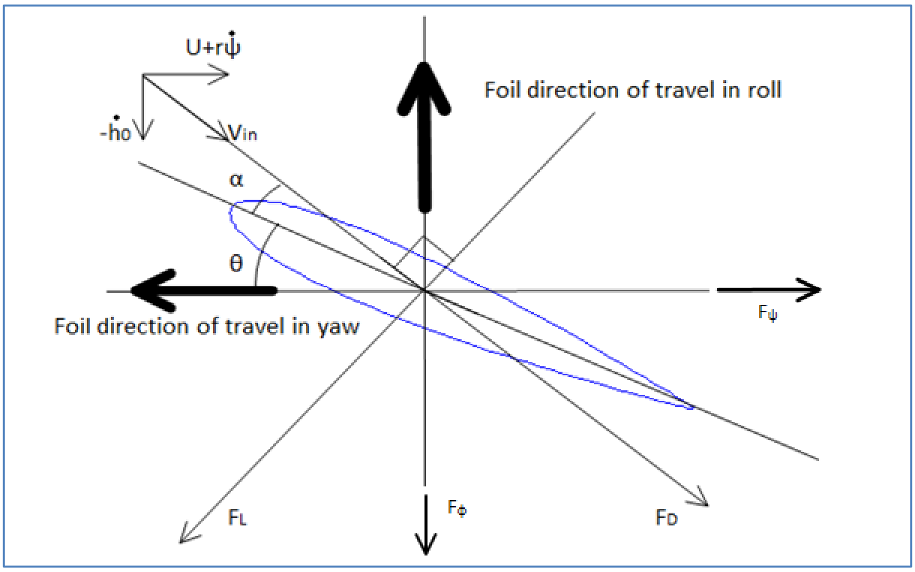

Figure 3-12 – Direction of forces on a 3 axis flapping foil

Since the foil inflow velocity is now a function of global inflow velocity, roll velocity and yaw velocity, the calculation for the local inflow angle (β) is modified to include yaw velocity in the calculation, as stated in equation (3-12).

$$\beta = arctan\left(\frac{r\dot{\phi}(t)}{U + r\dot{\psi}(t)}\right) \qquad (3\text{-}12)$$

The angle of attack also changed to include the additional yaw component. This new definition is stated in equation (3-13).

$$\alpha = arctan\left(\frac{r\dot{\phi}(t)}{U + r\dot{\psi}(t)}\right) - \theta \qquad (3\text{-}13)$$

The angle of attack of the foil can be used to find the lift and drag coefficient of the foil, either experimentally or using a look up table. One of the problems faced by analysis of propeller and thruster transient performance is the poor availability of aerofoil lift and drag data beyond the stall angles. Four quadrant lift and drag coefficient data, which is required to study reversal of flow, is even more scarce (Healey et al., 1994). The same problem is also found in the study of aquatic flight and other bio-inspired propulsion methods, which often involve angles of attack higher than the stall angle.

In addition to angle of attack, the lift and drag coefficients of a hydrofoil also depend on the Reynolds number. The experiment was designed to operate at a Reynolds number of 40,000. Unfortunately, there is no published four quadrant lift and drag data for the NACA0012 foil at this Reynolds number so an alternative must be found. The lowest available detailed four quadrant tabulated data sets for NACA0012 was measured at Re 160,000 (Sheldahl and Klimas, 1981) (Figure 3-13, Figure 3-14). Whilst this Reynolds number is higher than the one used by penguins and NIMBLE, other studies found the differences between the lift and drag coefficients at Reynolds number of 62,000 and 148,000 were relatively small (Worasinchai et al., 2011) (Figure 3-15 and Figure 3-16). Most of the differences occur between angle of attack of 50° and 60°, where there is a sudden change of flow behaviour on the suction side. In the lower resolution Worasinchai data set, the maximum lift coefficient reported for Reynolds number of 62,000, 86,000 and 148,000 were 0.778, 0.781 and 0.861 respectively. The maximum lift coefficient reported in the Sheldahl dataset for Reynolds number of 160,000 was 0.853, which mostly agreed with the Worasinchai dataset. Once the lift and drag coefficients of the flapping foil are known, they can be used to calculate the foil lift and drag force using equation (3-3) and (3-4).

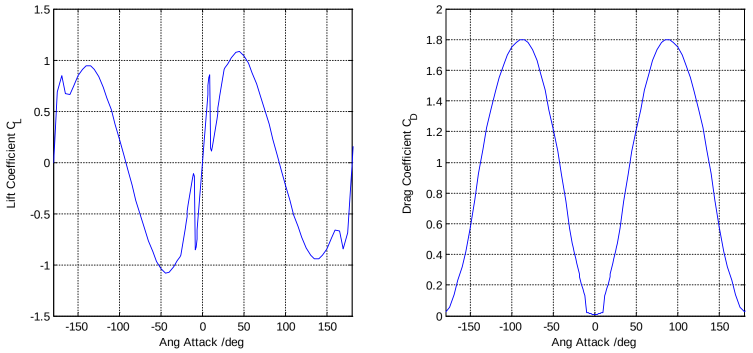

Figure 3-13 – 360° NACA0012 lift and drag coefficient at Re160000 (Sheldahl and Klimas, 1981)

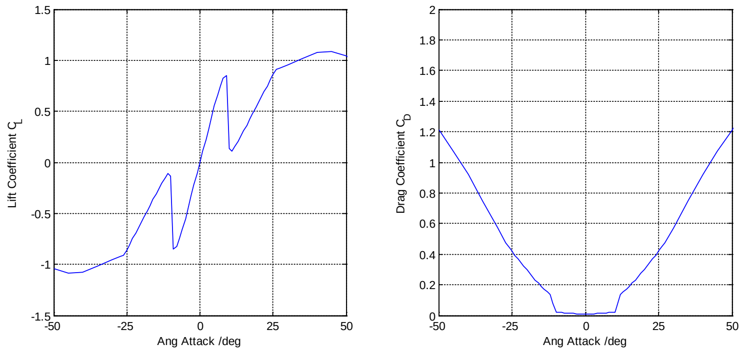

Figure 3-14 - Close up of lift and drag coefficient for angles of attack between ± 50°. Stall occurs at ± 9°.

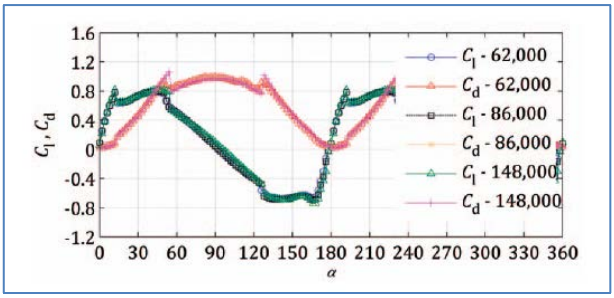

Figure 3-15 – Comparison of lift coefficient for NACA0012 foil at three Reynolds number(Worasinchai et al., 2011)

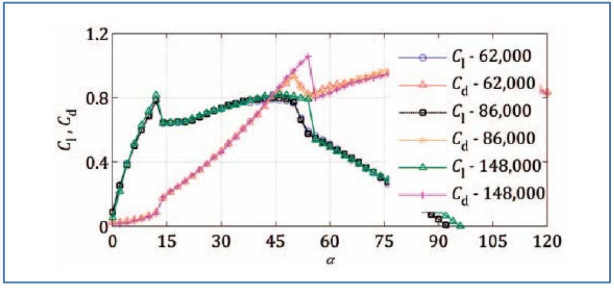

Figure 3-16 – Closed up Comparison of lift coefficient for NACA0012 foil at three Reynolds number (Worasinchai et al., 2011)

A Matlab program is used to interpolate the data table and retrieve the lift and drag coefficient (C_L, C_D) corresponding to the given angle of attack, which is then used to calculate the foil lift and drag forces using Equation (3-14) and (3-15).

$$F_L = \frac{1}{2}\rho v^2 A_{foil} C_L \tag{3-14}$$

$$F_D = \frac{1}{2}\rho v^2 A_{foil} C_D \tag{3-15}$$

The foil element lift and drag forces are aligned to the inflow direction. The inflow velocity and direction is a function of foil pitch and roll motion as denoted by equation (3-11) and (3-12). The lift and drag force would combined to produce horizontal thrust and vertical lift/vertical force on the foil. Since this total thrust and lift/vertical forces act along the foil's direction of motion, they would be denoted F_ψ and F_ϕ. Equation (3-16) and (3-17) are used to calculate (F_ψ, F_ϕ) from (F_L, F_D).

$$F_\psi = F_L\, sin(\beta) + F_D cos(\beta) \tag{3-16}$$

$$F_\phi = F_L\, cos(\beta) - F_D sin(\beta) \tag{3-17}$$

Unlike the simple model for a pure heave cycle or simple model for two-axis cycle, the foil thrust and lift/vertical force in the three axis cycle are tangential to foil's yaw and roll axis. This means unless both yaw and roll angles happened to be zero, the foil thrust and lift/vertical force vectors would not be aligned with the vehicle thrust and vertical force vectors in X and Y. Figure 3-17 illustrate the this problem by showing the various force vectors acting on one foil element. The foil forces F_ψ and F_ϕ acts perpendicular to the foil and tangential to the foil motion. Meanwhile the vehicle/actuator thrust and vertical force (F_x, F_y) are aligned to the vehicle's horizontal X and vertical Y axis. Therefore it will be necessary to convert the foil centric (F_ψ, F_ϕ) into vehicle/actuator centric (F_x, F_y) using Equation (3-18) and (3-19) in order to obtain the thrust and vertical force that will contribute to the vehicle's propulsion.

$$F_x = F_\psi \cos \psi \tag{3-18}$$

$$F_y = F_\phi \cos \phi \tag{3-19}$$

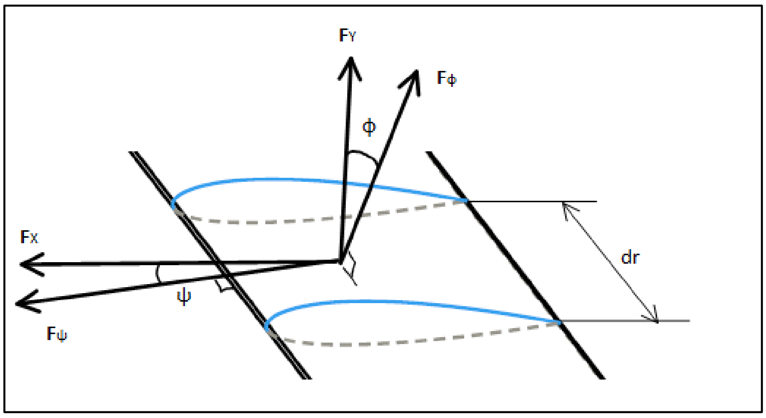

Figure 3-17 - Blade element theory - forces on a foil blade element

While it is more intuitive to control foil motion using pitch angle from a mechanical standpoint, it will be easier to perform the analysis if the motion were defined via angle of attack instead. This is because if Strouhal number was increased while keeping maximum pitch angle, roll amplitude, and inflow velocity fixed, it can result in an unreasonably large angle of attack. Since the angle of attack varies along the foil span, it will be necessary to define the maximum angle of attack at a certain point along the span of the foil. The point chosen was 0.7 span, because it is the position chosen in Licht's model (Licht et al., 2004b) and it is also the point normally used for studying propeller blades.

The pitch angle would be calculated from the defined maximum angle of attack at 0.7 span, $\alpha_{0.7Max}$. Since the model and experiment uses a rigid foil, the pitch angle would be constant throughout the foil span. Equation (3-13) can be rearranged to calculate the foil pitch angle from a predefined $\alpha_{0.7Max}$ (Equation (3-20)).

$$\theta = arctan\left(\frac{r\dot{\phi}(t)}{U + r\dot{\psi}(t)}\right) - \alpha_{0.7max} \qquad (3\text{-}20)$$

3.4.2 Modelling methods – Other Hydrodynamic Phenomena

Apart from the hydrofoil lift and drag forces, the literature review identified a number of other hydrodynamic phenomena that can affect foil performance when the foil operates in a transient condition. The added mass effect and Kramer effect (rotational flow) have been mentioned a number of times. The former can cause a lag in propeller’s transient response, while the latter is said to create additional lift in flying birds and insects. In addition to the added mass forces and Kramer effect, hydrofoil tip loss is another phenomenal that can affect the performance of open ended hydrofoil. Tip loss is a loss of lift caused by the fluid flowing along the foil span and then around the foil tip instead of travelling along the foil chord to the trailing edge. It affects any hydrofoil with a finite length, including wings on planes and blades on propellers.

This section will cover models used for analysing these phenomena. The results of these additional models will be incorporated into the BET model of aquatic flight propulsion.

3.4.2.1 *Added Mass*

The added mass force is the reaction force associated with acceleration of fluid surrounding the hydrofoil, specifically a cylinder of fluid with diameter equal to foil chord and a height equal to the length of the blade element. This force acts perpendicular to the foil section. The added mass model used in this investigation is adapted from the two-axis models used for calculating forces in insect flight (Truong et al., 2011; Ansari et al., 2006; Walker, 2002; Sane, 2003).

$$dF_{AM} = -\frac{\pi}{4}\,\rho {L_c}^2\, a_n dr \tag{3-21}$$

The formula for calculating added mass forces for each blade element is given by equation (3-21). In this equation, the density of sea water is ρ, the chord is L_c, the blade element span length is dr, and the acceleration is a_n. In two-axis aquatic flight, the foil acceleration is equal to the roll acceleration which is given by the second derivative of equation (3-2) and is listed in equation (3-22).

$$a_n = \ddot{\phi}(t) = -{\omega_\phi}^2 sin(\omega_\phi t + \omega_{\phi 0}) \tag{3-22}$$

However, when modelling three axis aquatic flight, it is necessary to account for acceleration in yaw as well as roll so a vector sum has to be performed for roll and yaw acceleration ($r\ddot{\phi}$ and $r\ddot{\psi}$) (3-23).

$$a_n = r\left(\ddot{\phi} + \ddot{\psi}\right) \tag{3-23}$$

The foil’s accelerations in roll and yaw are given by the second derivatives of the roll and yaw angle equations (3-9) and (3-10). These acceleration equation are listed in equation (3-24) and (3-25).

$$\ddot{\phi}(t) = -{\omega_\phi}^2 \phi_0 sin(\omega_\phi t + \omega_{\phi 0}) \tag{3-24}$$

$$\ddot{\psi}(t) = -{\omega_\psi}^2 \psi_0 sin(\omega_\psi t + \omega_{\psi 0}) \tag{3-25}$$

The magnitude of the resultant acceleration ($|a_n|$) is given by (3-26), and the angle of this acceleration (ε) is given by (3-27). The two-axis acceleration can be thought of as a special case of this where the acceleration angle ε is 0°. This is illustrated in Figure 3-18.

$$|a_n| = r\sqrt{|\ddot{\phi}|^2 + |\ddot{\psi}|^2} \tag{3-26}$$

$$\varepsilon = arctan\left(\frac{\ddot{\psi}}{\ddot{\phi}}\right) \qquad (3\text{-}27)$$

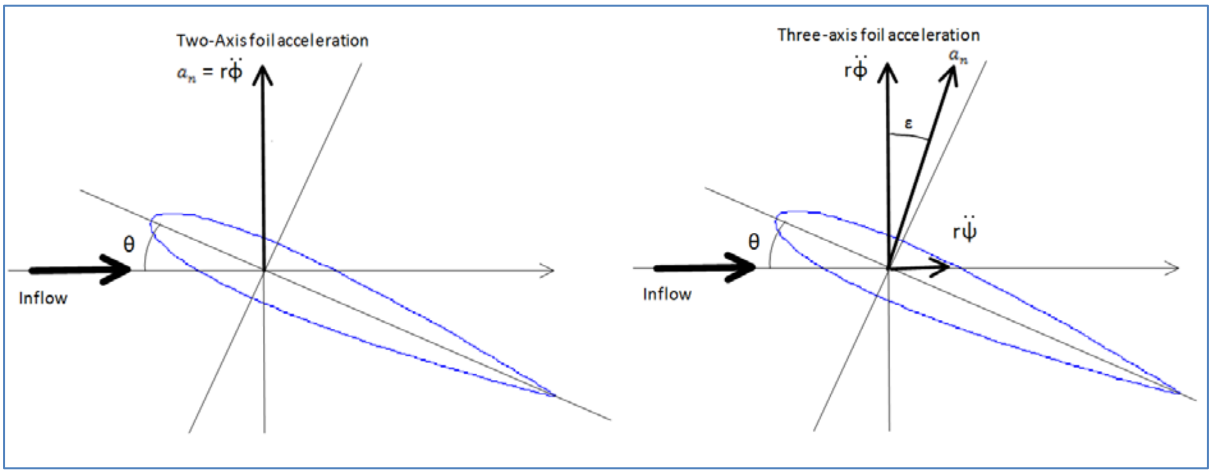

Figure 3-18 – Illustration of the foil acceleration angles as defined for two axis aquatic flight as used by previous studies and the newly defined foil acceleration vector for three-axis aquatic flight

In two axis aquatic flight, the added mass force acted perpendicularly to the foil section, so it was a simple to calculate the X (thrust) and ϕ (roll) components of the added mass force by calculating the sine and cosine of the pitch angle. The situation is less straight forward for three-axis aquatic flight, because the foil acceleration is no longer confined to roll. Instead the foil now accelerate at an angle ε, and the added mass force would be also produced following this angled acceleration vector. Therefore acceleration angle must be subtracted from the pitch angle before the yaw and roll component can be calculated. The added mass forces in roll and yaw are given by equations (3-28) and (3-29).

$$dF_{\phi AM} = \frac{\pi}{4}\,\rho \int_0^{L_S} {L_c}^2(|a_n|)\,cos(\theta-\varepsilon)\,dr \qquad (3\text{-}28)$$

$$dF_{\psi AM} = -\frac{\pi}{4}\,\rho \int_0^{L_S} {L_c}^2(|a_n|)\,sin(\theta-\varepsilon)\,dr \qquad (3\text{-}29)$$

3.4.2.2 *Kramer Effects*

In steady state fluid dynamics, when a foil with a sharp trailing edge moves through a fluid, the differences in flow velocity between the top and the bottom will cause the stagnation point to lie on the top surface. However, this will require flow from the bottom surface to turn sharply at the sharp trailing edge to meet the flow from the top. The energy required is very high and the viscous forces in the fluid will prevent this from happening. Instead the viscous forces will hold the stagnation point at the trailing edge and allow the flow from both surfaces to join smoothly and tangentially at the trailing edge. This is known as the Kutta condition (Sane, 2003).

However, it was discovered a flapping foil, where the foil both translates and rotates as it moves through a fluid, can violates the Kutta condition. As the foil rotates around the pitch axis, the stagnation point can move away from the trailing edge (Sane, 2003). This results in a velocity gradient which will lead to shear in the flow. The viscous forces in the fluid will counter act this by producing additional circulation to compensate, but it takes time to re-establish the Kutta condition. However, since the foil is rotating continuously in pitch, it will not be possible to re-establish the Kutta condition. This is because by the time the viscous forces were able to re-establish the Kutta condition for a foil at time t, the foil would have advanced to the new position at time $t + \delta t$.

Whilst the Kutta condition cannot be restored at any moment in time when the foil continues to rotate, the circulation produced to restore the Kutta condition may add or subtract to the total foil forces. This restoration forces, dF_{Kramer}, is proportional to the angular velocity of the rotating foil and is known as Kramer effect or rotational forces (3-30) (Truong et al., 2011).

$$dF_{Kramer} = \rho\, r\dot{\phi} d\Gamma_{Kramer} \qquad (3\text{-}30)$$

The roll velocity of the foil element is $r\dot{\phi}$ and the rotational circulation of the wing section is $d\Gamma_{Kramer}$. The latter can be calculated by equation (3-31).

$$d\Gamma_{Kramer} = c_{rot}\dot{\theta}{L_c}^2 dr \qquad (3\text{-}31)$$

The rotational (Kramer) force coefficient is c_{rot}. It is a function of the non-dimensional rotation velocity $\widehat{\omega}$ and position along the foil chord (3-32).

$$\widehat{\omega} = \frac{\dot{\theta} L_c}{V_{tip}} \qquad (3\text{-}32)$$

The rotational force coefficient was found experimentally by (Sane and Dickinson, 2002), and could be described by equation (3-33), where (x_c/L_c) is the position of the actuation axis with respect to the foil chord length. In the case of the model, the actuation axis is at 30% of the chord.

$$c_{rot} = \pi\left(0.75 - \frac{x_c}{L_c}\right) \tag{3-33}$$

The rotational forces described in (3-30) can be resolved into the roll and thrust component. The formula for calculating them are given by equation (3-34) and (3-35).

$$dF_{Kramer,\phi} = -\int_0^{L_s} dF_{kramer}\cos\theta \tag{3-34}$$

$$F_{Kramer,\psi} = \int_0^{L_s} dF_{kramer}\sin\theta \tag{3-35}$$

3.4.2.3 *Tip Loss Model*

When fluid flows over an aerofoil with a positive angle of attack, the flow going over the upper surface accelerates and generates a region of low pressure. The opposite happens on the lower surface where the fluid decelerates and generates a region of high pressure. In a foil with infinite span, the two streams would flow straight across the foil recombine at the trailing edge where the pressure eventually equalises at infinity. However, in a normal foil with finite span, the high pressure fluid from the lower surface can flow over the tip of the foil and recombines with the low pressure stream on the upper surface instead of travelling the length of the foil and recombining at the trailing edge. This can reduce lift near the foil tip and create a pressure differential that varies along the foil span.

Two tip loss models are tested for the aquatic flight BET model. The first is the elliptical lift distribution and the second is the Prandtl tip loss model.

3.4.2.3.1 Elliptical Lift Distribution

The first method models tip loss using a simple elliptical lift distribution. A tip loss correction factor (K_{TLC}) will be used to correct the lift force generated by each foil element based on their distance from the wing tip. Equation (3-36) shows the formula for calculating the correction factor. The distance from roll axis to the element is r_i. The minimum wing span r_0 represents the distance from the axis to the root of the flapping foil. The wing span (R) is the length of the active foil region.

$$K_{TLC}(r_i) = \sqrt{1 - \left(\frac{r_i - r_0}{R}\right)^2} \qquad (3\text{-}36)$$

3.4.2.3.2 Prandtl Tip Loss Model

The second tip loss model used in the analysis is the Prandtl tip loss model, which was developed to model ship propeller blades. It is also used for analysis of helicopter rotors and wind turbine (Seddon, 1990; Shen et al., 2005). Prandtl tip loss factor is given by (3-37) .

$$K_{TLC}(r_i) = \frac{2}{\pi} arccos\left(e^{\left(-\frac{B(R-r_i)\sqrt{1+\lambda^2}}{2R}\right)}\right) \qquad (3\text{-}37)$$

In the case of a flapping foil, the total number of blades in the propeller, B, is 1. The tip speed ratio, λ, is a function of the angular velocity, Ω, the free stream velocity, U, and the blade span, R. The equation to calculate λ is given by (3-38).

$$\lambda = \frac{\Omega R}{U_\infty} \qquad (3\text{-}38)$$

3.4.2.3.3 Foil forces With Tip Loss

The tip loss factor is applied to the lift component of the foil force, so the foil force equations (3-16) and (3-17) needs to be modified accordingly. The modified equation is shown in (3-39) and (3-40)

$$dF_{TL\psi,i} = K_{TLC}(r_i)dF_L\, sin(\beta) + dF_D cos(\beta) \qquad (3\text{-}39)$$

$$dF_{TL\phi,i} = K_{TLC}(r_i)dF_L\, cos(\beta) - dF_D sin(\beta) \qquad (3\text{-}40)$$

3.4.3 Total Foil Force

After calculating the individual component of force at different foil elements and time steps, the last step of the BET model is to integrate these individual results to produce the overall force acting on propulsor. The element forces are first calculated in roll and yaw, before being converted to the vehicle thrust and lift in X and Y ((3-41)and (3-42)).

$$\sum dF_T = \sum_{i=1}^{n} \left(dF_{TL\psi,i} + dF_{\psi AM,i}\, dF_{kramer} \sin\theta \right) \cos\psi \qquad (\ 3\text{-}41\ )$$

$$\sum dF_{VF} = \sum_{i=1}^{n} \left(dF_{TL\phi,i} + dF_{\phi AM,i} + -dF_{Kramer} \cos\theta \right) \cos\phi \qquad (\ 3\text{-}42\ )$$

Both horizontal thrust and the vertical forces varies throughout the flapping cycle, therefore it is necessary to calculate the average force for the whole cycle before it can be non-dimensionalised into the thrust and down force coefficient. The period of the flapping cycle can be calculated from the Strouhal number, global inflow velocity and flapping amplitude using equation (3-43).

$$T = \frac{1}{f} = \frac{L}{St\ U} = \frac{2r_{0.7}\phi_0}{St\ U} \qquad (\ 3\text{-}43\ )$$

The average thrust is given by equation (3-44) and the average vertical forces by equation (3-45). Since the flapping cycle is symmetrical, the average vertical force would be zero.

$$\overline{\sum F_T} = \frac{1}{T} \int_{t=0}^{T} \sum F_T \, dt \qquad (\ 3\text{-}44\ )$$

$$\overline{\sum F_{DF}} = \frac{1}{T} \int_{t=0}^{T} \sum F_{DF} \, dt \ = 0 \qquad (\ 3\text{-}45\ )$$

The average thrust can be used for calculating the non-dimensional thrust coefficient using the equation (3-46).

$$C_T = \frac{\overline{\Sigma F_T}}{0.5\, \rho A_{foil} U^2} \qquad (\ 3\text{-}46\ )$$

The non-dimensional thrust coefficient will allow comparison to be made between flapping cycles with different amplitude, frequency, and inflow velocity. It can also account for small changes in foil dimension, which can be useful when comparing different experiment setups.

3.5 Modelling Results – BET model for Two-axis cycle

3.5.1 Blade Element Theory Model

The single element SQS model's results showed similar patterns to the experiments carried out by MIT, however, quantitatively there were some differences. The next step of this investigation adds Blade Element Theory to the model to simulate the variation of flow along the span of the foil. The BET model initially divides the foil into 100 elements and calculates the thrust coefficient for various two-axis flapping cycles between Strouhal number 0.1 and 0.8 and at an inflow speed of 0.1ms^{-1}. The number of elements would be adjusted after examining the convergence of the results. A number of different foil geometries were examined but the main focus would be the foil used in the NIMBLE experiment, which is a NACA0012 foil with a span of 0.5m and a constant chord of 0.15m.

The first part of the analysis looked at the performance of individual elements along the span and examines the forces at 0.1, 0.3, 0.5, 0.7 and 1.0 span. Since the angle of attack of the foil varies along the foil span, the program calculates the amplitude of the foil pitch angle from a defined maximum angle of attack at 0.7 span ($\alpha_{0.7}$). Since the foil is rigid, the pitch angle of attack would be constant along the span and this pitch angle would be used to calculate the local angle of attack at each foil element.

The investigation will first focus on the blade element theory aspect of the model, so the sub-models for the other hydrodynamics effects would be disabled. It will examine the forces and the thrust coefficient of various cycles and the effect of variation in flow speed, foil dimension and roll amplitude. Then after the BET aspect is examined, the various scenarios will be repeated with the sub-models for other hydrodynamic effects enabled to analyse the effect of added mass, Kramer effect and tip loss.

After testing the model in two-axis and comparing the BET model results with existing data, the model will then proceeds to investigate the effect of three axis actuation. The three-axis model introduced an additional motion component in yaw. This introduced the possibility of different gaits. The literature review showed aquatic flight animals can adopt several actuation paths, but the most common is the figure-of-eight shaped path used by penguins or an oval shaped used by seals and turtles. The actual animal stroke is quite complex, so the model will examine idealised versions of these paths.

3.5.2 Modelling results

The first part of the modelling investigation will examine the effect of the Blade Element Theory model without the additional hydrodynamics sub-models for added mass and Kramer effect. The goal is to compare the results with the of the single element model and examine the effect of using BET to model aquatic flight. During this investigation, an example case of a flapping foil operating at 0.1ms^{-1}, St 0.5, $\alpha_{0.7}$ = 40° would be used. This represent a centre point of the investigated range and the region of interest where the Strouhal number is similar to the penguins swimming performance measured during the video investigation.

Figure 3-19 to Figure 3-23 show the position and forces of a flapping foil operating at the aforementioned example scenario. Figure 3-19 shows the foil roll and pitch position, angular velocity and angular acceleration over a period of 20 seconds. The input corresponds to a flapping frequency of 0.13Hz and pitch amplitude of 17.5°. The roll motion has a 90° phase lead over pitch motion. This also meant angular velocity has a 90° phase lead over its corresponding angular position in pitch and roll, while angular acceleration has a phase lead of 90° over the corresponding angular velocity and 180° over position.

Whilst the angular velocity shown in Figure 3-19 is constant along the foil span, the absolute velocity changes depend on the element's distance from the axis (radius). This leads to a variation of roll velocity, inflow velocity and angle of attack along the foil span. Figure 3-20 shows the angle of attack at different positions along the foil span, namely 0.1, 0.3, 0.5, 0.7 and 1.0 span. The foil motion was defined by the maximum angle of attack at 0.7 span, so the maximum angle of attack at 0.7 span was 40° as expected. Since foil elements at the tip of a flapping foil move with a higher roll velocity, it would have a corresponding higher inflow velocity. This results in a steeper inflow angle and a higher angle of attack. Likewise, since the root of the foil moves slowest, the corresponding angle of attack would be smallest among all the elements.

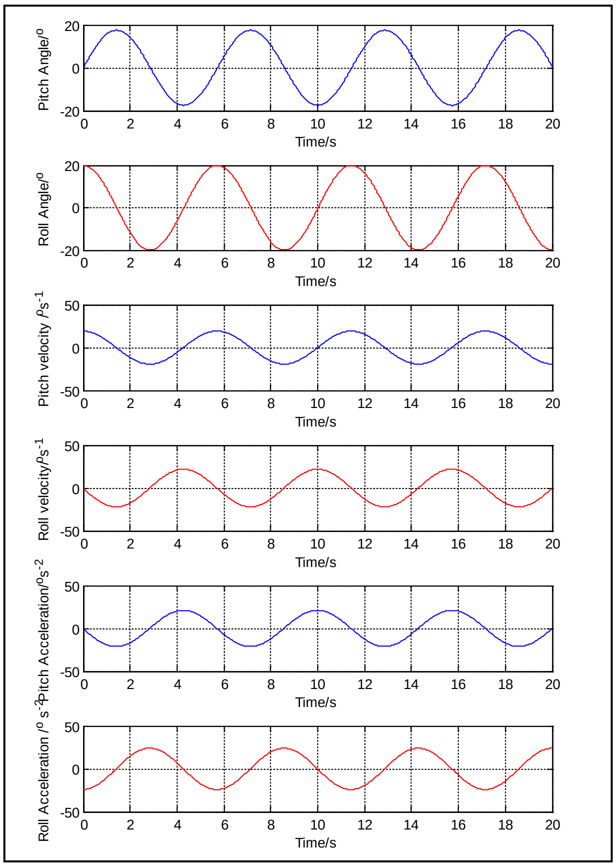

Figure 3-19 – Pitch and roll angle, velocity and acceleration of foil operating at 0.1ms^{-1}, St 0.5, $\alpha_{0.7}$ = 40°

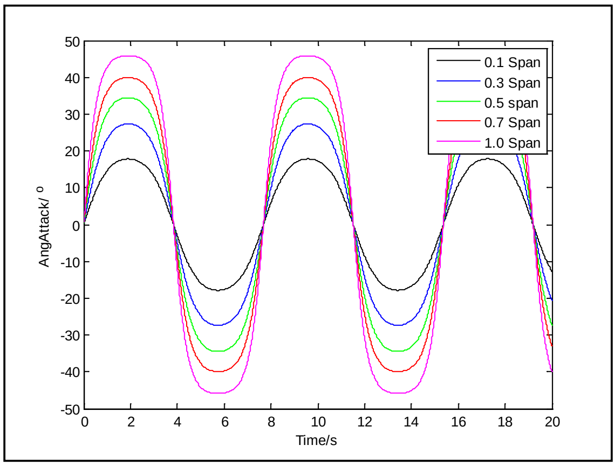

Figure 3-20 – Angle of attack of foil operating at 0.1ms^{-1}, St 0.5, $\alpha_{0.7}$ = 40°

The variation of inflow velocity and angle of attack along the span leads to different lift and drag force created by each element. Figure 3-21 (left) shows the lift and drag forces generated by various elements along the foil span. The plot shows the tip of the foil produced the highest force while the root of the foil generated the least. This is because the former had the highest inflow velocity and angle of attack, while the latter had the lowest. Since the foil's flapping motion rotates around the roll axis, the forces produced are tangential to the axis of rotation. A two-axis cycle has no yaw movement so the foil thrust force would be in line with X, but the tangential direction corresponding to the foil lift force changes with the roll position. Therefore, additional calculations would be needed to find the component of the tangential force (F_{ϕ}) that contributes to the vehicle vertical force in Y. The results of these calculations are shown in Figure 3-21 (Right).

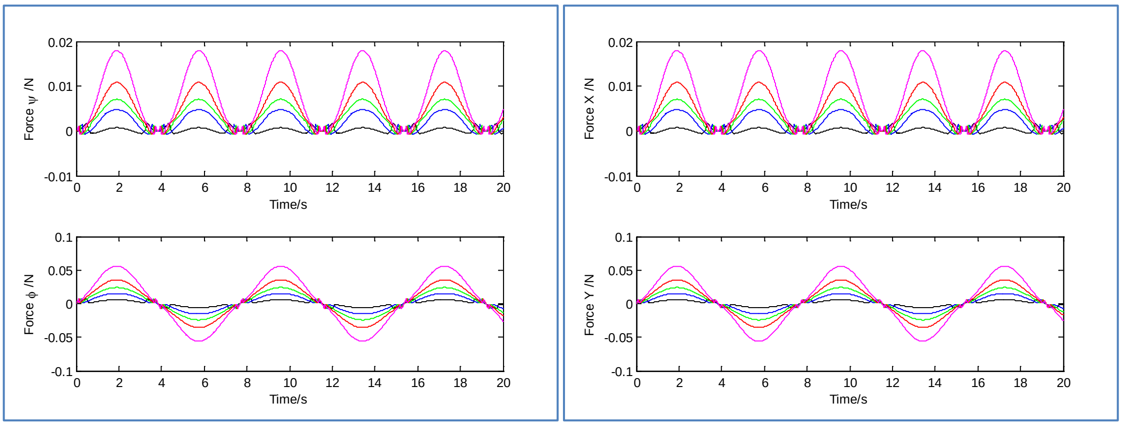

Figure 3-21 – (Left) Lift and drag forces generated by various elements along the span. (Right) The vertical and horizontal force corresponding to the foil's lift and drag force (Left). (0.1ms^{-1}, St 0.5, $\alpha_{0.7}$ = 40°

One of the assumptions of the SQS model and the existing investigation was the foil forces at 0.7span represented the average forces across the whole foil. The blade element theory model can check this assumption by examining the cycle peak force (Figure 3-22 (Left)) and cycle averaged force across the span (Figure 3-22 (right)). The former shows the maximum force achieved over one flapping cycle by each element, and the latter shows the element's force average over a cycle. The cycle maximum and cycle averaged force for each element is plotted in blue, while the averaged force across the whole foil span is plotted in red. The foil has a span of 0.5m, starting from 0.2m from the axis of rotation to 0.7m.

The plots show the maximum force first decreases from foil root to 0.27m and then gradually increased towards the tip. The averaged cycle force also shows a similar initial flat line at the root. Examination of the angle of attack graph (Figure 3-20) shows the foil angle of attack at 0.1span was between 10° and 20° for most of the cycle, which suggests the foil elements near the root have stalled for much of the cycle thus reducing the thrust produced. The line representing the horizontal element force averaged over a propulsion cycle has a similar shape to that of the maximum force, but with a lower magnitude. The vertical cycle averaged force has a value of zero, because the forces from up and down strokes cancelled out over one propulsion cycle. The foil element force line intercepted the average force level line at 0.48m, which is 0.56 foil span. This meant the increased forces near the tip of the foil balanced out the reduced forces near the root of the foil at 0.56span, rather than 0.7span as it was previously assumed.

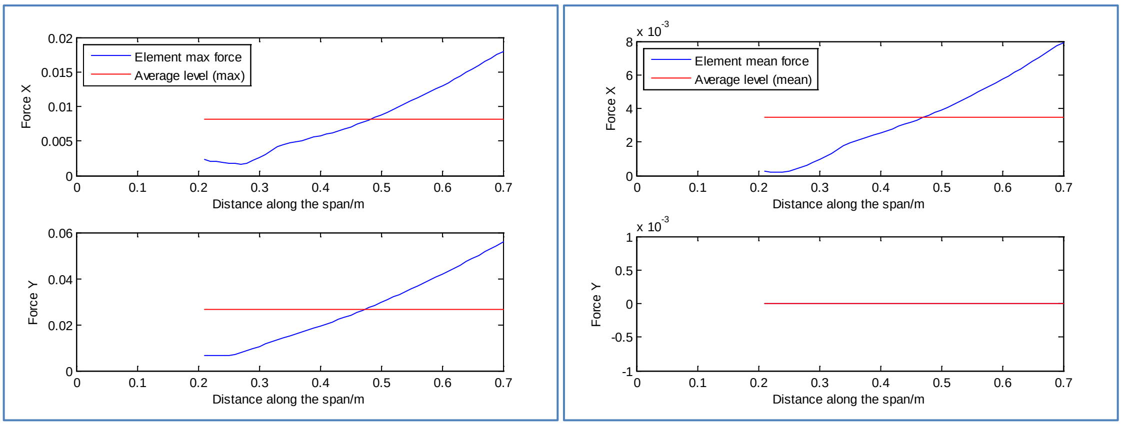

Figure 3-22 – Comparison between maximum (left) and average (right) force at each foil element and the average force generate by foil. While force Y has a high maximum, it is cancelled out over a cycle, resulting in an average vertical force of zero

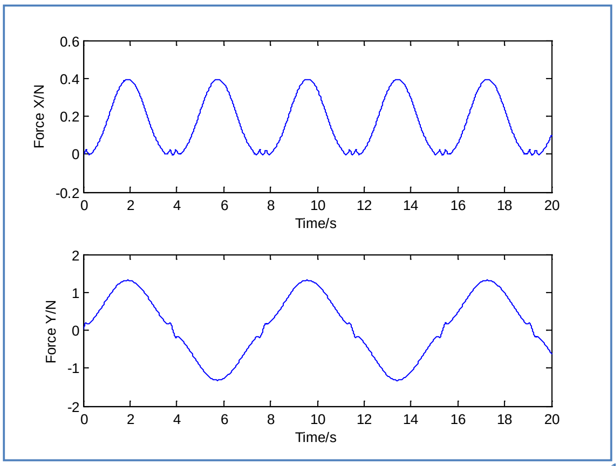

Figure 3-23 – Total horizontal and vertical forces of a foil operating at 0.1ms^{-1}, St 0.5, $\alpha_{0.7}$ = 40°

After evaluating the forces on individual foil elements, the element forces were added together to calculate the overall thrust produced by the flapping foil. Figure 3-23 shows the total horizontal and vertical forces on the foil over the flapping cycle. The horizontal force cycle produced thrust at doubled the frequency of the vertical force. This is because forward thrust is generated in both up stroke and down stroke, whereas the direction of the vertical force is dependent on the direction of the stroke. Whilst a thrust of 0.4N appears very small, this is because the foil was operating at a very low frequency of 0.13Hz (a period of 6.7s) to achieve the Strouhal number of 0.5 at 0.1ms^{-1}. The flapping frequency would be higher if the velocity was higher, which would also increase the thrust. If the foil operated at 1ms^{-1}, the corresponding peak thrust at Strouhal number of 0.5 is around 40N.

3.5.2.1 *Summary*

The blade element theory model demonstrated that the forces produced by each foil element increases as the distance from the rotational axis increase. This is the result of increasing foil tangential velocity, which is a function of the foil angular velocity and the foil element working radius. The increase foil velocity in turn increased the foil angle of attack and the foil inflow velocity, which increased the amount of force produced. The forces do not increase linearly along the span and can be affected by non-linear factors such as foil stall.

When the foil element cycle maximum force and cycle average forced was examined against their position along the span, it was found the foil centre of pressure is at 0.56span rather than the 0.7span that was initially assumed.

After individual elements was analysed, the model added the individual results from each element together to produce the overall force acting on the foil. It was found the horizontal forward thrust was produced in both up and stroke, but the direction of the vertical forces depended on the stroke direction. Generally up-stroke only produced downwards vertical force and down-stroke only produced upwards vertical force. As such, the horizontal thrust cycle’s frequency appears to be doubled that of the vertical force cycle. The foil forces in both directions reach their maximum when the roll velocity peaked mid-stroke.

3.5.3 Effects of Strouhal Number Variation

The Strouhal number is a function of frequency, amplitude, and flow velocity. Assuming the flapping amplitude and flow velocity remain constant, the Strouhal number can be treated as a non dimensionalised frequency. This section examines the effect of different Strouhal numbers on the flapping cycle. The roll amplitude is fixed at 20°, $\alpha_{0.7}$ at 40° and flow velocity at 0.1ms^{-1}.

The effects of three Strouhal number are examined in this example, namely 0.2, 0.5 and 1.0. This corresponds to flapping frequencies of 0.05, 0.13 and 0.21Hz. Figure 3-24 shows the roll and pitch angles of the foil corresponding to each Strouhal number. The pitch amplitude varied from 7.9° to 28.3°, because the foil had to maintain an angle of attack at 0.7span of 40°. When the inflow angle is relatively shallow at low Strouhal number, the pitch angle had to be small to maintain the angle of attack. Likewise, when the inflow angle is steeper at higher Strouhal numbers, the pitch angle had to increase to maintain the required angle of attack. The roll amplitude was predefined as 20°, so the roll amplitudes in the plot remain constant for all three cases.

Since the angle of attack is calculated by subtracting the pitch angle from the inflow angle, it would not be possible to produce angle of attack that is larger than the inflow angle. If the angle of attack requested is larger than the inflow angle, the pitch angle could become negative. This can happen at lower Strouhal numbers when the inflow angle is low. Figure 3-24 shows an example of this in the plot for St 0.2. The pitch angle of St0.2's case appeared to be 180° out of phase with the pitch angles for higher Strouhal numbers, because the inflow angle was smaller than 40°. This means in order to achieve 40° angle of attack the model has to force the pitch to become negative.

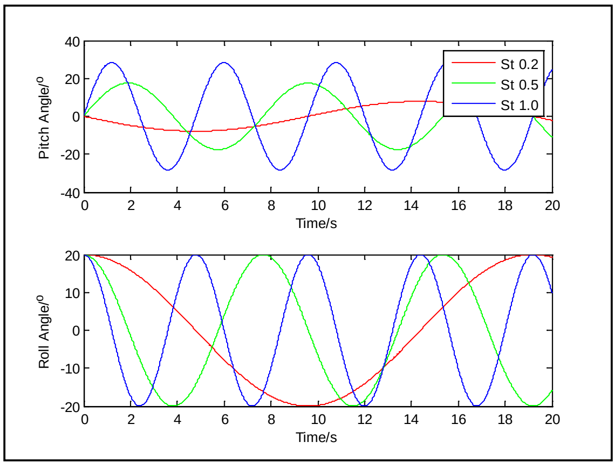

Figure 3-24 – Foil pitch and roll position at different Strouhal number

The net forces generated by the flapping foil at the three Strouhal numbers are shown in Figure 3-25. It can be seen more thrust is generated by the foil operating at higher Strouhal number. All horizontal force cycles contains a period of time when thrust is negative. This occurs at the top and bottom of each flapping cycle when the heave velocity and angle of attacks becomes zero. The foil could not produce any thrust during these phases of the flapping cycle to overcome drag, so the net force in these parts of the cycle is drag. Since a maximum angle of attack of 40° at 0.7span was not achievable at St0.2 and a flow speed of 0.1ms^{-1}, the pitch angle became negative. The effect can be seen in the graph where Force X was almost always negative. The negative Force X can be seen as drag or reverse thrust.

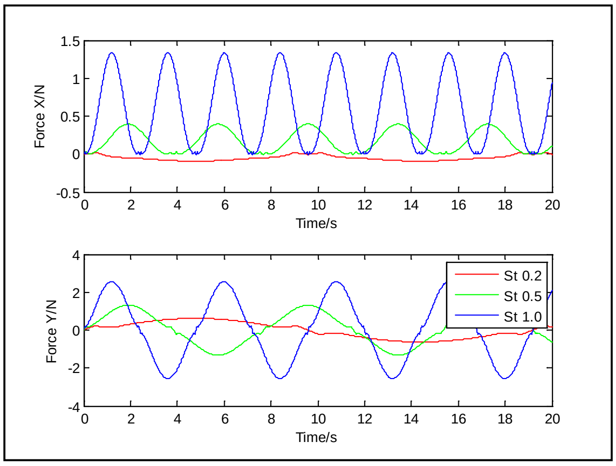

Figure 3-25 - Net force of flapping foil at different Strouhal number

When the foil angle of attack, roll amplitude and global inflow velocity is fixed, it was found increasing the Strouhal number will increase the flapping frequency, which will in turn increase the amount of thrust produced. The flapping frequency then determines the foil velocity, the foil inflow velocity and the foil inflow angle. As such, when a foil operates at low Strouhal number, special care needs to be taken to make sure the angle of attack is not excessively high. When the demanded angle of attack is higher than the maximum inflow angle (as in the case of Strouhal number of 2), it would cause the thrust direction to reverse and increase the drag produced.

3.5.4 Effects of Angle of Attack Variation

The foil angle of attack is one of the parameters that determine the foil lift and drag coefficients, which in turn determine the foil lift and drag forces. This section examines the effects of different angles of attack on the performance of the flapping foil. For this part of the investigation, the roll amplitude is fixed at 20°, Strouhal number at 0.7span is fixed at 0.5 and flow speed is fixed at 0.1ms^{-1}. The foil angles of attack examined are 20°, 40°, and 60°. The results are shown in Figure 3-26.

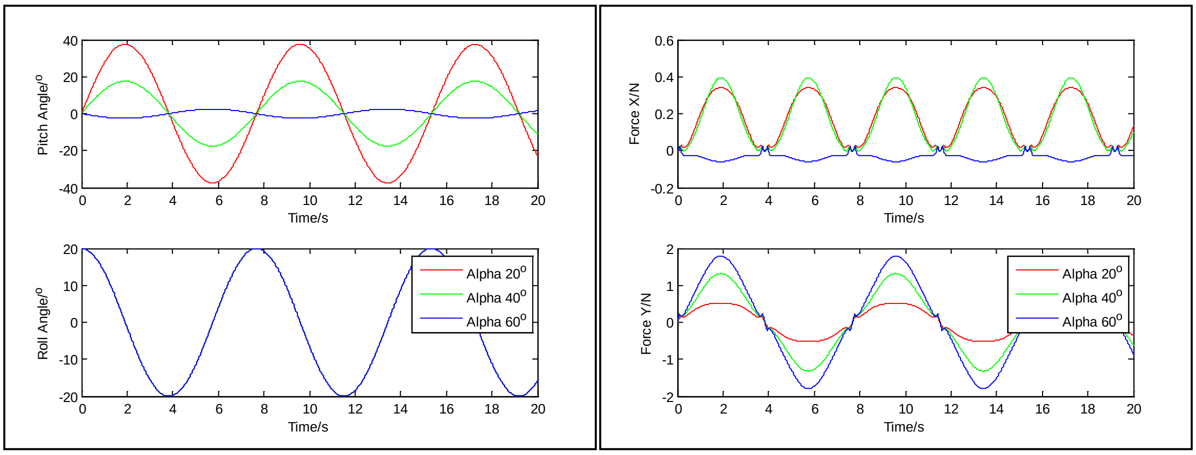

Figure 3-26 (Left) – Pitch and roll angles at different angles of attack. (Right) – Net forces generated by foil at different angle of attack

Figure 3-26 (Left) shows the pitch and roll position of the flapping foil. Since Strouhal number, roll amplitude and flow speed were fixed, the frequency would remained constant. Therefore, the roll angle plots for all three cases would be identical. Since inflow angle is a function of roll velocity and global inflow velocity, the inflow angle for all three cases would also remain constant. Unlike roll angle and inflow angle, pitch angle is calculated as the difference between the inflow angle and angle of attack, so the pitch amplitudes would change depending on the commanded angle of attack. If inflow angle is constant, a higher pitch angle would be required to achieve a smaller angle of attack. This can be seen in the graph where the pitch amplitudes required for maximum angles of attack of 20° and 40° were 37.5° and 17.5° respectively. The maximum inflow angle for a flapping foil operating at St=0.5 and flow speed of $0.1ms^{-1}$ is 57.4°, so it was impossible for the foil to achieve a maximum angle of attack of 60° in the given operating condition. As such, the model returned a negative pitch amplitude of -2.6°.

Figure 3-26 (Right) shows a plot of the net forces at different angle of attack. It can be seen the foil generated the largest amount of thrust when $\alpha_{0.7max}$ was 40°. Slightly less thrust was produced when $\alpha_{0.7max}$was 20°, although the difference is relatively small. However, when $\alpha_{0.7max}$was 60°, the foil cannot achieve the required angle of attack in the given condition. This caused the pitch angle to become negative during that cycle and resulted in the negative thrust being produced.

In summary, since angle of attack is the difference between inflow angle and pitch angle, increasing the angle of attack would cause the pitch angle amplitude to decrease. The inflow angle is a function of the global inflow velocity and the foil roll velocity, the latter of which is a function of the Strouhal number. As such, the inflow angle has a finite size, and the maximum angle of attack achievable must be smaller than the inflow angle. If the angle of attack exceeds the inflow angle (as in the case when $\alpha_{0.7} = 60°$), it could cause a reversal of thrust due to the pitch angle being forced into the negative. Since, the foil local inflow velocity and inflow angle varies depending on the distance from the roll axis, it is unavoidable the some sections near the foil root may have insufficient inflow angle, but situation can be worsen if the commanded angle of attack is high. Therefore, extra care should be taken when analysing cycles with high angle of attack or low Strouhal number.

The increase of angle of attack may or may not increase thrust output. If the angle of attack is low (~20°), increasing foil angle of attack can increase the thrust output, but if the angle of attack is already high (>40°), further increase in the commanded angle of attack can reduce thrust. Excessively high angle of attack input (>57.4° in this case) can cause the pitch angle to become negative and thrust direction to reverse.

3.5.5 Blade Element Theory Thrust Coefficient Map

In order to compare the results of the BET model with the experimental results reported by Licht, the program calculated the thrust coefficient (C_T) (3-46) at a range of angles of attack (10° to 60°) and Strouhal numbers (0.2 and 0.8). The results were plotted in a 3D surface plot and a contour plot (Figure 3-27).

The model shows the thrust coefficient increases as the Strouhal number increases, this occurs at all angle of attack examined. The thrust coefficient rises from 0 ($St_{0.7} = 0.2$) to over 1.6 ($St_{0.7} = 0.8$) at an angle of attack of 30°. The rise is slower at other angles of attack, but the thrust coefficients always increase when the angle of attack increases.

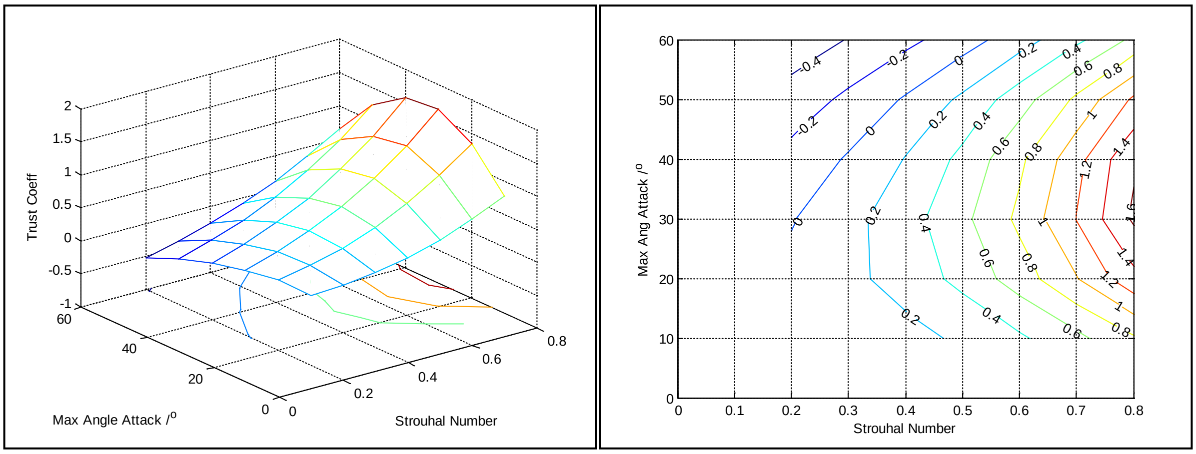

Figure 3-27 – Thrust coefficient map for flapping foil operating in two axis

While increasing the Strouhal number would increase the thrust coefficient, the same does not always apply to increases in angles of attack. As angle of attack increases from 10° to 30° the thrust coefficient also increases. However, the thrust coefficient begins to fall when the angle of attack becomes larger than 30°. Eventually the thrust coefficient can became negative for cycles with high angles of attack and low Strouhal number. This is caused by the thrust reversal created when the command angles of attack exceeded the foil inflow angle. This pattern was also observed in the single element model and in published literature. More detailed description of this can be found in the previous sections.

Since the thrust coefficient can rise and fall when the angle of attack is increased, it means there is an optimum angle of attack to maximise thrust coefficient. This optimum angle of attack increases as Strouhal number increase, but the increase is slow and mostly centred around $\alpha_{0.7max} \sim 30°$.

Non-dimensionalising the foil thrust and flapping frequency into the thrust coefficient and Strouhal number allows comparison to be made between different flow conditions as well and different systems. When thrust coefficients results from the BET model were plotted against the Strouhal number in a contour plot, it showed similar pattern to the experimental results published in the literature and modelling results of the SQS model.

Like the previous results, increasing Strouhal number would always increase the thrust coefficient, but the relationship is not linear. Meanwhile, increasing the angle of attack may not necessary increase the thrust coefficient, in some cases it could lead to significant reduction in the thrust coefficient. The optimum angles of attack were approximately 30° for most of the cases tested but they changes depending on the Strouhal number. If the angle of attack is less than the optimum and it is increased, the thrust coefficients would also increase, but if the angle of attack is higher than the optimum angle for that Strouhal number, the thrust coefficient will be reduced.

3.5.6 Effect of Flow Speed

One of the main reason for non-dimensionalsing the thrust and flapping frequency into thrust coefficient and Strouhal number is to allow analysis of flapping foil systems with slightly different set up, for example, whether operation at higher speed can be compensated by higher flapping frequency. In order to test whether the non-dimensionalisation has achieved this aim, the thrust coefficient calculated for a flapping foil operation at a speed of 0.1, 0.2, 0.5 and 1.0ms^{-1} is shown in Figure 3-28.

The plot shows all four thrust coefficient lines overlap and there are no differences between each line. This confirms variation in speed was compensated by changes in flapping frequency, so results taken at different flow velocities can be used for analysis against each other if the speed and flapping frequency are non-dimensionalised into Strouhal number. Therefore experimental verification can be carried out for certain scenarios that are previously unachievable due to hardware limitations by carrying out the test at different speed.

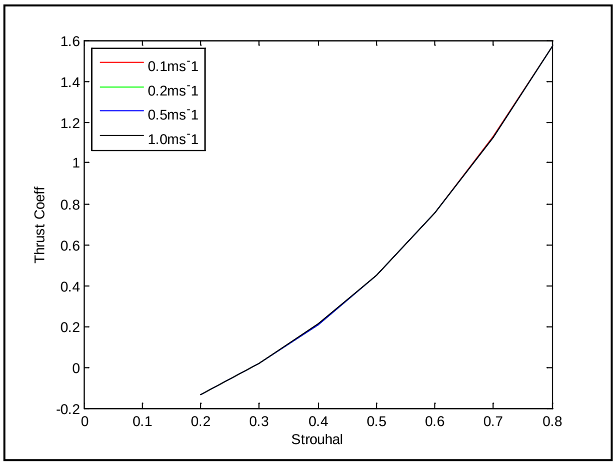

Figure 3-28 – Thrust coefficient of foil operating at different speed

3.5.7 Model Convergence

The blade element theory method is a finite element method where the forces on each foil element would be solved individually at each time step and then recombined to calculate the total force acting on the foil. The accuracy of this technique depends on how the structure is broken down into individual elements. Provided the calculation in each element is correct, increasing the number of elements can improve the accuracy, but it would also increase the computational work load. There is a diminishing return to the accuracy, so it is important to find the right balance between accuracy and computational resources. Blake's original BET analysis of the rowing diodontiform locomotion divided the fin into four elements (Blake, 1979), but his is probably inadequate so the initial BET model start with 100 smaller foil elements and then check for convergence to determine the optimum number of elements.

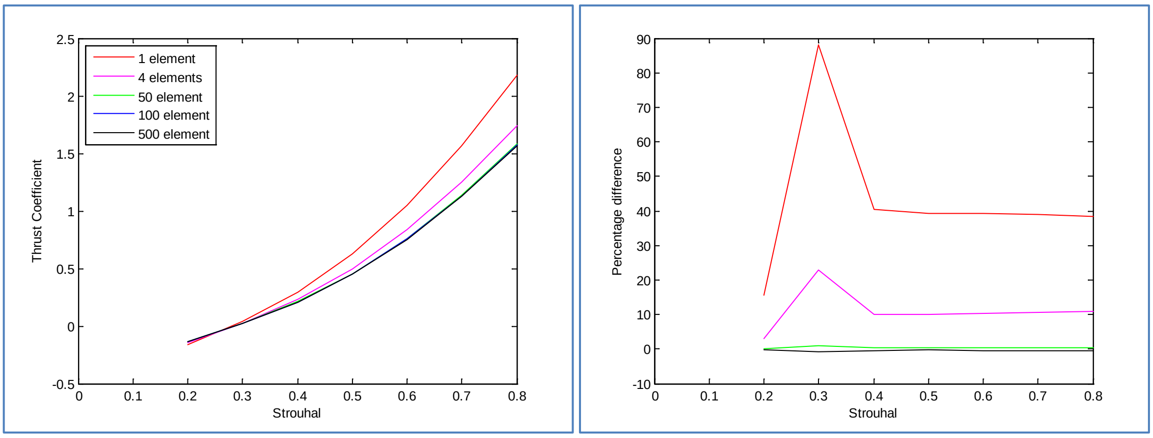

Figure 3-29 (Left) – Thrust coefficient comparison by BET models with different numbers of element. (Right) – Percentage differences between various model and the 100 element model ($U = 0.1ms^{-1}$, $\phi_o = 20°$, $\alpha_{0.7} = 40°$)

Figure 3-29 shows the thrust coefficient calculated by five models with different numbers of foil elements. These included a case for a single element and four cases with 4, 50, 100, and 500 elements respectively. It can be seen the single element case shows a considerably higher thrust coefficient than the other cases. The case using 4 elements improved the accuracy and its results begin to approach the models with more elements. The results between 50, 100, and 500 elements appear very close to each other.

The percentage differences between each of the cases were calculated against the case with 100 elements and the results were plotted in Figure 3-29 (Right). The difference between the single element and the 100 elements model is over 38% at a St = 0.8. The four elements model produced a closer thrust coefficient estimate just over 10% higher than the 100 element model. The percentage differences quickly reduced to 0.5% with for the model that utilised 50 elements. The BET model's results were converging, and it was concluded that 50 elements was sufficient for the BET model to be accurate to within 1%.

Since the test foil has a span of 0.5m, dividing it into 50 elements will yield an element span of 1cm. The overall results of the BET model showed, the thrust coefficient is reduced by 38% compared to the single element model. This is not unexpected because the BET model showed the hydrodynamic centre of the foil was at 0.56 span rather than 0.7span. When this is applied to the SQS model, it will reduce the foil tangential velocity and foil inflow velocity by around 15%, and thrust by just over 31%. Blake (1979) used a model with 4 elements to model his rowing foil, but the results of this section showed 4 elements is insufficient to capture the effect caused by flow (and flapping) velocity variations along the foil span (~10% over estimation). Therefore, the aquatic flight BET model will utilise 50 foil elements in its calculations.

3.5.8 Effect of Foil Shape

The model and the experiment used a NACA 0012 foil with a uniform chord and cross-section across the span. The foil has a chord of 0.15m, an active span of 0.5m and the foil root was position 0.2m from the roll axis. Experiments set up used by Flores, Licht and Techet have different foil dimension. Licht's foil has a span of 0.4m, a chord of 0.1m, and the root was position 0.25m from the roll axis(Licht et al., 2004b). Techet's foil has a span of 0.246m, an aspect ratio of 5 and was positioned 0.1m from centre of roll axis (Techet, 2008). Flores's used a NACA0015 foil that has a span of 0.243m, has a chord of 0.075m at the root which gradually tapered to 0.035m at the rounded tip. The foil root was a unspecified distance from the roll axis (Flores, 2003). Due to the very different shape and force coefficient associated with different foil cross sections, direct comparison of the dataset would be difficult.

It would be impossible to analyse all foil designs directly. Therefore it will be useful if there is a method that will allow quick comparison between similar foils. One of the reasons for performing the analysis using non-dimensional parameters is to allow comparison between similar but not identical set up. The foil thrust coefficient is non-dimensionalised against foil area, and Strouhal number non-dimensionalised against span through the flapping amplitude, so the model should be able to account for some changes in span and chord length. However, the model’s non-dimensionalisation cannot account for changes in the foil cross-sections, which would affect the lift and drag coefficients used in the calculation.

The foil shape analysis aims to analyse the effects caused by variation in foil span and chord length. It will determine the effect of changing the span and chord of the foil, and examine whether the use of non-dimensional parameters will allow comparison between different system, and whether foil size variation caused by manufacturing error will have a significant impact on the experimental results.

3.5.8.1 *Span*

The first part of the foil shape variation analysis looks at the effect of changing the foil span. The default NIMBLE BET model foil has a span of 0.5m. Four additional spans were tested in this analysis, including span of 0.3, 0.4, 0.6 and 0.7m. The foil chord and cross section remained constant from wing root to wing tip. The default foil chord of 0.15m, which would produce a foil aspect ratio of 3.33. The other aspects ratios were 2.00, 2.67, 4.00, and 4.66 for span of 0.3, 0.4, 0.6, and 0.7m respectively. The flow speed was 0.1m and the roll amplitude was 20°.

Figure 3-30 (Left) shows a plot of the thrust coefficient at $\alpha_{0.7}$ of 40°. The graph shows differences in thrust coefficients between different flapping foil. Contrary to expectation, the non-dimensionalisation do note fully compensate for the change in the foil length and the shorter spans produced marginally higher thrust coefficient than the longer span. Figure 3-30 (Right) shows the percentage difference in thrust coefficient when additional spans were compared against the default foil with a 0.5m span. The 0.3 meter foil’s thrust coefficients were about 6% higher than the default foil, while the longer 0.7m foil’s thrust coefficient were up to 3% lower. However, while there is a difference in foil thrust coefficient, the differences were smaller than one might expect from the differences in foil dimension. The 0.3m foil was 40% shorter than the 0.5m foil, while the 0.7m foil was 40% larger. As such the error caused by a foil manufacturing error of 1cm (0.01m) on the foil will be negligible.

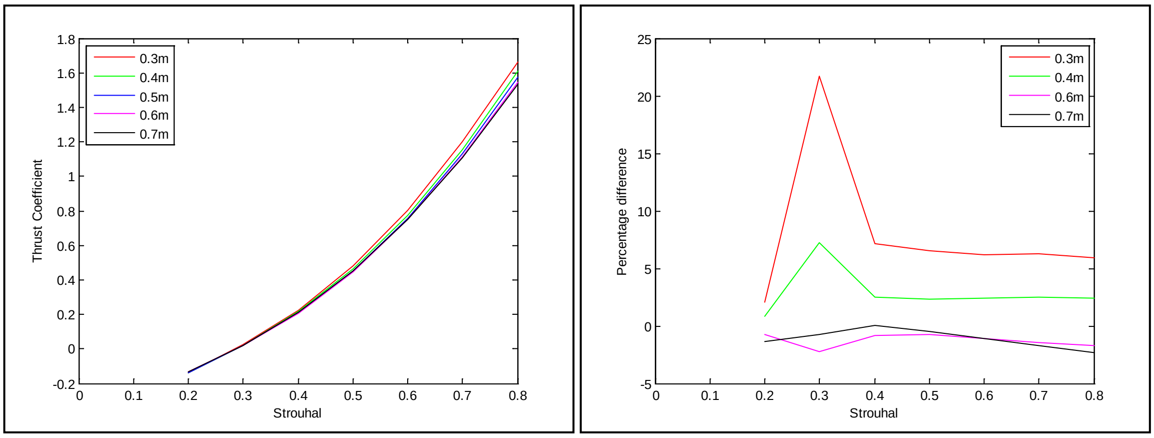

Figure 3-30 – (Left) Comparison of thrust coefficients between flapping foil of different span. ($U = 0.1ms^{-1},\ \theta_o = 20°$). (Right) Percentage differences between thrust coefficients generated by flapping foil with different span

Nevertheless, the non-dimensional parameters did not fully cancel out the effect of changing the span, and part of the reason for this is because the non-dimensionalisation of thrust coefficient and Strouhal number both depends on span and their effects interfere with each other. Since roll amplitude is a function of foil span and roll angle amplitude, the roll amplitude would increase if the foil span is increased. When flow velocity and Strouhal number were kept constant, any increase in foil flapping amplitude can be compensated by decreasing flapping frequency. It has already been demonstrated in previous sections that thrust coefficient and Strouhal number can account for changes in flapping amplitude.

However, increasing foil span not only increases the foil flapping amplitude, it also increases the foil area. This means it will also affect the non-dimensionalisation of the thrust coefficient. If the thrust output was constant, increasing the span would increase the foil area which will reduce the thrust coefficient. While this may sound counterintuitive that the larger foil produces lower thrust coefficient than a smaller foil, one must remember this is caused by the reduction in flapping frequency from the effect of the Strouhal number. If the frequency kept constant then the longer foil would generally produce higher thrust.

3.5.8.2 *Chord*

After analysing the effect of varying the foil span, the same analysis was carried out for the foil chord. Since Strouhal number is independent of foil chord, there should be no changes in flapping frequency. The analyses were carried out at an inflow velocity of 0.1ms^{-1}, roll angle amplitude of 20°. The chord lengths tested were 0.08, 0.10, 0.12, 0.15, and 0.18m, with

0.15m chord being the default chord used in the BET model. The foil's span was 0.5m with a constant chord and cross-sections from root to tip. The foil root starts 0.2m from the roll axis.

In summary, this part of the investigation found variation in foil chord is fully compensated in the calculation for the non-dimensional thrust coefficients. Since the Strouhal number is independent of chord length, the Strouhal number did not cause any interference like it did in the case of span variation. A plot of the thrust coefficient from five foils with different chord length is sown in Figure 3-31.

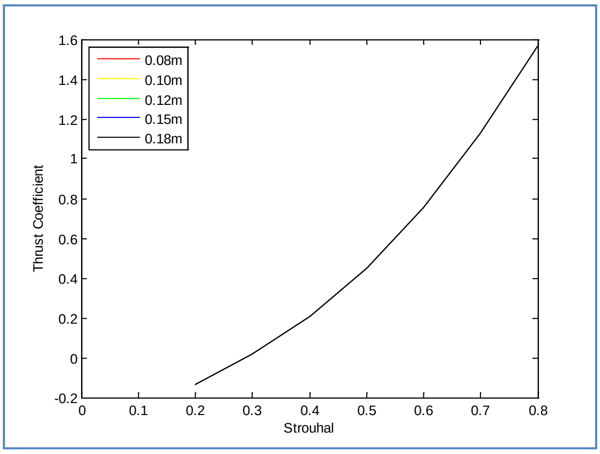

Figure 3-31 – Thrust coefficients for foil with different chord lengths. The thrust coefficients for all five cases were identical ($U = 0.1ms^{-1}$, $\theta_o = 20°$)

3.5.8.3 *Conclusion to foil shape analysis*

The investigation into variation in span and chord variation showed the non-dimensional thrust coefficient can accommodate different foil designs provided the foil shares similar lift and drag characteristics. Variation in chord can be fully compensated by non-dimensionalising thrust against foil area and other variables. The non-dimensionalisation of the thrust coefficient is also somewhat effective at correcting span variation, but changing span length also affects Strouhal numbers, which results in a change in the flapping frequency. This change in flapping frequency changes the thrust output, so different foil span can produced different thrust coefficients due to the interference Strouhal number and thrust coefficient. Fortunately the change is relatively small, where a 40% decrease in foil span only produces a 6% change in the thrust coefficient. While this may cause a minor problem when comparing very different setup, it would have negligible impact on the experiment foil which has a tolerance of around ±5mm on the foil span (1%) and chord (3%).

3.5.9 Conclusion to two axis cycle

The two-axis BET model breaks up a flapping foil into a numerous elements and then analyses the forces generated at each element before combining the results to calculate the total force acting on the foil. This method should produce a more accurate representation of the flow condition of a flapping foil than a simple quasi-steady model that uses an approximation at 0.7span.

The forces from the BET model were converted into non-dimensional thrust coefficient for analysis, and the results showed a similar patter to what was seen from the literature and the single element model, and as such this shows the BET model is sound. However the thrust coefficient calculated by the BET model is lower than that predicted by the single element model, which means the 0.7span approximation may result in an overestimation of the thrust. Examination of the force distribution along the span showed the foil centre of thrust is located at 0.56span rather than 0.7span, which means the assumption in the single element quasi-steady model that the forces should balance out at 0.7span may be incorrect. Discrepancy between the BET model and results in the literature could be due to the different set up, so it is important to perform experimental verification of the model as a form of verification.

The BET model was also used to tested effect of changing Strouhal number, angle of attack, foil geometry, flow speed and element numbers (convergence). The results show that as the Strouhal number increases, the thrust coefficient would follow. Conversely, increasing the angle of attack can increase the thrust coefficient if the initial angle of attack is low, but if the foil is already operating at a high angle of attack, increasing the angle of attack further reduce the thrust output.

The model also tested the effect of varying flow speed and foil geometry, and found neither have significant impact on the thrust coefficient, which confirms the non-dimensional thrust coefficient and Strouhal number can be used to perform comparisons between different systems. The convergence test found 50 foil elements would be sufficient to model aquatic flight to within 1%. A single element can lead to an overestimation of nearly 40%, while four elements will reduce this to 10%. The differences between 50, 100 and 500 elements were within 1% of each other, so there is no need to increase element number beyond 50.

After analysing the performance of the BET model in modelling two-axis aquatic flight, and forming an understanding of the effects of various parameters and forces, the investigation can then proceed to investigate three-axis aquatic flight.

3.6 Other Hydrodynamic Phenomena

In addition to the hydrodynamics lift and drag forces, the BET model also modelled the effect of added mass, Kramer effect and tip loss. These functions were not enabled in the initial BET model to allow closer examination of how the blade element theory method models the lift-drag mechanics of aquatic flight. By disabling the other sub-functions, the investigation can be certain any phenomena and changes seen in the results of the initial BET model would be the caused by hydrodynamic lift and drag, rather than these other effects.

After the examination of the base BET model is completed, the next part of the investigation would enabled the sub-models for added mass, Kramer effect, and tip losses, to examine how these other hydrodynamics effects affect hydrodynamics of aquatic flight. The three phenomena would be examined individually to avoid confusion with the others.

3.6.1 Added Mass

The first of the three phenomena to be analysed is the added mass. Added mass force is produced by the acceleration of the fluid mass around the flapping foil. Unlike foil lift and drag forces, which is a function of foil velocity, the added mass force is a function of foil acceleration. Therefore, the added mass force is expected to be out of phase with the lift and drag force cycle.

Figure 3-32 shows the added mass force generated by the flapping foil and the corresponding angular acceleration. The foil in the plot was operating at a Strouhal number of 0.5, flow speed of 0.1ms^{-1}, and roll amplitude of 20°. The vertical forces in Y is in phase with the angular acceleration in roll (Figure 3-32 (Right)). Since added mass is a function of acceleration and the fluid is accelerated and decelerated horizontally twice per flapping cycle (up and down strokes), the frequency of the horizontal added mass force is twice that of the vertical cycle.

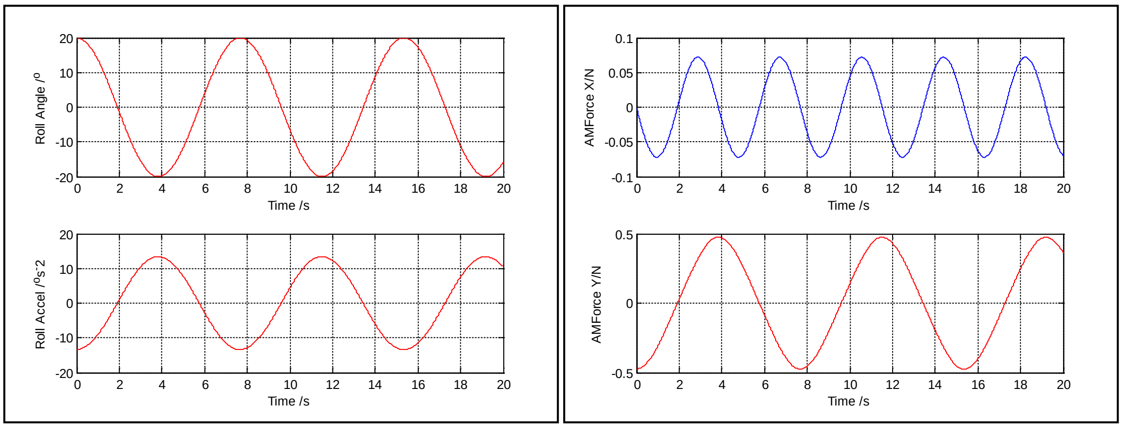

Figure 3-32 – Roll Position and acceleration of a flapping foil (Left) and the corresponding added mass forces (Right) $(U_{in} = 0.1ms^{-1}, St_{0.7} = 0.5, \alpha_0.7 = 40^\circ)$

The cycle shown in Figure 3-32 can be divided into 4 phases that last approximately two seconds each. From $t = 0 \rightarrow 2$s, the foil accelerate downwards in the first half of the down stroke, this produces negative added mass force which resists the change in roll motion. From $t = 2 \rightarrow 4$s, the foil decelerates in the second half of the down stroke, which produces positive thrust pushing the foil forward and resisting the change in roll velocity. The same pattern is mirrored in the upstroke from $t = 4 \rightarrow 8$s. It should be noted the added mass force is symmetrical, so any thrust lost in the acceleration phase of the stroke would be recovered in the deceleration phase. Therefore the net thrust from added mass forces would be zero. Since there are no changes in net thrust, the thrust coefficient would remain constant and independent of the added mass forces model. However, added mass effect could contribute to transient acceleration where this momentary loss of thrust and acceleration could affect whether an animal managed to escape its predator’s jaw.

Figure 3-33 shows a comparison between forces at different elements along the foil span without (left) and with (right) the added mass force function enabled. The plots show the overall amplitudes of the foil force did not change, but the gradient in the first quarter stroke (acceleration) appears steeper than the second quarter (deceleration). This is caused by the thrust reduction previously mentioned. Figure 3-34 showed the total force produced by the flapping foil operating at different angles of attack. The added mass forces act perpendicular to the foil so they are dependent on the pitch angle as well as the acceleration. Since angle of attack is a function of the pitch angle, changes in angle of attack can affect how the added mass forces are distributed between the vertical and horizontal direction, which in turn lead to the shift in peak positions in the total force plot in Figure 3-34.

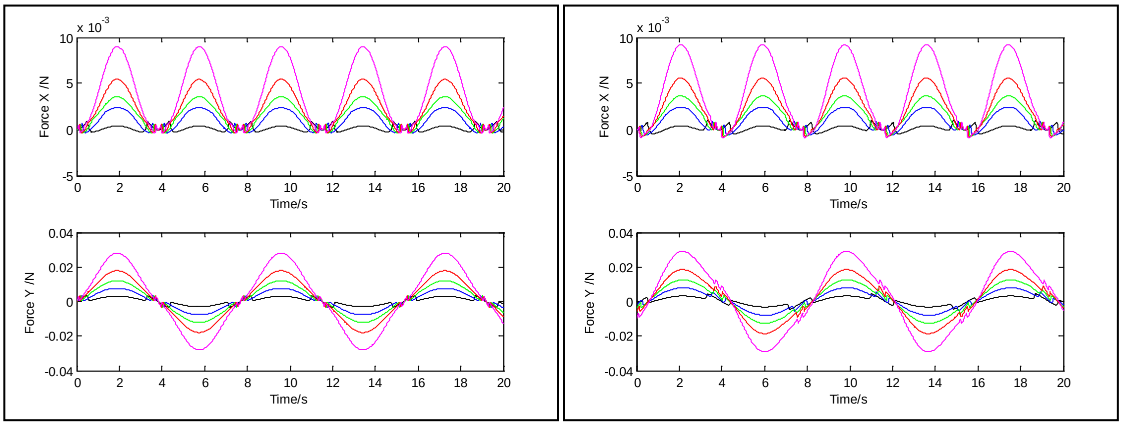

Figure 3-33 – Horizontal and vertical forces generated by various elements along the span of a foil WITHOUT (Left) and WITH (right) added mass force ($U_{in} = 0.1ms^{-1}, St_{0.7} = 0.5, \alpha_0.7 = 40°$)

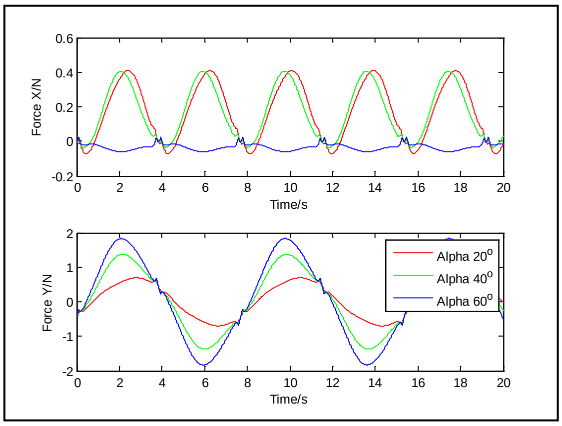

Figure 3-34 – Net vertical and horizontal forces, including forces associated with added mass. ($U_{in} = 0.1ms^{-1}, St_{0.7} = 0.5, \alpha_0.7 = 40°$)

In summary, added mass force can momentarily decrease the acceleration by reducing thrust. This mirrors the effects of added mass on marine propellers where the added mass force was known to cause a lag in the propeller’s response. Overall, added mass force cancels out over a stroke cycle, so it would not affect the thrust coefficient. If the foil is controlled every complete stoke cycle (Licht et al., 2004b), then it would not affect the acceleration performance of the foil propulsor. However, if the foil uses a more advanced controls system that allows correction within a flapping cycle, then it will need to take into account the effect of added mass.

3.6.2 Kramer Effect

The Kramer effect is the force produce when a hydrofoil’s pitch and roll motions are constantly changing. This results in a continuous ‘temporary’ violation of the Kutta condition and the viscous forces in the fluid would produce additional circulation to restore it. However the Kutta condition is never fully restored because the foil is moving and rotating continuously thus moving the point of restoration before Kutta condition can be re-established. The force produced by this circulation is the Kramer effect.

Figure 3-35 shows the forces produced by the Kramer effect and the corresponding pitch and roll angle and velocity. The Kramer effect produces horizontal force at double the frequency of the flapping motion, but thrust force in X is symmetrical, so it would cancel out over a period of oscillation and would not affect the thrust coefficient.

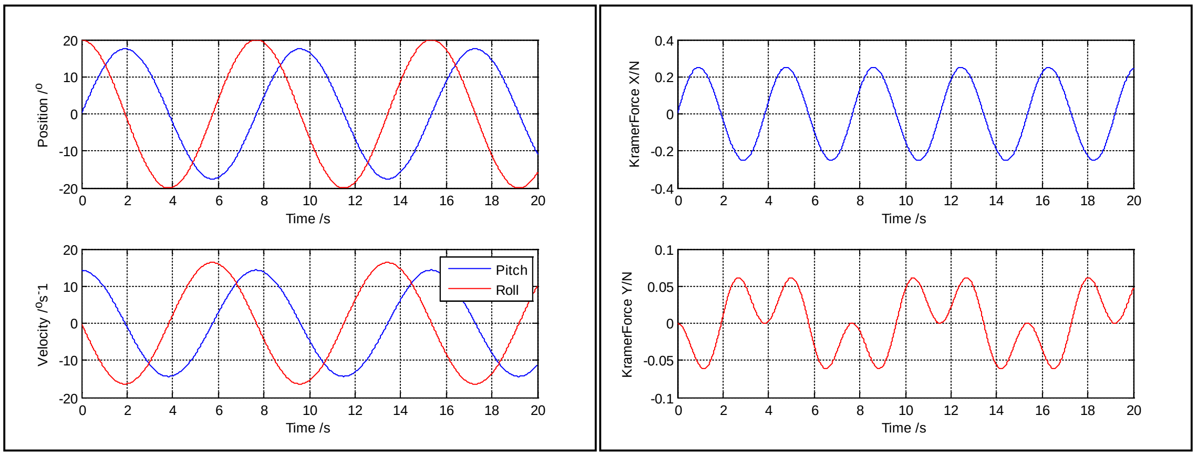

Figure 3-35 – Forces generated by the Kramer effect. (Left) The foil’s pitch and roll positions and velocities. (Right) The corresponding forces from the Kramer effect in X and Y directions ($St = 0.5, \alpha = 40°, U = 0.1ms^{-1}$)

The vertical forces in BET and added mass model were periodic sine waves that had the same frequency (or double frequency) as the foil flapping cycle. In contrast, Kramer force in Y is not a periodic sine wave, but a more complex periodic wave form with double peaks instead. This pattern is caused by the interaction between pitch angle, pitch velocity and roll velocity. In the example case shown in Figure 3-35, the resultant sign of the Kramer effect wave is summarised in Table 2.

Time (s)	Pitch angle	Pitch velocity	Roll velocity	Resultant sign
0-2	+ve	+ve	-ve	-ve
2-4	+ve	-ve	-ve	+ve
4-6	-ve	-ve	+ve	+ve
6-8	-ve	+ve	+ve	-ve

Table 2 – Table shows the sign of the pitch angle, pitch velocity and the roll velocity and how their interaction create the 'double' peaks seen in the vertical Kramer force

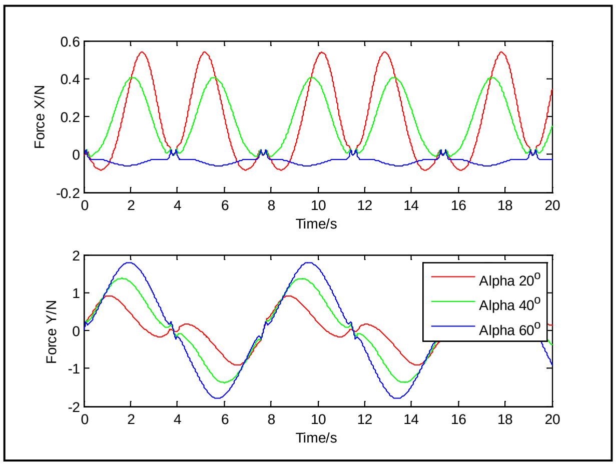

Figure 3-36 – Net force generated by foil with Kramer effect

Figure 3-36 shows the net force generated by the flapping foil with Kramer effects. The peaks of forces in both X and Y directions were shifted but the zeroes remained at the same position in time. In the horizontal X direction, the foil took longer to reach maximum thrust on the down stroke, but shorter to reach maximum thrust on the up stroke. Also, at lower angles of attack, the Kramer effect increased the peak thrust, but also increased the drag during 'recovery' period in the flapping cycle. A shift in the timing when the forces in Y reached maximum are also observed. The effect is more significant at lower angles of attack than at higher angles of attack. This is because Kramer effect is dependent on pitch velocity, and higher pitch amplitudes are required to achieve lower angle of attacks. If the frequency is kept constant, then increasing pitch amplitude would increase pitch angular velocity which would in turn increase the Kramer effect. This means while cases with lower angle of attack generated less force through hydrodynamic lift and drag, it generated greater Kramer forces due to higher pitch angle and pitch velocity. When these two factors were combined, it led to a more significant forward shift in peak force position during the down stroke, and more significant backwards shift during the up stroke.

In summary, the Kramer effect is affected by the foil pitch and roll motion, and its sign is dependent on the sign of pitch position, pitch velocity and roll velocity. The Kramer effect can lead to momentarily increase or decrease of foil thrust, but it does produce additional thrust over a symmetrical flapping cycle, so the thrust coefficient will remain unchanged. Nevertheless, the Kramer effect can affect transient manoeuvring where it may slow the initial acceleration within a propulsion cycle.

3.6.3 Tip Losses

The final phenomenon to be examined is the effect of tip loss on a flapping foil. When an aerofoil moves through a fluid at an angle of attack, it produces lift by creating a pressure differential between the top and bottom of the aerofoil. The flow is accelerated above and decelerated below the foil, forming a region of low and high pressure. If the foil has infinite length, the stream would recombine at the foil's trailing edge, but if the foil has a finite length, there is a tendency for the high pressure fluid from the underside of the foil to flow around the wing tip instead of travelling towards the trailing edge. This flow around the tip reduces the pressure differential and causes a loss of lift.

The investigations used two different methods to investigate the tip loss. The first is an elliptical lift distribution that's often used on fixed wings, while the second is the Prandtl tip loss model which is often used in propeller. Since biomimetic flapping foil is neither fixed nor continuously rotating, both methods should be examined.

3.6.3.1 *Elliptical Lift Distribution*

The elliptic lift distribution along the foil span, as described by equation (3-36), is shown in Figure 3-37 (Left). The foil starts at 0.2m from the axis of rotation and extends to 0.7m, with a span of 0.5m. The tip loss correction factor is unity (no tip loss) at 0m span and gradually reduced to 0 at the tip of the foil. The tip loss distribution on different element along the foil span is shown in Figure 3-37 (Right). It can be compared against Figure 3-22, which showed the distribution without tip loss. The plot showed the loss of lift is worst at the foil tip. Before tip loss was introduced, the element at the foil tip usually produced the highest force due to having the highest inflow velocity and angle of attack. When the tip loss correction is enabled, the thrust force first increase from the foil root towards the tip like the cases without tip loss, but begin to fall approximately half way across the span. Eventually the force is reduced to zero at the tip of the foil. In this model, the foil tip can no longer produce enough thrust to counter the drag and instead became one of the main contributors to drag.

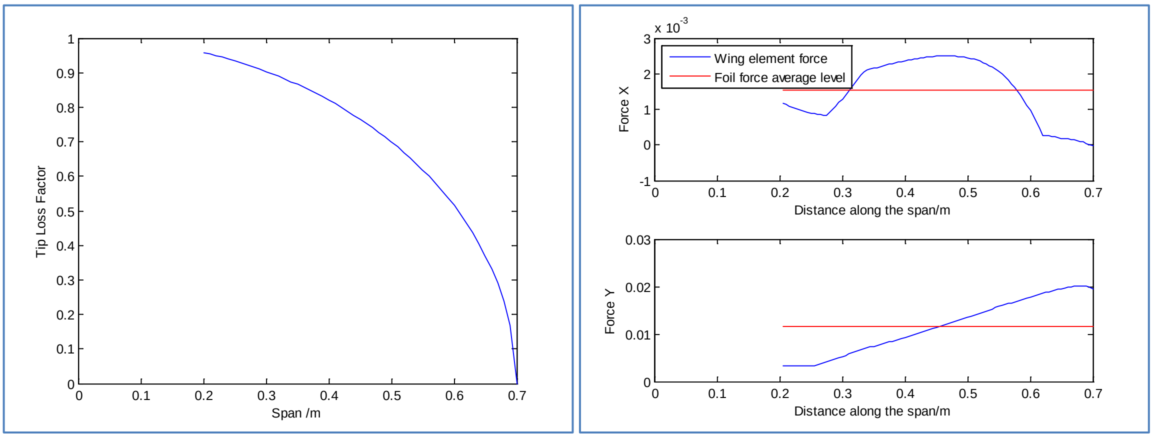

Figure 3-37 – (Left) Tip loss factor for elliptical lift force distribution. (Right) - Max force distribution along the foil span for elliptical tip loss ($St = 0.5, \alpha_{0.7} = 40^\circ$)

Figure 3-38 shows the net forces produced by the foil at different angles of attack. In the model without tip loss, the case with the 40° maximum angle of attack generated the largest amount of thrust. When tip loss was introduced, it affected the case with 40° maximum angle of attack more than the case with 20°, such that the 20° case now produce more thrust than 40° case with tip loss. The tip loss also has a severe effect on the case with $\alpha_{0.7}$ of 60° where the horizontal thrust is now very negative rather than nearly zero in the other cases.

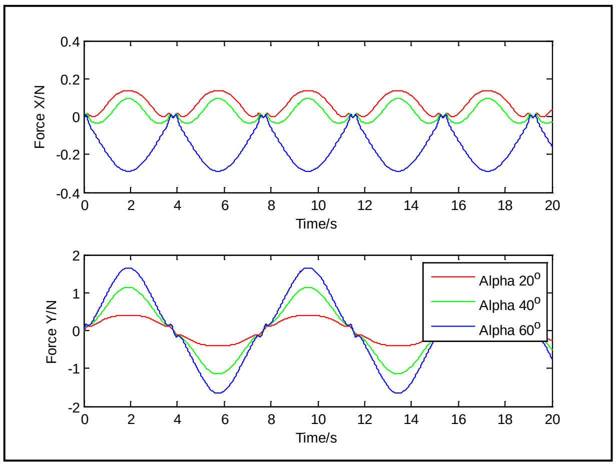

Figure 3-38 – Comparison between the net forces produced by a flapping foil with tip loss. ($St = 0.5$)

Figure 3-39 shows the contour plot for the thrust coefficients. It can be seen the thrust coefficient was significantly reduced by the loss of thrust near the tip. Comparing this contour plot with thrust coefficient contour plots published in the literature showed the results performed worse than the model without tip loss. The non-tip loss model appears to under predict the thrust coefficient when compared to experimental results, and adding a tip loss model would only make it worse. This suggested either flapping aquatic flight foil is not affected by tip loss or the tip loss may not follow the elliptical lift force distribution.

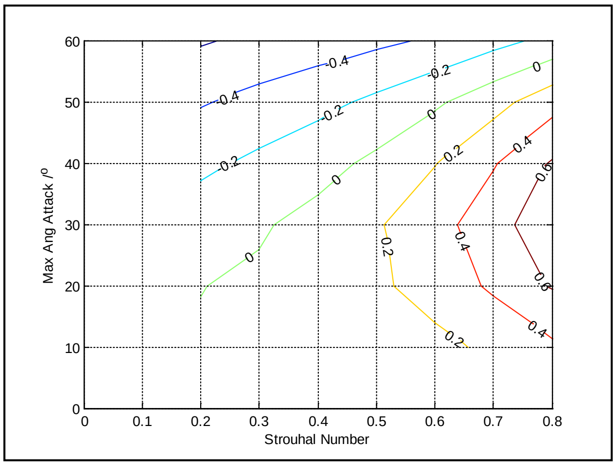

Figure 3-39 – Contour plot of the flapping foil with tip loss.

3.6.3.2 *Prandtl Tip Loss Model*

The second tip loss model candidate to be examined is the Prandtl tip loss model. The tip loss distribution is shown in Figure 3-40 (Left), and it showed Prandtl tip loss model has a more significant tip loss reduction than case with elliptical lift distribution. Whilst both tip loss model reduces the lift to zero at the tip, the correction factor is less severe in the elliptical distribution at the foil root at 0.2m from the axis of rotation (0.95 vs 0.6).

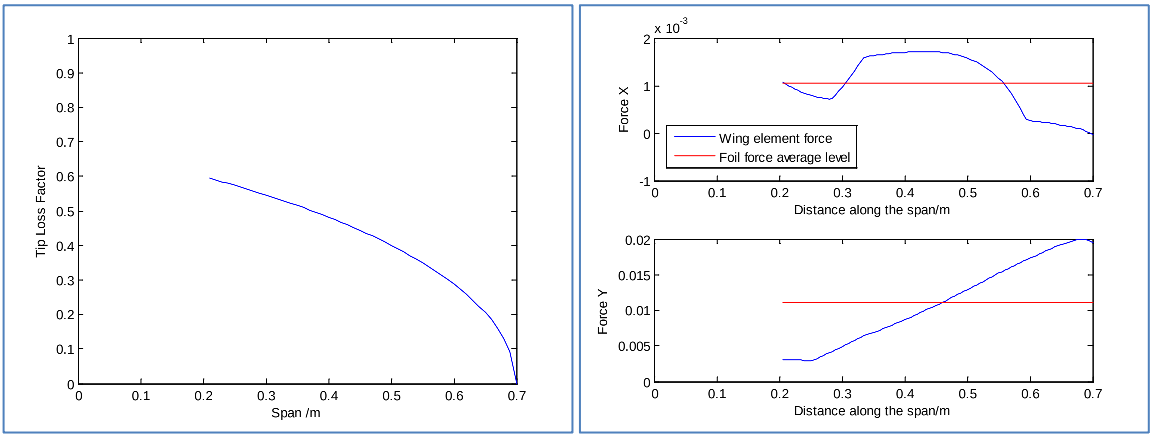

Figure 3-40 – (Left) Tip loss factor from Prandtl tip loss model. (Right) Max force distribution along the foil span with the Prandtl tip loss model ($St = 0.5, \alpha_{0.7} = 40°$)

Figure 3-40 (Right) shows the maximum force produced by the foil at different point along the span. The shape of the plot is similar to that of the elliptical lift distribution, but the magnitude of the horizontal forces is lower. The overall thrust coefficient of the model with Prandtl tip loss is shown in Figure 3-41. Whilst it retained a similar shape to elliptical distribution's result, the peak thrust coefficient was significantly lower. This means it faces the same problem as the elliptical distribution. Since the BET model already under predicts the thrust coefficient when compared to experimental results reported in the literature, applying tip loss correction would only make the situation worse.

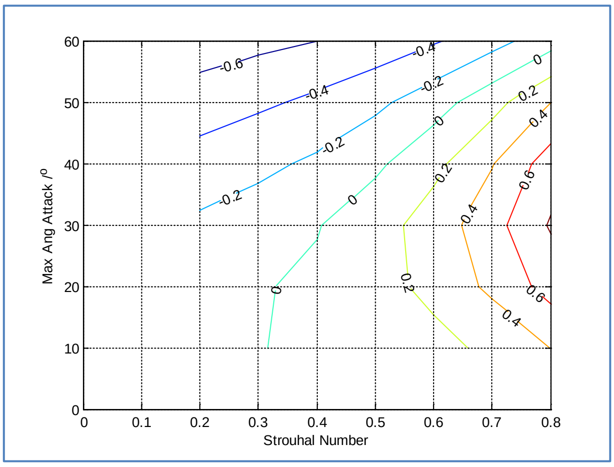

Figure 3-41 – Thrust coefficient for a two axis flapping foil with Prandtl tip loss model ($St = 0.5, \alpha_{0.7} = 40°$)

3.6.3.3 *Comparison of the Two Tip Loss Models*

Despite the question on whether tip loss phenomenon exists for flapping foil, it is still useful to compare the results of the elliptical and Prandtl tip loss model. Figure 3-42 shows a comparison between the thrust coefficients produced by the tip loss model at three different angles of attack. The case without tip loss has the highest thrust coefficient followed by cases with elliptical tip loss. Aquatic flight with Prandtl tip loss produces the lowest thrust coefficient of all three cases, often producing less the half the thrust of the model without tip loss.

Figure 3-43 shows a comparison of the horizontal thrust force (averaged over a propulsion cycle) distribution along the span of the foil with and without tip loss correction. The thrust in both tip loss cases are reduced compared to the non-tip loss model. In particular, rather than falling to zero at the tip of the foil, the thrust coefficient continued to fall further and become very negative at the tip. This is because while the tip no longer produces thrust, it continues to contribute to drag and the high inflow velocity near the foil tip makes the situation worse.

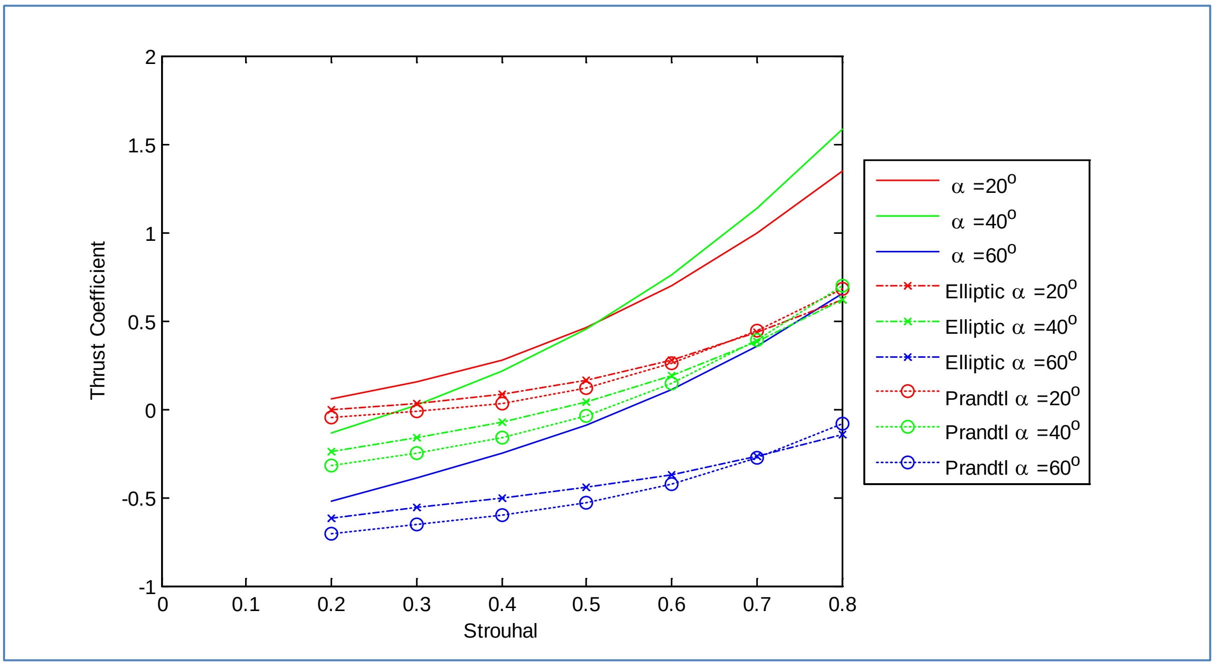

Figure 3-42 – Comparison of different tip loss model against normal aquatic flight.

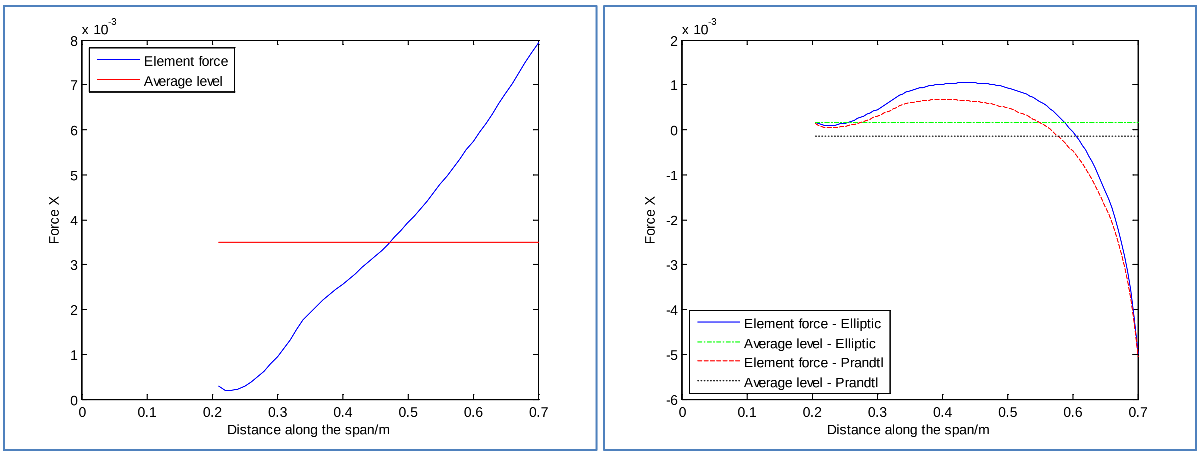

Figure 3-43 – Comparison between the horizontal thrust force for cases without tip loss (left) and cases with either elliptical or Prandtl tip loss (right)

Although a comparison with experimental results in the literature would show the model underestimated the thrust coefficient in a flapping foil, in which case it’s questionable whether the tip loss models are needed because they would only serve to widen the gap between modelling and experimental results, experiments performed by this investigation, as discussed in Chapter 6, would show the opposite. The BET model actually overestimated the thrust coefficients, and tip loss models are needed to explain the discrepancies between modelling and experimental results.

3.6.4 Conclusion

The investigation into the effect of added mass, Kramer effect and tip loss examined the other hydrodynamics phenomena that may affect thrust produced by aquatic flight. The result of this investigation found the added mass and Kramer effect only affected the thrust within a propulsion cycle, by cancels out over one complete cycle. As such these two phenomena do not affect the overall thrust coefficient that is being study, but their effect within a cycle is significant and should be noted in future studies that investigate transient manoeuvres.

Unlike Kramer effect and added mass, the tip loss effect was found to lower the thrust coefficient of the overall cycle, and the reduction is significant (>50%). Two different tip loss models were implemented, namely elliptical lift force distribution and Prandtl tip loss model. The Prandtl tip loss model causes a more significant thrust reduction than the elliptical model, but it is difficult to determine which is more accurate because the thrust coefficient of the base BET model is already lower than the thrust coefficient reported in the literature. Since the tip loss model lowers the thrust coefficient even more, it is unknown whether tip loss really affects aquatic flight until the current model can be verified by experiment.

3.7 Modelling results – three axis aquatic flight

Following the examination of the BET model using the two axis cycle, the model can now be employed to study three-axis aquatic flight. The goal of the three-axis BET model is to allow rapid analysis of three-axis aquatic flight and study different foil stroke path and the forces involved.

Three-axis actuation opened up a huge variety of possible actuation paths, and the paths used by animals are often very complex. This is further complicated by the fact that most animals' flippers are non-rigid and there are always some variations in the stroke path between different strokes. As such the investigation will not analyse the exact animal stroke path from motion capture studies, but will investigate the idealised version of those paths. Three such paths were examined, the figure-of-eight, oval, and reverse figure-of-eight. The first two paths are idealised version of the path based on ones used by penguins and sea turtles. The last one, the reverse figure-of-eight path, was created to test a hypothesis after the results from the first two were analysed and yielded some unexpected results.

The models tested angle of attack between 10° and 60° and Strouhal numbers between 0.2 and 0.8. The flow speed was 0.1ms^{-1} and the roll amplitude was 20°. The foil's dimension is identical to the standard foil used in the two axis model. i.e. NACA0012 foil, with a uniform chord of 0.15m, a span of 0.5m, and a foil root to roll axis distance of 0.2m.

3.7.1 Figure of Eight Paths with 3° Yaw

The figure-of-eight stroke path is one of the most fundamental symmetrical stroke paths in three-axis and as such it was examined in detail. In this stroke path, the foil sweeps backwards during the middle of the up and down strokes (power phase) when roll velocity is highest, and then moves forward at the top and bottom of the stroke cycle (recovery phase) when the roll velocity is lowest. Two cases of figure-of-eight stroke path will be presented in detail, and they have a yaw amplitude of 3° and 6°. The first case, with a yaw amplitude (ψ_0) of 3° (Figure 3-44 (Left)), represents the 'normal' three-axis actuation, while the latter case with a yaw amplitude of 6° shows the adverse effect of an excessive yaw amplitude.

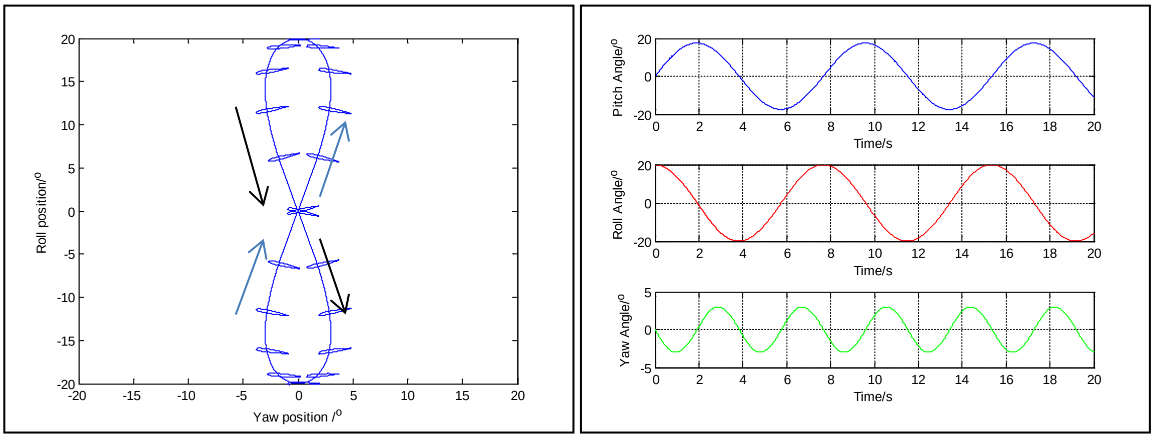

Figure 3-44 – (Left) Foil pitch, roll and yaw motion in three-axis. (Right) Corresponding pitch, roll and yaw angles of the flapping foil. ($\psi_0 = 3°,\ \alpha_{0.7} = 40°, U = 0.1ms^{-1}$)

Figure 3-44 (Right), showed the pitch roll and yaw angle when plotted against time at the example case of Strouhal number 0.5 and angle of attack of 40°. To produce a figure-of-eight stroke path, the roll motion has a 90° phase lead over the pitch motion, while the yaw motion has a phase lag of 180° and an actuation frequency that is double that of roll and pitch. The foil pushed backwards (towards positive yaw angles) during the power phase of the propulsion cycle, and advanced forward in the recovery phase (towards negative yaw angle).

The angle of attack at five different points along the span is shown in Figure 3-45 (Left) over a period of 20 seconds. The angle of attack is shown to have double peaks (at 2s, 6s, 10s…) instead of a following a sinusoidal function like previous cases. Whilst the angle of attack in previous cases would gradually rise to its maximum in the middle of the stroke, the angle of attack in the figure-of-eight cycle first rises rapidly and then decreased to a local minima mid stroke. The drop in the angle of attack is caused by the pitch angle increasing at a faster rate than the inflow angle, thus reducing the angle of attack. The reduction in the inflow angle is caused by the rearward yaw movement of foil mid-stroke which reduced the foil inflow velocity.

Figure 3-45 (Right) shows the forces produced by various elements at different points along the foil span. Despite the angle of attacks were shown to have double peaks in Figure 3-45, the plot showed the foil elements still produced force following a mostly sinusoidal pattern. This is because the increase inflow velocity at these parts of the oscillation was sufficient to compensate for the reduction in the angle of attack. However, a reduction in the maximum force can be observed which is contrary to the initial expectation that three-axis stroke should produce more force.

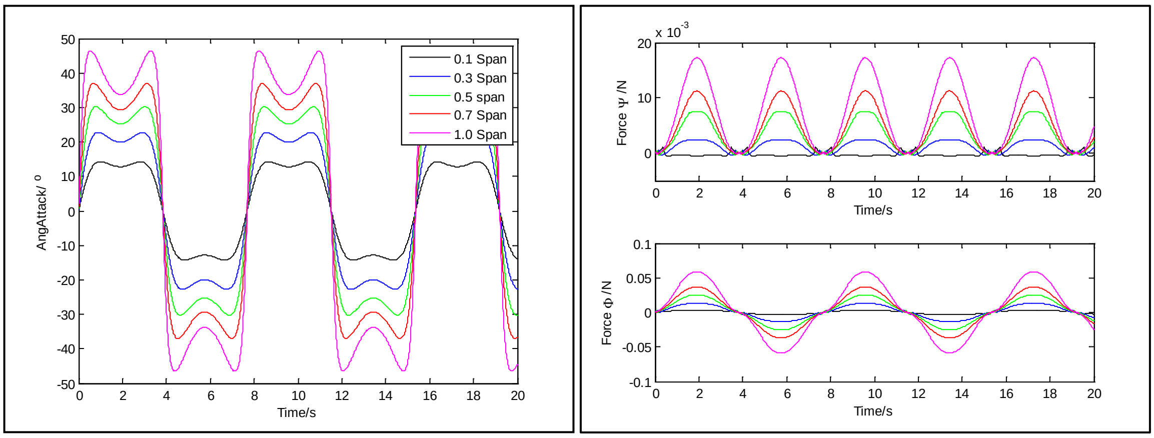

Figure 3-45 – (Left) Angle of attack of a three axis flapping foil, (Right) Forces generated by different elements along the span, $\psi_0 = 3°$, $\alpha_{0.7} = 40°, U = 0.1ms^{-1}$

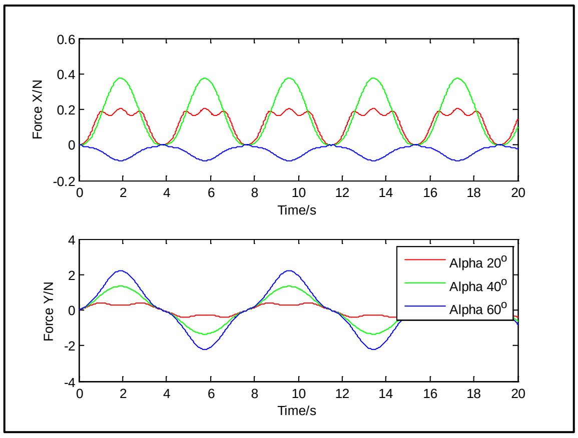

Figure 3-46 – Total foil force for three different angles of attack, $\psi_0 = 3°$, $\alpha_{0.7} = 40°, U = 0.1ms^{-1}$

After the total foil force was calculated, the net force produced by actuation cycles with angle of attack of 20°, 40° and 60° are shown in Figure 3-46. Whilst the pattern seen in the 40° and 60° cycle were similar to the two-axis model, the 20° cycle exhibited a triple peak in the horizontal net force in X and double peak vertical net force in Y. The triple peak is caused by a very prominent double peak in the foil angle of attack (Figure 3-47 (Left)). During the local minima between the double peaks, the angle of attack of some elements dropped below the stall angle, which caused a significant increase lift. At the same time other elements' angles of attack fell into the stall angle range, which lead to a reduction in lift. In the case of the foil root, the angle of attack had become negative, which meant thrust was produced in reverse and this caused a significant increase in drag. The combinations of these factors resulted in the triple peak in the horizontal Force X and the double peak in the vertical Force Y for the cycles with 20° angle of attack.

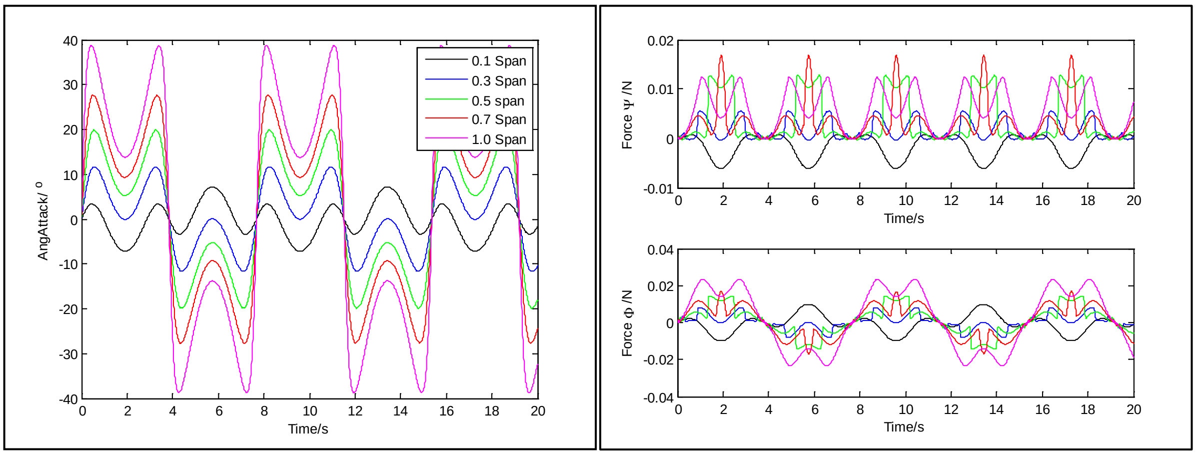

Figure 3-47 – Angle of attack of a three axis flapping foil, $(\psi_0 = 3°, U = 0.1ms^{-1})$.
(Left) $\alpha_{0.7} = 20°$, (Right) $\alpha_{0.7} = 40°$,

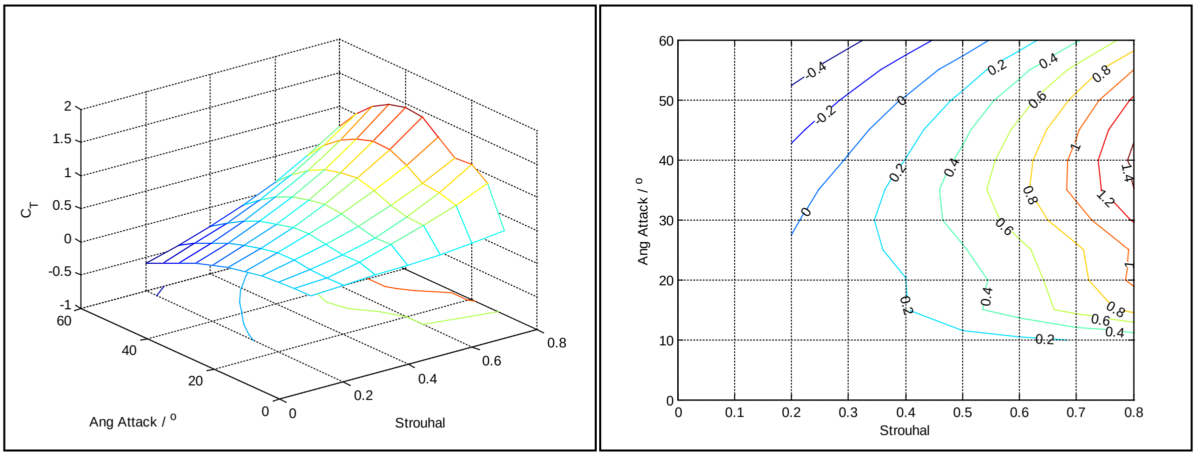

Figure 3-48 – Thrust coefficient for three-axis foil with 3° yaw

After the foil forces were calculated, the horizontal thrust was converted into thrust coefficient for analysis. Figure 3-48 showed the thrust coefficient for the three axis model with 3° yaw. A reduction in the thrust coefficient from a maximum of 1.6 in the two-axis cycle to a maximum of 1.4 in this figure-of-eight cycle can be observed. There is also a shift in the angle of attack corresponding to maximum thrust coefficient. The maximum thrust coefficient for the 3° yaw cycles is achieved at approximately 40°, which is higher than the angle of attack corresponding to the maximum thrust coefficient in the two-axis cycle (~30°). The reduction in the thrust coefficient suggests the three axis motion may reduce the performance of aquatic flight propulsion rather enhance it. Also, the two axis experimental results shows a continuously curved surface, but the three-axis cycle's thrust coefficient has a shoulder region between angle of attack of 15° and 25°, where the thrust coefficient decreased slightly as the angle of attack increased.

In summary, the three-axis aquatic flight analysis analysed the penguin inspired figure-of-eight stroke path with yaw amplitude of 3° in detail. Contrary to expectation, the additional yaw motion did not increase the thrust coefficient, but reduced it instead. The yaw motion disturbed the inflow angle and velocity and led to a situation where the pitch angle increased faster than the inflow angle. This reduced the angle of attack and caused the double peaks seen in the various plots. The reduced angle of attack reduced the foil thrust and the maximum thrust coefficient is reduced from ~1.6 to ~1.4.

3.7.2 Figure of Eight Path with 6° Yaw

The analysis of the figure-of-eight path with a yaw amplitude of 3° showed three axis motion may reduce thrust by disrupting the inflow angle and inflow velocity. The second case of figure-of-eight stroke path, with a yaw amplitude of 6°, shows what would happen if the yaw amplitude is excessive. The foil's actuation path and the corresponding pitch roll and yaw angle are shown in Figure 3-49. Apart from the increased yaw amplitude, the other parameters and settings are the same as the previous analysis.

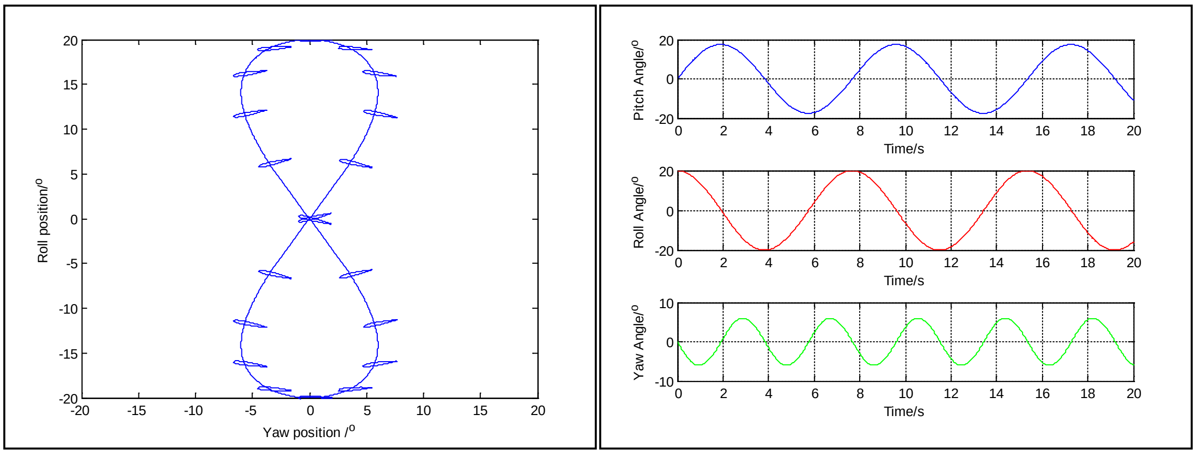

Figure 3-49 – (Left) Foil pitch, roll and yaw motion in three axis. (Right) Pitch, roll and yaw angles of the flapping foil. $\psi_0 = 6°,\ \alpha_{0.7} = 40°, U = 0.1ms^{-1}$

The angle of attack and element force at five different locations along the foil span for the 6° cycle is shown in Figure 3-50. It can be seen the angle of attack plot (Figure 3-50 (Left)) looked very different from that seen in the cases with 3° yaw. Whilst the angle of attack up to 0.7span still exhibits the double peaks seen in the case with 3° yaw, the angle of attack at the foil tip of the 6° yaw cycle looks very different. Instead of a double peak, the plot shows what looks like a quadruple peak. However, detail examination of the figure shows the first 'peak' is actually a trough from the previous cycle. This 'trough' occurs at the extreme ends of the roll axis motion during the recovery phase of the propulsion cycle, when the roll axis slows down, stops, and then reverses direction. However, yaw velocity reaches its maximum in this part of the cycle as foil moves forward in yaw in preparation for the next stroke. This forward yaw movement increases the foil's local inflow velocity. The combination of decreased roll velocity and increase inflow velocity resulted in a very low inflow angle. Furthermore, the pitch angle is non-zero on either side of the maximum roll and often higher than the inflow angle. Since the angle of attack is calculated by subtracting the pitch angle from the inflow angle, it can produce a very negative angle of attack in this situation. This negative angle of attack persisted until the roll velocity increased sufficiently to raise the inflow angle above the pitch angle.

Since the angle of attack in the 6° figure-of-eight stroke path is very different to the previous case, it is expected the forces it produce will also be very different. Figure 3-50 (right) showed the forces produced by elements at 0.1, 0.3, 0.5, 0.7, and 1.0 span. Unlike the previous example with a 3° yaw, the element forces showed double peaks in the 6° cycle. The normal patterns where the elements further from the axis tend to produce more thrust do not always apply here, because the plot shows the element at 0.1span (black) produces more thrust than elements at 0.3span (blue). This is because the element at 0.1span operated at a more efficient angles of attack (<10°) than the element at 0.3span (10°-20°) during the power phase of the propulsion cycle when the total foil velocity is highest.

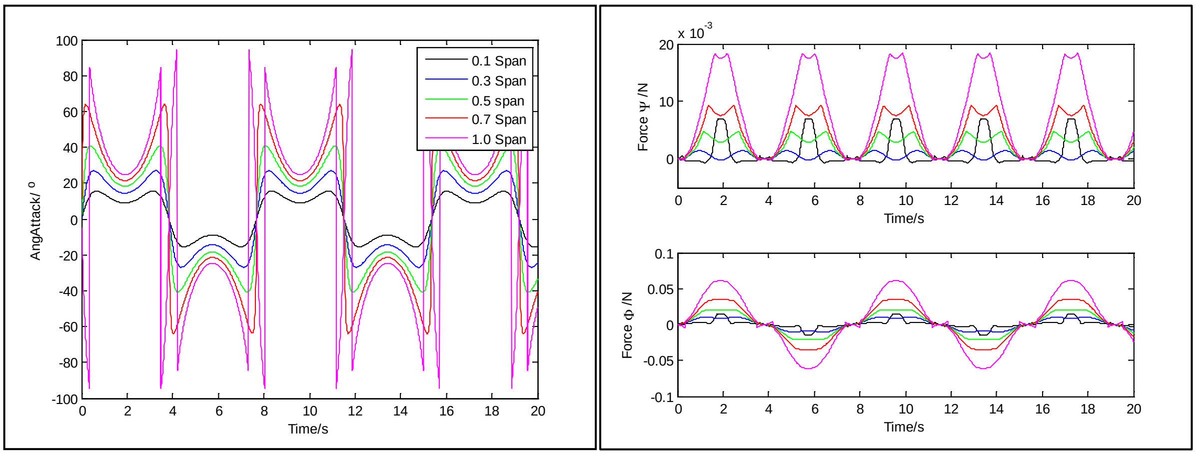

Figure 3-50 – Angle of attack and element force produced by a three-axis aquatic flight flapping foil following a figure of eight path. $\psi_0 = 6°,\ \alpha_{0.7} = 40°, U = 0.1ms^{-1}$

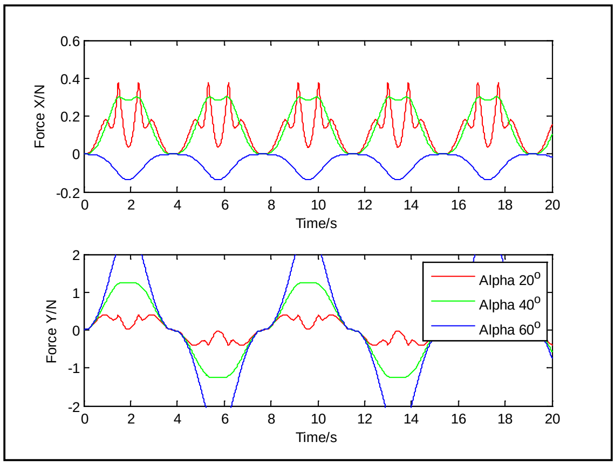

Figure 3-51 – Total forces generated by flapping foil. $\psi_0 = 3°,\ \alpha_{0.7} = 40°, U = 0.1ms^{-1}$

Figure 3-51 showed total forces produced by the flapping foil at angles of attack of 20°, 40° and 60°. As with the previous cases 60° angle of attack was too high and was not achievable at this Strouhal number. The 40° cycle shows its thrust cycle has a double peak, while 20° cycle was showed to have quadruple peak with a significant local minimum. This is caused by the effect of the yaw motion and its effect on the foil inflow angle and angle of attack, as discussed in the 3° yaw cycle analysis.

The yaw motion reduced inflow velocity and angle of attack and this lead to a reduction in thrust, which is reflected in Figure 3-52 which showed the thrust coefficient of the flapping foil with 6° yaw amplitude. The maximum thrust coefficient is less than 1.2 and occur between and angle of attack of 40°-50°. In comparison, the 3° cycle had a maximum C_T over 1.4 and the two axis cycle had a maximum C_T over 1.6, both of which occur at around an angle of attack of 30°. Whilst the two-axis motion's thrust coefficient map showed a fairly rounded surface, and the 3° yaw model showed a shoulder region between angle of attack of 15° and 25°. The shoulder in the 3° yaw cycle has become a prominent ridge in the 6° cycle, and a second peak can be seen between angle of attack of 20° and 30°.

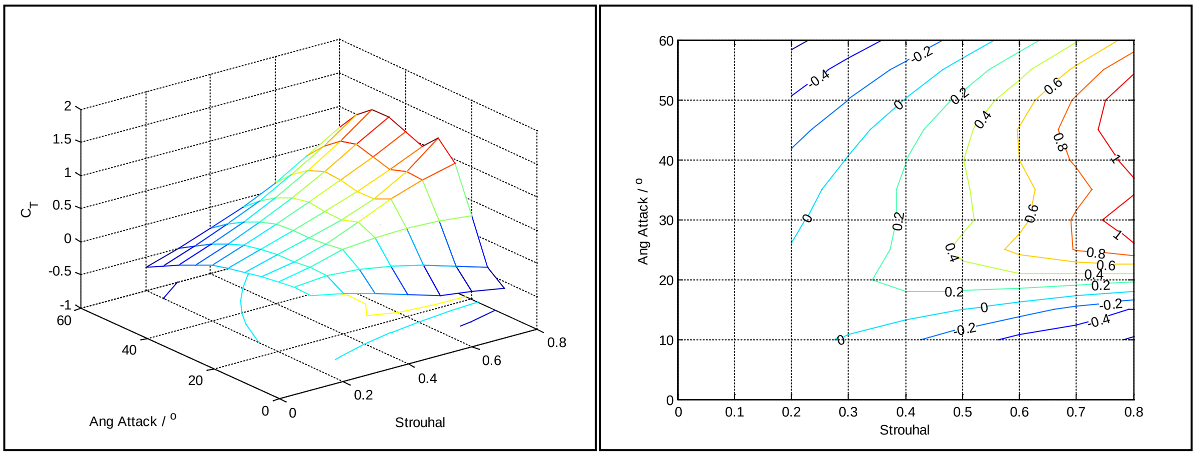

Figure 3-52 – Thrust coefficient for three axis foil with 6° yaw amplitude

In summary, the three axis propulsion cycle with 6° yaw was found to produce less thrust then the two-axis cycle and the 3° cycle, and various phenomena that appeared in the 3° cycle was amplified in the 6° cycle. The forward motion during the recovery phase of the cycle produces negative angle of attack and increase drag. Meanwhile, the backwards moving foil during the power phase reduces the inflow velocity and angle of attack. The combination of increased drag during the recovery phase and reduced thrust during the power strokes serves to reduce the overall thrust and thrust coefficient.

3.7.3 Oval Path

Apart from the figure-of-eight path, another idealised three axis path is also commonly found in the observation of marine animal. The oval stroke path is produced when the yaw motion had the same period as the roll and yaw (Figure 3-53). Unlike the symmetrical figure-of-eight path, the oval path is asymmetric and its up-stroke and the down-stroke followed different paths. In this example case of a 3° oval, the down stroke starts with a forward yaw motion follow by a rearward movement thus tracing a forward arc. The up stroke does the opposite and starts with a rearward yaw motion before return to the starting position with a forward movement and traces a rearward arc. The combinations of these traces an oval shape path.

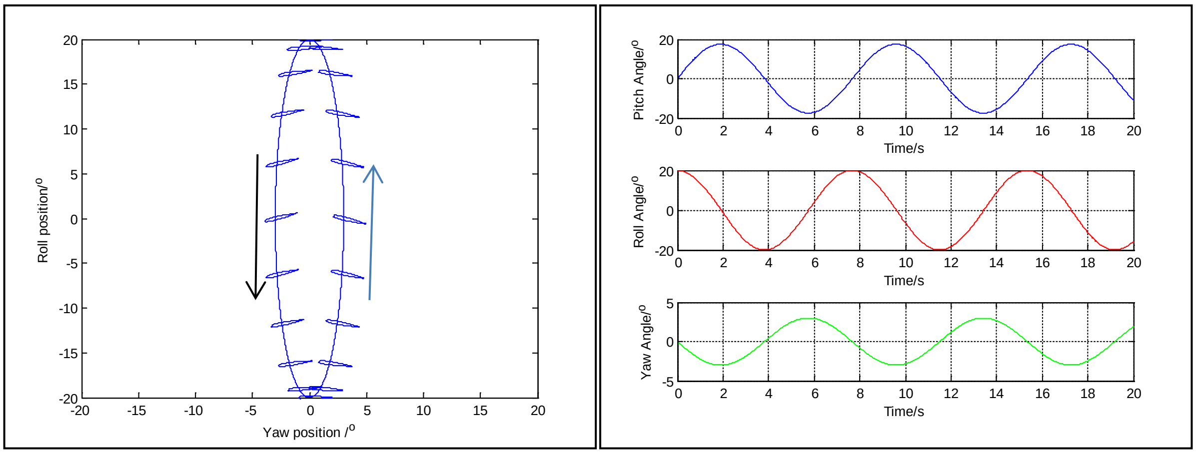

Figure 3-53 – Pitch, roll and yaw positions of a foil following an oval path. The down stroke is forward of the up stroke. $\psi_0 = 3°,\ \alpha_{0.7} = 40°,\ St = 0.5, U = 0.1ms^{-1}$

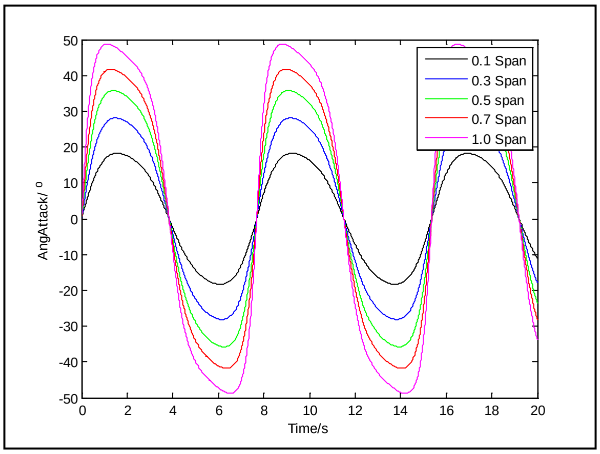

Figure 3-54 – Angle of attack for flapping foil following an oval path $\psi_0 = 3°,\ \alpha_{0.7} = 40°,\ St = 0.5, U = 0.1ms^{-1}$

As with the figure-of-eight case, the oval path's yaw motion also affects the foil's inflow velocity and angle of attack. Figure 3-54 shows the angle of attack corresponding to the oval path at different points along the foil span. There is a clear distortion to the normally sinusoidal shape of the angle of attack plot. The forward motion in the first quarter cycle increased the inflow velocity at the foil and temporarily increased the angle of attack. This is followed by a reduction in the angle of attack in the second and third quarter cycle, when foil moved backwards and reduced the local inflow velocity. In summary, the angle of attack is increased when the foil moved forward into the flow, but it is reduced when the foil moved back. This increased in the amount of force produced during the first and fourth quarter cycle (1-2s, 6-8s), but reduced force during the second and third (2-6s).

Figure 3-55 shows the forces at various foil elements along the foil span. It can be seen the foil forces were skewered by the asymmetric motion caused by the oval path. The forces in X took longer to reach its peak on the down stroke than the up stroke. There is also a difference in the ‘recovery’ phase of the propulsion gait, where the transition from down-stroke to up-stroke (~4s) showed more disturbance than the transition from up stroke to down stroke (~8s). This difference in the forces produced during the recovery phases is caused by differences in the yaw direction. The foil moved backwards during the down-stroke to up-stroke transition and forward during the up-stroke to down-stroke transition. This affected local foil inflow velocity, inflow angle, and angle of attack, and resulted in differences in lift and drag force produced between the two ‘recovery’ phases.

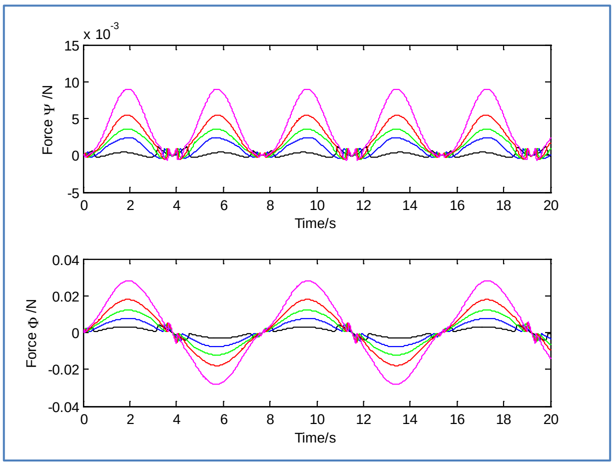

Figure 3-55 – Forces generated by various elements along the foil span. $\psi_0 = 3°$, $\alpha_{0.7} = 40°$, $St = 0.5, U = 0.1ms^{-1}$

The total forces produced by oval cycles operating at three different angles of attack are shown in Figure 3-56. The plot shows the maximum force is reached earlier in the cycle in the down stroke but the maximum force is delayed in the up stroke. This is caused by the increased inflow and angle of attack when the foil advanced forward during the first and last quarter cycle, and it means more thrust can be produced when the yaw motion pushes the foil into to the flow than pulling it away. The effect is more pronounced in the 20° cycle than the 40° cycle.

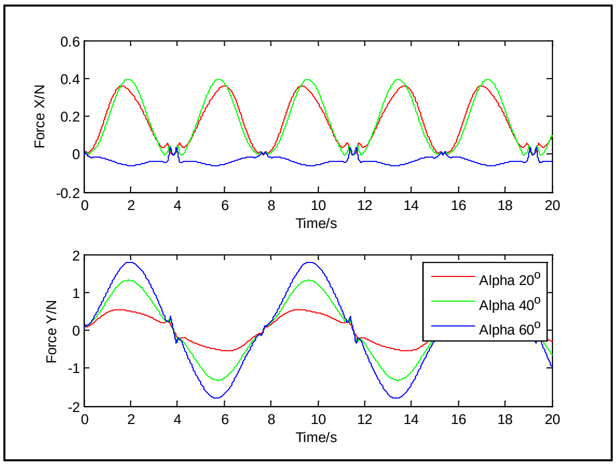

Figure 3-56 – Total forces generated by a flapping foil following an oval path, $\psi_0 = 3°$, $\alpha_{0.7} = 40°$, $St = 0.5, U = 0.1ms^{-1}$

Upon close examination of the foil angle of attack and element force during the 20° cycle, the reason for the increased shift becomes clear (Figure 3-57). Like the 40° cycle, the forward motion in the first and fourth quarter cycle temporarily increased the inflow, angle of attack, and thrust, while the backward motion in the second quarter temporarily decreased it. While the 40° cycle increased the angle of attack at 0.7span by 4.5%, the angle of attack in the first quarter was increased by 34% in the 20° cycle. This resulted in a larger increased in the force produced and it lead to a more significant shift in the time to reach maximum force.

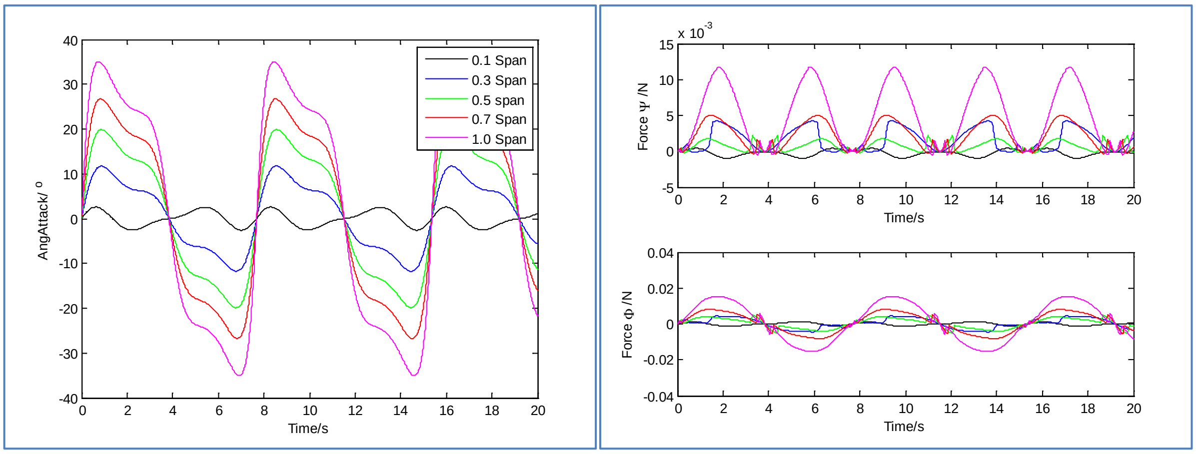

Figure 3-57 – Angle of attack and foil element force produced by a flapping foil following an oval path with a maximum angle of attack of 20°. $\psi_0 = 3°$, $\alpha_{0.7} = 20°$, $St = 0.5, U = 0.1ms^{-1}$

Figure 3-58 shows a plot of the thrust coefficient for the oval path. Whilst the overall thrust coefficient of the path was slightly lower than that of the of the two axis motion, the oval cycle’s maximum thrust coefficient was higher than that of the figure-of-eight (1.6 vs. 1.4). The shape of the thrust coefficient mesh produced oval path more closely resembles that of the two-axis locomotion’s than the meshes produced by the other three-axis cycles.

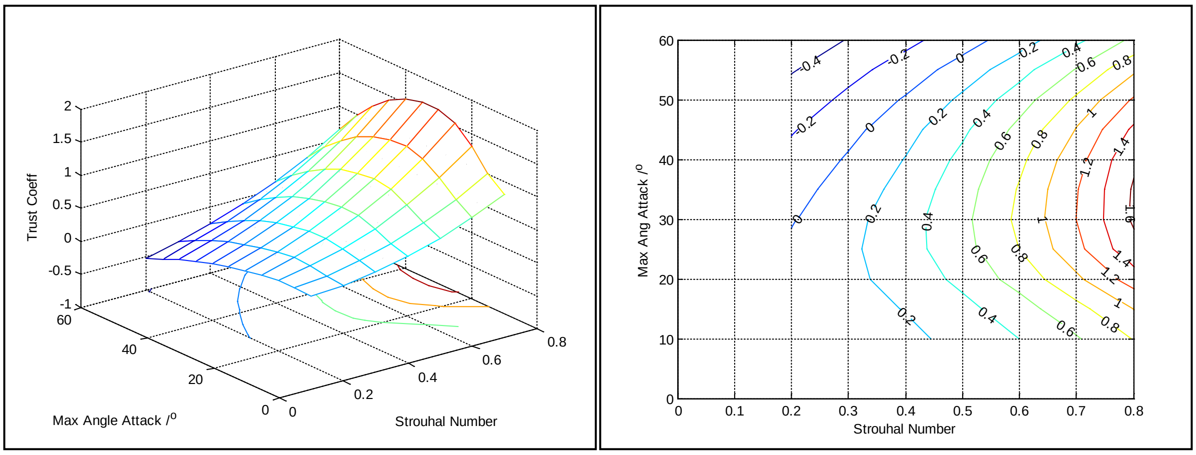

Figure 3-58 – Thrust coefficient of a flapping foil following an oval path

The oval path is the first foil path in this investigation where the up-stroke and down-stroke travelled in a different path. This asymmetry in the foil path causes asymmetry in the results. The foil generated more thrust in the first and last quarter of the flapping cycle when the foil moved forward, but this is countered by the reduced thrust during the second and third quarter of the flapping cycle when the foil moved backwards. The overall thrust of the propulsion cycle is fairly similar to the two-axis cycles, and this is reflected in the similarities between thrust coefficient plots of the oval cycles and the two-axis cycles.

3.7.4 Reversed Figure Of Eight

The reversed figure-of-eight path is another path studied by the investigation. In the ‘normal’ figure-of-eight path, the foil pushes backwards in yaw during the high speed ’powered’ phase of the up and down stroke, and moving forward during the slower ‘recovery’ period near the highest and lowest point of the roll cycle. The reversed figure-of-eight tested the opposite, where the foil moved forward during the ‘powered’ phase and moved backwards during the recovery phase. This new path should increase the foil local inflow velocity during the power phases and reduce the local inflow velocity during the recovery phases.

Figure 3-59 shows the foil path for the reversed figure-of-eight and the corresponding pitch roll and yaw angles. The NACA foil sections on the plot indicated the foil's pitch angle during the stroke. While this plot looked similar to the plot for the 'normal' figure of eight path, differences can be seen in the orientation of the NACA sections in that they point in the opposite direction. The yaw motion in the 'reversed' path oscillated in phase with pitch, instead of 180° out of phase as in the case of the 'normal' path. The angle of attack for the 'reversed' path followed a simpler sinusoid pattern with a single peak, which is different to the 'normal' path which exhibited double peaks.

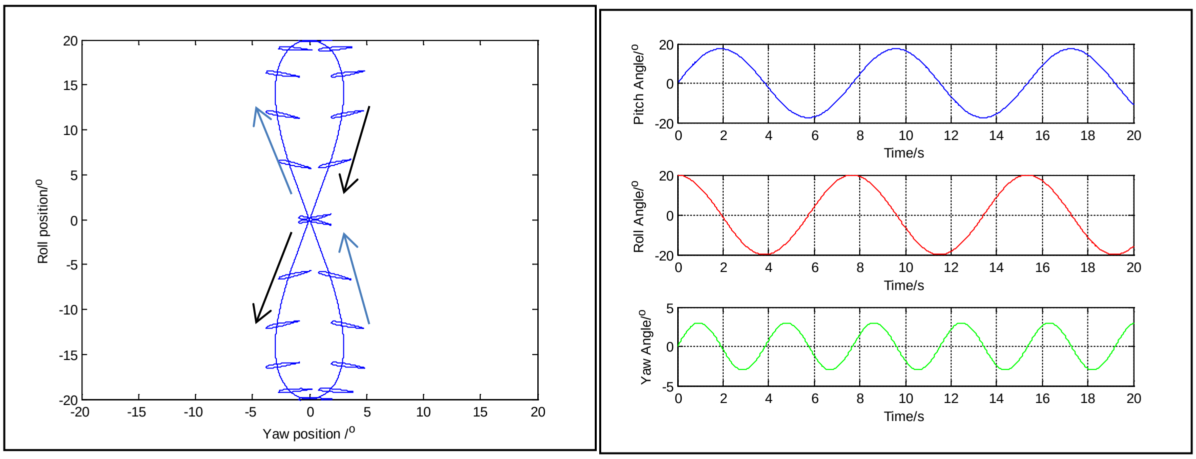

Figure 3-59 – The stroke path and the corresponding pitch, roll and yaw position of a foil following the reversed figure of eight path. Unlike the 'normal' figure of eight path, the foil advance forward in yaw during the 'power' strokes of the oscillation cycle

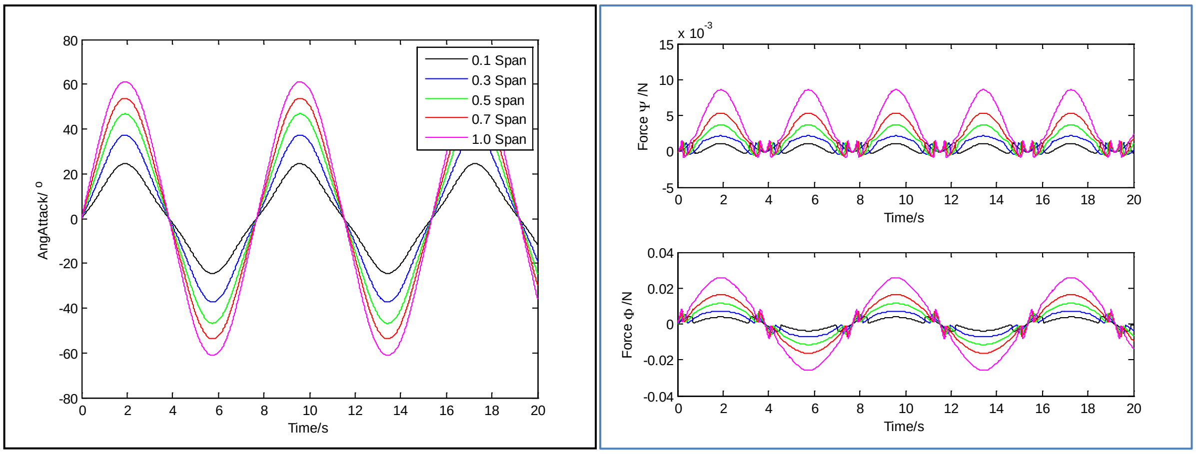

Figure 3-60 – Angles of attack and element forces at different point along the span for a flapping foil following the reversed figure-of-eight path. $\psi_0 = 3°$, $\alpha_{0.7} = 40°$, $St = 0.5, U = 0.1ms^{-1}$

Figure 3-60 shows the angle of attack and the element forces generated by different foil elements along the span. The results show a closer resemblance to the two axis path than the other three axis path examine, but there are some difference. The angle of attack is higher due to the way the yaw motion positively contribute to the propulsion cycle and raised to inflow velocity at the thrust producing mid-stroke while reducing it during the drag producing end-stroke. In the reverse figure-of-eight cycle the fastest moving foil elements at 1.0span produced the highest amount of thrust while the slowest elements near the foil root produced the least. This is different to the ‘normal’ figure-of-eight cycle where the foil at 0.1 span made a greater contribution the foil’s overall thrust than some elements further out due to operating at angle of attack below the stall angle. In the case of the reverse figure-of-eight cycle, the angle of attack at 0.1span has increased and moved into the stall range where the lift produced by the foil is greatly reduced.

The total net forces for a foil moving in the ‘reversed’ figure-of-eight paths are shown in Figure 3-61. The plot shows the total forces at three 0.7span angles of attack (20°, 40°, and 60°). While the cycle with an angle of attack of 60° did not generate any thrust, the 20° and 40° cycles did. In the cycles examined, the 20° cycle produced more thrust than the 40° cycle, and this was achieved with a lower vertical force.

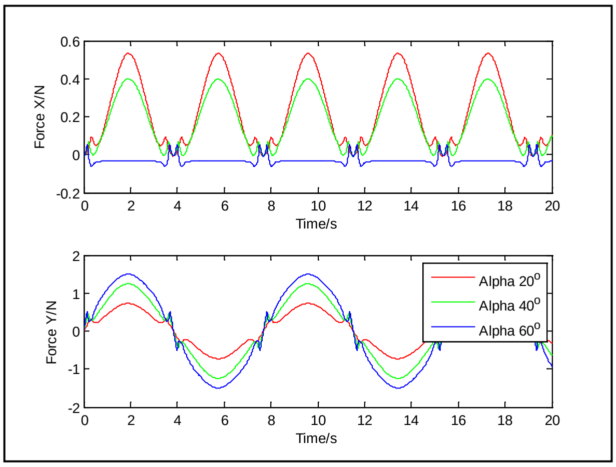

Figure 3-61 – Total forces generated by a flapping foil following a reversed figure of eight path, $\psi_0 = 3°$, $\alpha_{0.7} = 40°$, $St = 0.5, U = 0.1ms^{-1}$

The thrust coefficient for the ‘reversed’ path is shown in Figure 3-62. The mesh shows the thrust coefficient for the reverse path follows a smooth rounded curve. There are no notable features such as a shoulder and or a second peak. Whilst results from the other three axis models shows the third axis’s motion could reduce the foil thrust coefficient, the ‘reversed’ path’s plot appears to show a higher thrust coefficient than the two axis cycle (C_T >1.8), which means the reversed figure-of-eight can be employed to increase the foil thrust. The maximum thrust is achieved at angles of attack between 20°-30°, which reflects the results shown in Figure 3-61, where the foil with 20° angle of attack produced more thrust than the foil operating at 40° and 60°.

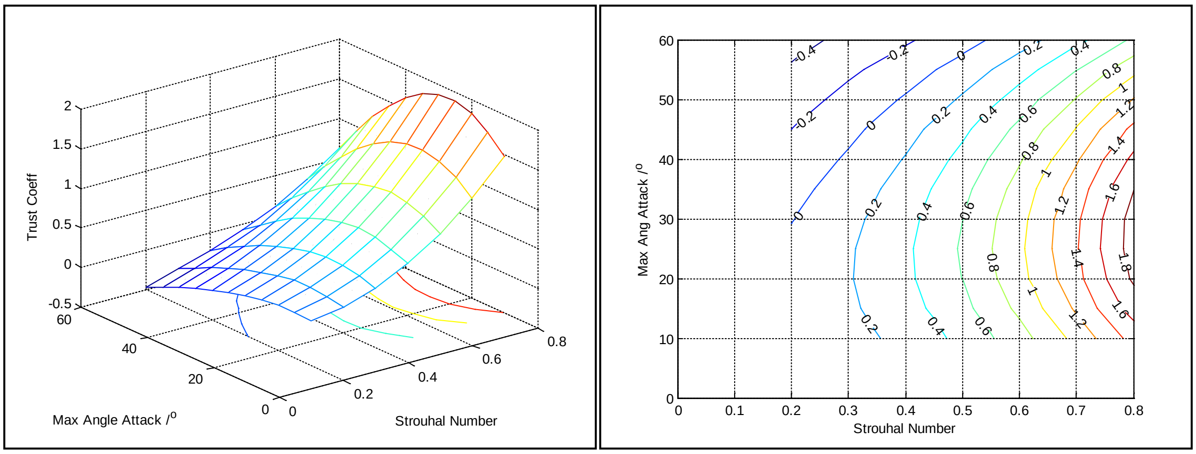

Figure 3-62 - Thrust coefficient of a flapping foil following a reversed figure of eight path

In summary, the ‘reversed’ figure-of-eight path changed the phase of the yaw motion by 180°, such that the foil now moved forward during the power phase and then move backwards during the recovery phase. This change increased thrust during the power phase of the up and down strokes (mid stroke) and reduced the drag during the recovery phase at the top and bottom of the stroke. This increased the total thrust produced over a propulsion cycle, which in turn increased the cycle’s thrust coefficient. The reverse figure-of-eight path is the only path in this investigation that was found to produce thrust coefficient higher than the two axis cycle.

3.7.5 Added mass effect

After looking at the results from the base BET model, it is necessary to analyse the effect of other hydrodynamic phenomenon such as added mass, Kramer effect and tip losses on the three axis cycle. Neither tip loss nor Kramer effect are affected by the three axis motion beyond what is already observed with the two axis cycles because one is a function of the foil span and the other is a function of pitch rotation. As such the analysis of their effect would not be repeated here. The added mass on the other hand did experience some changes due to the new yaw acceleration component. While the added mass forces of the two axis cycle were simple sine wave, the added mass forces in the three-axis cycles are found to have more complicated patterns due to the interaction between roll and yaw acceleration.

Figure 3-63 shows the added mass forces produced by a three-axis flapping foil following a figure-of-eight actuation path with yaw amplitudes of 3° and 6° respectively. Like the two axis cycle, the horizontal component of the added mass forces in X also followed a sine wave and its frequency is twice that of the forces in Y. The gradients of the added mass forces in Y become steeper and more ‘saw-tooth’ like. The forces in Y are visibly distorted in the cycle with 6° yaw. This distortion is caused by the added mass force contribution from yaw acceleration, which cycled at twice the frequency as the flapping motion in roll.

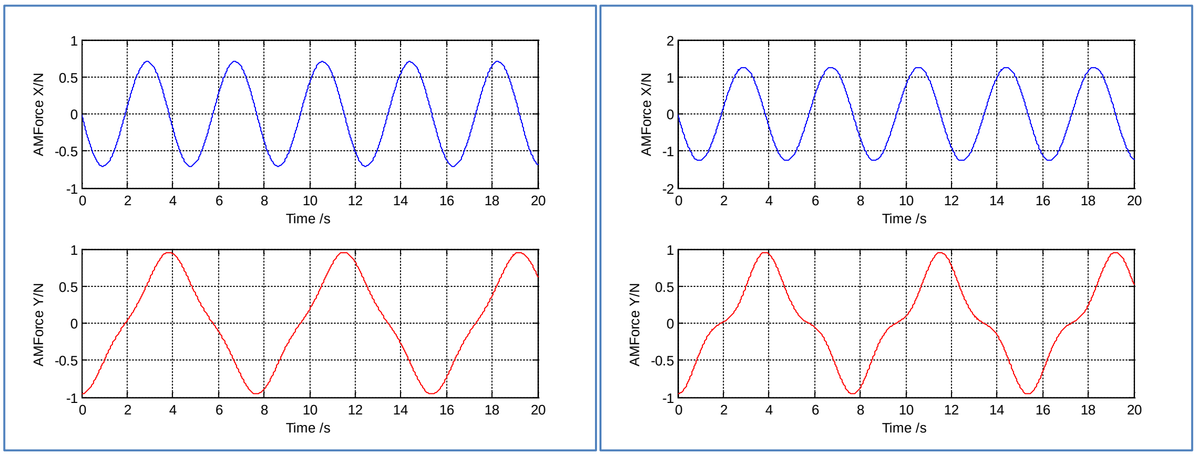

Figure 3-63 - Added mass force of the three axis foil with 3° (Left) and 6° (Right) yaw.
$\alpha_{0.7} = 40°$, $St = 0.5, U = 0.1ms^{-1}$

The yaw axis motion moved the foil forward from the stating position at 0° to the forward most yaw position between 0-1s. Then the yaw motion drove the foil downwards backwards from 1-3s until it reached the rear most yaw position. The foil then moved forward and downwards from 3-4s to the lower starting position in preparation of the up-stroke. During this down stroke, the yaw axis decelerated forward between 0-1s, and then accelerated backwards from 1-2. The foil decelerated backwards from 2-3s before stopping and accelerating forward to the lower starting position from 3-4s. This means the added mass force from yaw would reduce the foil force in Y during the power stroke but increases it at the ends of each stroke. The 6° cycle has higher acceleration than the 3° cycle hence the 6° cycle experiences greater effect from the added mass than the 3° cycle. This is why the 6° cycle in Figure 3-63 shows more deviation from the normal sine wave than the 3° cycle.

The contribution from added mass forces on the propulsion cycle can be observed in Figure 3-64, which plotted the total foil force for 3° and 6° yaw cycles with angles of attack of 20°, 40°, and 60°. It can be seen the added mass force has a significant contribution to the foil force, especially the cycle with angle of attack of 60° which did not produce thrust from foil lift. However, since the added mass forces in X and Y were symmetrical, they did not affect the thrust coefficient because the added mass forces would cancel out over a complete oscillation cycle.

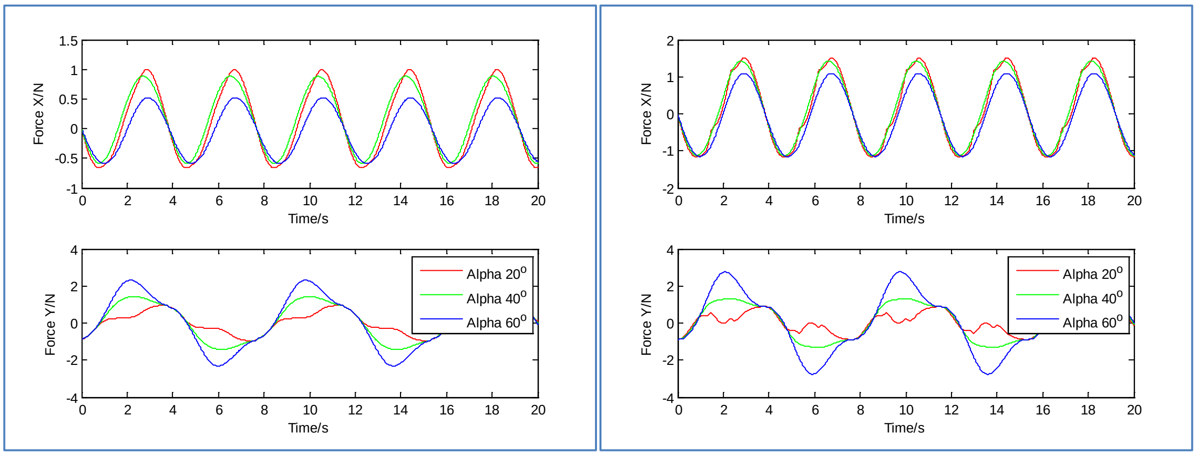

Figure 3-64 – Combined foil force with added mass function enabled for figure-of-eight stroke path with 3° (left) and 6° (right) yaw

In addition to the figure-of-eight stroke path, the added mass forces for the other two paths were also examined. Figure 3-65 shows the added mass forces of the reversed figure-of-eight path and Figure 3-66 shows the added mass force for the oval path. The added mass force of the reverse-figure-of-eight path showed a similar but opposite pattern to the ‘normal’ figure-of-eight path. The difference is caused by the opposite phase of the yaw axis, which caused a change in the total acceleration. At the beginning of the stroke where the ‘normal’ path would move forward and down, the ‘reversed’ path moved backwards and down, and the added mass force contribute positively to thrust. However, like the ‘normal’ path’s added mass force, the ‘reversed’ path’s added mass force in X is also symmetrical over an oscillation cycle, so the initial increase in thrust is cancelled by a reduction in thrust later in the cycle. This means the added mass force would not have a net contribute to the total thrust over a complete flapping cycle and the thrust coefficient would remain unchanged.

The effect of yaw motion in the oval path has a more significant effect on the added mass force than the symmetrical figure-of-eight path, as shown in Figure 3-66. Unlike the figure-of-eight paths’ added mass force, the added mass forces of the oval path in X did not follow a sine wave. This is due to the fact the cycle is not symmetrical and the up and down stroke follow a different path. Rather than a sinusoidal trace like the figure-of-eight paths, the oval path shows what looks like a function with a double peak that has the same period as the added mass force in Y. However, closer examination will show this is the results of a combination of different accelerations that cause certain the added mass force to be higher at some points in the cycles than others because the acceleration vectors contribute constructively or destructively. The plot shows the forward moving phases of the stroke cycle (0-2s, 6-8s) produced greater added mass force than the backwards moving phases (2-6s). Nevertheless, the added mass force still cancels out over a propulsion cycle, so there is no additional net thrust, and as such the thrust coefficient remains unchanged.

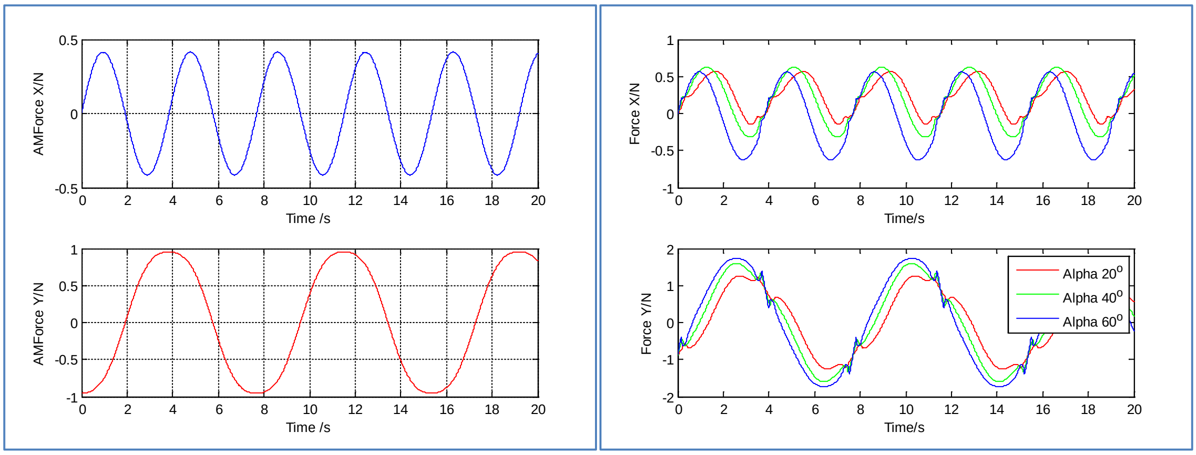

Figure 3-65 – Added mass force of a foil following a reverse figure of eight path. $\psi_0 = 3°$, $\alpha_{0.7} = 40°$, $St = 0.5, U = 0.1ms^{-1}$

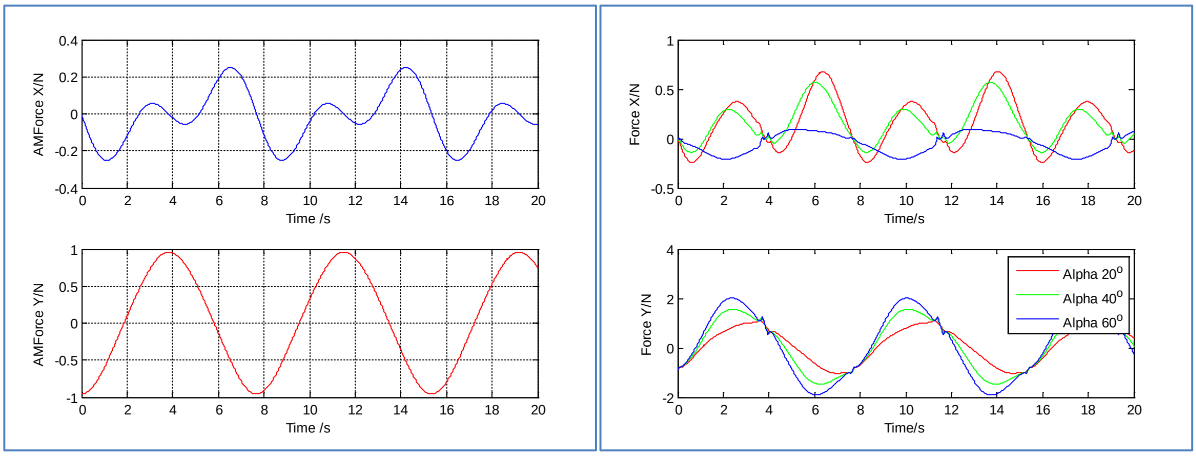

Figure 3-66 – Added mass force of a foil following an oval path. Note the force is X is not symmetrical, so it can contribute to the overall thrust $\psi_0 = 3°$, $\alpha_{0.7} = 40°$, $St = 0.5, U = 0.1ms^{-1}$

In summary, the analysis of the added mass force on the three-axis aquatic flight propulsion cycle showed while these forces can contribute to the forces within a propulsion cycle, their effects cancel out over the period of one cycle. Therefore they do not contribute to the overall propulsive thrust and the cycle’s thrust coefficient remains unchanged. Whilst they may not affect the overall propulsive thrust, their effects should be considered because if the control system can perform incomplete or asymmetric strokes, these effects can be utilised to increase manoeuvring performance.

3.8 Thrust Coefficient Comparison

After the analysis of individual three-axis propulsion cycles, this section will make a more detail comparison of the thrust coefficients for the different gaits at different angles of attack against the Strouhal numbers. The analysis investigated the thrust coefficients produced by several actuation paths and compared them against the results from the two axis cycle (i.e. the cycle with 0° yaw). These cases include three figure-of-eight paths with yaw amplitude of 1.5°, 3°, and 6°, two oval paths and two reversed figure-of-eight paths with yaw amplitudes of 3° and 6°. The thrust coefficients for the various cycles is shown in Figure 3-67 for the angles of attack of 20°, 30°, 40° and 60°. The percentage differences between these three axis results and the reference two axis results are shown in Figure 3-68.

The plot for cycles with 20° angle of attack showed the 3° reversed figure-of-eight path (red triangle dash) performed consistently better than the two-axis result (black asterisk), with a 21%-37% improvement in thrust coefficient from Strouhal number of 0.2 to 0.8. The 6° reversed figure-of-eight produced even higher thrust coefficient between Strouhal number of 0.2 -0.4 (improvement of 30-46%), but the thrust coefficient drop off rapidly at Strouhal numbers over 0.5. The 6° reversed cycle had the poorest thrust coefficient at Strouhal number over 0.7 due to excessive angle of attack mid-cycle.

After the 3° reversed figure-of-eight path, the normal two-axis cycle (solid black line with asterisk) has the second highest thrust coefficient. This is followed closely by the two oval paths (3°, and 6°), which had very similar performance to the two-axis cycle. The difference between the two-axis and 3° oval were approximate 1.5% to -3%, and differences with the 6° oval were approximately ±6%. The ‘normal’ figure of eight path, where the foil pushes backwards during the ‘powered’ phase of the stroke, performed consistently worse than the two axis cycle. The difference ranged from -15% in thrust coefficient for the cycle with 1.5° yaw to -80% for the cycle with 6° yaw. In the case of 6° yaw, the thrust coefficient began to fall when Strouhal number was above 0.5, while the thrust coefficient in the other cases continued to rise.

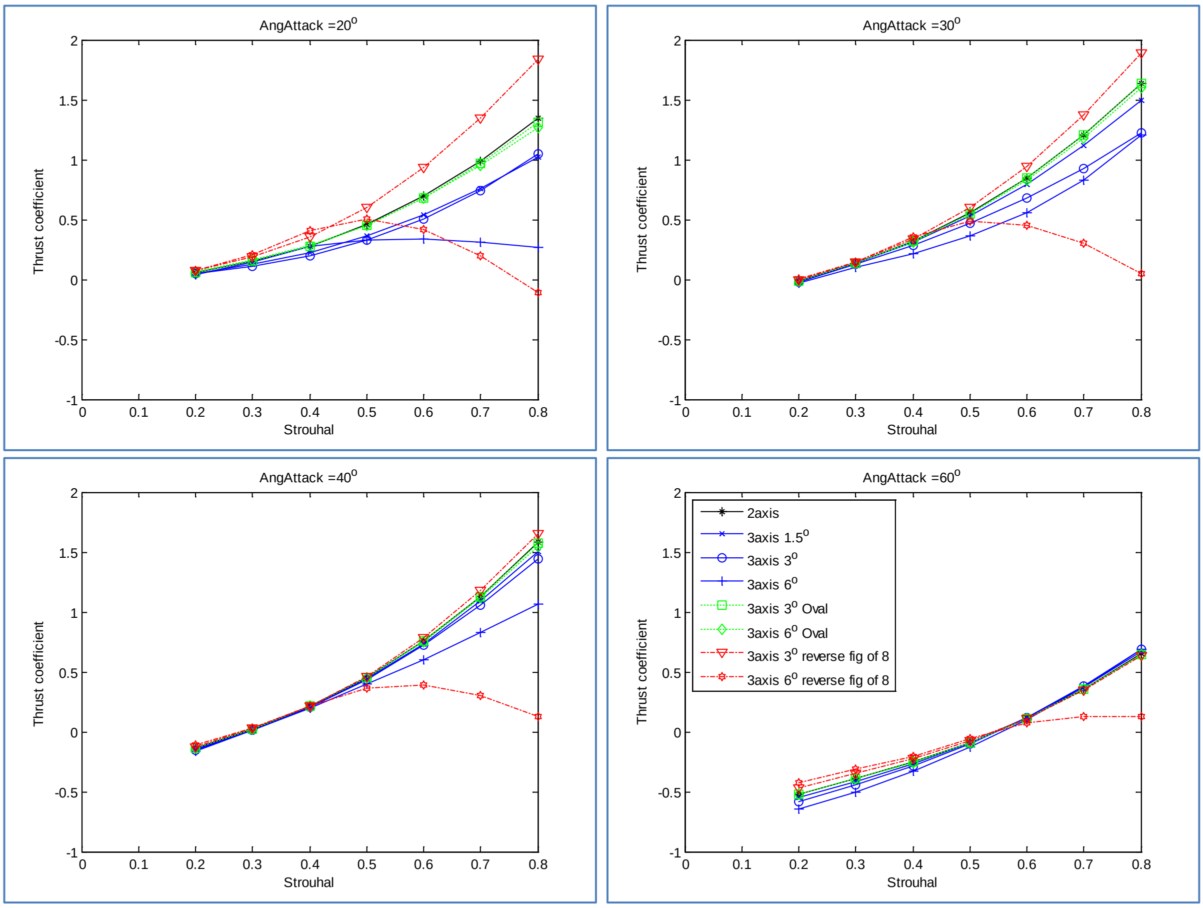

Figure 3-67 – Comparison of thrust coefficients of different three-axis foil actuation paths $\alpha_{0.7} = 20°, 30°, 40°, 60°$

In the cases of cycles with 30° angle of attack, the thrust coefficient at Strouhal number of 0.2 was negative in the two axis model, so the results between St=0.2 and St=0.3 were ignored. Similar to the cycles with 20° angle of attack, the 30° case showed the 3° reversed figure-of-eight produced the highest thrust coefficient with up to 15% improvement over the two axis model. The 6° reversed figure-of-eight achieved higher thrust coefficients between a Strouhal number of 0.3 and 0.4, but its thrust coefficients fall off rapidly beyond that. The two oval paths performed almost exactly the same as the two axis model with a reduction of around -0.2% for the 3° oval, and up to -2% for the 6° oval. Like the previous case, the three axis models following the ‘normal’ figure-of-eight paths performed worse than the two-axis model, although all three followed the same trends showed by the other paths. The 1.5° path experienced a -9% reduction in thrust coefficient, while the 6° path performed worst, with up to -35% drop in the thrust coefficient. However, the 6° path improved after St=0.6 and the differences between it and the two axis model was reduced to 26% at St=0.8.

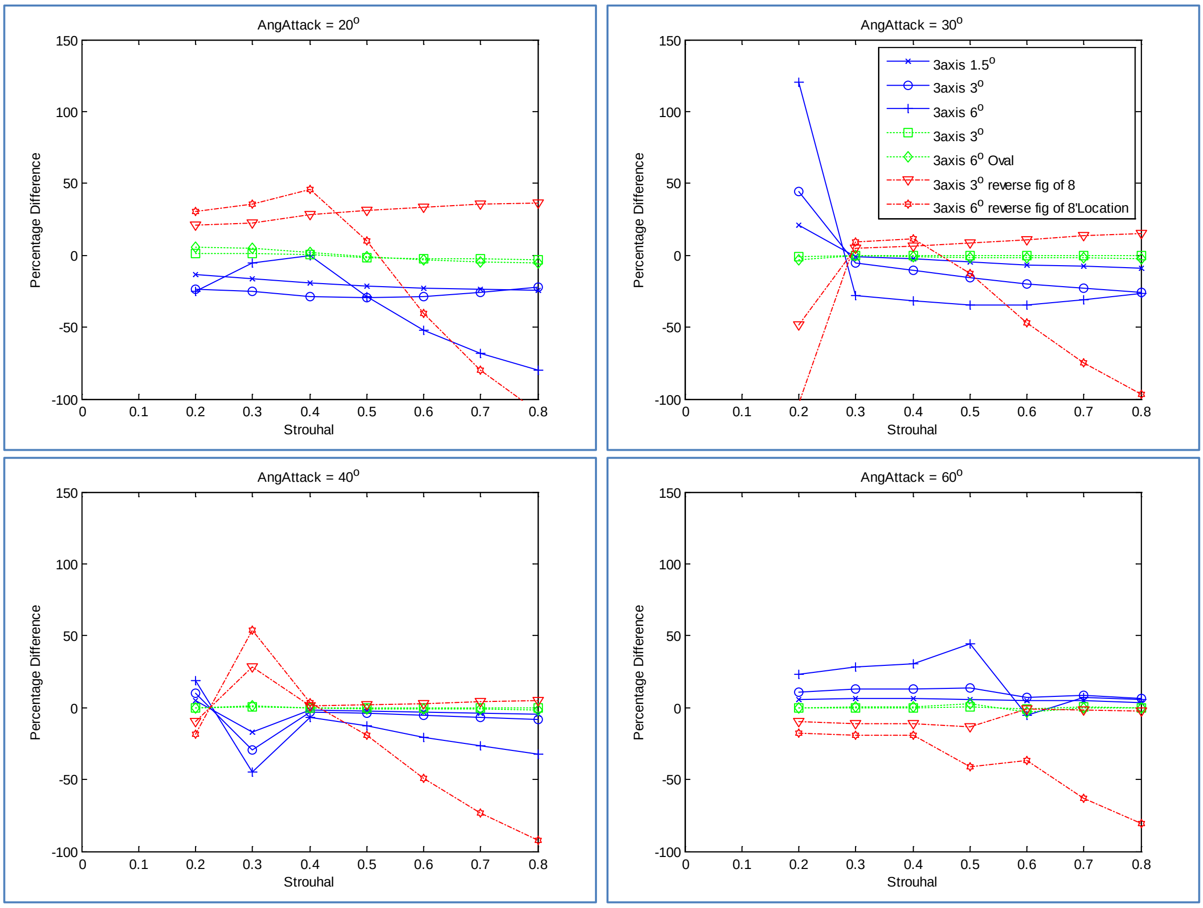

Figure 3-68 – Percentage errors between different foil paths' thrust coefficient and the 2 axis model

In the cases with angle of attack of 40°, the actuation path with the highest thrust coefficient is still the reversed figure-of-eight, but the improvement over the 2-axis cycle is less than 5%. The two oval paths performed very similarly to the two axis model with less than 0.5% differences between the two. Again the 'normal' figure of eight performed worse, although the differences were less than -5% for the path with a yaw amplitude of 1.5° and -10% for the case with 3° yaw amplitude. The performance of the 6° path was the worst of the three figure-of-eight paths, with a -6% reduction at St=0.4 to a -32% reduction at 0.8. However, its thrust coefficient is higher than that of the 6° reversed figure-of-eight path from Strouhal number of 0.5 to 0.8. The thrust coefficient of the 6° 'reversed' path drop off rapidly at Strouhal number above 0.5, and was 92% lower than the two-axis results by the time Strouhal number reached 0.8.

Finally in the case with angle of attack of 60°, the thrust coefficient up to St=0.5 was negative and remained relatively small but positive at Strouhal number higher than 0.6. The two reversed figure-of-eights path had the least negative thrust coefficient. The 3° 'reversed' path’s thrust coefficient were approximately 10-13% higher than the two axis path, while the 6° reversed path were 18-41% higher. The two oval paths’ performances were very close to the two-axis cycle and the differences were less than 1% between Strouhal numbers of 0.2 to 0.6. The ‘normal’ figure-of-eight paths continued to produce the lowest thrust coefficient with the 6° cycle’s thrust coefficient being up to 44% worse. However, a reversal occurred at Strouhal number higher than 0.6. The thrust coefficient produced by the 3° ‘normal’ figure-of-eight was 7% higher than the two axis model. This is followed closely by the 6° and the 1.5° paths, each achieving 5.3% and 3.4% improvement respectively. The oval paths performed almost exactly the same as the two-axis path, while the 3° reversed path were around -2% worse. The thrust coefficient for 6° reversed figure-of-eight path levelled off above a Strouhal number of 0.6, and it was over 80% lower than the two axis cycle at Strouhal number of 0.8,

3.8.1 Summary of the comparison between thrust coefficients of different stroke paths

The thrust coefficient comparison showed that the reversed figure-of-eight path with a 3° yaw amplitude produced the highest thrust coefficients for three-axis aquatic flight. The increased the local inflow velocity associated with the forward yaw motion improved the thrust output during the ‘powered’ section of the stroke. Meanwhile drag was reduced by moving the foil backwards and reducing the local inflow velocity during the ‘recovery’ section of the stroke. The 6° reversed figure-of-eight path can achieve even higher thrust coefficient, but the performance rapidly decrease as the Strouhal number rose above 0.5 as the angle of attack became excessive and exceeded 90° mid-stroke. The 3° and 6° oval paths have very similar performance to each other and the two-axis cycle, which means the yaw motion have almost no effect on the overall thrust coefficient. The ‘normal’ figure-of-eight paths, believed to be used by penguins, performed consistently worse than the two-axis path. In particular, the 6° cycle caused significant disruption to the foil flow and resulted in a significant reduction in thrust coefficient at lower angle of attack. This is a surprised as literature and video evidence suggested this is the three axis gait adopted by penguins. It is possible this may be an indication of a physiological limitation in the animal, or there may be additional hydrodynamic effect that has not been modelled.

3.9 Summary

Aquatic flight propulsion is used by many animals and has great potential for development into a novel AUV propulsion mechanism. Previous engineering studies of aquatic flight investigated aquatic flight as a one or two axis problem (pitch and roll), but zoological literature of animal aquatic flight and a short video investigation carried out by this research showed animal stroke has a third component in yaw. The effect of this yaw component and three-axis aquatic flights in general is not well understood.

As such, this research began investigating the three axis aquatic flight through a two prongs approach using modelling and experimentation. The existing quasi-steady model for aquatic flight is two axis and is based on simple propeller theory that do not fully account for the changes in flow condition along the foil span. This investigation incorporated blade element theory (BET) into a new model and adapted it for use in modelling aquatic flight in three-axis.

Three-axis aquatic flight is an inheritably three axis transient problem that can be expensive to model using traditional RANS based CFD methods. The three axis BET model is a quasi-steady model is designed to rapidly analyse hundreds of cases in a short amount of time and identify cases with special interest for detail experimental or RANS based CFD studies.

The research first examined the two-axis aquatic flight stroke path in detail so it can be used as a reference case for the investigation into the three axis aquatic flight stroke paths. It found the BET model predicts a thrust coefficient that is lower than the single element model, which suggest the 0.7span approximation used in traditional propeller analysis may be insufficient for analysis of aquatic flight as the 0.7span approximation resulted in an overestimation of the thrust. Examination of the force distribution along the span showed the foil centre of thrust in an aquatic flight foil is located at 0.56span rather than 0.7span.

The two axis cycle investigation used the model to model tested effect of changing Strouhal number, angle of attack, foil geometry, flow speed and element numbers (convergence). The results show that as the Strouhal number increases, the thrust coefficient would follow. Conversely, increasing the angle of attack can increase the thrust coefficient if the initial angle of attack is low, but if the foil is already operating at a high angle of attack, increasing the angle of attack further reduce the thrust output. While the thrust coefficient was lower than what has been shown in the literature, it can be caused by the different set up and foil design. Despite the differences, the model results showed the same pattern that was observed in the published experimental result, which suggest the model is on the right path.

The BET model also tested the effect of varying flow speed and foil geometry, and found neither have significant impact on the thrust coefficient, which shows the non-dimensional thrust coefficient can be used to perform comparisons between similar systems. The convergence investigation found 50 foil elements would be sufficient to model aquatic flight to within 1% of that predicted by a model with 100 and 500 foil elements. A model with a single element can overestimate the results by nearly 40% compared to the 50 element model, while a model with four elements will overestimate by around 10%.

In addition to lift and drag forces, the model also investigated the forces produced by added mass, Kramer effect and tip losses. Added mass and Kramer effect contribute forces to the flapping cycle, but their effects cancel out over a complete cycle, so they do not affect to the thrust coefficient. However, the tip loss can cause a significant loss of thrust, which suggested tip loss may not affect aquatic flight. This is because prior to the experimental verification, the BET model without tip loss appeared to underestimate the thrust coefficient when compared to results published in the literature. Adding tip loss to the BET model would've increase the discrepancy.

After forming a detailed understanding of the two axis aquatic flight and the BET model, the investigation in to three axis motions can begin. The three axis aquatic flight study investigated the figure-of-eight, oval and reversed-figure-of-eight stroke paths with various yaw amplitudes.

The symmetrical figure-of-eight path is the idealised path used by flying animals as well as penguins. While a flying animal needs to create additional lift to support the animal in air, a neutrally buoyant animal or vehicle in water does not need additional lift, so a symmetrical stroke path can be used in aquatic flight rather than an asymmetric one. As such this figure-of-eight actuation path was considered the default or ‘normal’ path for the three axis investigation.

However, to the surprise of the investigation, the three axis ‘normal’ figure-of-eight path reduced the thrust coefficient instead of improving it. On closer examination of the forces generated by different elements along the span and the corresponding angle of attack, it was found the yaw motion reduced the inflow angle during the ‘powered’ phase of the stroke when roll velocity was at its maximum. The reduction in inflow angle and angle of attack was caused by a reduction in foil inflow velocity, which in turned was the result of the yaw motion driving the foil backwards. Increasing the yaw amplitude further reduces inflow velocity at the foil element at the time when roll velocity reaches maximum, this lead to further reduction in the thrust produced. The forward motion of the foil during the recovery phase increased drag and reduced the overall thrust over a propulsion cycle. Initially it was expected the additional thrust during the ‘powered’ phase would compensate for the additional drag, but when it was discovered the yaw motion actually reduced thrust, the additional drag from the recovery phased made the situation worse.

When it was discovered the ‘normal’ figure-of-eight paths reduce thrust coefficient, it was decided to investigate the effect of reversing the figure-of-eight path. Unlike the ‘normal’ path, the foil was driven forward into the flow during the ‘power’ stroke, and return backwards along the flow during the ‘recovery’ phase at the limits of the roll cycle. The reasoning behind this path was the forward motion of the power stroke would increase the inflow velocity at the foil and the inflow angle, while moving the foil backwards during the recovery phase would lower the foil’s inflow velocity and reduce the drag. After running the BET model using this new path, it was found the thrust coefficient increased by up to 37% at lower angles of attack.

In addition to the figure of eight paths, the three axis investigation also examined the oval paths where the foil would perform asymmetric strokes. The oval path motion was found to have very similar performance to the two-axis cycle with performance difference being less than one percent.

The three-axis BET aquatic flight model calculated the thrust coefficient for a large combination of Strouhal number, angle of attack and various forces components, and it discovered some interesting and unexpected results and they need to be verified. In particular the BET model appears to underestimate the thrust coefficient compare the existing models, but this will need to be checked experimentally (Chapter 6). As it happens, the experimental verification would later show the BET model overestimated the thrust coefficient and tip loss is in fact an important factor to consider in the modelling of aquatic flight. This demonstrates the importance of experimental verification for the BET model.

This page is intentionally left blank

Chapter 4: Asymmetric Stroke

4.1 Introduction

In the previous chapter, the NIMBLE BET model was used to investigate symmetrical aquatic flight for straight line propulsion. However, in addition to producing thrust for propulsion, aquatic flight can also be used for producing force for steering the vehicle.

An aquatic flight propelled vehicle can produce manoeuvring force using a number of methods. It can steer by varying the output of the left and right foils to produce differential steering force. The vehicle can also steer by stopping the roll motion of the actuator on one side of the vehicle and turn its foil's pitch angle to 90° to create very high braking (drag) force that will swing the vehicle around. The foils can also be used as oversize control surfaces for controlling the vehicle's roll or pitch motions, which can be combined to turn the vehicle. Marine animals such as penguins and seals perform high speed turn by first rolling their body and then turn rapidly in pitch. This method utilise both flippers and can potentially generate more manoeuvring force than using the differential steering method alone.

In addition to turning, most AUVs also need to produce a constant down force to maintain depth, because most AUVs are designed to be positively buoyant as a failsafe. In most vehicles without controllable ballast, the down force is produced either through a constant negative angle of attack in the control surfaces or vehicle hull, or via vertically mounted thrusters. While an aquatic flight propulsor can perform the function of a simple control surface or a dive plane, this is not the most efficient use of its ability.

An aquatic flight propulsor can produce off-axis thrust with a vertical component that can be used for manoeuvring or to counter the vehicle buoyancy force. This gives vehicles driven by aquatic flight propulsors additional control options for manoeuvring that conventionally propelled vehicles don't have. Licht (2008) demonstrated asymmetric two-axis cycle can redirect some thrust out of the horizontal plane into the vertical direction for depth control by either introducing a pitch angle bias to the two-axis flapping cycle. A three-axis foil, such as the one investigated by NIMBLE, will have an additional option of combining the yaw motion with pitch and roll, thereby rotating the whole foil paths to vector thrust and opens up many more possible gaits for manoeuvring and depth control.. This chapter looks at the use of asymmetric stroke for producing off axis thrust by changing the balance between the up- and down-stokes of a flapping cycle.

Three types of asymmetric stroke paths would be investigated in detail, namely, pitch angle bias two-axis path (0° yaw), three-axis slanted path and three axis slanted path with pitch bias. The first type of path introduces a pitch angle bias into the motion equation such that the magnitude of the pitch angle would be different between the up and down stroke. It will also serve as a reference for the three axis path. The second type introduced yaw motion into a normal flapping cycle and produced a propulsion path with an inclination. The final type, the rotated path, added a pitch angle bias to the slanted flapping cycle such that the foil angle would be perpendicular to the stroke path at the apex of each stroke. Three-axis asymmetric strokes can be very complex and have large number of possible strokes so the investigation will be restricted to that of the slanted and rotated path. A more detailed description would be given in the respective section for each asymmetric stroke path.

4.1.1 Vertical Force and Combined Force Coefficient

Previously, the BET model non-dimensionalised propulsor thrust into thrust coefficient, so comparison can be made for the outputs of different systems. The same non-dimensionalisation was not carried out for vertical forces in Y because the vertical forces cancelled out over a cycle. However, this is no longer the case for cycles with asymmetric strokes. The asymmetry creates net vertical thrust, and the vertical component of the propulsive thrust will need to be non-dimensionalised for analysis. This second thrust coefficient in the Y direction is sometime referred to as the lift coefficient (Licht, 2008), but it will be called the vertical force coefficient here to avoid confusion with the aerofoil lift coefficient used elsewhere in the investigation (4-1).

$$C_{VF} = \frac{F_Y}{\frac{1}{2}\rho A U^2} \qquad (4\text{-}1)$$

In addition to the vertical force coefficient, it is also useful to know the total thrust output of the flapping foil propulsor. The combined force coefficient is the non-dimensional coefficient defined from the resultant force between thrust and vertical force, and its definition is given by equation (4-2).

$$C_{\Sigma F} = \frac{\sqrt{F_X^2 + F_Y^2}}{\frac{1}{2}\rho A U^2} \qquad (4\text{-}2)$$

4.2 Two-axis stroke with angle and phase bias

The first asymmetric stroke to be investigated is the two-axis cycle with angle bias. The flapping foil motion of a basic aquatic flight cycle can be described by three sinusoidal equations ((4-3), (4-4), (4-5)). The three motion equations have three angle biases, two phase bias and two controllable frequencies, which allows for more complicated foil paths and gait patterns than the two-axis cycle.

$$\theta(t) = \theta_0 \, sin(\omega_\theta t) + \theta_{bias} \qquad (4\text{-}3)$$

$$\phi(t) = \phi_o \, sin\big(\omega_\phi t + \omega_{\phi 0}\big) + \phi_{bias} \qquad (4\text{-}4)$$

$$\psi(t) = \psi_0 \, sin\big(\omega_\psi t + \omega_{\psi 0}\big) + \psi_{bias} \qquad (4\text{-}5)$$

Normally, the roll and pitch frequencies are identical to each other and the yaw frequency changes depending on the path (same frequency to pitch and roll plus 180° phase lag for oval path and double frequency for figure-of-eight path). In symmetrical aquatic flight, roll motion has a phase lead of 90° over the pitch motion and an actuator operating with this phase offset will produce equal amount of thrust on both up and down strokes. However, when a pitch angle or phase bias is introduced into the flapping motion, the up and down strokes will become asymmetrical and one stroke can potentially produce more thrust than the other. Also, the unequal up and down strokes means the vertical forces will no longer cancel out over a complete cycle which will result in a net vertical thrust. The yaw motion will be kept zero for this particular investigation.

The two-axis asymmetric stroke investigation examined the effect of pitch angle bias and the effect of phase bias. The angle bias investigation examines pitch angle offsets between -40° to +10°, and the phase bias examined a range of phase offset. The investigation found while angle bias can produce a significant change to thrust and produce a sizeable vertical force, phase bias was found to have negligible impact on the thrust coefficient and did not produce any net vertical force, so the investigation will focus on the effect of angle bias.

4.2.1 Pitch Angle Offset

When a pitch angle bias is introduced to the equation of motion, it caused a vertical translation in the pitch angle sine wave. This means one of the strokes will have much higher pitch angles than the other, and as a result the angle of attack throughout the up and down strokes will be different. The analysis will examine the effects of -20°, -10°, -5°, and +10° offset in detail, including its effect on the foil positions, element forces, total foil forces and the non-dimensional force coefficients. The angular positions of these cycles are shown in Figure 4-1.

Like the analysis in the previous chapters, the case with flow speed of $0.1ms^{-1}$ and Strouhal number of 0.5 would be chosen as the example cases for this analysis. The angle of attack is more complicated, because it is also a function of the pitch angle. If the mid-cycle or maximum angle of attack definition is used, it would cause the pitch amplitude to change and this can make comparison of the effect of the angle bias difficult because the changes observed can be caused by reduction in the pitch angle range instead of the angle bias. Therefore, the pitch amplitude would be determined from the amplitude of the non-bias cycle with angle of attack of 40°, and the angle bias would be added to this function.

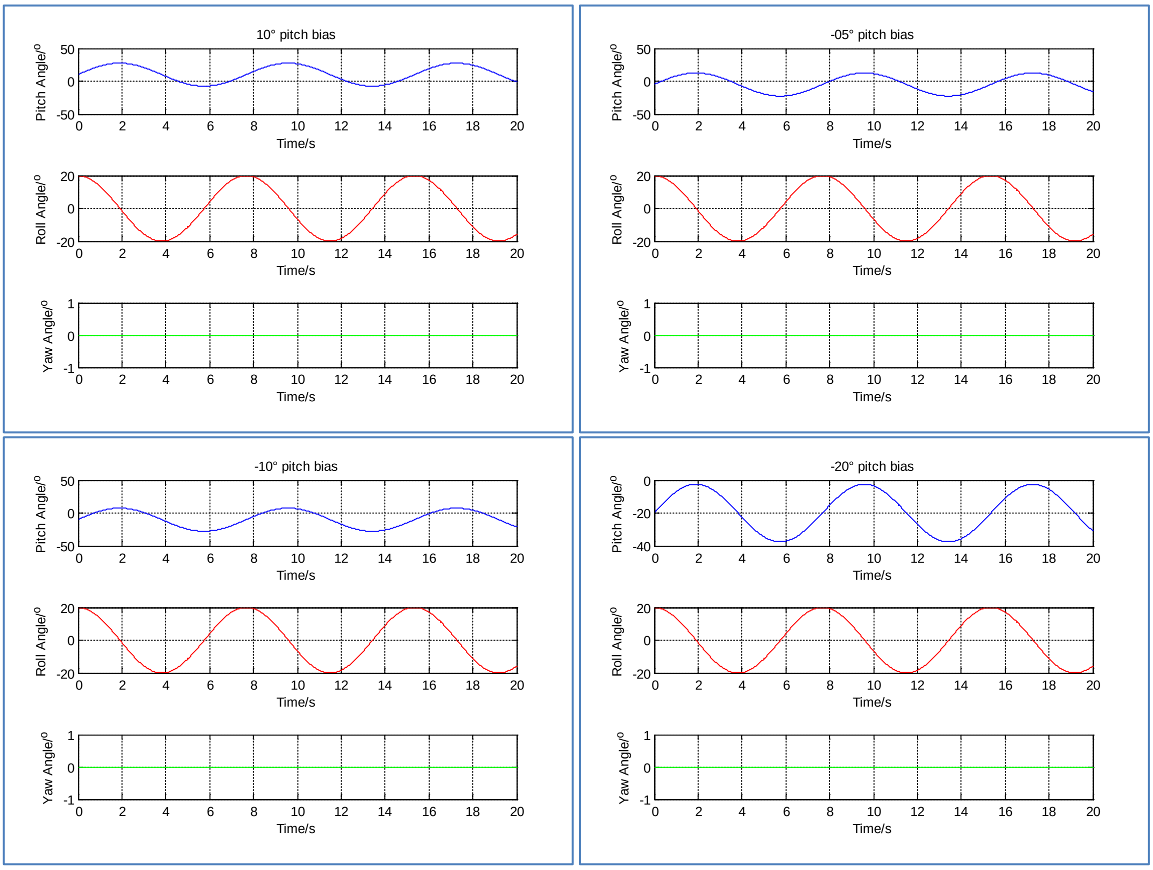

Figure 4-1 – Foil positions of a foil undergoing asymmetric flapping cycle with pitch bias of -10°, 5°, 10°, and 20° ($\boldsymbol{St_{0.7} = 0.5, \alpha_{0.7} = 40°, U = 0.1ms^{-1}}$)

4.2.2 Foil Force

The foil force is a function of the inflow velocity and angle of attack. The angle of attack is the difference between the inflow angle and pitch angle. Although the inflow angle remains unchanged, the pitch bias shifts the pitch angle, which causes the angle of attack in the up and down strokes to get larger or smaller depending on the sign of the angle bias. The forces produced by different foil elements from foil with different pitch bias are shown in Figure 4-2. The sub-models for Kramer effect, added mass, and tip loss were disabled for the analysis in order to better illustrate the effect of angle bias on the lift and drag force.

The plot shows amplitude of thrust (X) and vertical force (Y) produced by the up and down strokes are no longer equal. This is shown in the plot by the uneven peaks in the horizontal thrust. The cycle with a positive pitch bias produces its maximum thrust in the down stroke, while the cycle with negative pitch bias produces its maximum thrust in the up stroke. The magnitude of the maximum thrust in the negative bias cycle's down stroke is equal to the maximum thrust in the positive bias cycle's up stroke (e.g. thrust in cycles with ±10° bias).

In the case of the cycle with -20° bias, the pitch motions has shifted all the way into the negative, which lead to the thrust being produced only by the up stoke and no thrust is produced during the down stroke.

Since the tip loss effect is excluded in this analysis, the element forces increases towards the tip. Foil stall can further reduce the thrust near the foil root if the element’s angle of attack is between 10° and 20°. An example of this this can be seen in the case with $\pm 10°$ bias, where the element at 0.3span produced less thrust than the element at 0.1span.

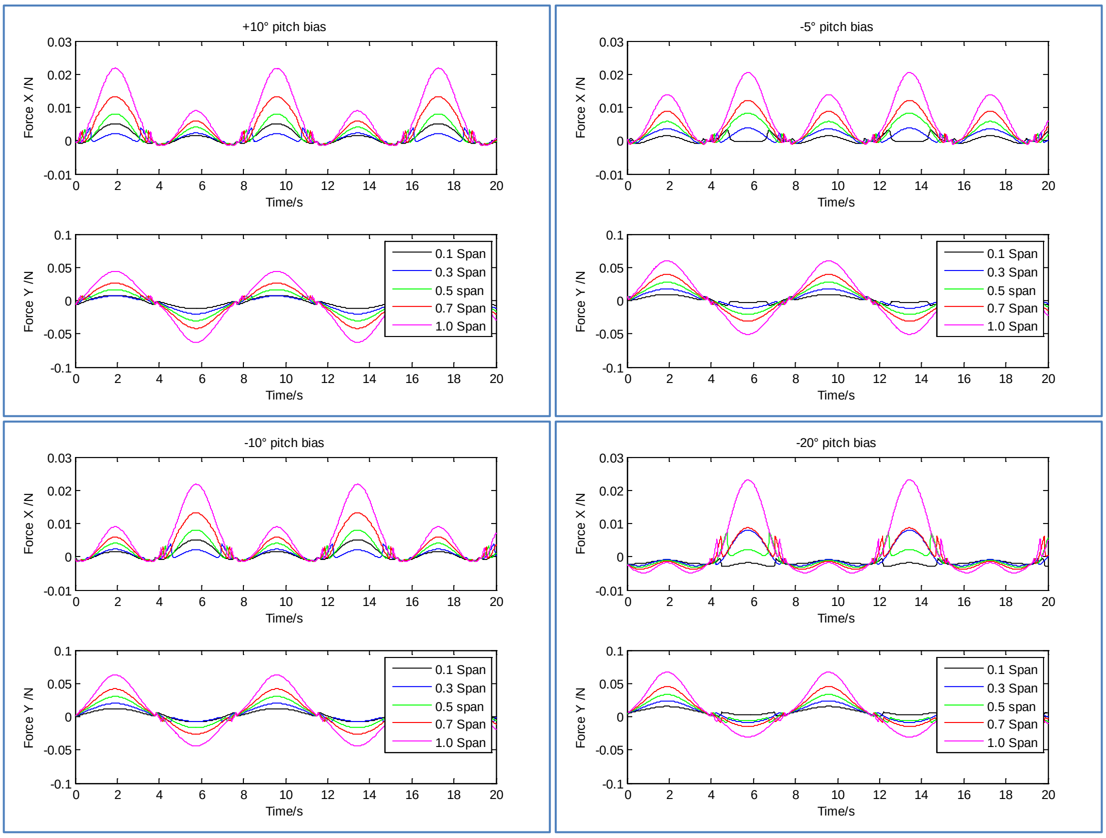

Figure 4-2 – Element force of a foil undergoing asymmetric flapping cycle with pitch bias of -10°, 5°, 10°, and 20° ($St_{0.7} = 0.5, \alpha_{0.7} = 40°, U = 0.1ms^{-1}$)

The vertical forces are also affected by the pitch bias and the forces from the up and down strokes no longer cancel out over a propulsion cycle. This lead to a net vertical force that is either positive or negative depending on the bias. In the cycles with negative pitch bias, it leads to a reduction in up force in the down stroke and increase in down force in the up stroke. This results in a net down force that will push a vehicle downwards. The opposite occurs for flapping cycles with positive pitch bias where the up force is higher than the down force, which will cause the vehicle to ascend.

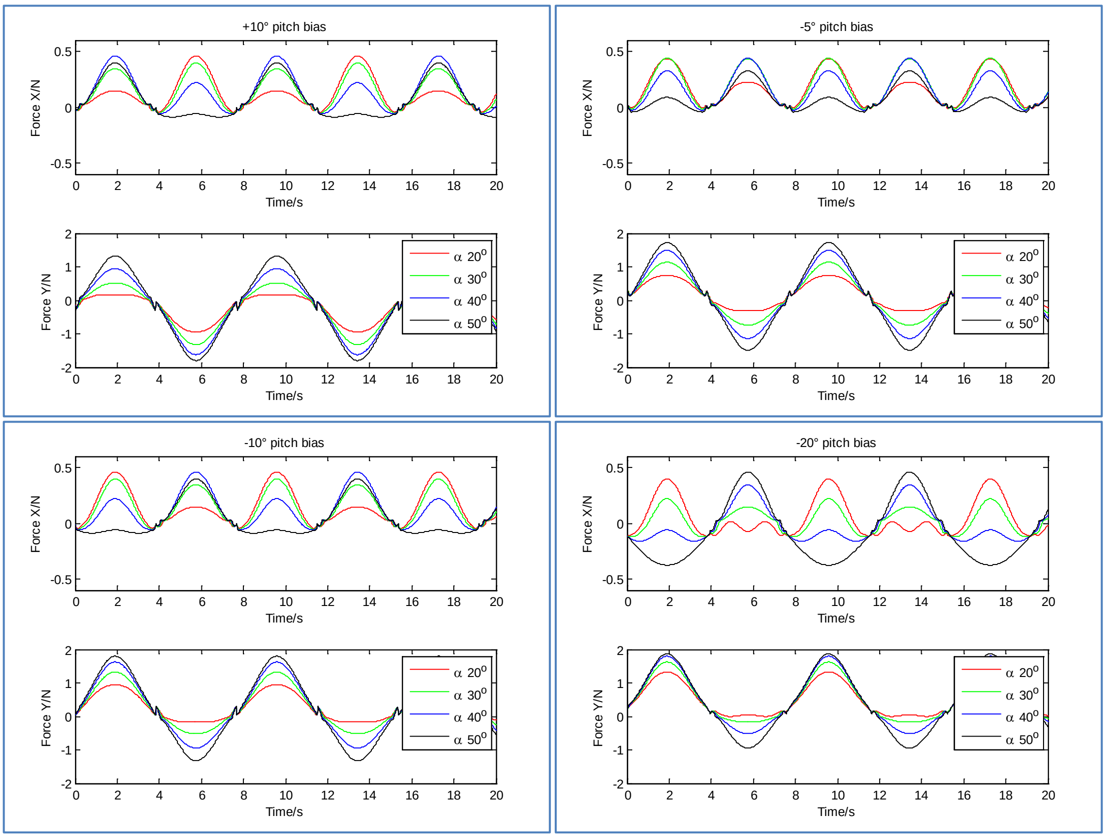
+10° pitch bias

-5° pitch bias

-10° pitch bias

-20° pitch bias

Figure 4-3 – Total foil force at different angle of attack for a foil undergoing asymmetric flapping cycle with pitch bias of -10°, 5°, 10°, and 20° ($St_{0.7} = 0.5,\ U = 0.1ms^{-1}$)

The total foil force for cycles with four different angles of attack is shown in Figure 4-3. The pre-determined angles of attack can change the corresponding pitch amplitudes, and this can have a significant effect in the foil forces. The plots show the foil generates more forward thrust in the up stroke than the down stroke in the flapping cycles with a pitch bias of -10° and angle of attack of 40°. In addition, the down stroke produced more vertical up force than down force was produced by the up stroke. This pattern is also observed for the cycles with 50° angle of attack, but the opposite occurs in the cycles with angle of attack of 20° and 30°, in which the down stroke produces more horizontal thrust and vertical up force than the up stroke.

The reason why the cycle corresponding to -10° bias and angles of attack of 20° and 30° produced less thrust during the upstroke is because of foil stalled. The pitch angle bias increased the angle of attack during the down stroke but reduced it during the up stroke. For the cycle with operating angle of attack of 20°, the pitch bias increased down stroke's mid-stroke angle of attack to around 36°, while the up stroke's mid-stroke angle of attack is reduced to less than 16°. This means the foil is stalled for the most of the up stroke, which reduces the foil lift, and that in turn reduces thrust. Meanwhile the cycle with operating angle of attack of 40° achieved maximum angle of attack of 56° in the down stroke and 36° in the up stroke. When this is combined with the increased pitch angle magnitude in the up stroke, which increases the contribution of lift force to forward thrust. This results in the up stroke producing more thrust in the cycle with operating angle of attack of 40° than cycles with smaller angles. Plots of the angles of attack at various positions along the span during a flapping cycle are shown in Figure 4-4.

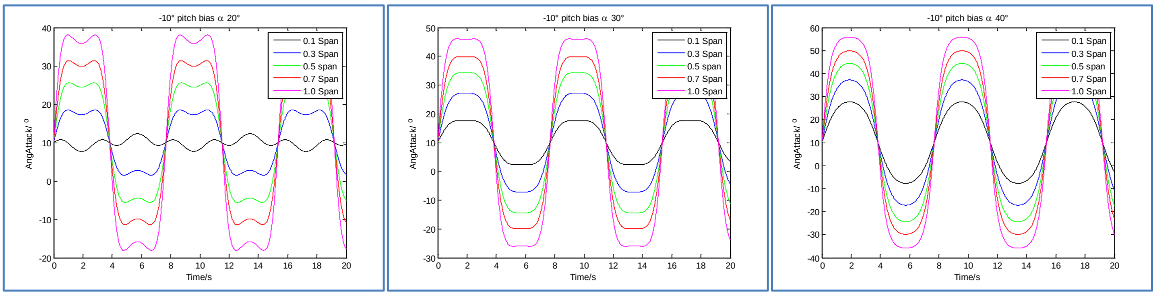

Figure 4-4 – Angles of attack for flapping cycles with -10° pitch bias

Due to the unequal peaks between up and down strokes, it is important to examine the differences between the two. A thrust ratio was calculated by dividing the thrust level at mid stroke of the up stroke with the thrust level at mid stroke of the down stroke. The results of the calculation are shown in Figure 4-5. A positive thrust ratio indicates the flapping foil produces forward thrust in both up and down stroke. On the other hand a negative ratio means one of the strokes only produces backward drag. The down force ratio is always negative because up stroke always produces downward force and down stroke always produces upward force.

It can be seen from the diagram the thrust from up and down strokes can differ by as much as 370% (-5° bias, 50° angle of attack) if both strokes produced forward thrust. If one of the strokes only produced drag, the differences between the magnitude of thrust and drag can differ by as much as -670% (-10° bias, 50° angle of attack). Generally the plots show the differences between the up and down strokes increase as the angle of attack increase. This is true for both thrust and down force. In the thrust ratio plot, the angle bias adds another layer of complexity because increase in angles of attack causes decrease in pitch angles. Therefore, there comes a point when the pitch bias can shift the entire pitch cycle above or below the 0° pitch. When this occurs, one of the strokes will only produces drag and as a result it leads to a change of sign in the thrust ratio plot. The effect of angle bias on the down force is more straight forward. The magnitude of the down force ratio increases as the pitch angle bias decrease, and the ratio are always negative because the vertical forces from the up and down stroke always have opposing sign. The difference is up to 87% for the cycle with -5° pitch bias and up to 51% for the cycle with -20° pitch bias.

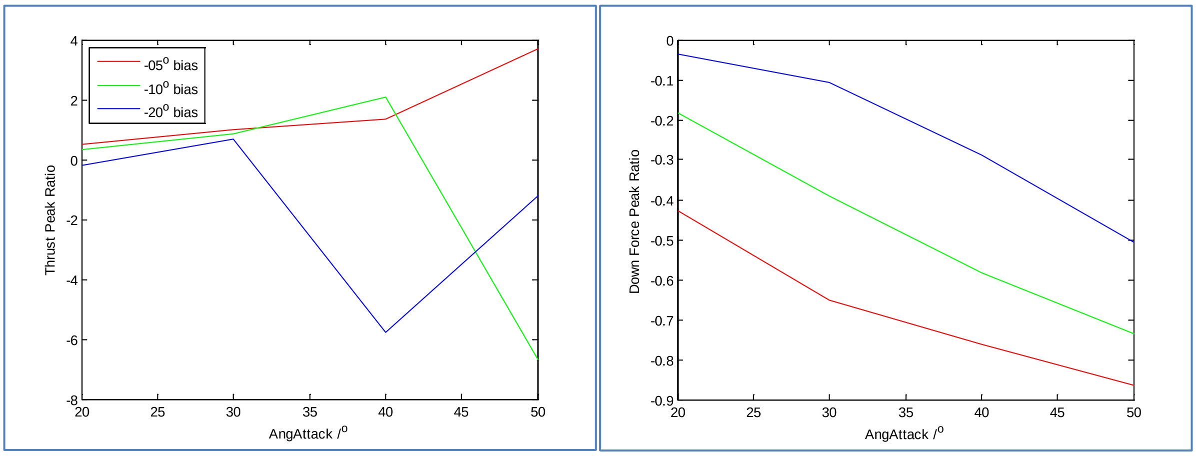

Figure 4-5 – The thrust ratio between the magnitude of the down stroke peak and the up stroke peak. ($\alpha = 40°$)

4.2.3 Thrust Coefficient

After analysing the individual cases, the horizontal thrust is non-dimensionalised into the thrust coefficient to enable easier comparison between the different cases. The thrust coefficients for the flapping cycles with -10°, 5°, 10°, and 20° are plotted in Figure 4-6. It can be seen the thrust coefficient gradually decreased as the angle bias increased.

The contour plots can be difficult to read in detail, so cross sections of the contour plots were taken at four different angles of attack (20°, 30°, 40°, 50°), and the results are plotted in Figure 4-7 for cycles with bias from -40° to 10°. It can be seen the normal two-axis cycle with no pitch angle bias produces the maximum horizontal thrust which increases as the Strouhal number increases. Generally, the thrust coefficient increases as Strouhal number increases in all cycles up to the one with 30° pitch bias, but this changed when the pitch bias reached 40°, where the reverse happened and the thrust coefficient became more negative as the Strouhal number increases.

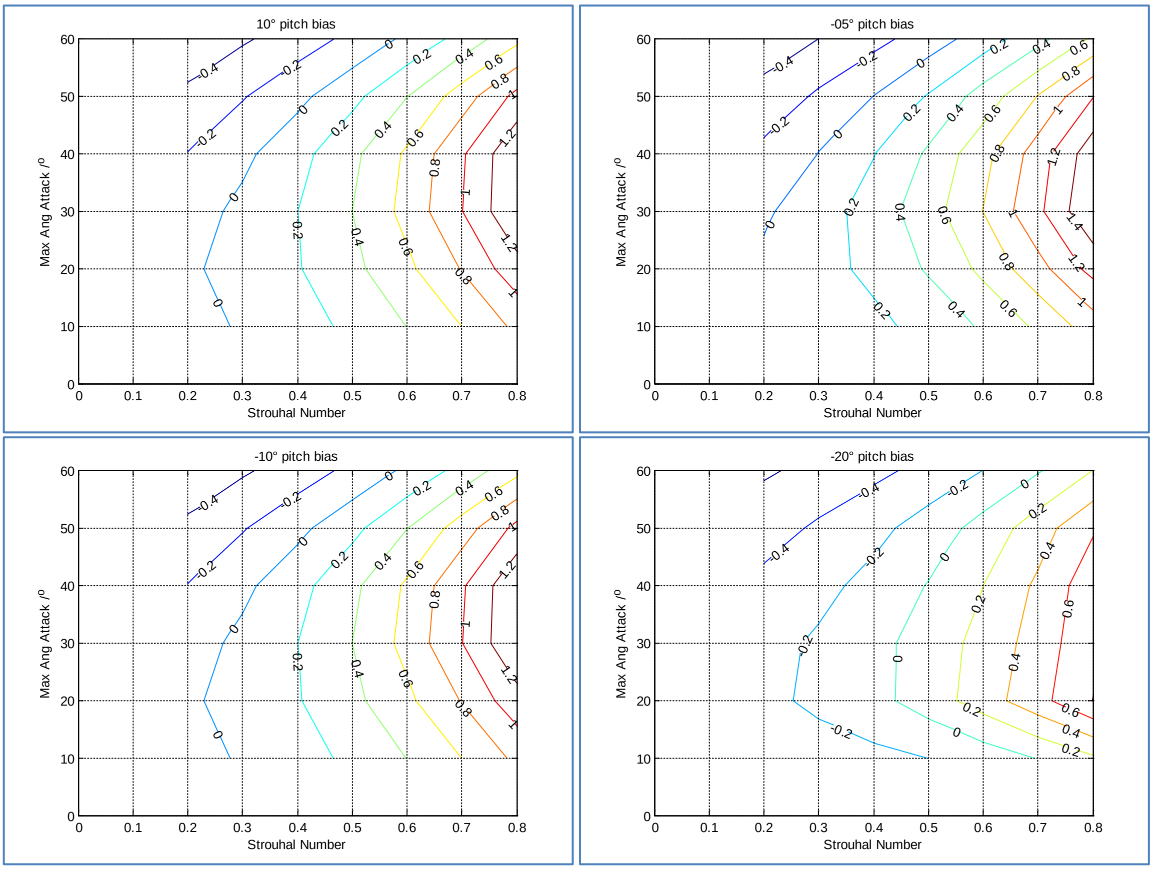

Figure 4-6 – Thrust Coefficient of a foil undergoing asymmetric flapping cycle with pitch bias of -10°, 5°, 10°, and 20°

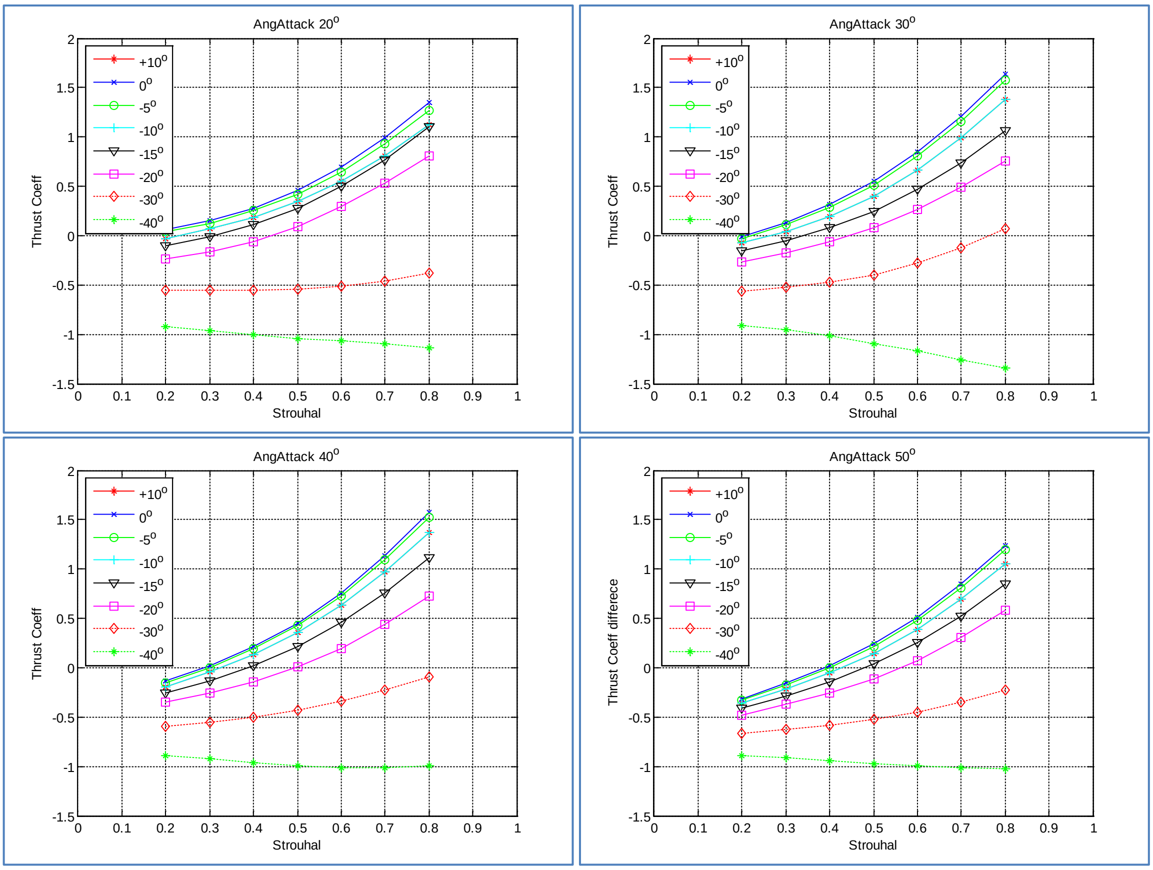

Figure 4-7 – Thrust coefficient for various angles of attacks (20°, 30°, 40°, 50°)

The thrust coefficients gradually decreases as the angle bias increases, and the cycles only produced negative thrust at 30° pitch bias in all but one of the cases examined (Strouhal number of 0.8 and angle of attack of 30°). In cycles with 40° pitch bias, the thrust coefficient is negative for all cases examined. Since the thrust coefficient is calculated from the average thrust in the flapping cycle, the thrust coefficient is not affected by the sign of the angle bias. Therefore a cycle with +10° bias will produce the same thrust coefficient as a cycle with -10° bias, and as such the plot line for +10° bias overlaps exactly with the line of for -10° bias.

4.2.4 Vertical Force Coefficient

The vertical force coefficient is calculated from the averaged resultant vertical force in a complete flapping cycle. A cycle with no pitch bias will produce no net vertical thrust, so the vertical force coefficient will be zero throughout the analysis range. However, if there is a pitch bias in the cycle, the vertical forces from the up and down strokes will not cancel out and the cycle will produce a net vertical force. The vertical force coefficient for cycles with 10° to -20° pitch bias are shown in Figure 4-8.

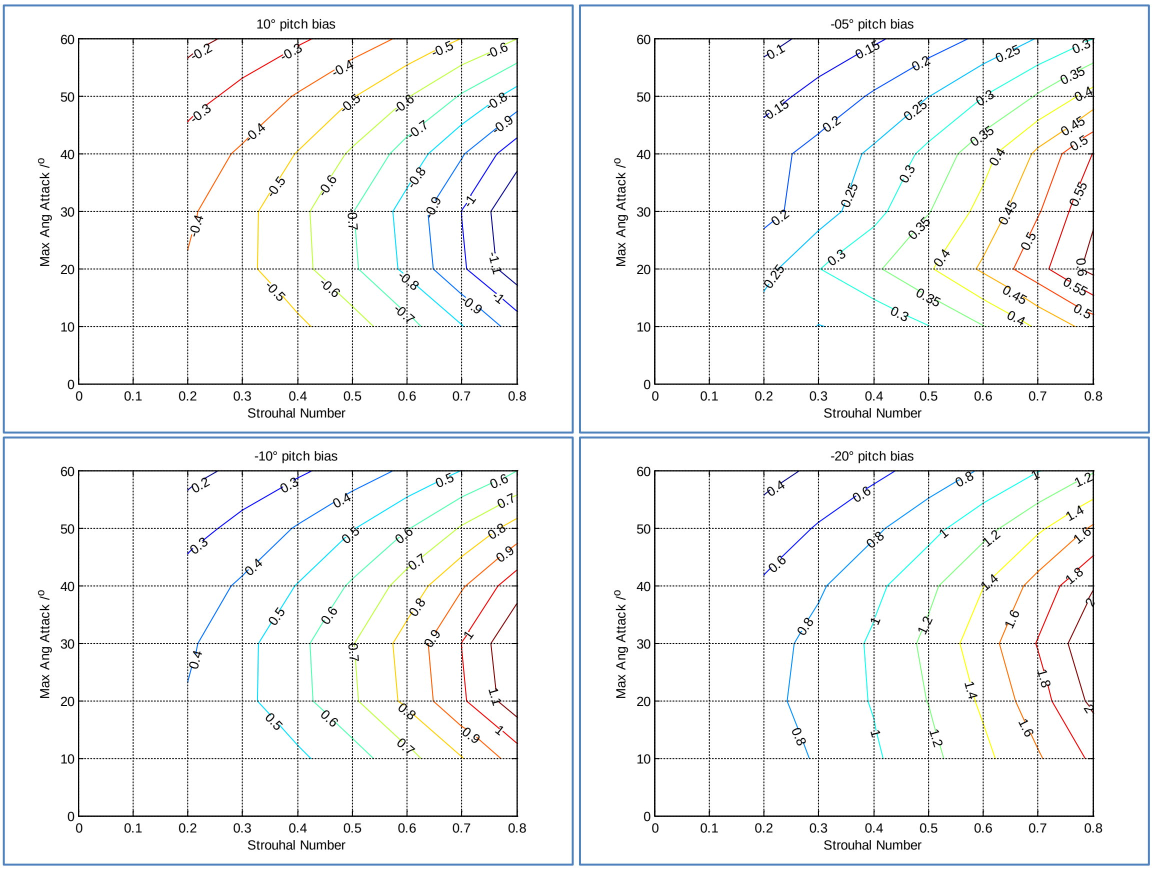

Figure 4-8 – Vertical force coefficient of a foil undergoing asymmetric flapping cycle with pitch bias of -10°, 5°, 10°, and 20°

Cross sections of the contour plots are taken at angles of attack of 20°, 30°, 40°, and 50°, and the results are plotted in Figure 4-9. Since the cycle with 0° bias produces a vertical force coefficient of zero, it is shown in the plot as the blue line that lay directly on the X-axis. The cycle with +10° and -10° produces down force that is equalled in magnitude but opposite in direction. Cycles with negative bias creates positive vertical force that will pushes the actuator upwards. Meanwhile the cycle with positive bias will produce negative force which pushes the actuator downwards. The vertical forces increase as pitch angle bias increase, and the cycles with pitch bias higher than 20° are able to produce down force with greater magnitude than the maximum horizontal thrust produced by the 0° cycle with no bias.

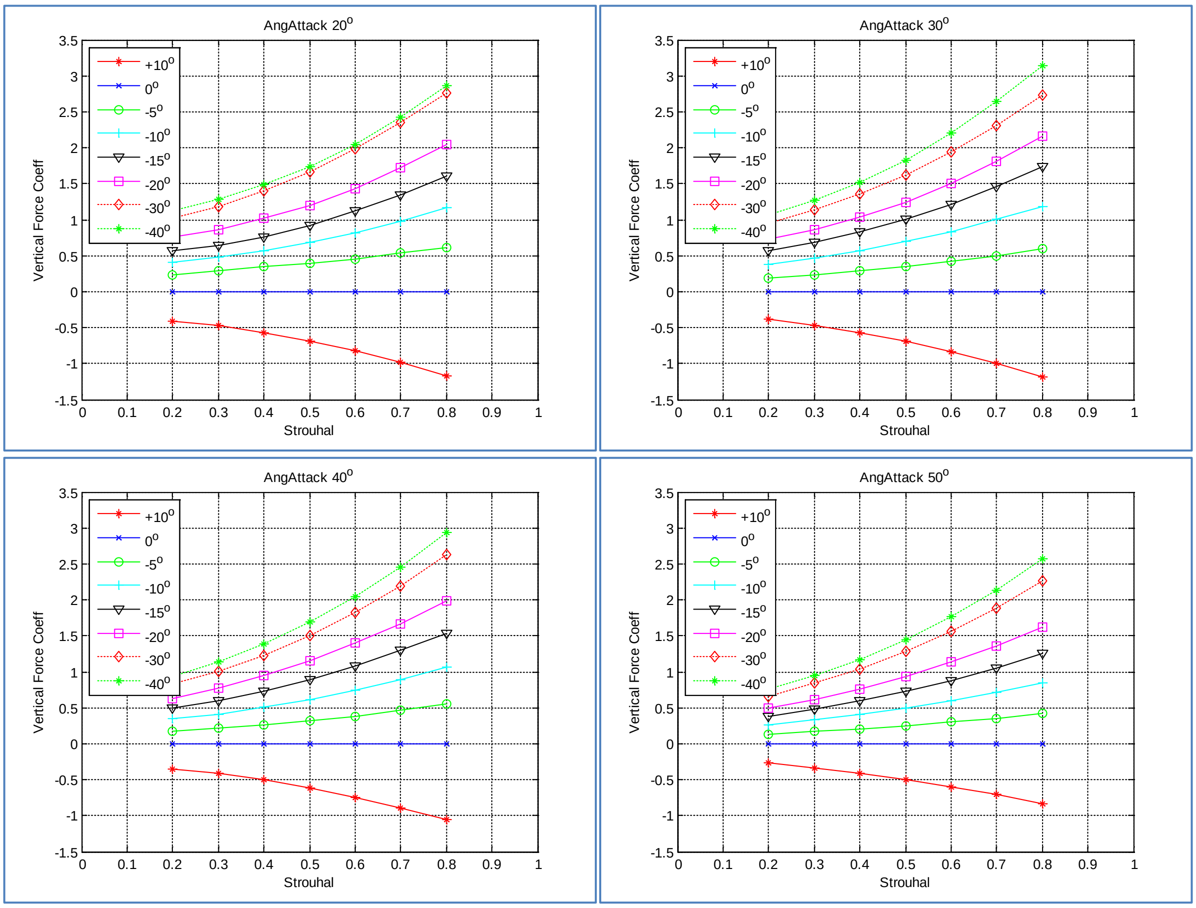

Figure 4-9 – Vertical force coefficient for various angles of attacks (20°, 30°, 40°, 50°)

4.2.5 Vertical Force Coefficient – Thrust Coefficient Ratio

Since aquatic flight propulsion cycles with pitch bias diverted some horizontal thrust into the vertical direction, the vertical force to thrust output should be examined. The vertical force coefficient to thrust coefficient ratio (VFC/TC) is calculated by dividing the vertical force coefficient by the thrust coefficient. Figure 4-10 shows the contour plots of the VFC/TC ratio for four different pitch bias angles. At first sight, all three plots appear to show very different behaviour, but upon closer examination, these patterns are cause by the complex interaction between the thrust coefficients and vertical force coefficients. The zero contour lines in these plots represent cases where the thrust coefficients are significantly higher than the vertical force coefficients, while areas with very large VFC/TC ratios represent cases where vertical force coefficients are significantly higher. The former can be caused by the vertical force coefficient being closed to zero and the latter can be cause by the thrust coefficient being close to zero.

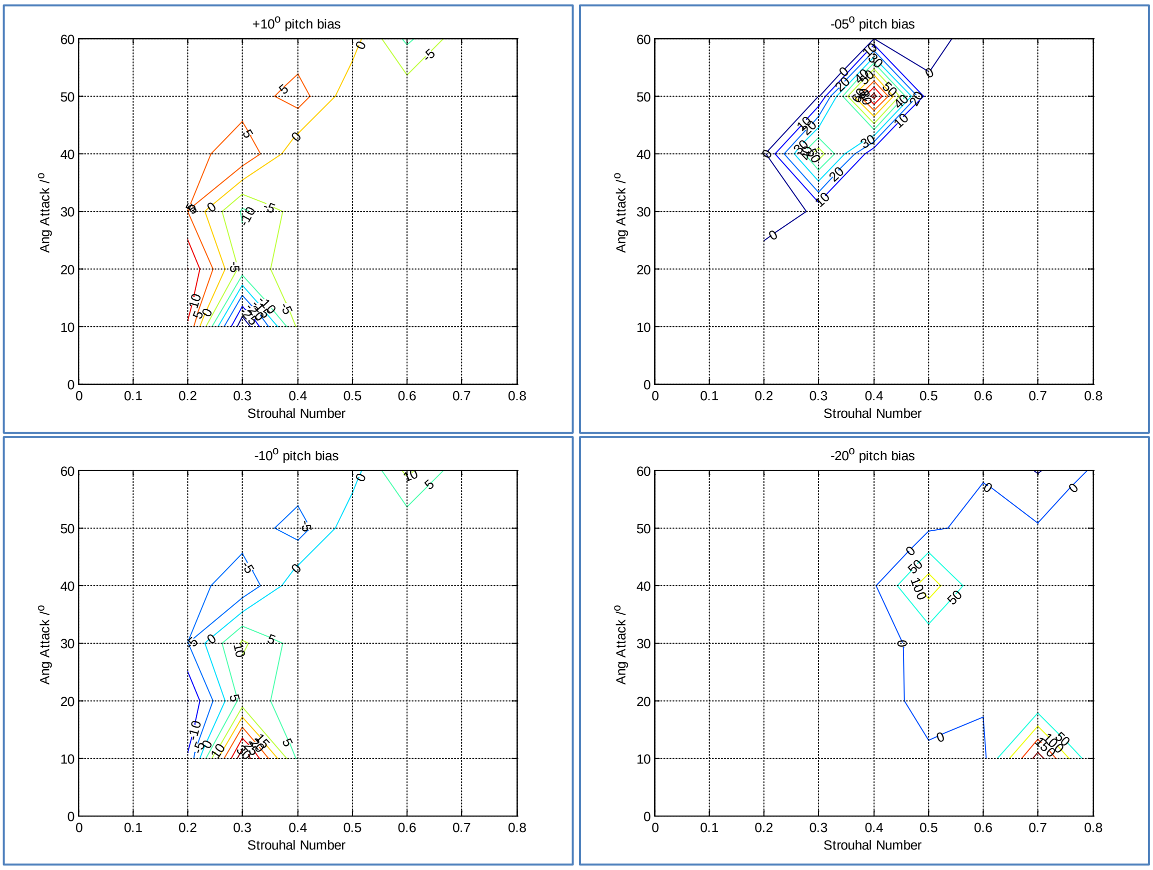

Figure 4-10 – Vertical force coefficient to thrust coefficient ratio for four bias angles

Due to the way the VFC/TC ratio is calculated, the contour plots are dominated by the points where vertical force coefficients are significantly higher than the thrust coefficient. Cases where the two force coefficients are almost equal or where thrust coefficients are larger are not well represented in the contour plot. As such cross-sections of the contour plots were taken at four different angles of attack to make it easier to read. Since the vertical spread of the VFC/TC ratio is very large, the ratio was plotted on a plot with on a logarithmic axis (Figure 4-11).

The 10^0 line in the plot represents the cases where vertical force coefficient and thrust coefficient are equal (VFC/TC ratio equals unity). Cases with VFC/TC ratio below this line represents cases where thrust coefficient are larger, and vice versa for cases above this line. The plots show the VFC/TC ratio began relatively small for cases with bias angles from -5° to -20°, which then increase significantly at Strouhal numbers between 0.3 to 0.6, after that the ratio began to fall. The vertical force coefficients are significantly higher than the thrust coefficients in most of the cases analysed, but the plots also show some exceptions such as some cases at higher Strouhal numbers for cycles with -5° and -10° pitch bias.

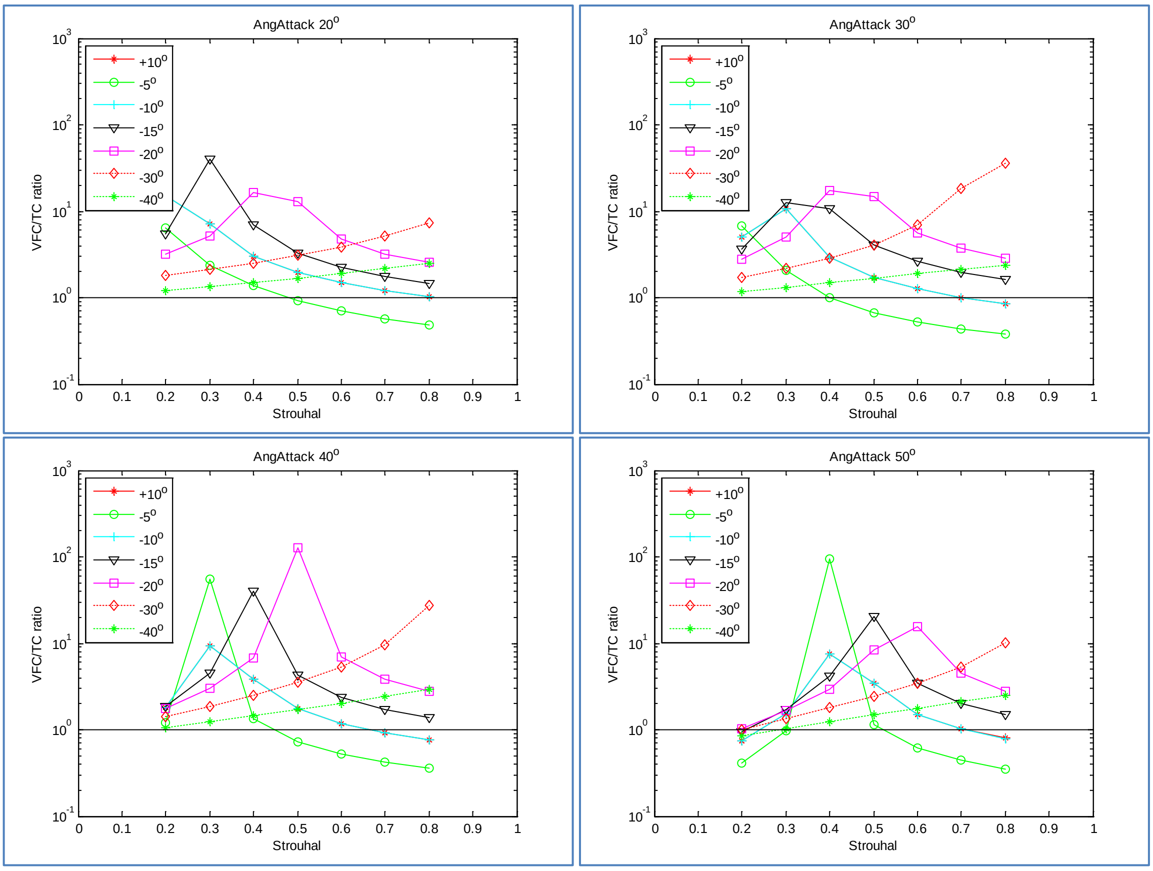
AngAttack 20°

AngAttack 30°

AngAttack 40°

AngAttack 50°

Figure 4-11 – Cross sections of vertical force coefficient to thrust coefficient ratios for cycles with different pitch bias. The cross section was made at four different angles of attack (logarithmic)

Cycles with -30° and -40° shows a different pattern to cycles with smaller bias. Instead of starting with a small VFC/TC ratio that first increases and then decreases as Strouhal number increase, the ratios for these two cycles starts small but they increase steadily with no sign of decrease. In all cases examined, the ratio shows the vertical force coefficient for these two cycles are larger than the thrust coefficients, which means more vertical force is produced than horizontal force. The plots also show the VFC/TC ratio are symmetrical regarding the pitch bias angles, as the line representing the ratio for the +10° bias (red solid) and -10° bias (turquoise solid) overlaps each other exactly. In a plot without logarithmic axis, they would appear mirror image of each other.

4.2.6 Combined Force Coefficient

After looking at the thrust and vertical force coefficients separately, their combined force coefficients were calculated from the magnitude of the resultant force between the horizontal thrust and vertical down force. Contour plots of the combined force coefficient are shown in Figure 4-12 for four different pitch bias angles. The plots for 10° and -10° pitch bias are identical because the magnitude of the resultant thrust is identical between the two cycles. Their resultant thrusts only differ in directions which are not shown in the combined force coefficient calculation.

Cross-sections of the contour plot were taken and plotted in Figure 4-13. It shows the combined force coefficients increase as the bias angle increases. The normal cycle with no pitch bias produces the lowest coefficient at all angles of attack examined, and the cycles with the highest pitch bias examined (40°) produces highest coefficients. The combined force coefficients for cycles with positive and negative bias are identical. An example can be seen in the cycle with +10° and -10° bias, where the line for their combined force coefficient matches exactly.

In summary, the pitch bias adds down force to the flapping cycle while reducing the horizontal thrust. However, the trade-off between vertical and horizontal forces are not straight forward and the plot shows the thrust coefficients of the cycles with pitch bias often produce more total force compared to cycles with no pitch bias.

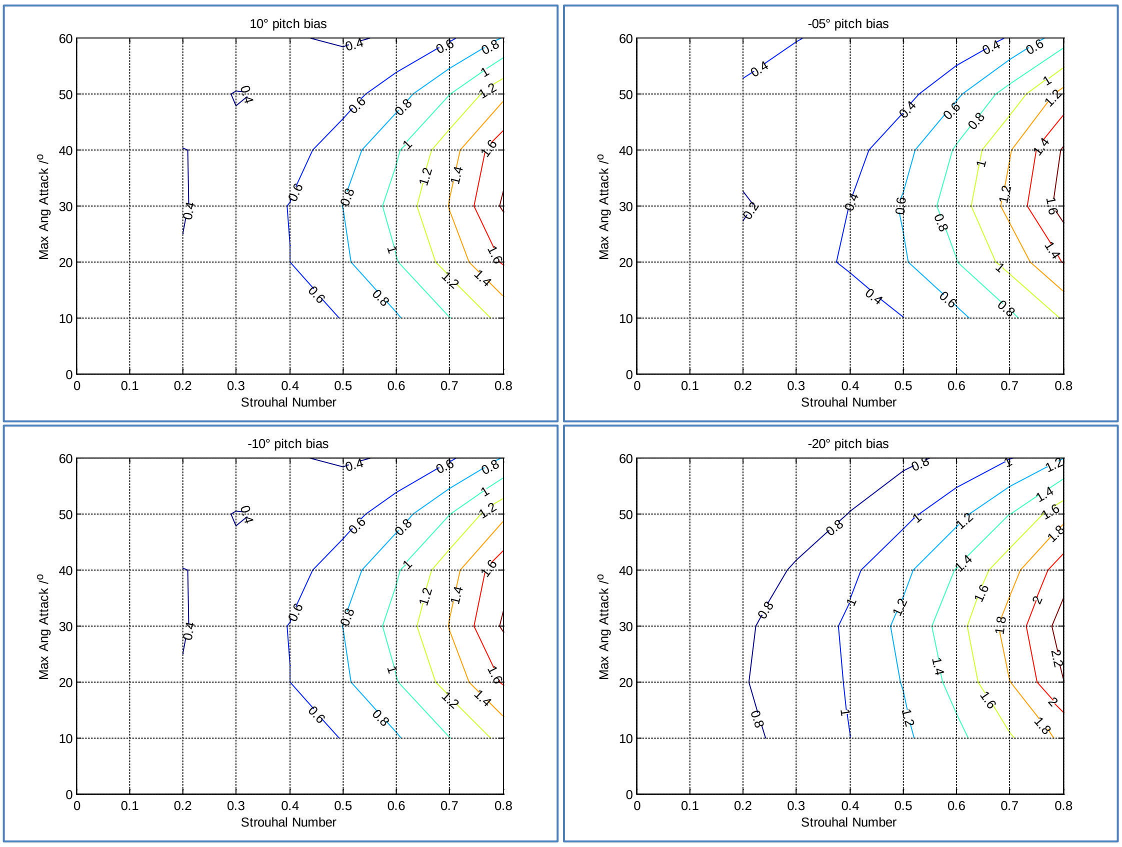

Figure 4-12 – Combined Force Coefficient of a foil undergoing asymmetric flapping cycle with pitch bias of -10°, 5°, 10°, and 20°

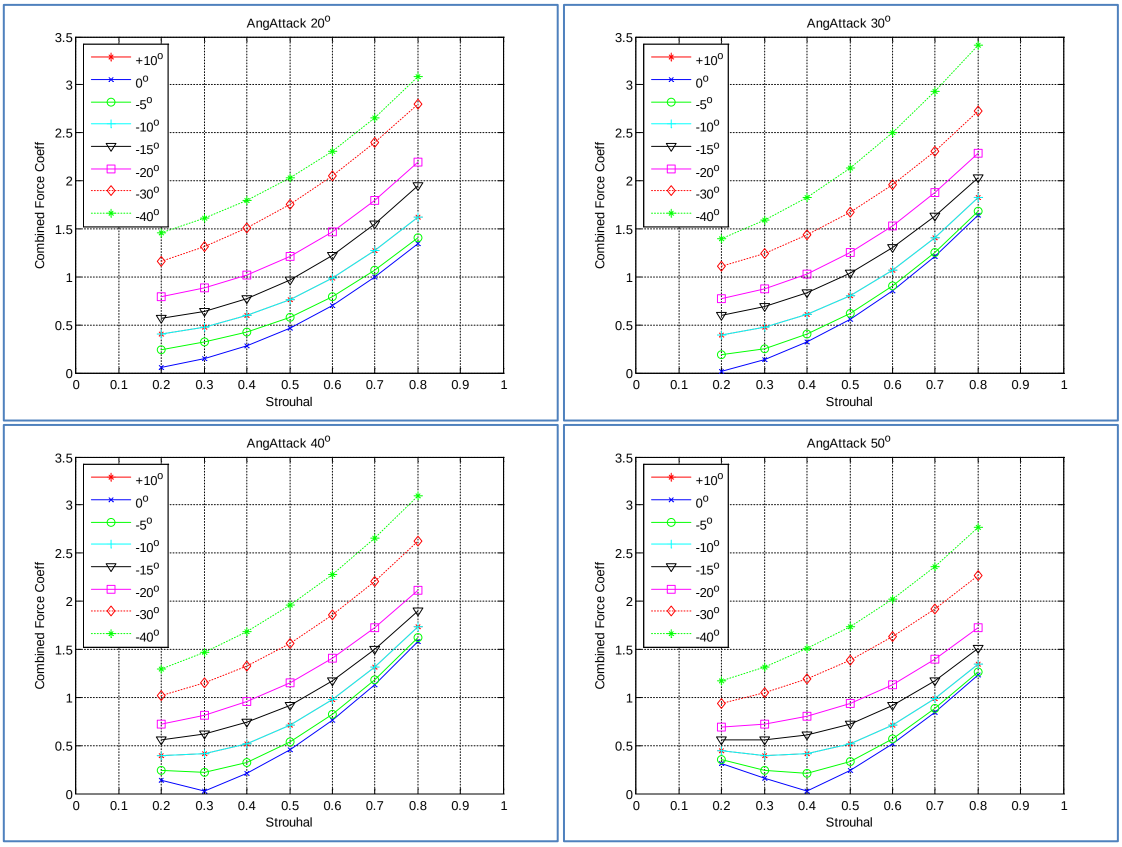

Figure 4-13 – Combined Force coefficients at different angle of attack. The plot show combined force coefficients from cycle with +10° to -40° pitch bias.

4.2.7 Summary of Two Axis Asymmetric Strokes

The investigation into two-axis aquatic flight analysed the effects of adding pitch bias angle to the pitch cycle and looked at the effect of 7 pitch angle bias in detail. It found introducing a pitch angle bias into the propulsive cycle can produce useful off axis manoeuvring force. The pitch angle bias changes the pitch angle in a flapping cycle which changes the angle of attack. The change in the angle of attack causes an unbalance of force between the up stroke and the down stroke in an aquatic flight propulsion cycles. This in turn leads to the up stroke and down stroke producing different level of horizontal and vertical forces. Generally, as pitch angle bias increase, the magnitude of the horizontal thrusts decrease but the magnitude of the vertical down forces increase. Depending on the magnitude of the angle bias it is possible to generate more thrust in the vertical direction than the horizontal direction. When the two forces are non-dimensionalised and combined, it was found the combined force coefficients for flapping cycles with pitch angle bias are higher than that of the cycles without, throughout the range of the analysis.

4.3 Three Axis Asymmetric Stroke – Slanted path

The second part of the asymmetric stroke investigation analysed the effect of asymmetric stroke produced by a slanted actuation path. The slanted path is produced by three axis actuation through introducing yaw oscillation to the two axis motion. Normally, when the yaw axis oscillates at the same frequency as pitch and roll, the foil will follow an oval path. If the phase difference between roll and yaw is 90° or -90°, it will results in a semi-symmetrical oval path seen in the Chapter 3 (Figure 4-14). A +90° phase angle (i.e. 180° out of phase with pitch) will produce an oval path that moves the foil forward at the top of the flapping cycle and moves the foil backwards at the bottom of the flapping cycle. The reverse happens if the yaw motion has a -90° phase difference with roll (i.e. in phase with pitch). If the phase angles between roll and yaw were not ±90°, it will results in a tilted oval path (Figure 4-15 (Left)). A negative phase difference rotates the path anti-clockwise, while a positive phase difference rotates the path clockwise. In the special case when yaw motion is in phase or in anti-phase with roll motion (0° or 180°), the foil upstroke and the down stroke will overlap and create a slanted two axis flapping cycle actuation path (Figure 4-15 (Right)).

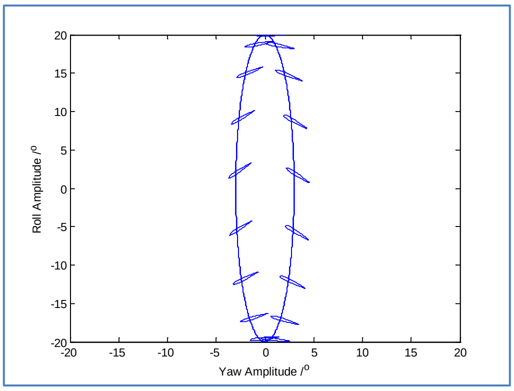

Figure 4-14 – Normal oval path – yaw has a 90° phase lead from roll

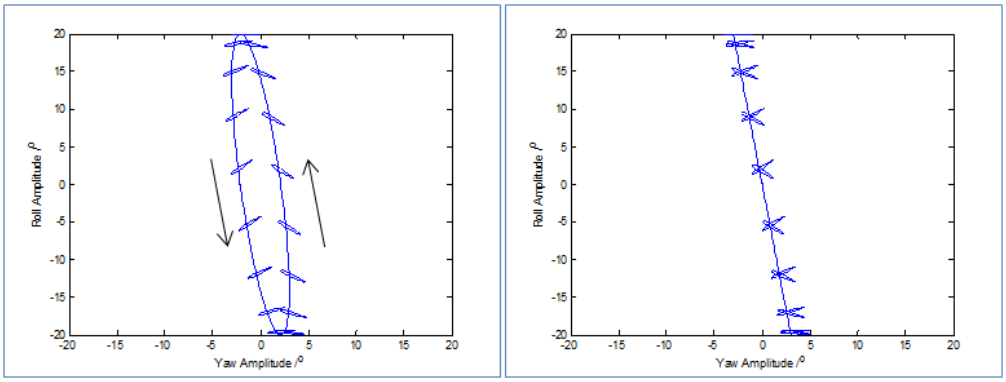

Figure 4-15 – (Left) Oval foil path rotation caused by a 135° phase lead between yaw and roll. (Right) oval foil path rotation caused by a 180° phase lead between yaw and roll.

The foil actuation paths and the corresponding angular positions for cases with yaw amplitude of 3°, 6°, and 10° are shown in Figure 4-16. It can be seen from the plots the yaw motions have a 90° phase lag compares to the pitch motions (or yaw 180° out of phase with roll). The slant angle of the path depends on the yaw and roll amplitudes, and it can be found by calculating the arctangent of the two (4-6). The three yaw amplitudes (3°, 5° and 10°) analysed in this investigation produce tilt angles of 8.5°, 14.0° and 26.7° respectively.

$$\gamma = arctan\left(\frac{\psi_0}{\phi_0}\right) \qquad (\ 4\text{-}6\ )$$

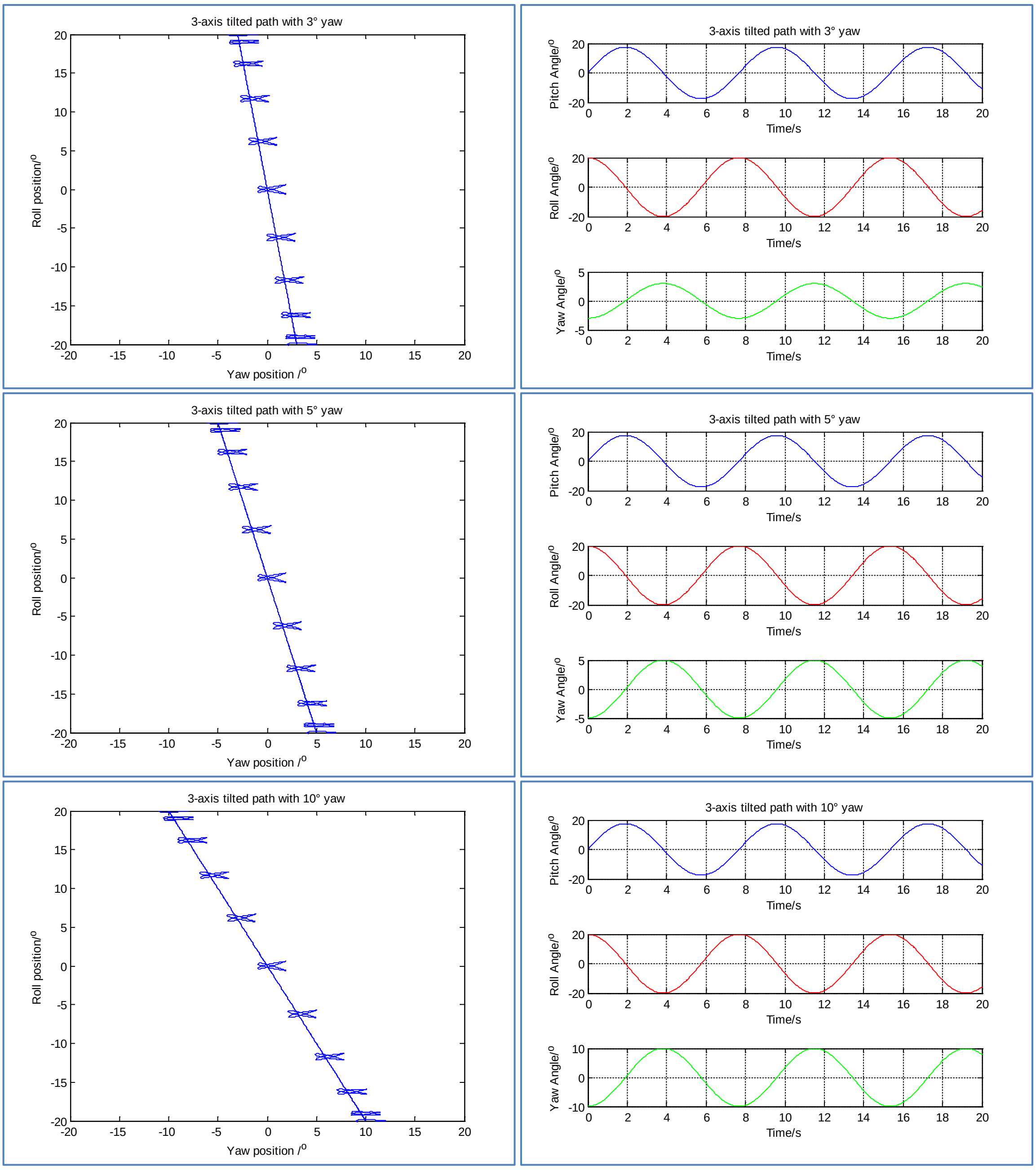

Figure 4-16 – Tilted foil path created by a combination of pitch roll and yaw. The yaw amplitude is 3°, 5°, 10°. ($St_{0.7} = 0.5,\ U = 0.1ms^{-1}$)

4.3.1 Foil Total Force

Due to the yaw motion, the foil advances forward in the up stroke and retreat backwards in the down stroke. This increases the up-stokes' inflow velocity and as a result more force can be produced. The total foil force of the three cycles with yaw amplitudes of 3°, 5° and 10° are plotted alongside the plot for the normal un-tilted two axis cycle in Figure 4-17.

As predicted, the plots show the up strokes can produce more horizontal thrust than the down strokes. The vertical forces are also affected, and the magnitudes of the vertical forces produced by the down strokes (up-force) are greater than the vertical forces produced by the up strokes. Superficially, these results resembled the forces produced by two-axis cycle with pitch angle bias, but the underlying mechanism is different. In cycles with two axis angle bias, the thrust differences are caused by differences in angles of attack between the up stroke and the down stroke. In the case of the tilted foil path, the thrust differences are caused by the variations in inflow velocity between the two strokes, which results in different inflow angles and angles of attack. Therefore the titled actuation paths produce different lift and drag forces between the up and down strokes due to a combination of different angle of attack and inflow velocity.

The differences in the vertical and horizontal force increases as the yaw amplitude increased. The angles of attack also affect the forces produced – the forces produced by the cycle with 20° angle of attack is very different between the up and down strokes, whereas the forces produced by the cycle with angle of attack of 50° were very similar between strokes.

There is another major difference between the forces produced by the three-axis actuated tilted foil path and forces produced by biased pitch angle beside the different mechanisms. The resultant vertical forces produced by flapping cycles with a pitch angle bias were all in the same direction across the range of angles of attack studied. The forces were either net up or net down. By contrast, the tilted foil path's resultant vertical force depends on the foil angle of attack and can be net up despite the tilt the direction of the propulsion path tilt. In other word, a forward tilted path can produce up thrust or down thrust.

The vertical force plots for the cycle with 3° yaw (Figure 4-17) shows in the cycles with 20° angle of attack produced 1.7 times more vertical thrust in the upstroke than the down stroke, resulting in a net down force, while the cycles with 50° angle of attack produced 1.2 times more vertical thrust in the down stroke than in the up stroke resulting in a net up force. When the angle of attack was 40°, the foil produces roughly the same amount of thrust in both up and down strokes. The difference between the two strokes increases when yaw amplitude is increased to 5° and the foil produces more force in the up stroke than the down stroke.

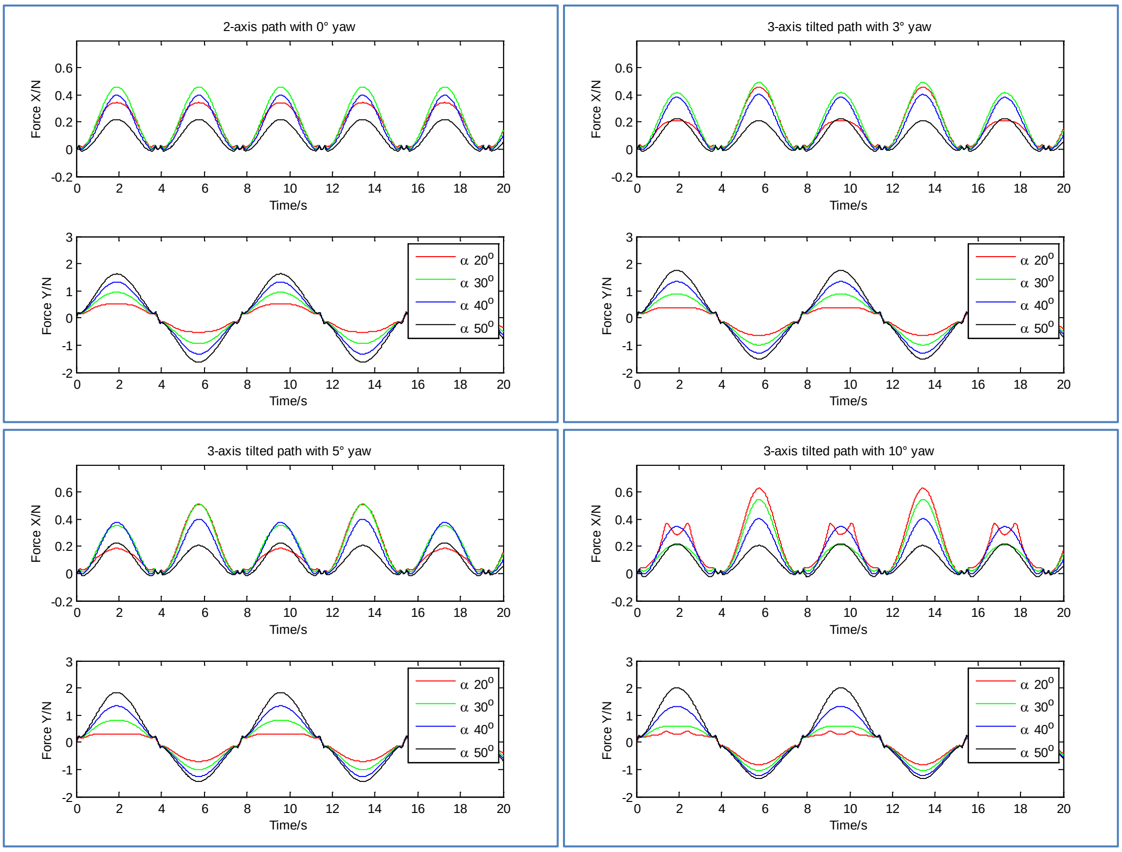

Figure 4-17 – Total foil force at different angle of attack for aquatic flight foil utilising tilted foil path. ($St_{0.7} = 0.5$, $U = 0.1ms^{-1}$)

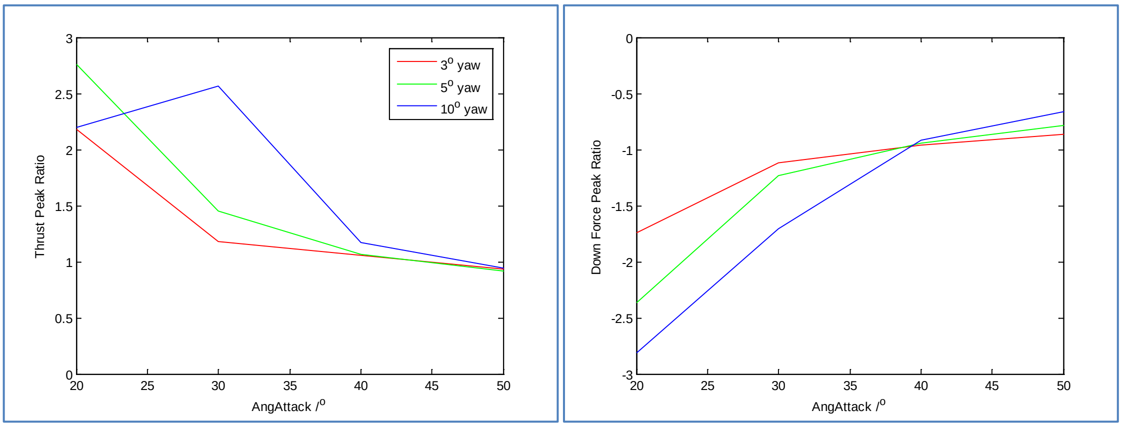

Figure 4-18 – Ratios between forces produced by the up-stroke and down-stroke.

The peak force ratios for the three yaw amplitudes are plotted in Figure 4-18. It shows the discrepancy in forces between the up stroke and down stroke are highest at lower angles of attack, but the magnitude decreases as the angle of attack increases. The differences in peak horizontal and vertical force between the two strokes at angle of attack of 20° are above 220% and (-)170% respectively. The differences between the two strokes reduce as angles of attack increase, and the ratios fell below a factor of ± 1 at angle of attack of 50°.

4.3.2 Thrust Coefficient

After looking at the thrust of individual cycles, the thrust coefficients across the analysis range is calculated and plotted in Figure 4-19. It can be seen from the plot the thrust coefficient decreases as the yaw angle increases, but the change is minimal for yaw amplitudes up to 5°. When the yaw amplitude was increased to 10°, the pattern of the thrust coefficient changed drastically. The thrust coefficients in the 10° case are much lower than that of the other cycles with smaller yaw amplitudes, and it can decrease quickly when the Strouhal number increased above 0.5 – 0.6. This is in contrast with the other cases where the thrust coefficients continue to increase as the Strouhal numbers increase.

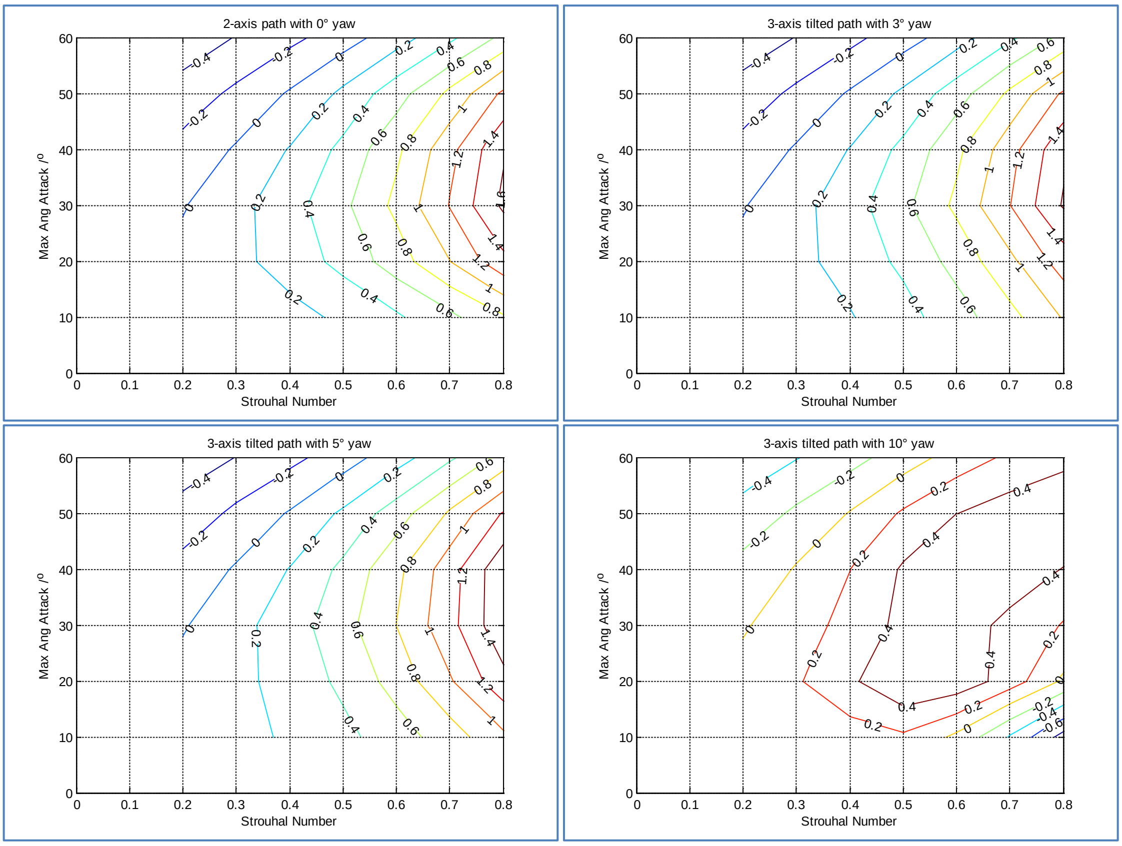

Figure 4-19 – Thrust coefficient produced by cycles with three axis tilted foil actuation path.

Cross-sections of the contour plots were taken for a more detailed comparison of the thrust coefficient at various angles of attack, as seen in Figure 4-20. The thrust coefficient for the cases with 3° and 5° yaw are very close to that of the normal two-axis cycle, but the thrust coefficient in the case with 10° yaw are only close to the other cases at lower Strouhal numbers and it deviated rapidly when Strouhal number increased above 0.5. The percentage errors for the cases with angle of attack of 40° are shown in Figure 4-21. The plot shows the differences between the normal cycle and cycle with yaw amplitudes of 3° and 5° were less than 2% for most of the analysis range. On the other hand, the differences between the normal cycle and cycle with 10° yaw can be higher than 55%.

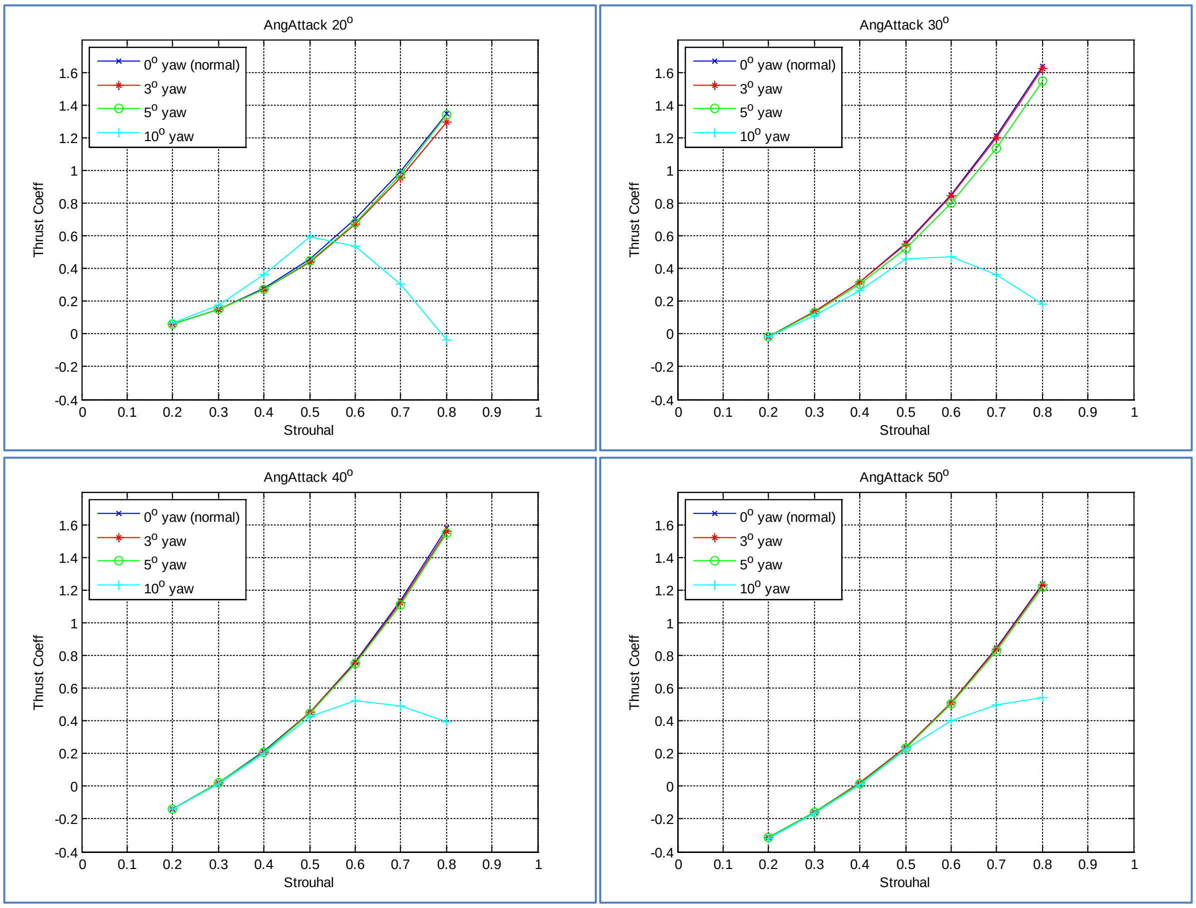

Figure 4-20 – Thrust coefficient comparison between foils with different yaw amplitude at various angles of attack

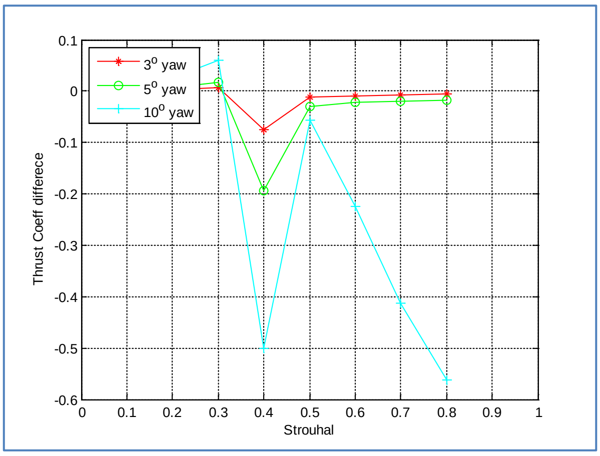

Figure 4-21 – Fractional differences between the thrust coefficient of the tilted cycles and the normal 2 axis cycle with no tilt. ($\alpha_{0.7} = 40$)

4.3.3 Vertical Force Coefficient

The tilted foil actuation paths' asymmetric strokes also produce net vertical force, which are non-dimensionalised into the vertical force coefficients as shown in Figure 4-22. The pattern shown by the cases with 3° and 5° yaw are very similar, but the cases with 10° yaw show a very different pattern. There is a zero contour line in each plot that represents the points where net vertical thrust of zero. If the angle of attack was set higher than this line, then the cycle will produce positive vertical force coefficient which indicate a net upward force. If the angle of attack is less than that indicated by the zero contour line the vertical force coefficient will become negative which indicates there is a net downwards force. The vertical force coefficients are about equally spread above and below the zero contours for the 3° and 5° cycles, but the 10° cycles show a different pattern. Whilst the 10° cycles can still produce net-up or net-down force, it can produce significantly higher positive vertical force coefficient (>3) than it is able to produce negative vertical force coefficient.

Figure 4-23 shows cross sections of the contour plots taken at four different angles of attack. At lower angles of attack such as 20° and 30°, the vertical force coefficients produced by the cycles with 3° and 5° yaw amplitude become more negative as the Strouhal number increases, but the cycles with 10° yaw amplitude behave differently. While initially the vertical force coefficient became more negative as the Strouhal number increases, it reaches a minimum point at Strouhal number of 0.5, where the vertical force coefficient begins to increase as the Strouhal number increases further. The vertical force coefficients became positive at soon after (~0.64 and ~0.58 for cycle with angle of attack of 20° and 30° respectively), and continue to increase much faster than the decrease in cycles with smaller yaw amplitudes. As the angle of attack increased to 40°, the vertical force coefficients for all three yaw amplitudes started as positive, but increases in Strouhal numbers gradually decrease the coefficient and it became negative at Strouhal number over 0.7. The 10° cycle is the only exception, the downward decreasing trend is reversed at Strouhal number of 0.5 and the vertical force coefficient became positive very quickly. When the cycle's angle of attack reached 50°, the vertical force coefficients for the cycles with 3° and 5° yaw gradually increase as the Strouhal number increased, but at a much slower rate than the increased seen in the cycle with 10° yaw.

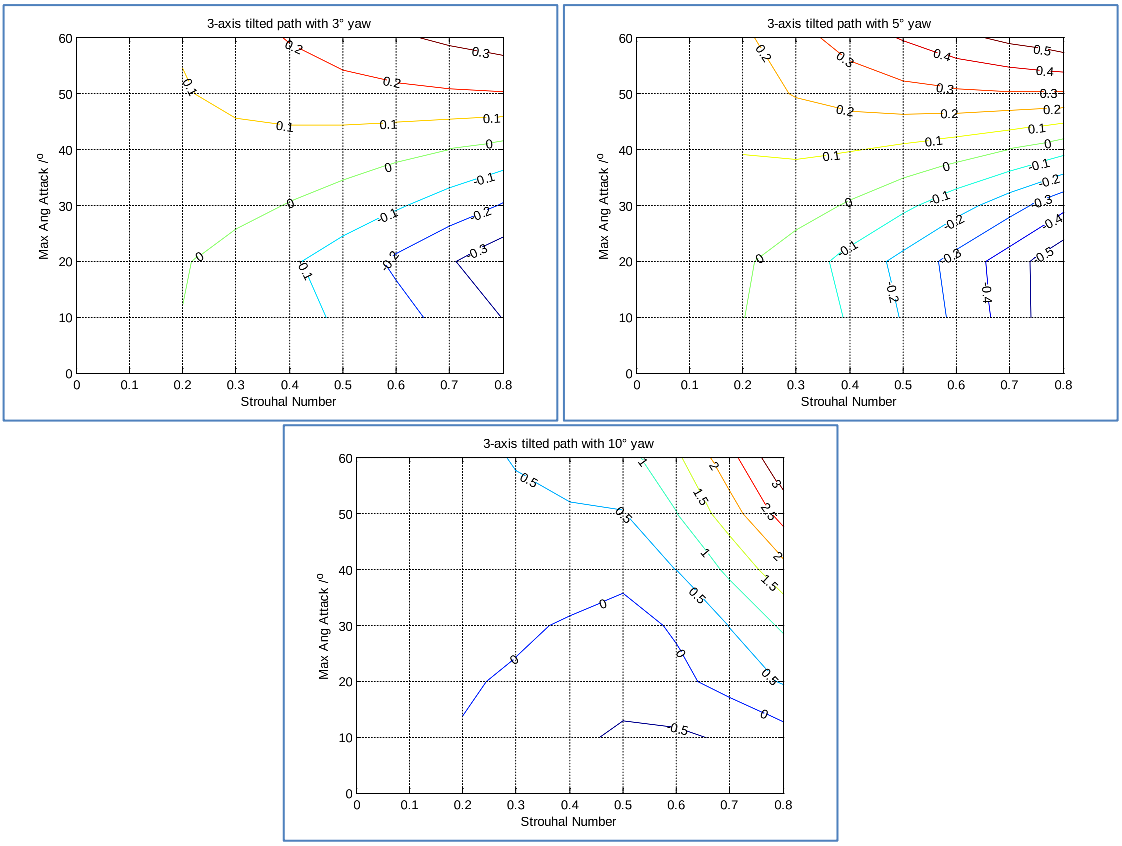

Figure 4-22 – Vertical force coefficient produced by cycles with three axis tilted foil actuation path.

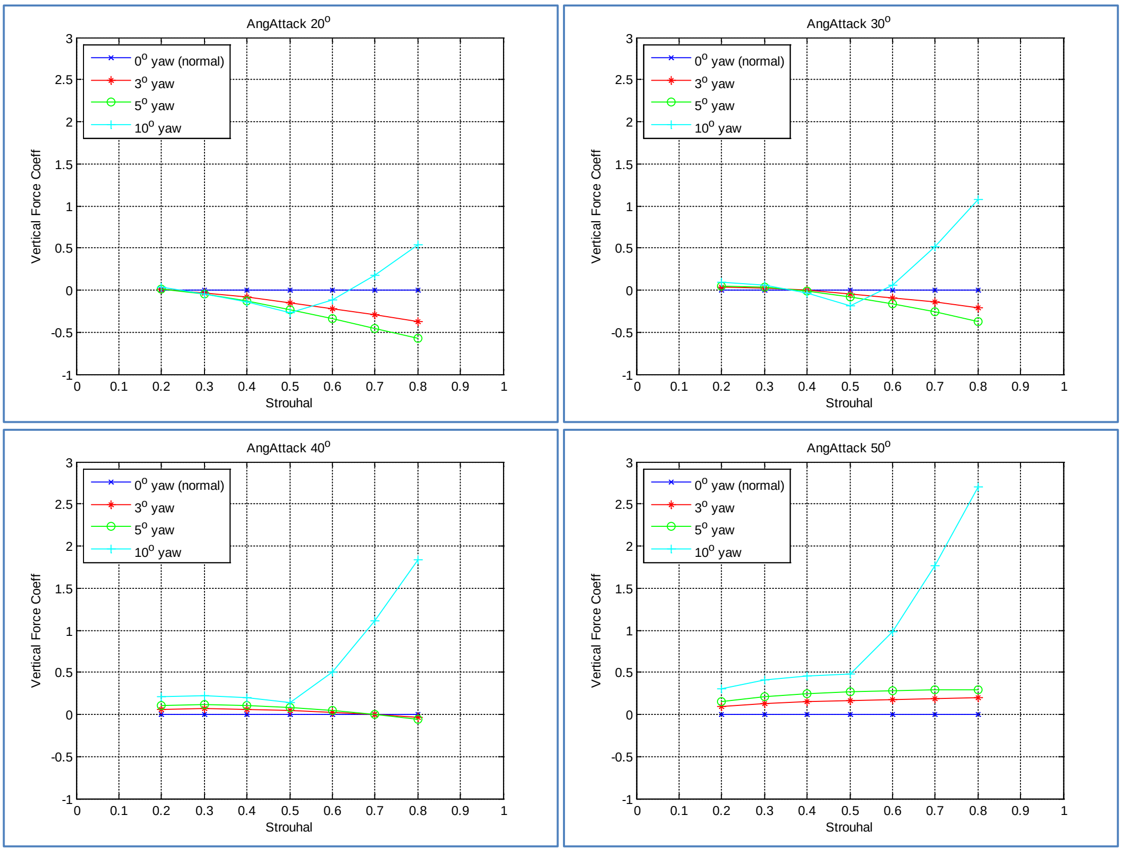

Figure 4-23 – Comparison of the vertical force coefficient between foils with different yaw amplitude at various angles of attack

4.3.4 Vertical Force Coefficient – Thrust Coefficient Ratio

The vertical force coefficient to thrust coefficient ratio was calculated to determine how these two forces are distributed by the three axis actuation path. The results are plotted in a logarithmic graph in Figure 4-24. Unlike the previous cases with two-axis pitch bias, the plot show most of the cycle produces more horizontal thrust than vertical thrust. Generally VFC/TC ratio increases as the yaw amplitudes increase. The troughs observed in the 30° angle of attack plot at Strouhal number of 0.4 and the troughs observed at 0.7 for the 40° angle of attack plot are caused by the proximity to the zero vertical force coefficient line at these Strouhal number. Likewise, the peaks observed at Strouhal number of 0.3 for the 40° angle of attack plot and at Strouhal number of 0.4 at the 50° angle of attack plot are caused by its proximity to the zero thrust coefficient lines. Cycles operating with 20° angle of attack have the lowest variation in the VFC/TC ratio, and the vertical forces were between 10%-50% of the horizontal thrust for most cases. By contrast cycles with 40° operating angle of attack have the largest variation, where the vertical force can range from 1400% (10° yaw, $St = 0.3$) to 0.03% (3° yaw, $St = 0.7$) of the horizontal thrust.

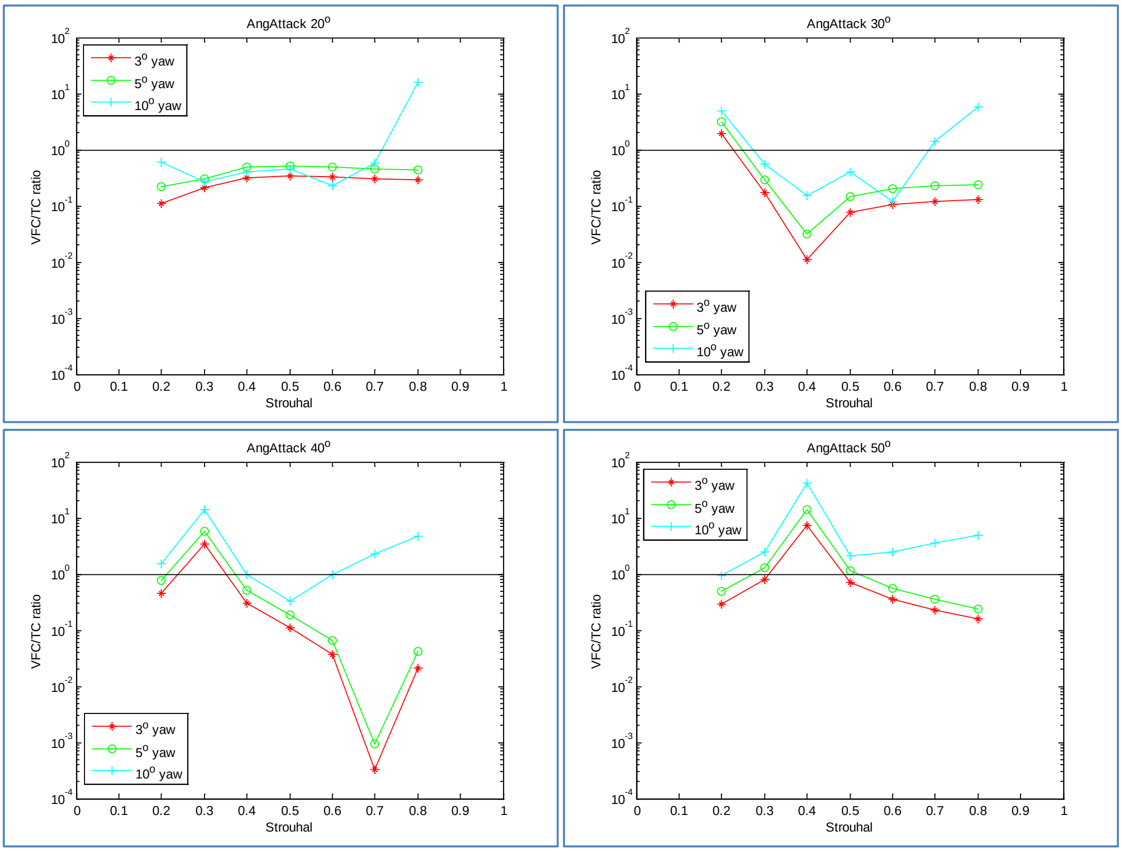

Figure 4-24 – Vertical force coefficient to thrust coefficient ratios at four different angles of attack (logarithmic)

4.3.5 Combined Force Coefficient

The total resultant force from the horizontal thrust and vertical force are non-dimensionalised into the combine force coefficient and the result is plotted in Figure 4-25. Whilst the horizontal thrust coefficient contour plots for the cycles with yaw amplitude of 3° and 6° looks similar to the plot for the normal two axis cycle, the combined force coefficient plots show a shift in the contour line due to contributions from the net vertical force. In particular, the contour line representing a coefficient of 0.2 changed direction when the operating angle of attack exceeded 50° and 40° for the cycles with 3° and 5° yaw.

Whilst the cases with yaw amplitudes of 3° and 5° still preserved the curved shape of the normal two-axis cycle's plot when the combined force coefficient was higher than 0.6, the shape of the contour plot for the cycle with 10° yaw looks very different. Instead of reaching an optimum at around the 30° angle of attack, the highest combined force coefficient in the case with 10° yaw is achieved when both angle of attack and Strouhal number are at their maximum. The maximum combined force coefficient also increased by a significant amount (> 3.0) compared to the cases with lower yaw amplitudes (< 1.6).

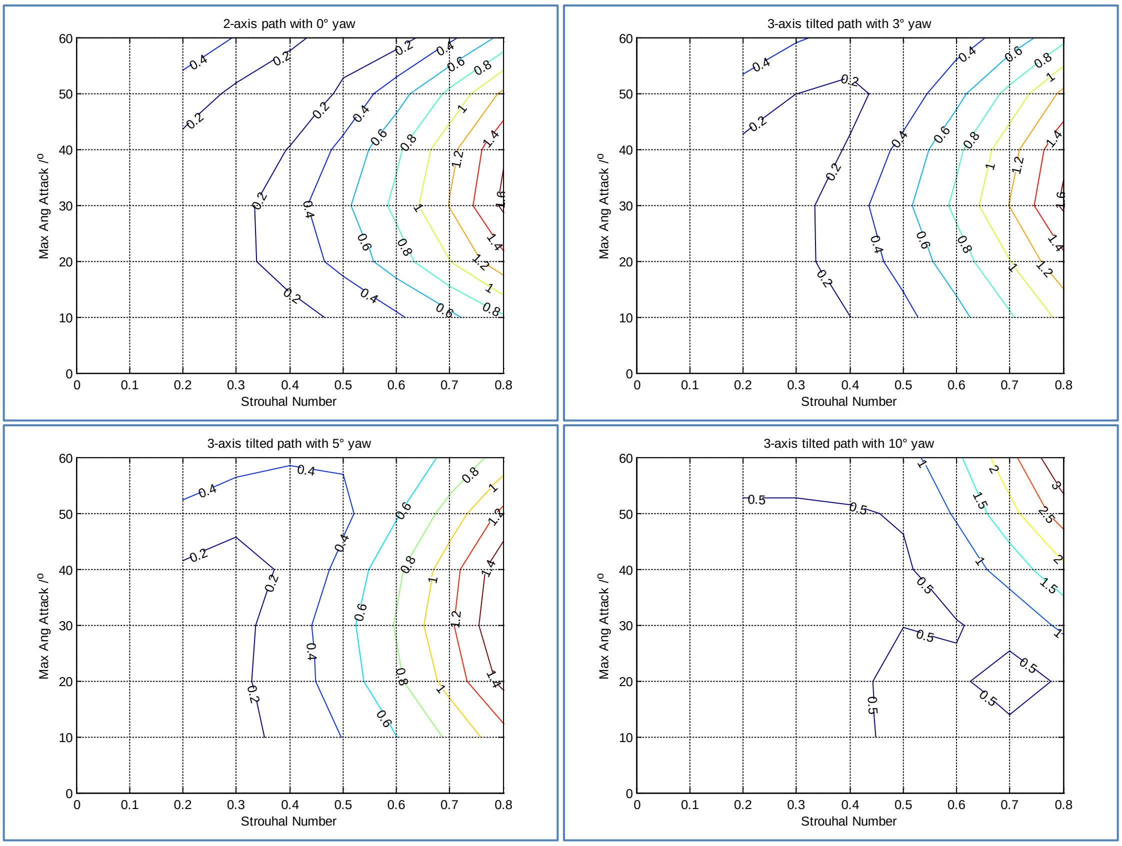

Figure 4-25 – Combined force coefficient from cycles with three axis tilted foil actuation path.

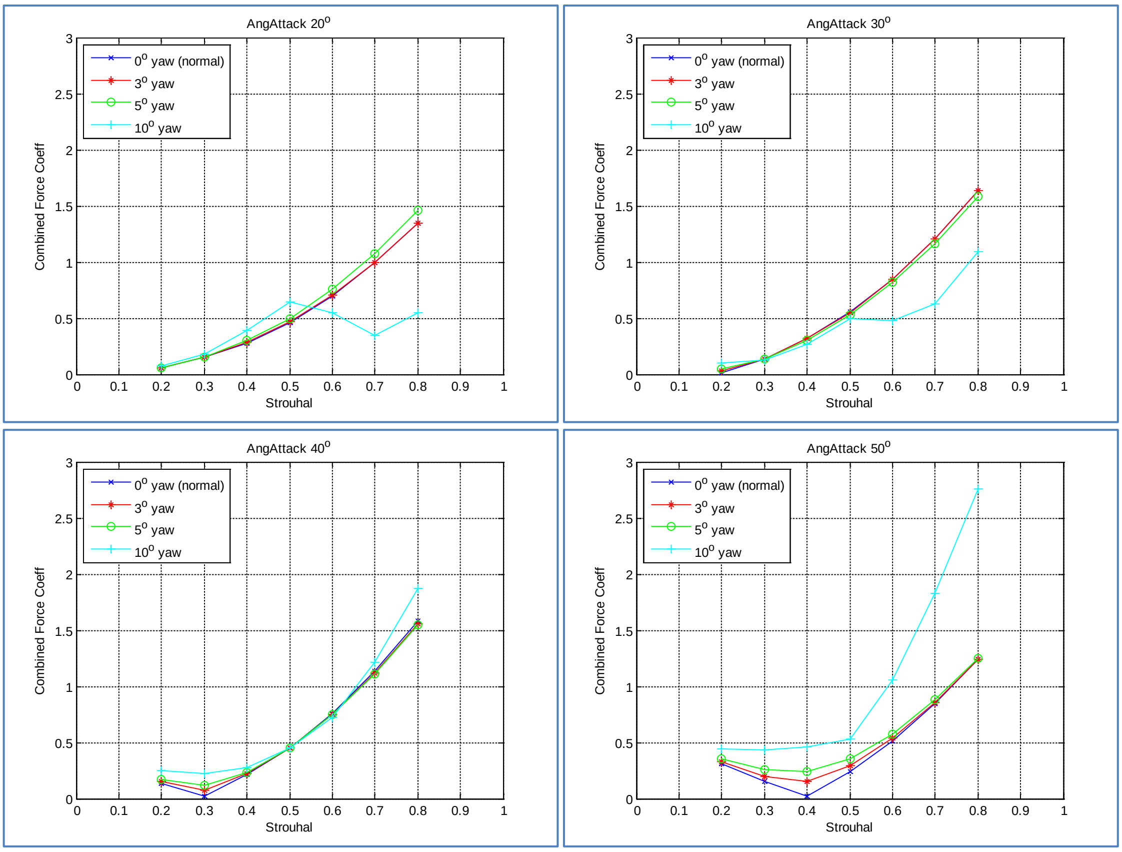

Figure 4-26 – Comparison of the combined force coefficient between foils with different yaw amplitude at various angles of attack

More detailed analysis of the combined force coefficient can be carried out by looking at the cross sections of the contour plots, which are shown in Figure 4-26. The plots show the combined force coefficient lines for the cycles with 3° and 5° yaw are very closed to the lines for the two-axis cycle at angle of attack of 20° and 30°. When the operating angle of attack reached 40° and 50°, the combined force coefficients initially diverged from the results of the two-axis cycle at lower Strouhal number, but then re-converged as the Strouhal number increases. The cycles with 10° yaw diverge from the two-axis line quickly at lower Strouhal number and changed direction all together when Strouhal number exceeded 0.5. It continues to diverge as the Strouhal numbers increase above 0.5. The significant change observed in the plot for cycles with 10° yaw is cause by the significant increase in the contribution from the vertical force coefficient compared to other cycles with smaller yaw amplitudes. The change in direction observed at Strouhal number of 0.5 is also the result of a shift in the down force produced.

4.3.6 Summary of three axis slanted actuation path

Analysis of the tilted foil actuation path found the foil horizontal thrust coefficient is not significantly affected by the yaw motion. The differences between the cycles with yaw amplitudes of 3° and 5° and the normal two-axis cycle are less than 2%. Meanwhile the flapping cycle can produce useful vertical force that can be used for maintaining depth. However, if the yaw amplitude was too high, such as in the cycles with yaw amplitude of 10°, the thrust coefficient can drop off quickly at higher Strouhal numbers but the vertical force coefficient can also increase quickly. The vertical force coefficients for most cycles are less than 100% of the horizontal thrust coefficient. The exact ratio between the two forces are dependent on the yaw amplitude, Strouhal number and angle of attack, but generally as yaw amplitude increases, the vertical force coefficient would follow.

The combined force coefficient for the tilted foil actuation path is higher than that of the normal two-axis cycle, which shows thrust is not simply diverted into the vertical direction. Instead it shows the yaw motion generated additional thrust. In particular the combined force coefficients of the 10° cycles are much higher than the other cycles with smaller yaw amplitudes. Such cycles can be useful if the vehicle need to change depth or manoeuver quickly.

4.4 Three Axis Full Rotation with Pitch Offset

The third type of asymmetric aquatic flight stroke path to be examined is the stroke path with full rotation. The previously analysed slanted actuation path was produced by a combination of row and yaw motions, but the phase of pitch motion remained unchanged, so the pitch angle remained zero at the top and bottom of the flapping cycle. The investigation into full rotation path adds a pitch angle offset such that the pitch angle at the apex of each stroke will be perpendicular to the tilted foil path. The roll amplitude is also reduced such that the full stroke will sweep amplitude of 20°, effectively rotating the normal two axis cycle by a certain amount. This is similar to the action of a steerable thruster or a vehicle operating in a cross flow. The model analysed four yaw amplitudes (3°, 5°, 8° and 10°), which represents a rotation of 8.6°, 14.5°, 23.6° and 30°. The foil's position in pitch, roll, and yaw, as well as the actuation paths for three cases are shown in Figure 4-27.

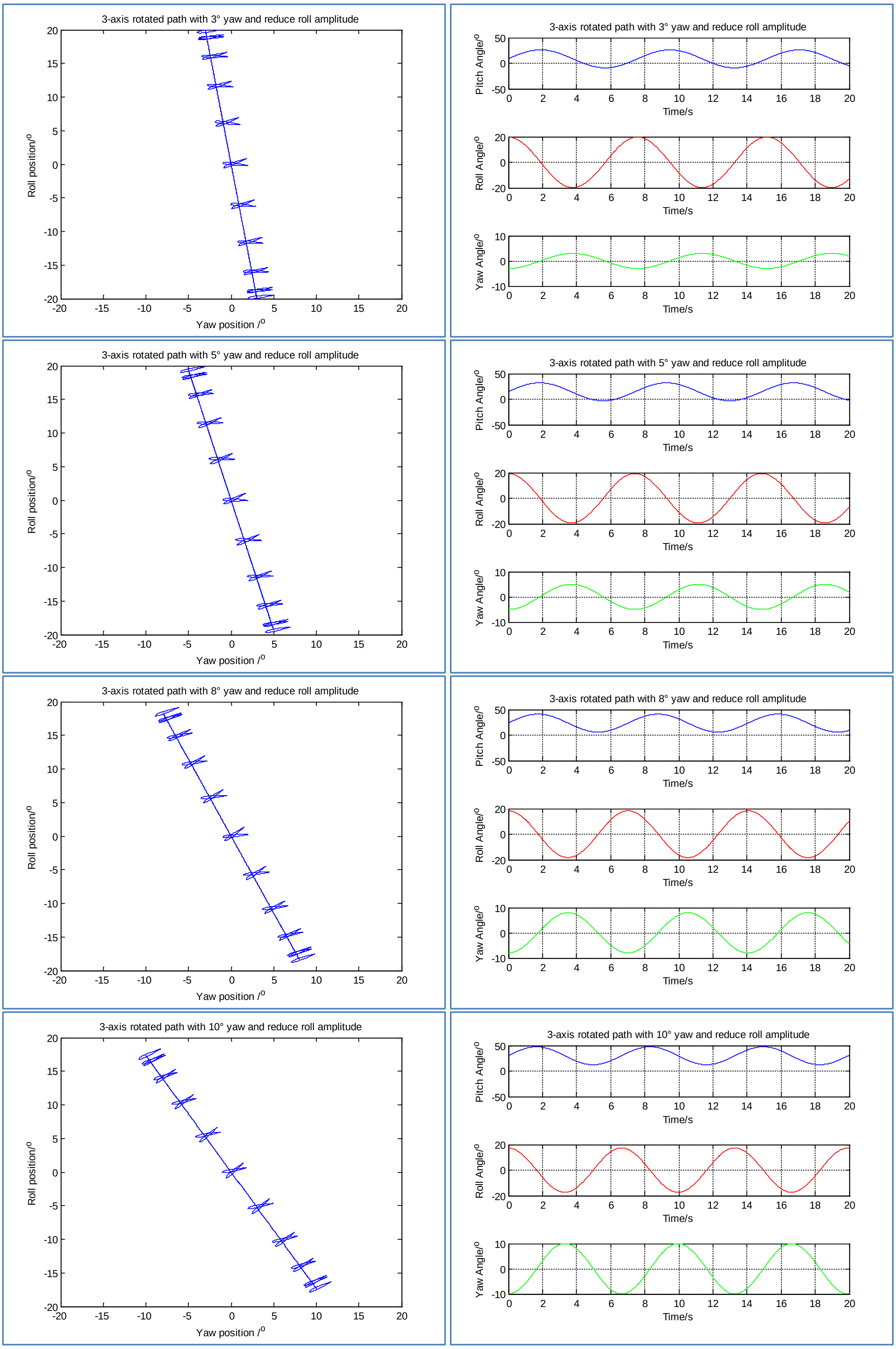

Figure 4-27 – Foil actuation path and the angular position of pitch roll and yaw during a rotated flapping cycle pitch bias and reduced roll amplitude. The flapping amplitude is maintained at a constant 20°.

4.4.1 Foil Total Force

The actuation path rotation with pitch bias caused a significant change to the way force is produced. The total foil forces for cycles with yaw amplitudes of 5° and 10° are plotted in Figure 4-28 for four different angles of attack. In all previous scenarios, forward thrusts are produced in both up and down strokes, but this is changed in cycles with rotated actuation path with pitch bias. One of the cycles with yaw amplitude of 5° (cycle with 20° angle of attack), and all cycles with yaw amplitude of 10° have one stoke producing positive forward thrust and another producing negative reverse thrust (drag). The reverse thrust is often comparable in magnitude to the forward thrust and in many cases it is the bigger of the two. The problem is more pronounce for the cycles with 10° yaw where the cycle reverse thrust can be much higher than forward thrust. This is an indication that the inflow angle exceeded 90° and the foil is producing thrust in the reverse direction.

The vertical thrust also did not follow the normal pattern where the down stroke produces upwards force and up stroke produces downwards force. The plots show in some cases both up and down strokes will produce a negative vertical force that will push the vehicle downwards, such as the cycle with yaw amplitude of 5° and angle of attack 20°. This means the vertical force will increase by a significant amount, because the forces from up and down strokes reinforce each other rather than cancel out. This may be useful if the vehicle needs to ascend or descend quickly.

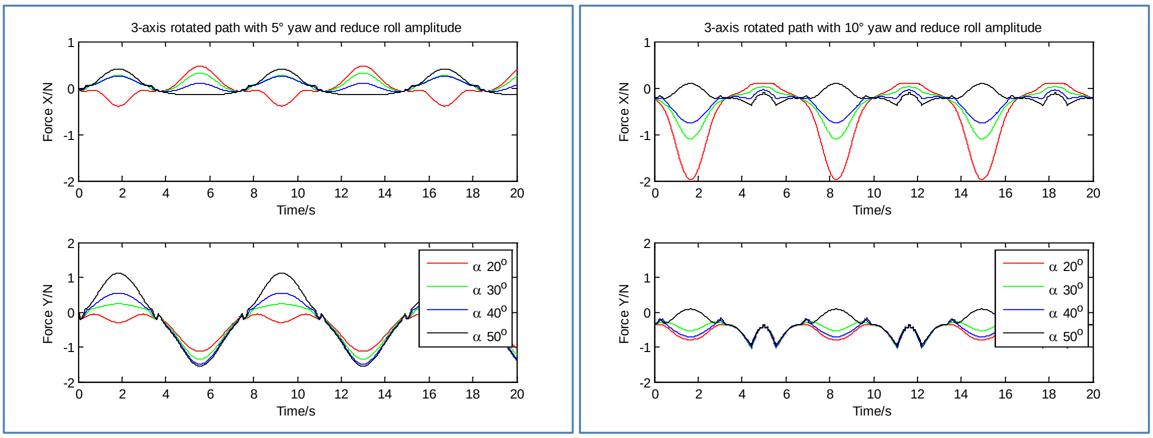

Figure 4-28 - Total Force produced by rotated foil actuation path ($St_{0.7} = 0.5,\ U = 0.1ms^{-1}$)

4.4.2 Thrust Coefficient

The thrust coefficients of the rotated paths are shown in Figure 4-29 as contour plots. It can be seen the thrust coefficients plots gradually changes from the curved shaped forward thrust dominated plot to the reversed thrust (drag) dominated thrust coefficient plot as yaw amplitude increases. Cross sections of the contour plots are shown in Figure 4-30. They show the thrust coefficient for the normal two axis cycles (i.e. no rotation) are the highest among all of the cases examined, and the thrust coefficient gradually decreases as the yaw amplitude increases. The cycles with 8° and 10° yaw amplitude also show a different trend compared to the other cases with smaller yaw amplitudes. At smaller angles of attack, the thrust coefficients of cycles with these two amplitude decrease as Strouhal number increases, which is opposite to the trend shown by the other cycles. As angle of attack increases further, the magnitudes of the negative thrust for cycles with 8° and 10° amplitudes decrease, but the thrust coefficients remained negative in all but two of the cases examined. The two cases which was able to produce positive thrust were two cycles with 8° yaw amplitude, high Strouhal numbers (>0.7) and high angle of attack (50°).

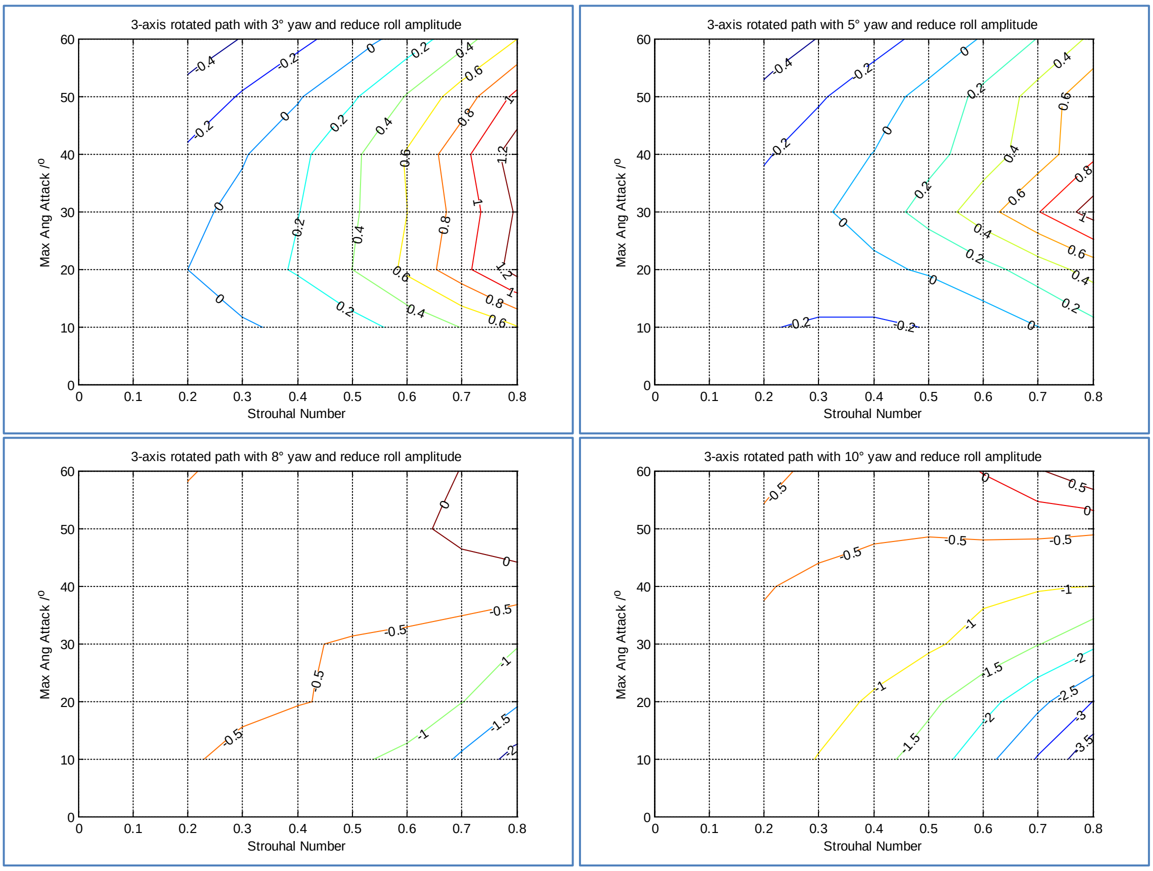

Figure 4-29 – Thrust coefficient of a rotated actuation path with pitch bias and reduced roll amplitude

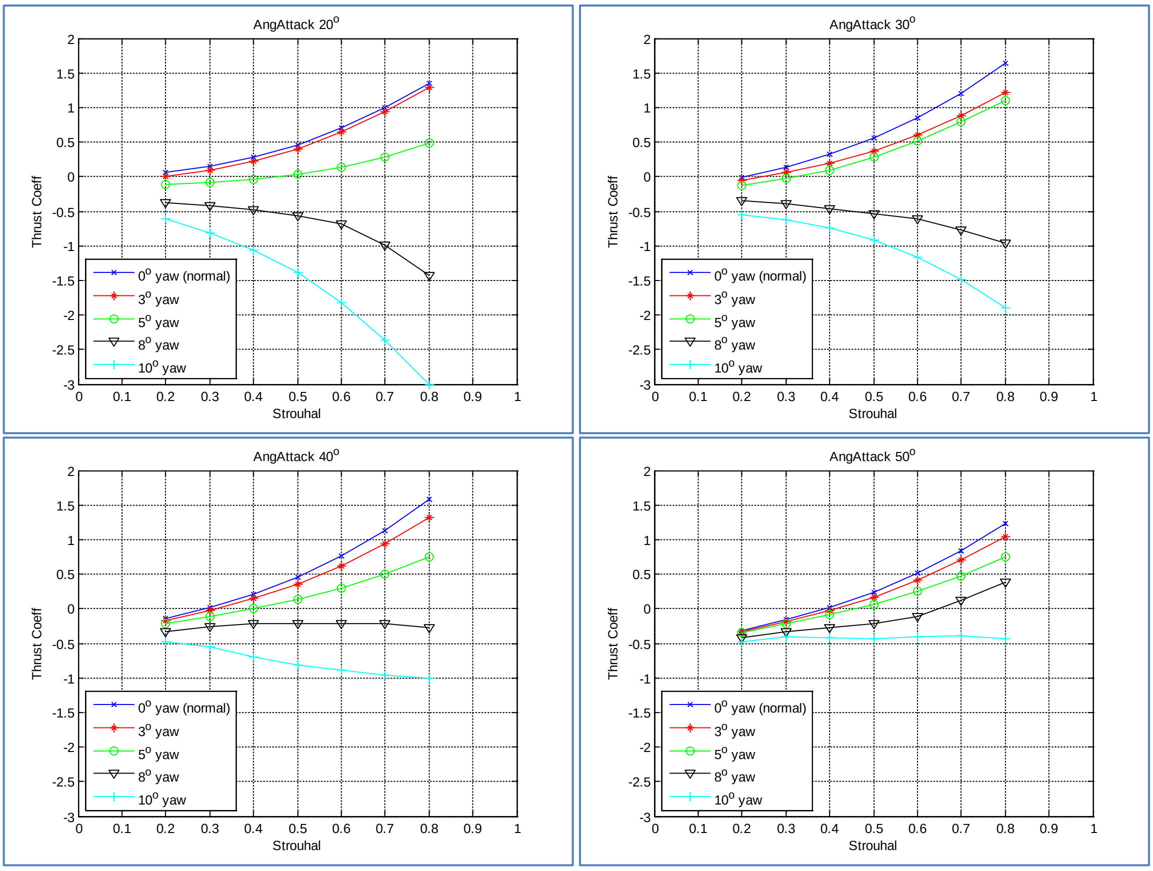

Figure 4-30 – Cross sections of the thrust coefficient contour plot at four different angle of attacks

4.4.3 Vertical Force Coefficient

The vertical force coefficients of the rotated path with reduced roll amplitude are shown in Figure 4-31. The patterns shown by the contours are similar to that of the fully rotated actuation path with normal 20° roll amplitudes. The vertical force coefficients are negative in all of the cases examined, except at very high Strouhal numbers and angles of attacks for the cases with 10° yaw. Cross sections of the vertical force coefficient plots were taken and plotted in Figure 4-32. Like the thrust coefficient, the results for cycles with 3° and 5° yaw again show a different pattern to the results for cycles with 8 and 10° yaw. The former becomes increasingly negative as the Strouhal number increases, while the coefficients for the latter first decrease as Strouhal number increases but then change direction at Strouhal number between 0.5 and 0.6. After that point the 8° and 10° cycles’ vertical force coefficients acquire a positive gradient which increase as Strouhal number increases.

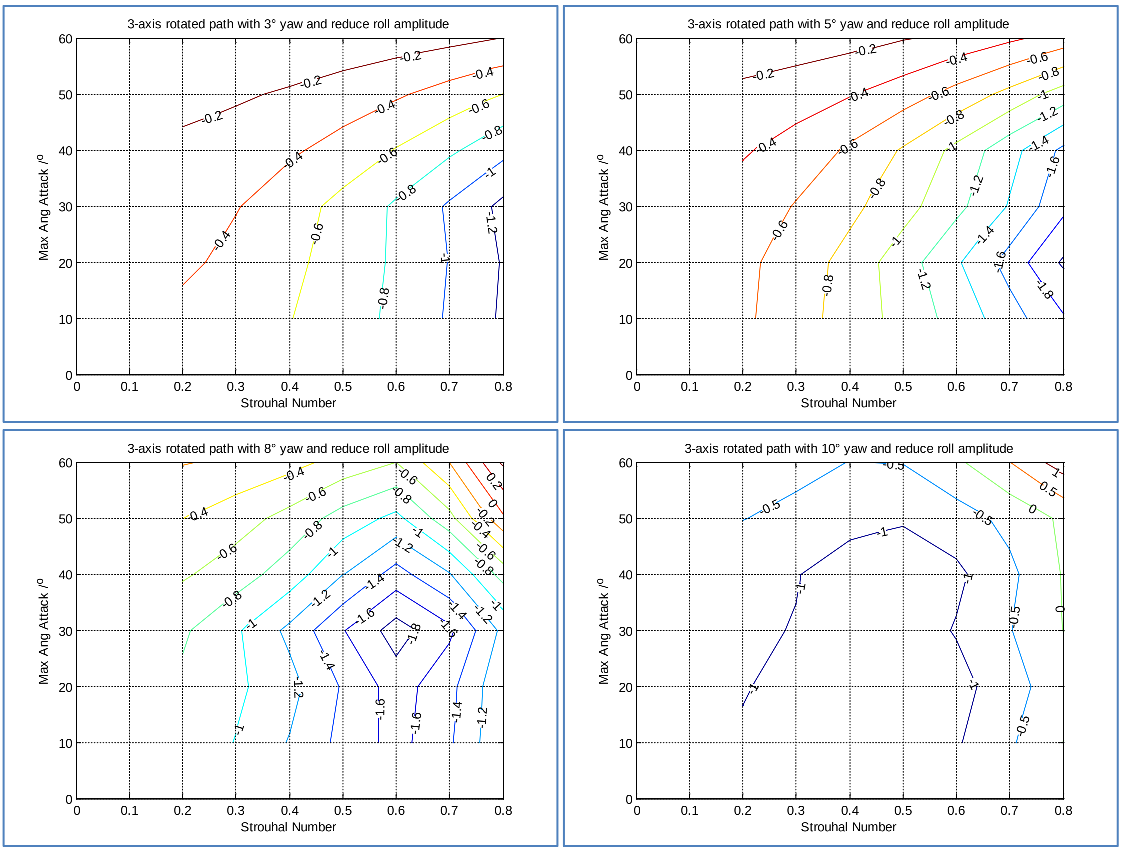

Figure 4-31 – Vertical force coefficients of rotated actuation path with pitch bias and reduced roll amplitude

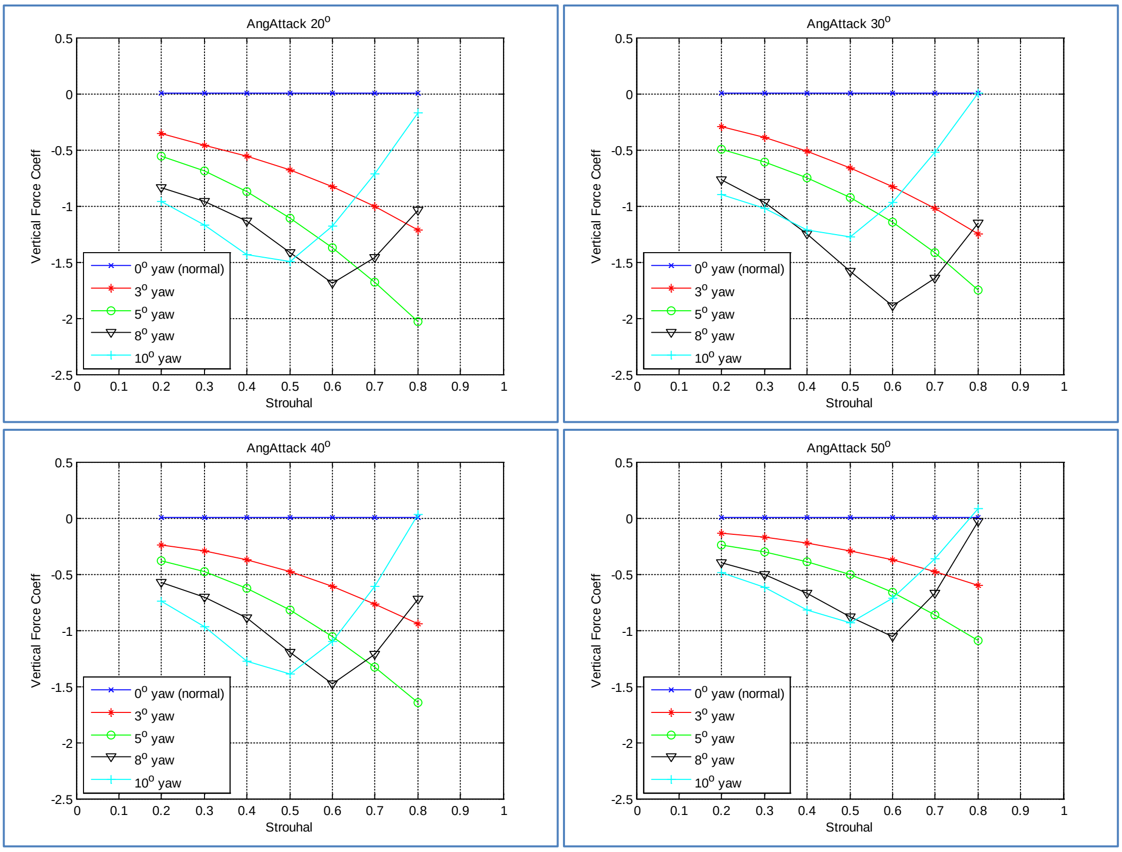

Figure 4-32 – Cross sections of the vertical force coefficient plot at four different angle of attack

The plots also show the vertical force coefficients increase as the yaw amplitude increases at lower Strouhal numbers. However, the gradient of the vertical force coefficients for the cycles with 8° and 10° yaw change sign at mid Strouhal number, and the magnitude of the vertical force coefficients for larger yaw amplitudes decrease as Strouhal number increases. At Strouhal number of 0.8, the 10° cycles have the smallest vertical force coefficients followed by the 8° cycles. Since the 3° and 5° cycles did not have similar changes in their gradient, the 5° cycles have the largest vertical force coefficient at Strouhal number of 0.8.

4.4.4 Vertical Force Coefficient to Thrust Coefficient Ratio

The vertical force coefficient to thrust coefficient (VFC/TC) ratios for the rotated actuation paths with pitch bias and constant amplitude are plotted in Figure 4-33. The plots show the vertical force are higher than the horizontal thrust for the majority of the cases except for a few cases at Strouhal number higher than 0.6. The cycles with yaw amplitudes of 10° have the lowest ratio followed by the cycles with yaw amplitudes of 3°. The ratio for the cycle with yaw amplitude of 5° are always higher than 1.0 (10^0) which means the vertical force coefficients for the 5° cycles are always larger than the horizontal force coefficients.

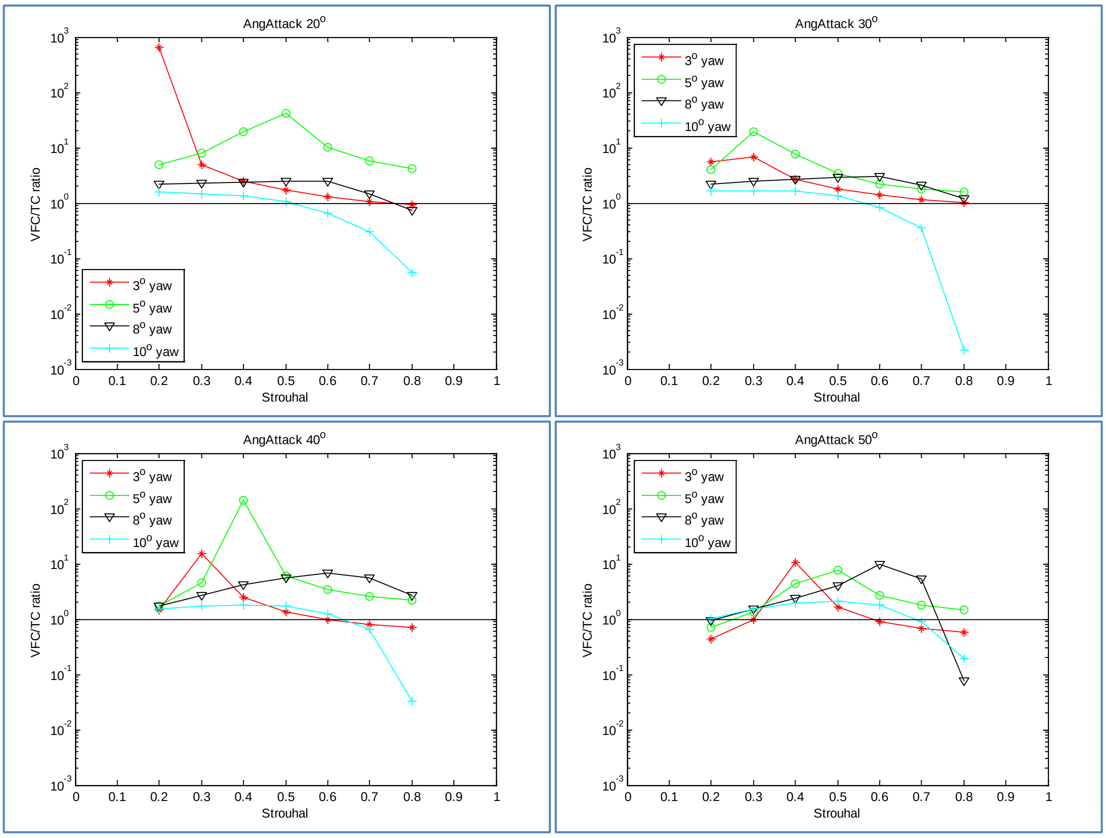

Figure 4-33 – Vertical force coefficient to thrust coefficient ratio

Meanwhile, the cycles with yaw amplitudes of 10° have very small VFC/TC ratio at the highest Strouhal numbers, which means the horizontal thrust is much higher than the vertical force. However, the horizontal thrust coefficients for the 10° yaw cycles are mostly negative, which means the foil is producing a lot of reverse thrust/drag without useful vertical force.

4.4.5 Combined Force Coefficient

As well as analysing the ratio between the vertical force and horizontal thrust, the combined force of the rotated cycles with reduce roll amplitude were calculated and plotted in Figure 4-34. The pattern shown by the plots resembles those shown by the rotated cycles without roll amplitude reduction. Like the latter, the combined force coefficient contour plots for cycles with smaller yaw amplitudes (less path rotation) resemble that of the normal two-axis cycle, but the discrepancy increased as the yaw amplitude increased.

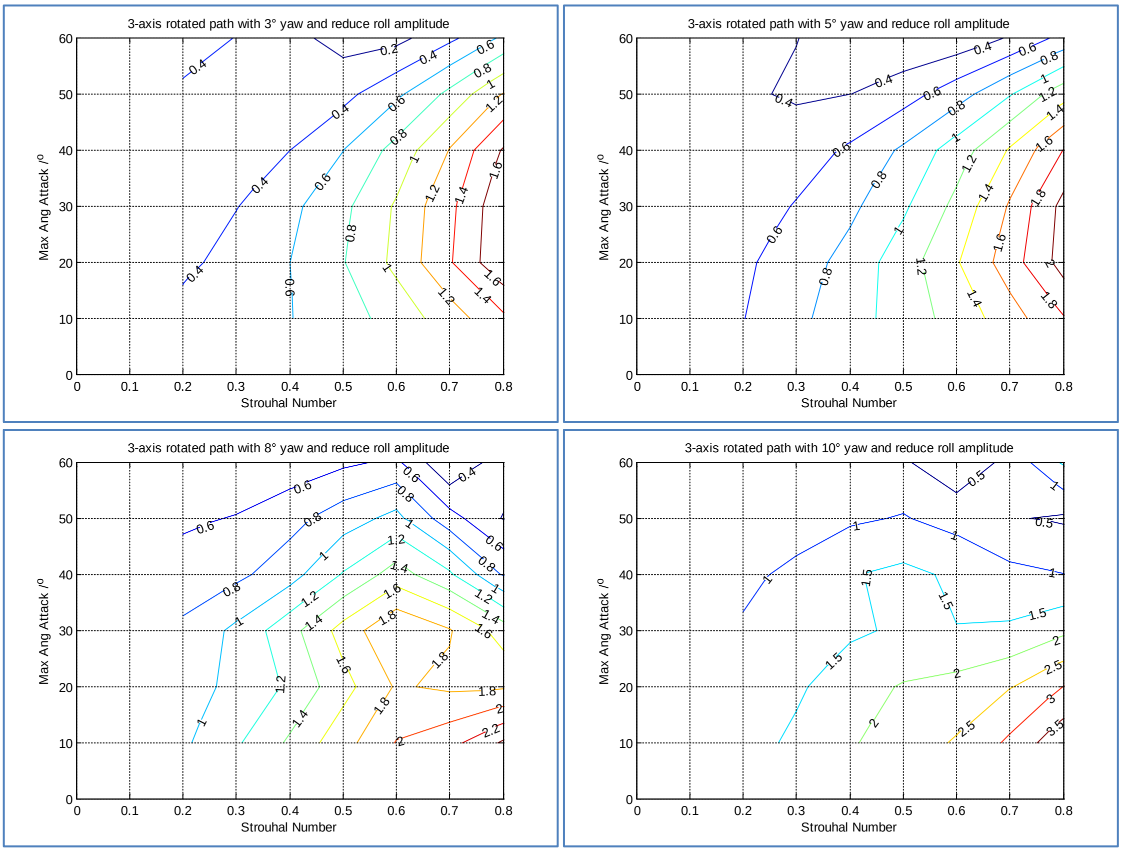

Figure 4-34 – Combined force coefficient of rotated actuation path with pitch bias and reduced roll amplitude

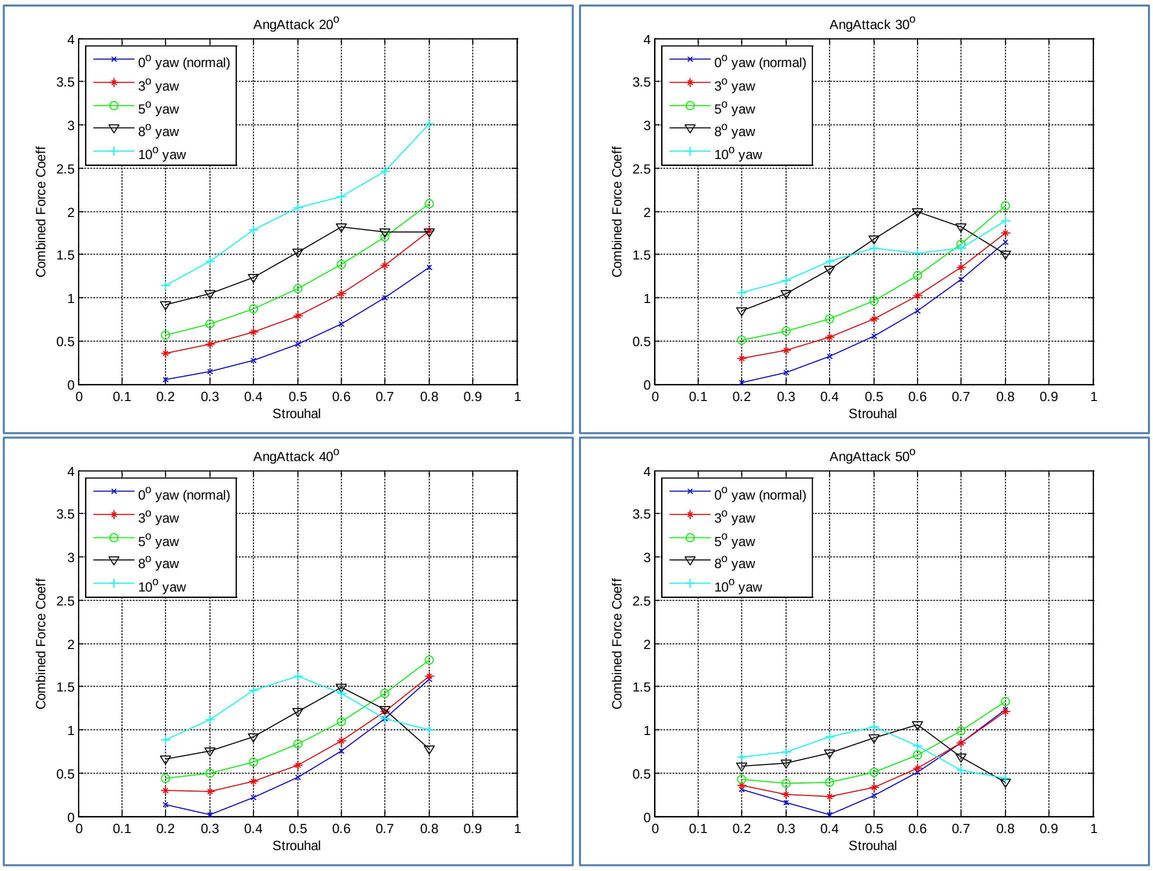

Figure 4-35 - Cross sections of the combined force coefficient plot at four different angle of attack

Cross sections of the contour plots were taken and plotted in Figure 4-35. The plot show the combined force coefficients for the cycles with 3° and 5° bias resemble the results of the two-axis cycle, and the coefficients increase as the Strouhal number increases. The combined force coefficient for the 8° and 10° cycle follow a different pattern. The combined force coefficient for the 8° cycle began following a similar pattern to the cycles with smaller yaw amplitude, but there is a sharp change in gradient at Strouhal number of 0.6 where the upwards increasing gradient is replaced by a downwards gradient. The combined force coefficients then decrease as the Strouhal number increases, and at higher angles of attack the combined force coefficients of the 8° and 10° cycle can fall below the coefficient for the two axis cycle.

4.4.6 Summary of three axis rotated actuation path

The three-axis rotated actuation path can represent two common situations, one is when the flapping foil propulsor utilise this path to simulate a steerable thruster to produce manoeuvring thrust, and the other is when the whole vehicle operates at an angle to the inflow current. The analysis of this path shows it can produce significant amount of down force. The vertical down force produced by the tilted actuation path with pitch bias is higher than those from cycles with slanted actuation path but no pitch bias, and for most cases the vertical force is also higher than the horizontal thrust.

The increased pitch bias also significantly reduces the horizontal thrust produced by the cycle, to the extent that many cycles produces net reverse thrust. This will quickly slow the vehicle, making this stroke less useful for the travelling AUV than the strokes without pitch bias. The combined force coefficients for the rotated path are higher than the coefficients from the two-axis cycle, and it shows greater variation in magnitude compared to the cycles from tiled actuation path without pitch bias.

When a propeller based thruster operates at an angle to the water flow, the general direction of the jet can be determined fairly easily. The thruster output of the angled propeller varies in a fairly predictable manner as the thruster angle changes. By contrast, the direction and magnitude of the thrust produced by a flapping foil propulsor varies depending on the pitch angle bias, the roll and yaw amplitudes, angles of attack and Strouhal number. A large number of cycles cannot produce forward thrust, so this type of stroke is more likely to be used for manoeuvring than maintaining depth.

4.5 Summary

The study into aquatic flight with asymmetric stroke examined several changes to the normal aquatic flight motion to analyse their usefulness for producing manoeuvring thrust. These include a two-axis actuation path with pitch angle bias, the three-axis slanted actuation path and the three-axis rotated actuation path as well.

The two-axis asymmetric aquatic flight studies analysed the effect of introducing pitch angle bias into the aquatic flight motion. The analysis showed the pitch angle bias can be used to generate useful lift/down force which can be used for depth control, pitch control and roll control. The studied also briefly investigated the phase bias but found it had limited used for AUV manoeuvring as it does not produce any net lift or down force.

Three-axis motion involves pitch, roll and yaw so it can perform many different gaits, each with a different set of manoeuvring characteristics. Therefore it will be necessary to restrict the analysis to a small sub set of gaits. The analysis into three-axis vectored thrust investigated two type actuation paths, the first used the yaw and roll motion to create a forward tilting actuation path. A 180° phase offset was set between roll and yaw such that the foil path moves along the same line in both the up stroke and the down stroke, essentially producing 2.5-axis aquatic flight. The second 3-axis analysis built on the first and added a pitch angle bias to the pitch motion such that the foil chord will be perpendicular to the actuation path at the end of each stroke. It also reduced the roll amplitude such that the full stoke amplitude remains 20°. The analysis found the slanted actuation path without pitch bias can generate a small amount of net vertical thrust with very little loss to the horizontal thrust output. The second type of actuation path greatly increased the vertical force coefficient, but also results in a more significant reduction in the horizontal thrust coefficient.

In summary, in addition to the horizontal propulsive thrust, the two-axis cycle with pitch angle bias and the two three-axis cycles with tilted action paths can produce useful vertical force that can be used for manoeuvring. Since, an aquatic flight propelled vehicle have at least two a winged propulsors – one on each side of the vehicle, they can be used to control the vehicle’s depth, pitch, and roll depending on how the pair of foil work together. The vehicle can also combines the roll and pitch control to execute rapid change of direction, by first rolling the vehicle to the side with asymmetric stokes from each actuator, then synchronise the strokes to rapidly pitch up/down.

Page intentionally left blank

Chapter 5: NIMBLE Experiment Design

5.1 Introduction

This chapter outlines the design philosophy for the Nature Inspired Manoeuvrable Bio-Locomotion Experiment (NIMBLE) test rig for three-axis aquatic flight. This test rig was designed by the author to provide the first detailed investigation into three axis aquatic flight. It is intended to provide the experimental verification for the Blade Element Theory (BET) aquatic flight model that was discussed in Chapter 3. The experiment consists of a three-axis actuator driving a hydrofoil through various pre-programmed foil actuation paths in a recirculating water channel. The foil forces inline and perpendicular to the foil chord are measured with strain gauges attached to the actuator. The force measurements are then used in the calculation of the thrust coefficient for that particular combination of Strouhal number and angle of attack. Figure 5-1 shows a photo of the test rig as installed in the Chilworth recirculating water channel and Newcastle Wind Wave Current tank.

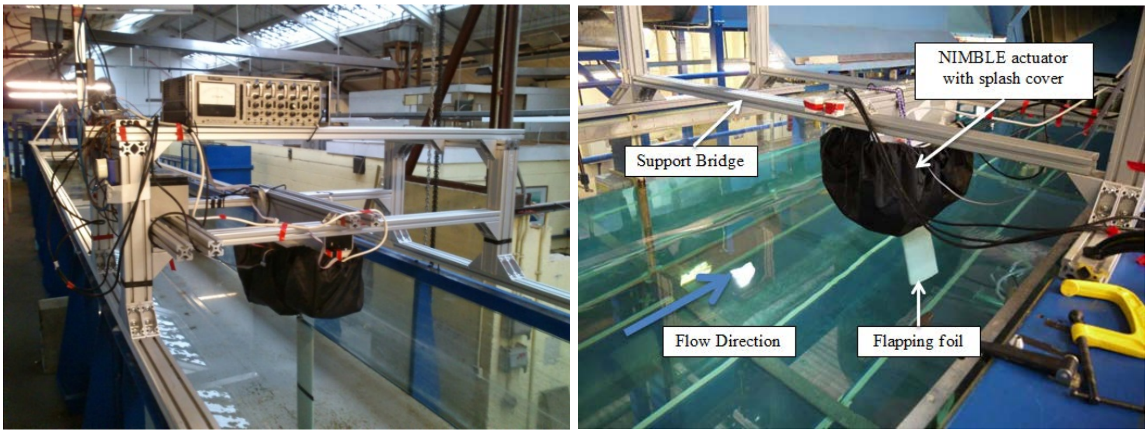

Figure 5-1 – (Left) The experiment test rig as it was installed in the Chilworth Internal Flume. (The drive mechanisms are protected inside the black splash cover). (Right) NIMBLE actuator performing experiment at the Newcastle University WWC tank

This chapter is separated into three sections. The first provides an overview of the experiment design, the NIMBLE foil actuator, and the measurement system. The second section is a summary of the available test facilities and the third section provides the details of measurement and calibration procedures.

5.2 NIMBLE Actuator Design

5.2.1 Design Specification

The experiment and the foil actuator are designed to verify the BET model, so it should be as close to the model set up as possible. The model itself was designed to simulate aquatic flight in marine animals, which provided a list of parameters and performance data as a guideline to start the design for the experiment, despite the BET model being incomplete at the beginning of the design process.

One of the key species for investigation is the penguin and the initial performance requirements were based on that of the emperor penguins due to their similar size and displacement to the average small AUV. This also means the foil actuator that simulates their wings can be built on a 1:1 scale, which can avoid complications associate with scaling.

The foil actuator needs to drive the hydrofoil through a body of moving water. This can be achieved with an actuator suspended above the water surface or one that is immersed in it. While the actuator must be fully waterproofed and immersible if it is used in an AUV, these features are not a necessity if it is only used in a locomotion experiment. A simpler design with an actuator suspended above water is sufficient and would less expensive to design and build. As such, the NIMBLE actuator was designed and built as a non-waterproof actuator that is suspended above the water surface, and it would drive a hydrofoil that penetrates into a stream of moving water below. This also avoids the complex issue of sealing the system against water ingression, particularly the problem of sealing a rotating shaft with a large varying lateral load.

The initial specification based on penguin is as follow

- Operation at speed of up to 4ms^{-1}.
- Strouhal number up to 0.5
- 0.6m flapping foil similar to a penguin wing

These requirements was revised a number of time during the design process to accommodate limitation on materials, facility, cost and time.

The final target specification for the foil actuator is as followed

- Operation at speed up to 0.5ms^{-1}.
- Flapping frequency between 0.1 and 0.4 Hz
- Roll amplitude of 20°, maximum pitch amplitude of 40°, maximum yaw amplitude of 10°
- NACA0012 foil, 0.5m span, 0.15m constant chord and wing root was 0.2m from axis of rotation
- Actuator operates in air but drives a foil that is submerged in water

Calculation for the various forces involved can be made after this set of performance parameters were lay down. Since the BET model was not finished at this stage of the design process it is difficult to accurately predict the forces involved. However, it is possible to estimate the maximum force involved using relatively simple calculation and the results of these forms the bases of the stress requirement in the test rig.

The roll axis is force and power requirement were estimated by calculating the maximum lift force at the maximum operating speed, which was estimated to be around 120Nm for the initial requirement of 4ms^{-1}. A similar method was also used by Licht (2008). This method also estimated the power requirement to be around 90W for a foil operating with a Strouhal number of 0.5, assuming 100% transmission efficiency. The performance requirements were later reduced once the single element Simple-Quasi-Steady model was finished and found the initial force and power calculation grossly underestimated the foil force. Nevertheless, testing up to 2ms^{-1} was still possible with the motor and gearbox that were ordered for the initial requirement.

The pitch motor force and power were easier to estimate due to the wealth of model and data for designing ship’s rudder as well as the pitch axis motor spec used by Finnegan (20W) which was described in Licht (2008). The initial calculations estimated the power and torque requirement to be 36W and 12Nm for operation up to 2ms^{-1} at a Strouhal number of 0.5.

Finally the yaw axis force and power requirement was calculated using the worst case scenario of the foil set at 90° angle of attack against the flow. The results show the force would be in the order of 24Nm at 2ms^{-1} and 94 Nm at 4ms^{-1}. The power requirement was between 20W and 100W for operation at 2ms^{-1} and 4ms^{-1}. However these are very rough guidelines because little is known about three axis actuation when these estimates were made.

A set of motors and gearboxes were ordered based on these initial estimates and the experimental foil actuator would be built around them. It was clear experimenting at 4ms^{-1} was not achievable realistically so the target speed was reduced to 2ms^{-1}. This was further reduced to the final specification as the available testing facilities were examined and other limitations were discovered.

5.2.2 The NIMBLE Three-axis Aquatic Flight Foil Actuator

The NIMBLE experimental foil actuator design process produced several actuator designs using Solidworks before settled on a final design as shown in (Figure 5-2). The actuator is constructed from four main components, the chassis, the yaw cradle, the pitch unit and the hydrofoil. It was designed to actuate a 0.5m hydrofoil in three axes (pitch, roll, and yaw) as illustrated in Figure 5-3.

The actuator chassis houses the drive mechanism for the roll axis, including the roll motor, encoder and transmissions, as well as the mounting points to the support frame. The yaw cradle houses the yaw motor, encoder, transmission mechanisms and the pitch unit. The pitch unit houses the pitch motor, encoders and transmission as well as the load cell for force measurement. Finally the hydrofoil module contains the NACA 0012 foil and the connection shaft.

The NIMBLE actuator would be attached to the circulating water channel using a support frame (Figure 5-4). The Chilworth’s Internal Flume has a Machine Building System Profile 8 rail on each side of the recirculating water channel for mounting equipment, so a support frame was designed using this aluminium profile system to maintain compatibility with the mounting system used by the flume. Figure 5-4 shows a picture of the support frame for the NIMBLE actuator. The frame was designed to allow the actuator to be raised or lowered. This enabled adjustment of the actuator’s height above water surface.

Although the actuator is suspended above water and do not require a fully waterproof, there is still a risk of water splashes damaging the electrical system onboard the actuator. Therefore, the actuator is protected with a splash cover during operation. In order to reduce interference from the splash cover, the cover is made from a light weight waterproof synthetic rip-stop fabric similar to those commonly used in outdoor recreation activities. The cover has a loose fit over the actuator that will further reduce any resistance to actuator movement.

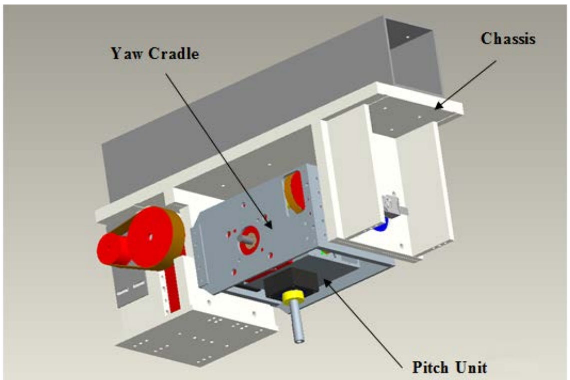

Figure 5-2 – The design of the NIMBLE three axis foil actuator. The chassis contains the roll drive mechanism that rotates the yaw cradle, pitch unit and the foil in roll. The yaw cradle drives the pitch unit with a forward-backward yaw motion, and the pitch unit control the foil pitch.

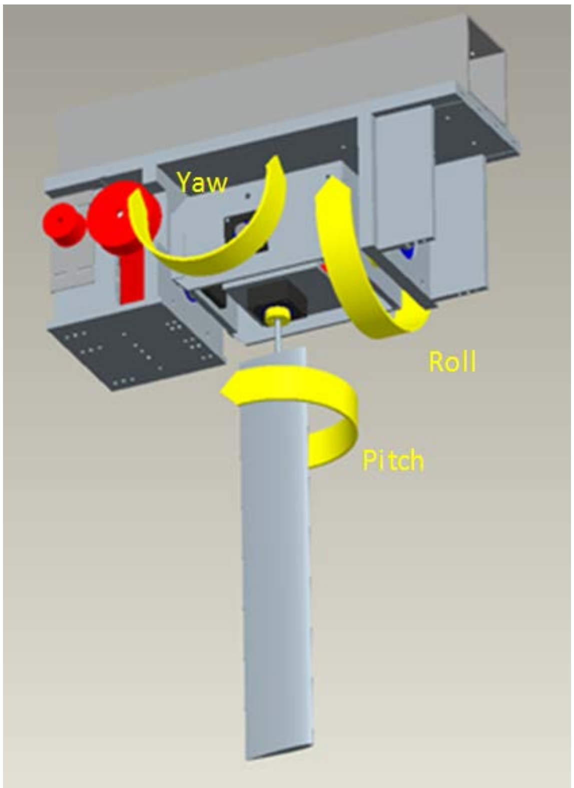

Figure 5-3 – NIMBLE Foil Actuator. The arrows indicate the three axes of motion (pitch roll and yaw)

Figure 5-4 - NIMBLE actuator support frame – The actuator is suspended between the two horizontal aluminium profiles in the centre.

5.2.3 Motors and gear boxes

The initial calculations produced an estimate of the torque and power requirements for the motor and gearboxes, and since these were the heart of the actuator they were the first to be ordered. Maxon Motors was chosen as the motor supplier because they manufacture a large variety of modular motors that are often used in control application. Their products can be fitted with various types of optional accessories such as encoder, gearboxes, and brakes, which meant their motors can be customised to meet the need of the actuator's requirement.

The National Instrument CompactRIO and NI9505 motor controllers were already available for the investigation. However, the NI9505 drive modules can only be used with brushed DC motors and quadrature encoders, which limited the types of motors that can be used.

A 60W Maxon RE30 motor was chosen as the pitch axis motor, and a 200W RE50 motor was chosen for roll, both of which operated at 24V. The yaw axis was driven by an 18V 90W Maxon RE35 brushed DC motor that was loaned to this research project by Maxon free of charge. Since this loaned motor operated at a different voltage to the two purchased motors, the actuator's power supply was designed to supply DC current at both voltage (18V and 24V). The specifications of the three motors are given in Table 3.

Each motor was ordered with 500CPT HEDL quadrature encoders, which will provide position feedback on the motor at a resolution of 2000 counts per motor revolution. In addition to motor control, the motor position feedback would be used to infer the foil position.

	Pitch	Roll	Yaw
Motor	RE30	RE50	RE35
Voltage /V	24	24	18
Power /W	60	200	90
Speed /rpm	8810	5950	7180
Torque /mNm	85.6	405	73.1

Table 3 – Specifications of the motors

The motors cannot produce enough torque to drive the flapping foil directly, so reduction gearboxes were needed to increase output torque. Since the gearboxes are the most highly stressed component in the whole actuator, designing a suitable gearbox would be difficult and time consuming. As such, it was decided to purchase commercial readymade gearboxes instead in order to reduce development cost and time. Several types of gearboxes were available, including planetary gear, spur gear and worm drive.

Maxon can supply planetary gearboxes that can achieve a very high reduction ratio, but they have a limited maximum output torque that was insufficient to meet the estimated force for the worse case scenarios. In addition, the Maxon gearboxes are mounted in line with the motors, which increase the space requirement to fit the gearbox. This can become a major disadvantage in the limited space available for the pitch axis.

The main alternative was worm gearboxes from Ondrive, which have a higher maximum torque rating, a relatively high reduction ratio of up to 1:120, but limited efficiency. The 1:60 and 1:120 Ondrive worm gearboxes have self-locking output, which prevents the gearbox input to be driven backward from the output. This would allow the actuator to hold position without consuming energy, and would prevent the fluid forces on the hydrofoil from driving the actuator out of its allowable range even if the actuator lost power. After evaluating the advantages of the Ondrive gearboxes, three 1:60 antibacklash worm gearboxes were chosen for the actuators. These worm gearboxes were relatively compact and allowed the motor to be mounted 90 degrees to the output shaft. The gearboxes were linked to the motor using reduction belt drives. This combination allows the motor to ‘fold’ behind the gearbox, thus reducing the space requirement. The Maxon motors were connected to the worm gearbox via a belt drive, which had a reduction ratio of 2.17, 3.00 and 3.00 for pitch, roll and yaw, respectively. This gives an overall reduction ratio of 130, 180 and 180 for pitch, roll and yaw. This also corresponds to 181, 250, 250 encoder clicks per degree of movement in each axis

Once the motor and gearboxes for the NIMBLE foil actuator was decided, the design process for the rest of the actuator can begin.

5.2.4 Roll Axis Design

The oscillatory roll motion is the dominant motion in aquatic flight propulsion, so the roll axis design is the most important part of the foil actuator design. The roll axis will need to handle the load from propulsion, as well as to support the drive mechanisms for the other two axes. Therefore, the drive mechanism for roll is designed as part of the actuator chassis to maximise strength.

The chassis was designed around three blocks – the roll drive block, pitch/yaw mechanism area (reserved for the yaw cradle) and the yaw cradle support block (Figure 5-5). The roll drive block houses the drive mechanism for the roll axis, while the yaw cradle support block house has a large diameter roller bearings designed to support the enlarged yaw cradle support shaft and motor housing. The roll drive block is design around the Ondrive gearbox and roll motor. The roll motor is mounted on two sliding aluminium plates which are bolted to the chassis. The sliding feature is used to tension the belt drive which connected the motor output shaft to the gearbox input shaft. The motor mounting plates are removable and it allowed the roll motor to be upgraded from a 90W motor used in the initial development to the 200W motor used in the experiment without any major rebuild of the chassis. Most of the chassis was built out of 10mm thick Delrin plates, but thickness was doubled in a number of key areas, such as the plate supporting the roll axis bearing and the plates supporting the roll gearbox. Delrin was chosen for it strength, ease of machining and cost. A 6082 aluminium square section ($0.61 \times 0.12 \times 0.12$m with 5mm thick walls) was bolted to the chassis base plate to increase stiffness.

An Ondrive P60-60A worm gearbox was used to reduce the motor rotation speed and increase output torque. The gearbox has a self-locking output that prevent the fluid forces from driving the motor backwards, and an anti-backlash mechanism that reduces the gearbox backlash to 8 arcminutes or 0.13°. The gearbox has a 1:60 reduction ratio and the belt drive linking the motor output shaft to the gearbox input shaft has a 1:3 reduction ratio. In total these two reduction mechanisms reduced the motor output speed by 1:180.

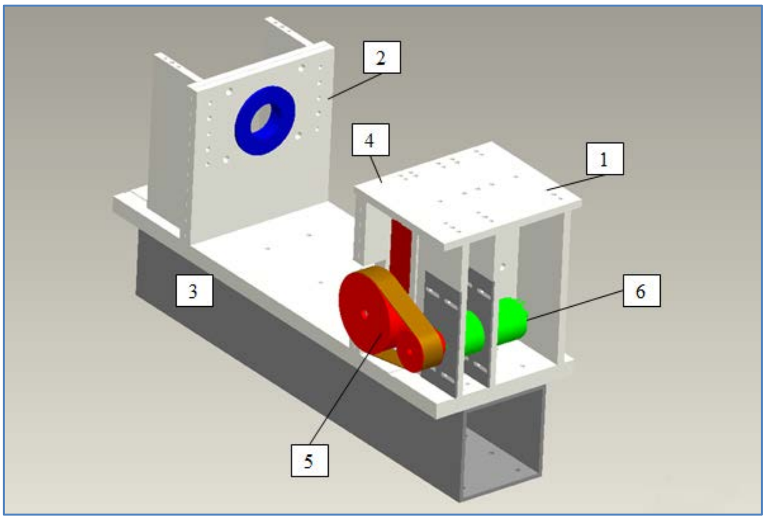

Figure 5-5 – Chassis. 1. Housing for roll drive mechanism. 2. Yaw cradle support (non- drive side). 3. Chassis stiffening beam. 4. Roll output shaft (Hidden behind housing). 5. Reduction belt and pulley. 6. Worm gearbox
Red – Transmission, Blue – Bearings, Yellow – Shaft clamps. Green – motor and encoder

5.2.5 Yaw Axis Design

The yaw axis cradle is designed to house the pitch unit and to actuate the hydrofoil and the pitch unit in yaw. An illustration of the yaw cradle is shown in Figure 5-6. The yaw axis cradle was built around the pitch unit and an Ondrive P45-60A gear box. It was constructed by bolting four aluminium plates together forming a box as Delrin was found to have insufficient strength for this application. The end plates (one connected to the roll axis drive shaft, and the other one connected to the roll axis free shaft) were made from 10mm thick 6082 aluminium. The two side plates that house the yaw bearings are 5mm thick. In addition to the 10mm aluminium, an additional 10mm thick Delrin plate was bolted to the drive side end plate to increase gripping area for the roll output shaft's keyway. The free side of the yaw cradle has a large hollow shaft big enough to accept the Maxon 90W motor inside.

The yaw bearings which supported the pitch unit are mounted on the drive side side-plates. It allows the pitch unit to rotate in yaw (forward-backward). The non-drive side side-plate has holes for locking bolts which can be used to lock the yaw axis movement when the actuator operates in two axis mode.

Putting the yaw motor in the non-drive side roll shaft allowed the motor to rotate with the yaw cradle, thus eliminating the need for additional algorithms to compensate for roll movement that would be required if the motor was mounted stationary on the chassis. However, since the distance between the roll shaft and the yaw gear box input is fixed, it was not possible to use the sliding motor belt tensioning method used in the roll and pitch axis. Therefore a simple belt tensioner made with an aluminium arm and a bearing was used to tension the belt instead.

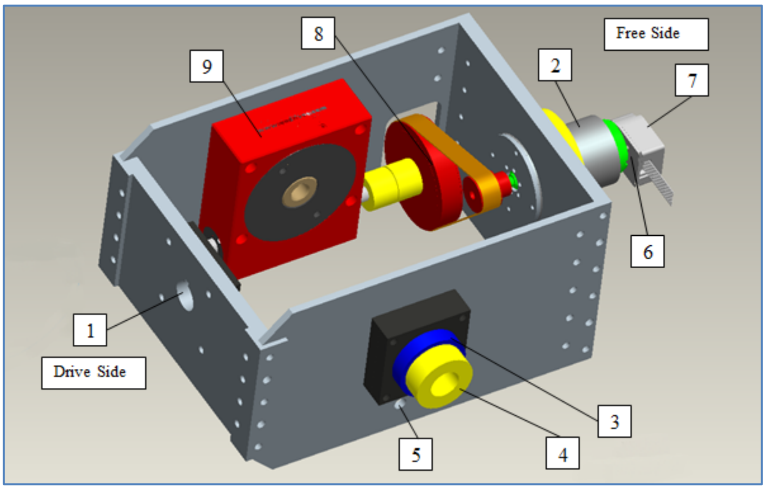

Figure 5-6 - Yaw Cradle – 1. Roll Shaft hole. 2. Free side support shaft. 3. Pitch unit support bearing. 4. Bearing holder, 5. Yaw locking bolt, 6. Yaw motor, 7. Yaw Motor Encoder, 8. Yaw pulley and belt, 9. Yaw Gearbox. Green – Motor, Red – Pulley, Blue – Bearings, Yellow – Shaft clamp

5.2.6 Pitch Axis Design

The pitch axis is mounted inside the yaw cradle and is tasked with rotating the hydrofoil in pitch. An illustration of the pitch unit is shown in Figure 5-7. The pitch shaft and bearing unit is installed from the outside and extended through the wall of the pitch unit housing. The output shaft extends to the other side of the housing and into pitch gearbox output. The pitch shaft is secured to the bearing unit using two shaft collars. A first glance, the shaft may appear to be mounted off centre on the pitch unit, but this was intended to offset the clearance for the yaw mechanisms in the yaw cradle. When fully assemble, the foil shaft would line up with the roll and yaw shafts to avoid any eccentricity in the motion.

The pitch unit was designed and built around the motor and the Ondrive P40-60A gear box. The gearbox and motor is bolted on to a Delrin chassis (Figure 5-8). This chassis is secured onto the pitch box housing using a number of bolts. The housing is made of a 120x120mm aluminium 6082 box section with 5mm thick walls. The pitch housing has a number of bolts holes for the pitch bearings assembly and the yaw shafts. The pitch unit is attached to the rest yaw cradle via the two yaw shafts. The non-drive side support shaft was made of 6082 aluminium and is supported by roller bearing in the yaw cradle. The drive side shaft is made from stainless steel with a smaller diameter than the non-drive side shaft, because the yaw gearbox limited the diameter of the drive side shaft, and aluminium shaft of that diameter is not strong enough to handle the estimated torque and forces.

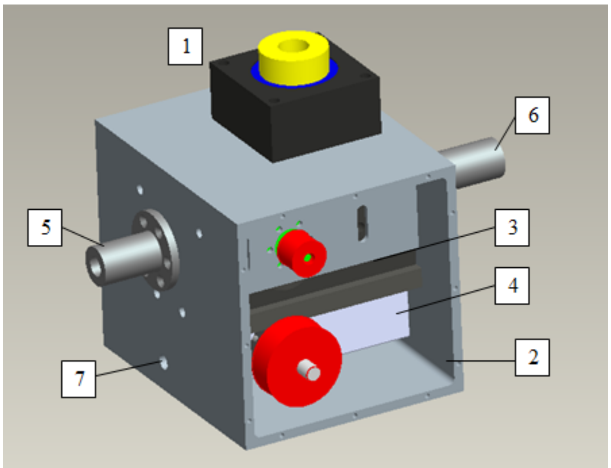

Figure 5-7 - Pitch unit – 1. Foil Shaft holder. 2. Pitch unit housing. 3. Pitch Chassis. 4. Ondrive P40-60 gearbox. 5. Short shaft - cable route 6. Long shaft – Yaw Drive side. 7. Yaw axis locking hole. Black – Delrin, Grey – Aluminium, Red – Transmission, Blue – Bearings, Yellow – Shaft clamps. Green – motor and encoder (hidden)

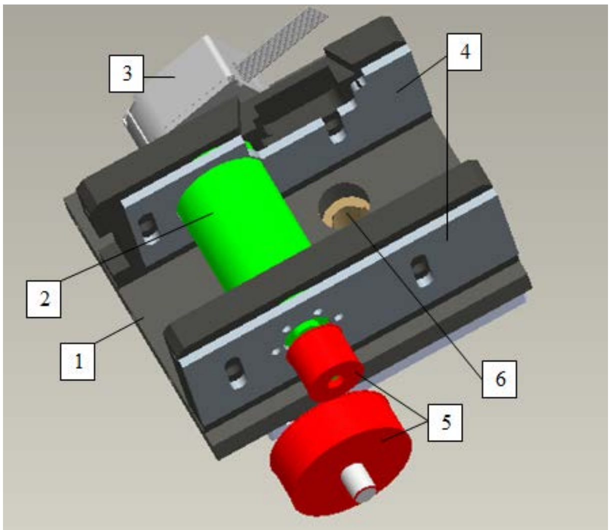

Figure 5-8 - Pitch Chassis – 1. Delrin Chassis 2. Maxon 60W RE30 Brushed DC motor 3. Maxon HEDL encoder. 4. Motor mounting plate 5. Reduction pulley and belt drive. 6. Ondrive P40-60A worm gearbox. Black – Delrin, Grey – Aluminium, Red – Transmission, Blue – Bearings, Yellow – Shaft clamps. Green – motor and encoder (hidden)

The pitch output shaft with load cell would be secured on the pitch bearings assembly. The gearbox was mounted on the opposite side of the pitch output shaft to redistribute weight in the pitch unit and improves balance. The gearbox was first secured onto the pitch chassis by four mounting bolts. The motor was bolted to the chassis via a sliding motor mounting plate which also doubled as the belt tensioner for the belt drives that connected the motor output to the gearbox input. The motor and chassis assembly then slid into the pitch unit housing and secured with bolts.

5.2.7 Design of the Foil

The foil used in the experiment is a NACA0012 foil with a 0.5m span and a 0.15m chord. It was rigid and had a constant cross section. The foil is constructed with a glass fibre reinforced epoxy resin skin enclosing a foam core. High tensile steel studding runs through the foam core and was bonded to the foam using Araldite 2015 structural epoxy adhesive. The studding provided both structural strength and a point of connection to the actuator. The studding is located at 25% of the chord near the foil’s hydrodynamic centre to minimise the torque require to pitch the foil.

Figure 5-9 – Fibre glass reinforced NACA0012 foil build for the actuator.

5.2.8 Pitch output Shaft and Load Cell

The pitch shaft was designed to take a load of up to 100Nm in roll and it is constructed from a 12mm stainless steel shaft. The shaft was designed to transfer the lateral load through the pitch bearings assembly into the pitch housing, so it can tapered down to a smaller diameter to fit the pitch gearbox output while remaining stiff enough to handle the load in roll.

The output shaft has a M10 female thread in the output end for attaching to the internal studding of the foil. The foil was screwed into the shaft and then locked into place using a two opposing locking nuts and thread locking glue. The medium strength thread locking glue (Bond-it A43) is a relatively weak adhesive that glues the male and female thread together. The bond can be broken with torque of approximately 25Nm for a M10 nut at 20^{o}C. The use of thread locker prevented the foil from coming lose in pitch.

Foil forces were measured by strain gauges fitted to the pitch output shaft (Figure 5-10). The shaft has been fitted with two pairs of linear strain gauges (Micro-measurement CEA-06-240UZ-120) set 90° from each other and one pair of rosette strain gauge (Micro-measurement EA-06-060RZ-120/E). The gauges were bonded using Vishay M-bond 200 and following the procedure described in Vishay instruction bulletin B-127-14.

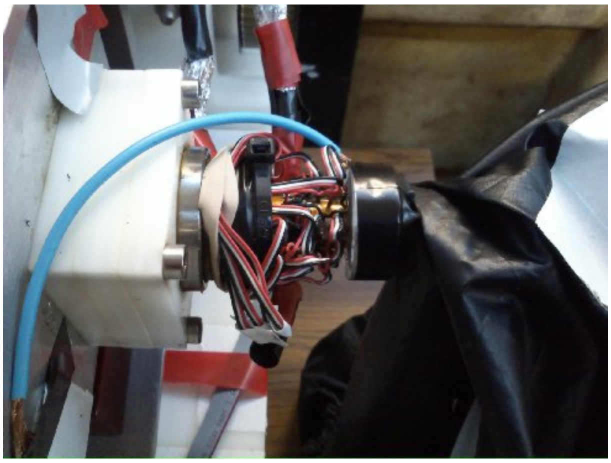

Figure 5-10 – The strain gauge systems on the pitch shaft. The three colour wires (red, white black) are the strain gauge lead wire. The blue wire is the ground wire for the drive shaft.

Each gauge was connected to an output terminal tab, which was also bonded to the pitch output shaft. The wire connections between the terminal and the gauge incorporated a strain relief loop. The lead wires connecting the shaft with the stain gauge amplifier input were soldered to the terminal. The body of these lead wires were secured on to the shaft collar with cable ties and electrical tape. The lead wires for all individual gauges were bundled together and shielded using aluminium foil sheath. Then this lead wire bundle is passed through another strain relief point on the chassis before they are connected to the strain gauge amplifier input terminals. This multistep connection is designed to protect the fragile strain gauges. Any movement of the lead wire caused by movement of the output shaft would be stopped by the anchor point. Any residue movement would be stopped by the strain relief loop before the output terminal. Also, if the lead wire had to be changed and reattached, the de-soldering and re-soldering would take place on the expendable output terminal tab rather than the difficult to replace strain gauges.

The strain relief before the chassis strain gauge amplifier input terminal serves the same purpose, but the screw type connections used in the input terminal were more durable and easier to service than the soldering connection at the strain gauges, so a less sophisticated strain relief system would be adequate.

5.2.9 Electrical System

A number of subsystems in the NIMBLE experiment required electrical power supply. These include the NIMBLE actuator, the CompactRIO, the strain gauge amplifier and the control laptop. The NIMBLE actuator required DC power, while the strain gauge amplifier required mains electricity. The control laptop can run on battery or mains, while the CompactRIO requires a DC input.

The NIMBLE actuators are driven by three DC motors and controlled by a National Instrument CompactRIO. The roll motor and pitch motor were 24VDC, while the yaw motor was 18VDC. The yaw motor was an obsolete unit from Maxon that was loaned to this research program free of charge, so the voltage difference was an acceptable compromise. However, this meant the actuator will need to be supplied by two different DC sources.

The original plan was to power the motors using bench power supplies. However, it was discovered despite the current draw of the motor were well below the limits of the power supplies, the initial current spike associated with starting the motor was too high and was able to trigger short circuit protection on all the power supply tested. Therefore, lead acid batteries were employed instead. The batteries could not be recharged during the experiment, so they must be of a sufficient size to supply enough electrical power for a day’s experiment before being recharged overnight. The roll axis would be powered by two 12V 24Ah batteries connected in series to give a 24VDC output, while the pitch axis was supplied by two 12V 7Ah batteries. The yaw axis used a three 6V 7Ah batteries to supply the 18VDC require by the motor.

The batteries would be connected to the CompactRIO motor controller through the switch and fuse box. The switch and fused box houses the safety kill switch for the circuit which would cut off current to the motor controllers. This in turn would stop the motors immediately. The circuit was also protected by a set of automotive fuses. These fuses would blow if there is an overcurrent in the circuit. Figure 5-11 shows an illustration of the electrical system layout in the NIMBLE experiment.

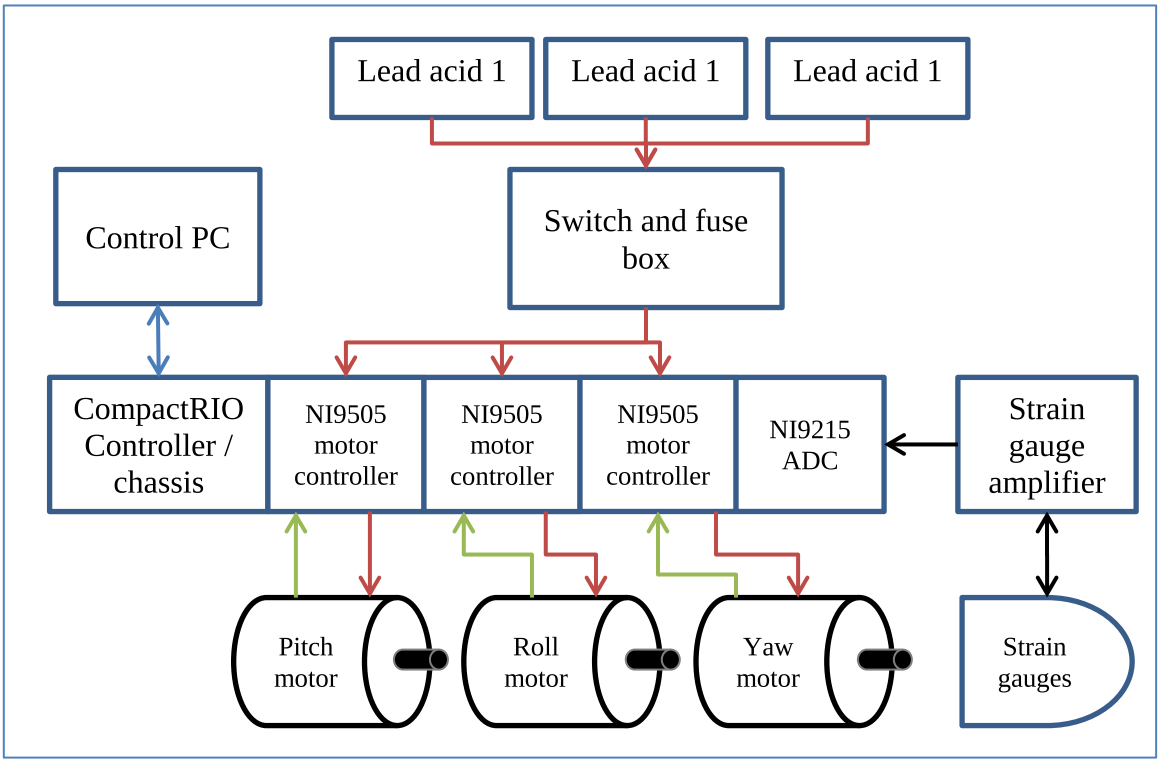

Figure 5-11 – Electrical connections of the nimble actuators. (Red – DC power supply, Green – Encoder, Blue – Ethernet, Black – Strain gauge analogue voltage)

While the CompactRIO can be powered by a DC source between 9V and 35V, it was powered by a mains power supply instead of the lead acid battery because it would allow the CompactRIO to be powered indefinitely. This allowed the CompactRIO to remain ON when the batteries were removed for charging. The CompactRIO chassis also supplied power to the motor controller modules, the analogue to digital converter module, and the encoders on the motors.

The strain gauge amplifier (Yokogawa Electrical Works Type 3107) and computer were powered directly from mains electricity. Since the experiment was preformed near water, residual current device (RCD) connectors must be used between the appliance and the mains.

The RCD is a safety circuit breaker that would automatically disconnect the circuit when it detects a current leak, such as when an instrument accidentally comes into contact with water.

5.2.10 Control System

The motion of the NIMBLE actuator was controlled by a National Instrument CompactRIO (CRIO). The CRIO is a modular and reconfigurable system for real time control and acquisition. Each CRIO system consists of a Real Time Controller, a chassis and a number of optional C-series plug-in modules. The NIMBLE Experiment used four modules, one for data acquisition and three for motor control.

The CRIO Real Time Controller contains a fully functional computer with processor, memory and flash storage that will allow the CRIO to operate independently from a PC. It is also equipped with a USB port for external storage. The Real Time Controller connects to the control computer using Ethernet via its RJ45 port. The CRIO chassis contains a reconfigurable FPGA core for time critical applications. The FPGA runs faster than the real time controller, but it has limited computational power and has a more restrictive function sets. For example, the FPGA cannot accept floating point digits. Any decimal number must be converted to Fixed-point-numeral (FXP) or rounded to Integer (INT). The size of the FPGA array also limits the maximum sized of program that can be implemented.

The control computer provided the user interface for the CompactRIO during experiment. It allowed the user to start and stop the program, change program input parameters and view the results. However, it does not perform any calculations for controlling the experiment. All real time calculations and data recording were all carried out by the CRIO’s real time controller and FPGA. Since all time critical processes are carried out inside the CRIO, it avoided the time lag issue normally associated with using Ethernet connection.

The control programs for NIMBLE is written in Labview and can be separated into two layers. The Real-time Controller layer handles the high level processes such as File I/O, user interface, data recording, and initial data processing. A simplify flow chat of the Real-time layer is shown in Figure 5-12. The Real-time layer is responsible for making calculations to translate the user inputted parameters such as amplitude and frequency into parameters for the low level control program, such as motor-encoder clicks per clock cycle. It also receives periodic update from the FPGA loop and display the actuator result in real-time (the very short delay is not noticeable for the user).

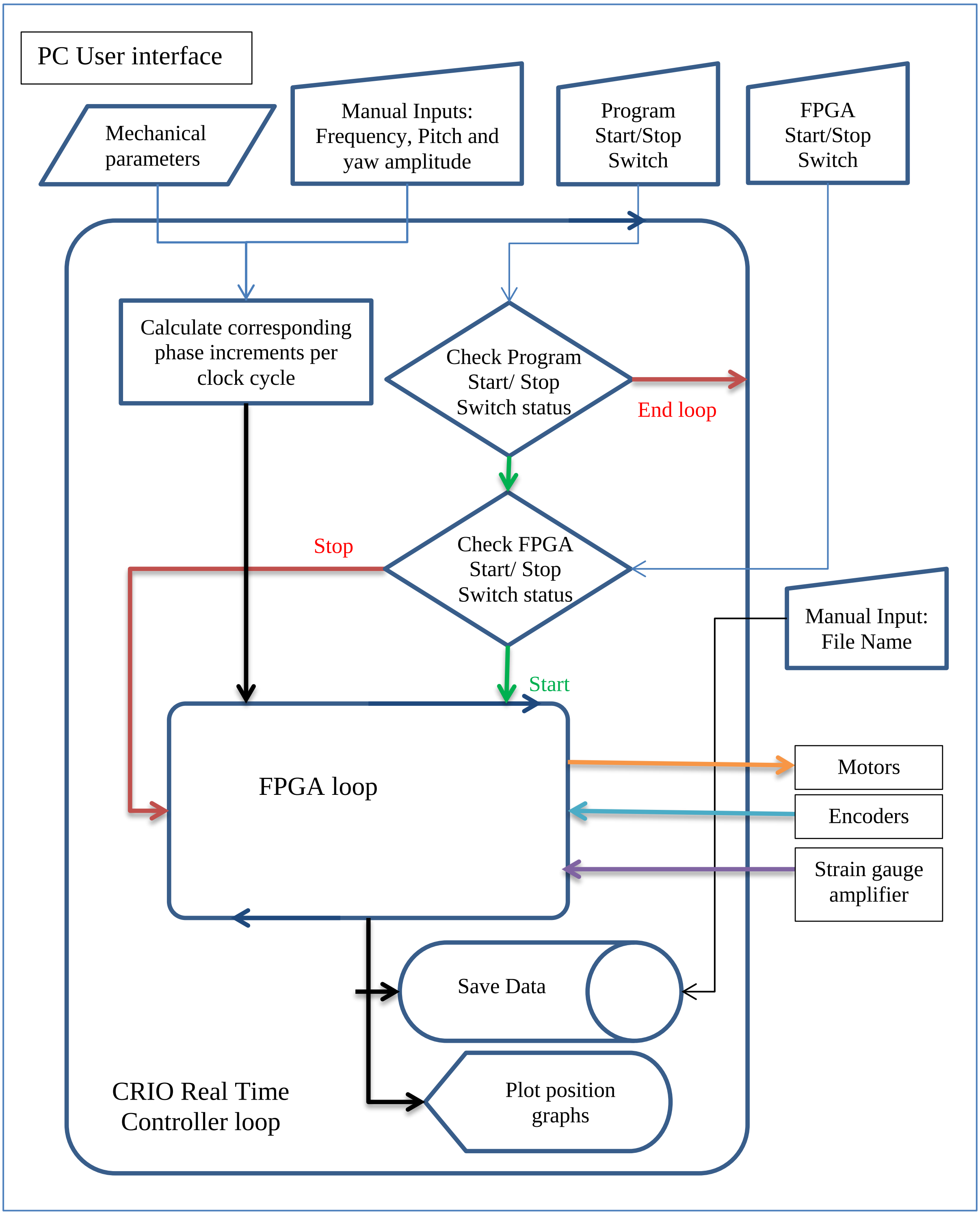

Figure 5-12 – Simplified control system flow chart for the NIMBLE actuator's high level control program

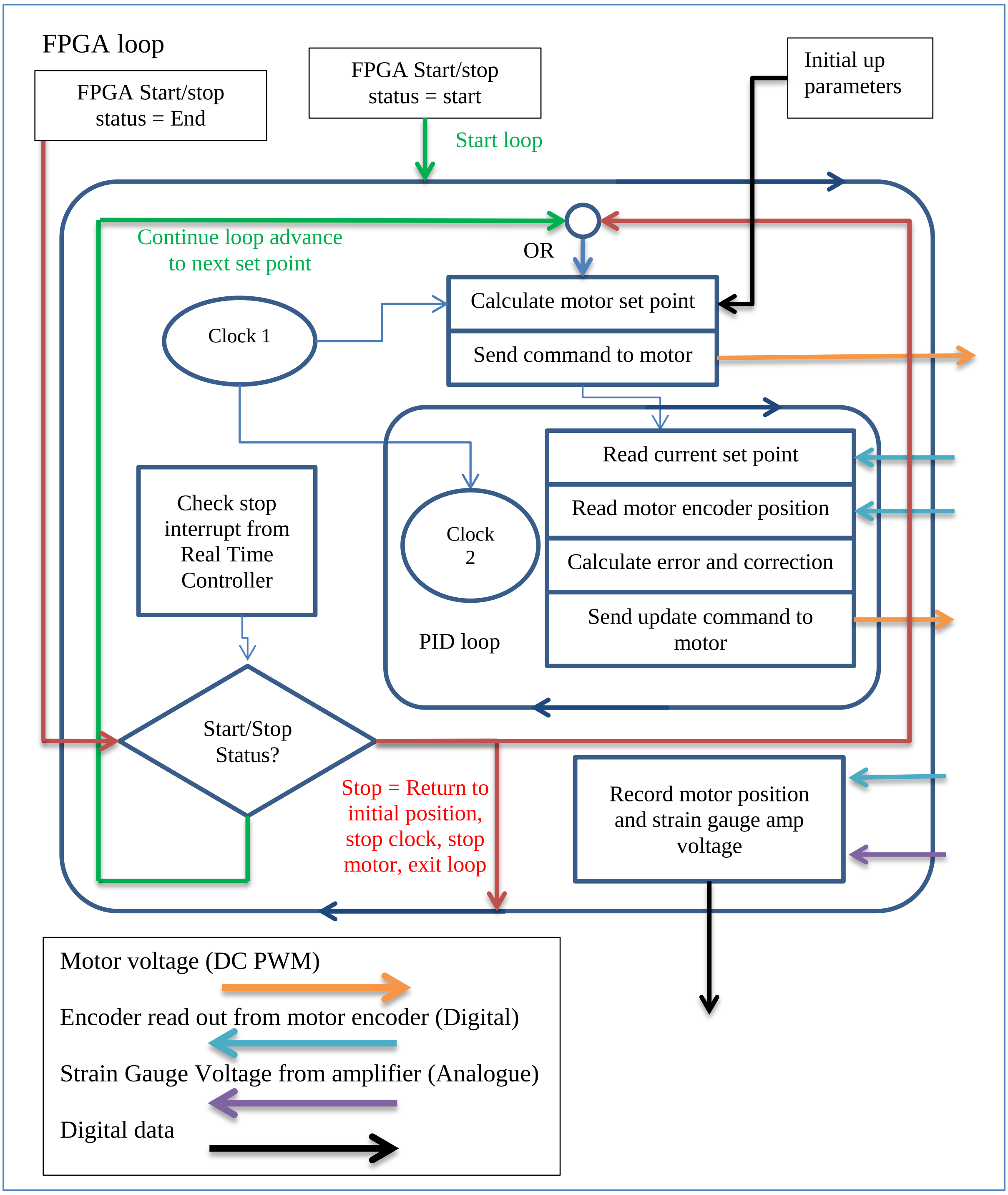

Figure 5-13 - Illustration of the simplified FPGA Loop

Meanwhile time critical processes such as set point generation, motors command, reading encoder feedback, PID control, and data acquisition from strain gauge amplifier are carried out by the much faster FPGA layer which makes thousands of correction per second to ensure the motor moves as commanded and the collects time accurate encoder/amplifier read out. The FPGA loop has two layers as illustrated in Figure 5-13. The base FPGA layer operates at a clock speed of 100Hz (Clock 1) and it is responsible for directing the motion of the foil through the path generator and collects the position and force data from the motor encoders and strain gauge amplifier. The second layer, the PID loops layer, operates at a much faster clock speed of 10 kHz (Clock 2). It reads the motor encoder position continuously and make sure the foil stays on path and advances the motors towards the set points set by the path generator.

5.3 Test Facilities

5.3.1 Chilworth Drop Test Tank

The Chilworth Drop Test Tank is a tank located in the Chilworth Hydraulics Laboratory. The drop test was used for system development. This tank is a relatively small static body of water, so it was used for bollard pull and software development. The tank's water provided the necessary damping for testing various software algorithms.

5.3.2 Chilworth Internal Flume

The Chilworth Internal Flume is a recirculating water channel located in University of Southampton Chilworth Hydraulics Laboratory (Figure 5-14). It is 40m long, 1.4m wide, 0.6m deep and capable generating water flow speed up to 0.5ms^{-1} according to its specification. A recirculating water channel, or a flume, pumps water through the test channel while the test model is held stationary. It has the advantage of being able to operate continuously and maintain a constant flow speed indefinitely.

Figure 5-14 – Chilworth Internal Flume

The Chilworth Internal Flume uses three electric pumps to pump water from the storage tank into the testing channel. Pump No.1 is the most powerful of the three pumps, followed by

No.3. Pump No.2 is weakest and cannot maintain full channel depth on its own. The flow rate of each pump can be fine-tuned using their corresponding output valves. A gate at the end of the test channel can be used adjust the water depth. However, increasing water depth will reduce the water flow speed, and obtaining the correct combination of flow speed and water depth is difficult and requires a series of trial and error on valves positions and gate height.

The Chilworth flume has two parallel 80x40 machine building system aluminium profiles running alongside the entire length of the channel for mounting instrument. A supporting structure was needed to support the actuators over the channel and this structure will need to be compatible with these instrument mounting profiles.

5.3.3 Newcastle Wind Wave Current Tank

While Chilworth internal flume was being used for system development, Pump No.1, the main pump, suffered extensive foreign object damage and had to be taken out of operation before the experiment began. The remaining pumps could not achieve a flow rate more than 0.2ms^{-1} at full depth. This means it is necessary to find another recirculating water channel to carry out the experiments.

Newcastle University granted the use of their Wind Wave Current (WWC) tank. The wind wave current tank is a very advanced recirculating water channel with full computer control on the flow speed. It is 11m long, 1.8m wide and 1m deep recirculating water channel with a wave generator and a wind tunnel. It can generate a maximum water flow velocity of 1ms^{-1}, wind velocity of 20ms^{-1} and a wave height up to 0.2m. The wind tunnel and wave generator were not used in this experiment.

5.4 Measurement and Calibration

Before the foil actuator can be used, it must first be tested to ensure its input measurements and output positions correspond to the real world measurements. The raw data from the experiment is acquired as strain gauge voltage, position clicks and time. The strain gauge voltage corresponds to the bending moment on the pitch axis shaft which in turn corresponds to forces acting on the foil. Therefore it is necessary to calibrate the strain gauges and find the relationship between the gauge voltage and foil force. The encoder position clicks measure the foil's positioning in pitch, yaw and roll. Position clicks measurement is assumed to have negligible read error, because the motor encoder output its reading as a digital wave. However, since there are mechanical inaccuracies in the NIMBLE actuator, there will be small but measureable differences between the position reported by the motor encoder and the foil's actual position. Finally, time is measured by the FPGA internal clock, and the timing error on the FPGA clock is assumed to be negligible.

5.4.1 Force Measurement

The foil forces are measured by two pairs of strain gauges on the pitch drive shaft. These gauges measured the forces inline and perpendicular to the foil chord. These forces are referred to as chord force (F_C) and perpendicular force (F_p). When the foil is subjected to a force, it will create a bending moment on the pitch shaft, which will cause the shaft to bend. The strain gauges were attached directly to the shaft, so any deformation to the shaft (strain) will also deform the strain gauges, causing the gauges to either extend or contract in length. The strain gauge amplifier's gain setting do not have click stop or marked position, so they were set to the maximum setting in order to ensure repeatability between experiments.

The stain gauges were calibrated by suspending a 1.83kg weight on the foil at several pre-set distances from the roll axis, namely 0.30, 0.35, 0.4, 0.45, and 0.5m as shown in Figure 5-15. The voltage respond was recorded by the CompactRIO and is shown in Figure 5-16. The original unprocessed voltage data contains amplifier drift and noise. However, since the gauge calibration test was static, it was possible to calculate the mean voltage for each position and create the calibration curve. The differences between zero level at the start of the measurement and the zero level at the end of the measurement would indicate the amplifier drift.

Figure 5-15 - Foil undergoing strain gauge calibration

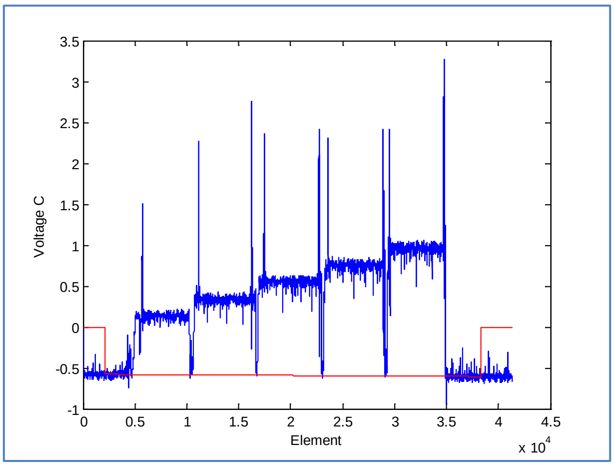

Figure 5-16 – Blue - Strain gauge responds – Chord gauge, Amplifier setting 500$\mu\varepsilon$. Red – Strain gauge drift line

After calculating the mean voltage level for each calibration positions and correcting for stain gauge drift. The voltage was plotted against the applied moment (Figure 5-17, Figure 5-18). This moment recorded by the strain gauges during calibration has two components. The first component is the moment induced by the calibration mass, $m_{cali}x_{cali}$, while the second is the moment induced by the weight of the foil, $m_{foil}x_{foil}$. The calibration weight moment is plotted on the Y axis, and the amplifier voltage is plotted on the X axis. The Y axis intercept represents the foil’s own weight. Finally the gradient of the moment calibration line is the voltage-moment conversion factor, K_{mv}. The foil moment during experiment, τ_{exp}, can be calculated using this conversion factor, and the amplifier voltage, V_{exp}. A summary of the calculation are listed in equations (5-1) – (5-4).

$$M\bar{X} = m_{cali}x_{cali} + m_{foil}x_{foil} \qquad (5\text{-}1)$$

$$m_{cali}x_{cali} = K_{mv} \times V_{cali} - m_{foil}x_{foil} \qquad (5\text{-}2)$$

$$K_{mv} = \frac{(m_{cali}x_{cali} + m_{foil}x_{foil})}{V_{cali}} \qquad (5\text{-}3)$$

$$\tau_{exp} = K_{mv} \times V_{exp} \qquad (5\text{-}4)$$

Figure 5-17 showed the relationship of the calibration moment and strain gauge voltage for the perpendicular gauges at two different amplifier settings. The experiment may use both settings so both lines must be measured. It can be seen the line is very tight and the spread of the data point measurements and their repeats were very small. Using standard deviations, the errors were found to be less as 2.5% with 90% certainty. The gradients of the perpendicular moment-voltage calibration lines were found to be 1.8 and 4.2Nm/V for amplifier settings of $200\mu\varepsilon$ and $500\mu\varepsilon$ respectively. Figure 5-18 showed the calibration line for the two chord gauges. The gradient of the chord moment-voltage line were found to be 1.6 and 3.9Nm/V respectively. The results from the calibration test are summarised in Table 4.

Force direction	Amplifier Setting	Moment-Volt conversion Nm/V	Intercept
Chord	$200\ \mu\varepsilon$	1.763 ± 0.045	2.08 ± 0.135
	$500\ \mu\varepsilon$	4.196 ± 0.080	2.30 ± 0.094
Perpendicular	$200\ \mu\varepsilon$	1.567 ± 0.018	2.02 ± 0.048
	$500\ \mu\varepsilon$	3.874 ± 0.043	2.10 ± 0.047

Table 4 – The moment-volt conversion factor and the Y axis intercepts (90% certainty)

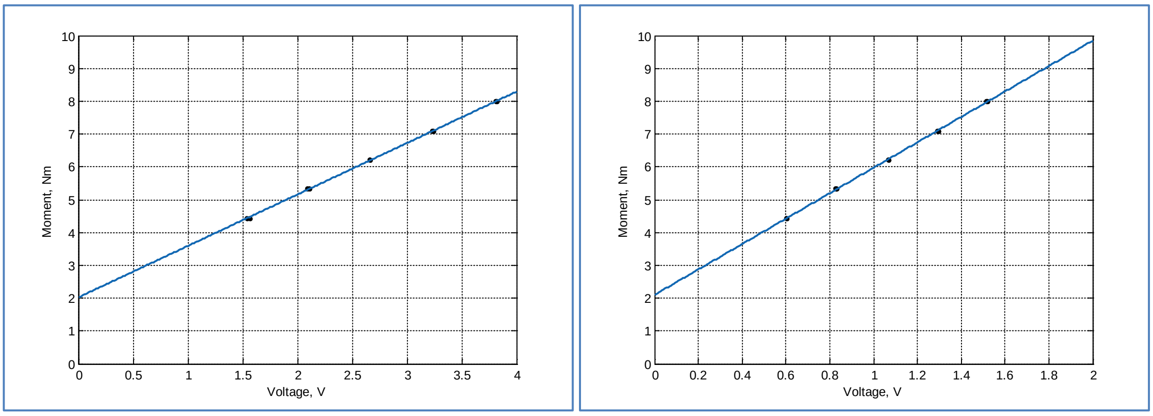

Figure 5-17 - Strain gauge calibration line - Perpendicular gauge. (Left) Amplifier setting $200\mu\varepsilon$. (Right) Amplifier setting $500\mu\varepsilon$

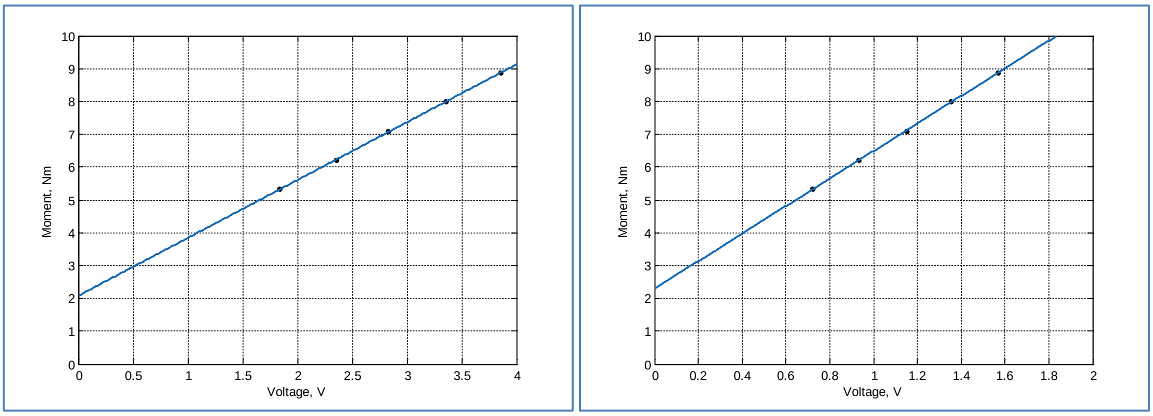

Figure 5-18 - Strain gauge calibration line - Chord gauge, (Left) Amplifier setting 200$\mu\varepsilon$, (Right) Amplifier setting 500$\mu\varepsilon$

After the moment-voltage conversion line is known, it can be used to calculate the foil force. First, the forces were measured by the strain gauges as moments in line and perpendicular to the foil chord (τ_c, τ_p). Then the foil moment would be converted into foil forces by multiplying the moment by the radius to the foil centre of thrust, r_{CT} ((5-5), (5-6)). The two axis model found foil centre of thrust was located at 0.56span in chapter 3, which is around 0.48m from the axis of rotation.

$$F_p = \tau_p(t)\, r_{CT} = \left(K_{mv,p} V_p\right) r_{CT} \tag{5-5}$$

$$F_c = \tau_c(t) r_{CT} = \left(K_{mv,c} V_c\right) r_{CT} \tag{5-6}$$

The forces measured by the strain gauges were aligned with the foil chord and its perpendicular. They are offset from the actuator's polar ϕ and ψ by an angle equal to the pitch angle. Equation (5-7) and (5-8) showed the formula for converting the foil chord and perpendicular force into roll and yaw force.

$$F_\psi(t) = F_p(t)\, sin\big(\theta(t)\big) + F_c(t) cos(\theta(t)) \tag{5-7}$$

$$F_\phi(t) = F_p(t)\, cos\big(\theta(t)\big) - F_c(t) sin(\theta(t)) \tag{5-8}$$

In two axis oscillation the force in yaw force (F_ψ) equals the force in X, but force in Y is a function of the roll force (F_ϕ) and the roll angle (ϕ). In three-axis oscillation, the thrust (F_x) is a function of the yaw force (F_ψ) and yaw angle (ψ). Equation (5-9) and (5-10) show the formula for calculating the horizontal force, F_x (thrust and drag), and vertical force, F_Y, from axis force F_ψ and F_ϕ.

$$F_x(t) = F_\psi(t)\,cos\big(\psi(t)\big) \tag{5-9}$$

$$F_y(t) = F_\phi(t)\,cos\big(\phi(t)\big) \tag{5-10}$$

The foil forces change during the oscillation cycle, so the average force of complete oscillation cycles are used for calculating the thrust coefficient. The analysis program can identified the oscillation cycles and calculate their mean thrust, which is then used to calculate the overall thrust coefficient.

5.4.2 Noise Filtering

The experiment measured forces through a set of strain gauges mounted on the pitch drive shaft, but the signal from the strain gauges was found to contain a lot of noise and interferences. Figure 5-19 shows the results from a typical test, which starts with a pre-test rest period, follows by a test period, and then a post-test rest period. A close up of one of these tests can be seen in Figure 5-20. In addition to the pitch and roll positions, the plot also includes a graph showing the strain gauge response. When the test starts, the foil is quickly manoeuvred into the starting position, and this rapid acceleration created the initial spike in the strain gauge reading. As such, the first cycle of every test was excluded from the analysis. After the first cycle, the system settled into regular oscillation and the strain gauge voltages were shown to oscillate at the same frequency as the foil motion. As expected, the perpendicular gauge recorded significantly higher force than the chord gauge.

Figure 5-20 also shows while the foil position data is very smooth, the force data from the foil appears very noisy. A number of measures were introduced in the hardware to reduce the noise level. These include:

1. The pitch axis shaft, the pitch box, strain gauge input terminals, stain gauge amplifier and the CompactRIO were connected to a common electrical ground.
2. Aluminium foil sheaths were added to the strain gauge lead wires bundles to shield the lead wire bundles form interference. The sheaths were also grounded.

3. The cables connecting the CompactRIO and strain gauge amplifier were replaced with shielded cables

These measures significantly reduced the signal noise, but they still not enough as it is evidence in the plots. Therefore, the signal would undergo additional software processing before being analysed.

The first step of the analysis is to identify the likely sources of noise. One of the most common sources of noise comes from the 50Hz mains electricity lines. Other electrical devices, such as mobile phones, are also known to cause interference. The source of the interference may be identified if its frequency is known and this can be achieved by calculating the frequency spectrum using Fourier transforms. Figure 5-21 (Left) shows the frequency spectrum from the test with flapping frequency of 0.3Hz, and flow speed of $0.1ms^{-1}$. A close up view of the spectrum between 0 and 5Hz is shown in Figure 5-21 (Right). The graph did not show any noticeable peak at 50Hz, which suggested the electromagnetic shielding and grounding of the rig were effective in removing interference from the mains electricity supply. A significant peak can be observed at 0.3Hz which matches the flapping frequency of the foil. The additional peaks appeared to be multiple of 0.3Hz, which suggests they are harmonics of the flapping frequency. Since the spectrum does not show any significant peak at high frequency, it suggested the source of high frequency noise was random. A low-pass or band-pass filter will be required to remove this high frequency noise. A number of filtering methods were tested, including an average window, Butterworth and Chebyshev filter.

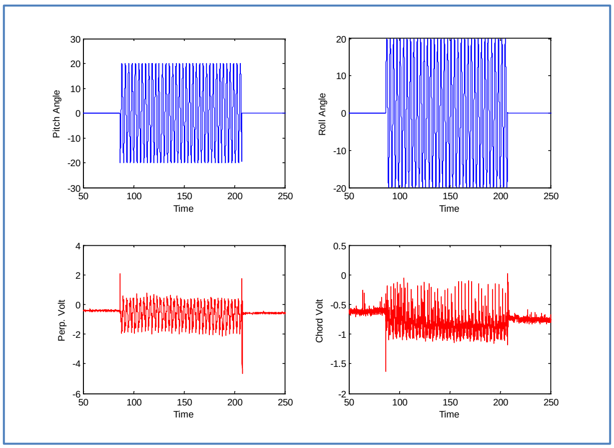

Figure 5-19 - RAW angle and voltage plot – 0.1ms^{-1}, 0.3Hz, 20^{o} pitch.

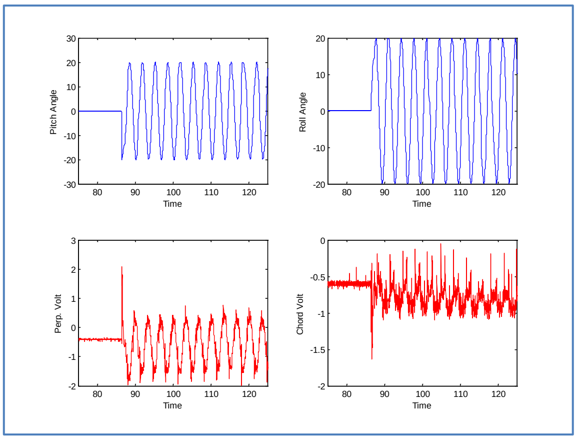

Figure 5-20 – Close up of RAW angle and voltage plot – 0.1ms^{-1}, 0.3Hz, 20^{o} pitch.

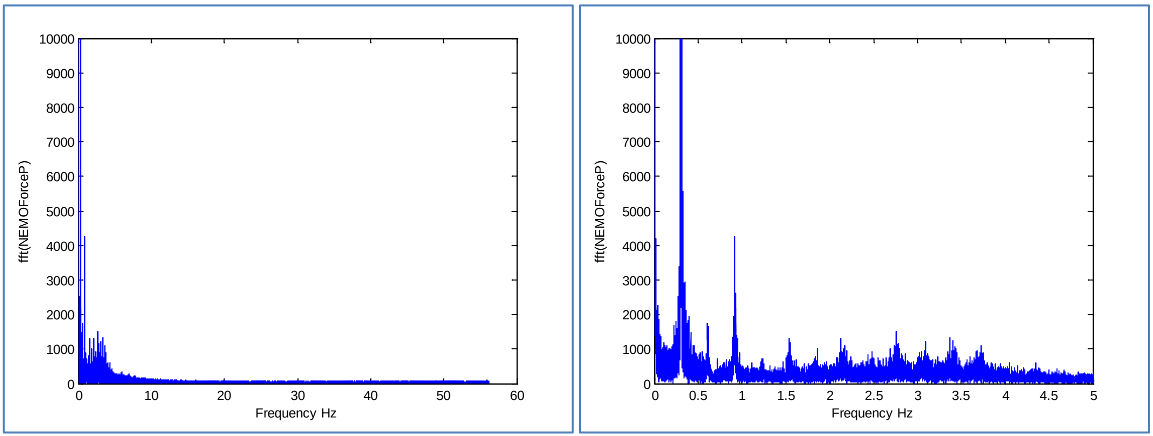

Figure 5-21 – (Left) Frequency spectrum of strain gauge output– 0.1ms^{-1}, 0.3Hz. (Right) a close up

5.4.2.1 *Averaging window*

The averaging window reduces high frequency noise by calculating an arithmetic mean from neighbouring data points and this averaging process were repeated throughout the data span. Whilst the averaging windows can reduce signal amplitudes, the effect could be minimised if the length of the window is significantly shorter than the signal's wavelength. The CompactRIO sampled at a frequency of approximately 100Hz, which was significantly faster than the flapping frequency in the test (0.4Hz). A filter window that is 30 data points long is long enough to remove the high frequency noise but short enough that it would have minimal impact on the quality of the signal. If the noise was truly random, the arithmetic mean of these variations should be zero. Therefore the mean signal level in the filtering window should represent the true signal level at the data point.

Figure 5-22 shows the perpendicular and chord force data from a flapping foil before and after noise filtering. It can be seen the high frequency noise has been reduced, but the post filter data for the perpendicular foil force shows an upwards drift. This signal drift needs to be analysed and removed before the results analysis can take place.

Analysis of the test data shows the zero level before and after each test may be different, so the slow drift observed in the data can be caused by a drift in the strain gauge and amplifier's zero. This drift can be caused by many factors, such as temperature variation and amplifier design. Although some measures were taken against temperature drift (e.g. using strain gauge in pairs and wiring them in a half-bridge circuit that self-compensate), they may not be sufficient. Therefore, a drift correction algorithm is needed to remove this drift in the zero-level.

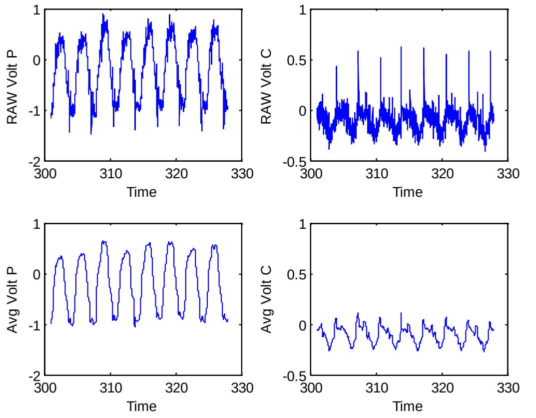

Figure 5-22 - Force data before (Top) and after (Bottom) noise filtering

Static strain gauge readings were recorded for a period between 30 seconds and 1 minute before and after each experiment run to measure the strain gauge response when the foil is not moving. This measurement will provide a zero force level for the experiment. The mean readings during these static periods were used to create linear drift correction lines from which the drifts were subtracted from the experimental results. This method is similar to the method used during the strain gauge calibrations.

5.4.2.2 *Band pass filter*

Since the raw strain gauge data contains interference from high frequency random noise and low frequency drift, they must be removed from the data before the experiment results can be analysed. The averaging filtered only removed high frequency noise, and the drift correction only corrected for linear drift between the start and end of the test. As such there is room for improvement because there is no guarantee the signal drift is linear.

Therefore the investigation also examines the use of band-pass filters, such as Butterworth and Chebyshev filter, for noise reduction. These filters are commonly used in signal processing and could allow signal from a certain frequency range to past almost unhindered, but attenuating frequencies, both high and low, outside that range.

The Butterworth filter is a common signal processing filter known for its flat pass band. The frequency response for a fourth order Butterworth filter with a band-pass of 0.05Hz to 1Hz is shown in Figure 5-23. It can be seen the response fall off quickly below 0.05Hz, but the fall off is much slower at higher frequency. The cut off frequency was set to 0.05Hz and 1.5Hz to ensures the frequency most relevant to the investigation, i.e. 0.2 to 0.4Hz, remained on the flat plateau area of the frequency responds curve.

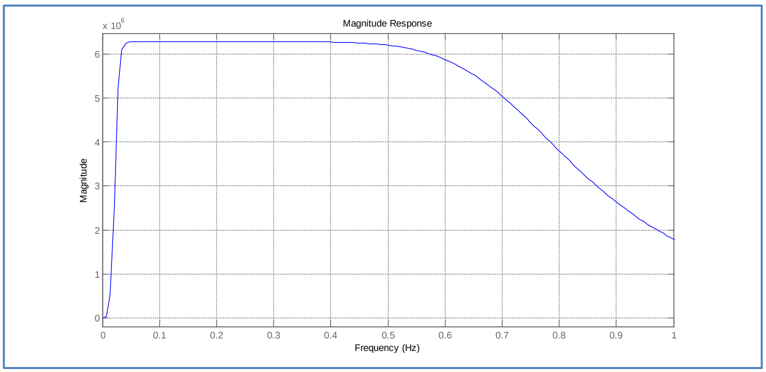

Figure 5-23 – Frequency respond of a 4th order Butterworth band-pass filter – Pass band is 0.05Hz and 1Hz

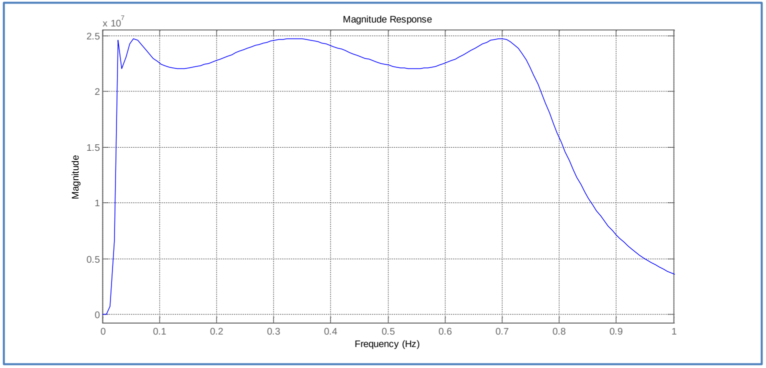

Figure 5-24 – Frequency respond of a 4th order Chebyshev band-pass filter – Pass band is 0.05Hz and 1Hz

The Chebyshev filter is another commonly use signal processing filter. It has a steeper cut off than the Butterworth filter, but it can have a ripple in the pass band. This ripple may cause potential problem when comparing the results from different flapping frequency. Figure 5-24 shows the frequency response of a 4th order Chebyshev filter with a band pass of 0.05Hz to 1Hz. The fall off below 0.05Hz and above 0.7Hz is steeper than that of the Butterworth filter, but the ripple between 0.5 and 0.7 is also quite prominent.

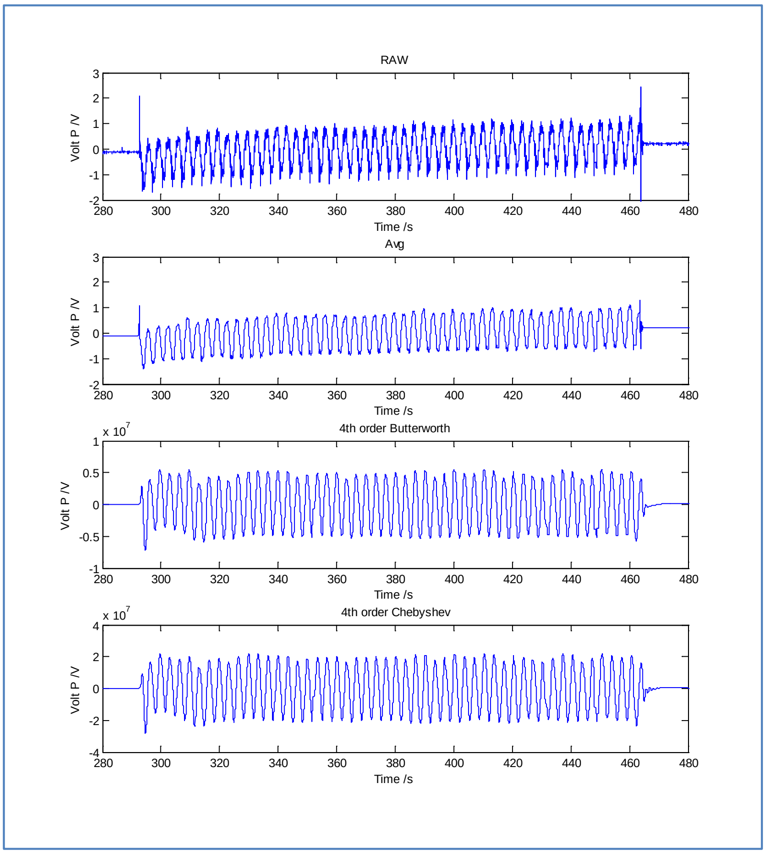

Figure 5-25 – Comparison between filters. Pitch amplitude = 25°, Frequency = 0.3Hz, Flow speed = 0.1ms^{-1}. (Note: the amplitude of the signal was not preserved in the two band pass filters)

Figure 5-25 shows a comparison between the raw unprocessed data and results after they were processed by the three filter algorithm from the beginning of the test to its finish. The raw signal in this test shows a drift during the experiment. The drift is also present in the averaged data, but not in the Butterworth and Chebyshev band-pass filters' result. This suggests the band-pass filter is more effective in removing the low frequency drift than the averaging filter with drift correction.

Figure 5-26 shows a close up of the results from another test. The graph shows, the Butterworth and Chebyshev filters are very effective at removing high frequency noise. However, both Butterworth with and Chebyshev filters did not preserved the signal amplitude which will require further correction by additional algorithms. In addition, both band pass filters also generated a phase shift, which is undesirable because the foil position data and the foil force data need to be synchronised for the analysis. The averaging window was the only one of the three methods that preserved the phase of the oscillation.

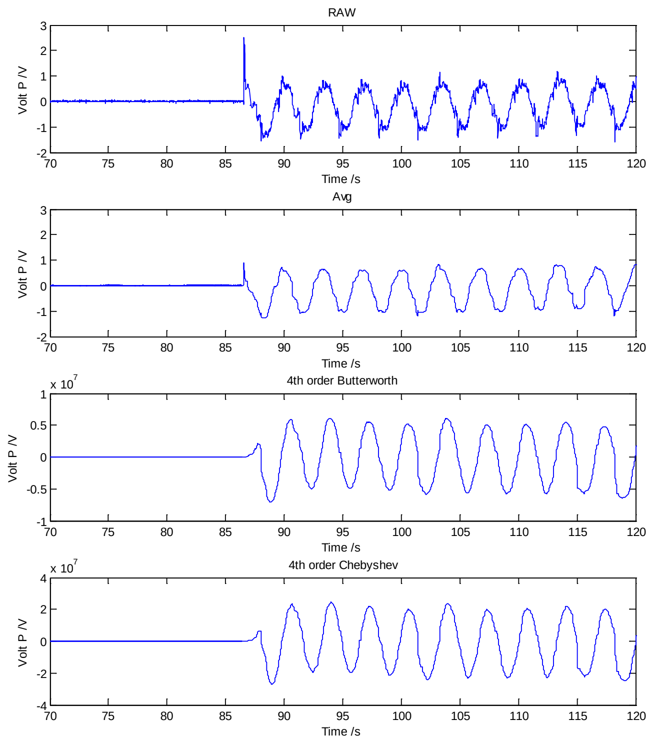

Figure 5-26 - Comparison between filters. Pitch amplitude = 20^o, Frequency = 0.3Hz, Flow speed = 0.1ms^{-1}. (Note: the signal amplitude was not preserved in the two band pass filters)

5.4.2.3 *Summary*

After examining the various noise reduction algorithms, it was found the averaging window appears to be the most effective. Although Butterworth and Chebyshev filters demonstrated better results in reducing high frequency noise and low frequency drift, these filter cause a phase shift in the results. Phase shift is a problem for both band-pass filters, and the drawback of using them outweighs the benefits. Therefore the investigation uses the 30 point averaging window with linear drift correction as the filter used for processing the raw signal.

5.4.3 Angle Measurement

Due to mechanical error in the transmission system, the roll axis is estimated to have a backlash error of 0.7° the yaw axis is estimated to have an error of 1.0° and the pitch axis has an error of 0.8°. The mechanical error was measured using the Wixey digital angle gauge, which has an accuracy of + 0.1° and was calibrated on a calibrated workshop levelling table in University of Southampton and Newcastle University respectively.

5.4.3.1 *Roll Angle Error*

When the chassis was installed, a sprit level was used to ensure the bridge was levelled, but this is not critical because the roll stating position can be adjusted to compensate for minor tilt. When the actuator is stationary, the roll axis angle can be directly measured with a digital angle gauge. This measured value can be used to estimate the error in the position reported by the motor encoder.

The roll axis mechanical error and belt drive slippage error are the two main sources of error in roll. The roll axis mechanical error is caused by backlash error in the gearbox, roll axis shaft keyway connection to the gearbox and to the yaw cage. The problem was reduced when additional grub screws were added to the yaw cage which mostly eliminated the play between the roll drive shaft and yaw cage. However, some of the mechanical play remained in the connection between the roll drive shaft and the roll gearbox. The total play in there roll axis was 0.7° as measured by the digital angle gauge, which represents a percentage error up to 4%.

5.4.3.2 *Yaw Angle error*

The main source of yaw angle error is the connection between the yaw axis drive shaft and the yaw gearbox. Therefore, the yaw axis is normally locked into position using the yaw locking bolt unless the actuator was required to perform three-axis experiment. The mechanical error in the yaw axis is measured to be 1°. This equates to an error between 15 and 30% based on yaw axis motion between 3° and 6°.

5.4.3.3 *Pitch Angle and force measurement error*

Pitch axis angle error consists of small mechanical play in the pitch axis and strain gauge alignment error. The mechanical play in pitch axis was 0.8° which represent a percentage error up to 4%. It is normally assumed that the forces measured by the stain gauges were parallel and normal to the foil chord. However, since the foil was screwed into the pitch shaft and then locked into placed with locking bolts, there is a potential for alignment error in gauge and foil misalignment as it is illustrated in Figure 5-27. When the angle of attack is zero, the lift force will be zero and there would be no perpendicular force as it would be aligned with lift. If the strain gauges were correctly aligned, then the perpendicular gauge force would also equal to zero, while chord gauge force would equal to drag. However, if there was a misalignment, the forces would be shared between the two gauges. A method was devised to calculate the gauge misalignment from these forces by setting the foil to different angles of attack.

However, when this method was employed in the experiment, it was found to be ineffective. When the channel flow speed was low, the foil could not produce sufficient force to generate sufficient response in the strain gauges and the signal was mostly hidden by the background noise. When the foil operated at higher flow speed, the flow becomes turbulent and the signal was corrupted by the forces generated by the turbulence. Therefore it was assumed that the gauges and foil were reasonably aligned.

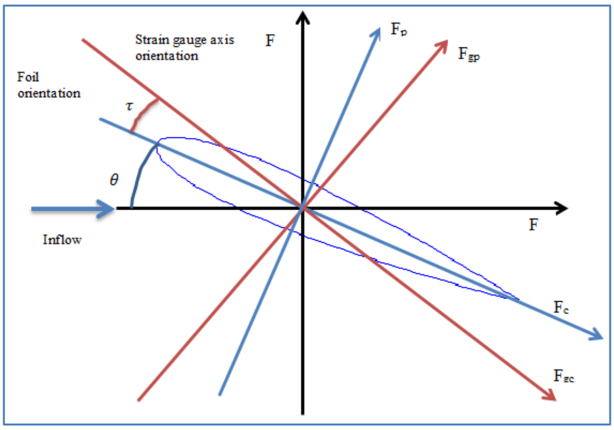

Figure 5-27 – Actual foil forces, and measured foil forces

5.4.4 Channel Flow Speed Measurement

Water flow speed in the Chilworth recirculating water channel is controlled by various combinations of pumps, gate height and valve position. The water speed was estimated by averaging the transit time of floats in the channel over a span of 5 metres. This also provides an estimate of speed variation in the channel. The Chilworth recirculating water channel was only used for test at 0.1ms-1. The actual flow speed measured was 0.122ms-1, with a standard deviation of 0.008ms-1, calculated from 15 samples.

Water flow speed in Newcastle WWC tank is controlled directly from the control console. Since flow measurement equipment was not available for the investigation, the flow speed given by the control console was accepted.

5.5 Summary

The NIMBLE experiment foil actuator was designed and constructed to perform experimental verification of the BET aquatic flight model for two and three axis aquatic flight. The actuator has three independently actuated axes designed to drive a 0.5m NACA 0012 foil in pitch, roll and yaw, up to a speed of $0.5ms^{-1}$ and at a Strouhal number up to 0.8. Higher Strouhal number can be achieved if the flow speed is reduced.

The actuator measures foil forces both parallel and perpendicular to the foil chord using a number of strain gauges. This would be converted to actuator thrust using angular position data from the motor encoders. Strain gauge calibration was carried out using a sliding weight, which produced strain gauge respond lines for two different amplifier settings for each pair of strain gauges. The calibration line’s gradient would be used to calculate foil moment and foil force, which would be used to calculate the thrust coefficient and to verify the predictions made by both the two-axis and three-axis BET model.

Whilst the hardware design expended great effort into minimising the noise level of the strain gauge responds signal, there are still random noises and interference that remains in the signal. A number of different software noise filtering methods were examined, and it was found the best method for removing noise from the signal is through a simple moving averaging window.

The experiment set up is estimated to have a systematic error up to 23%. The main contributors to the error are backlash and play in the mechanical drive train and the inflow velocity at the foil. Both the backlash error and flow velocity error could only be corrected with significant additional expense by replacing existing the worm gear boxes with high precision harmonic gear boxes and modifying the recirculating water channel to reduce turbulence.

Chapter 6: NIMBLE Experiment

6.1 NIMBLE Experiment

This chapter presents experimental results captured by the NIMBLE aquatic flight actuator experiment. 181 different aquatic flight actuations cycles were tested at the Newcastle University WWC tank and University of Southampton's Chilworth Internal Flume. These include 105 two-axis tests and 76 three-axis figure-of-eight tests, each with different combinations of pitch amplitude, flow speed and flapping frequency.

A typical test lasted 4 minutes – 3 minutes were for testing followed by 1 minute of rest. The rest period gives time for the water to calm after the each experiment and reset the conditions for the next test. The test typically produces 36 to 72 complete cycles, which are averaged to calculate the average thrust. The data acquisition system also recorded forces for one minute before and one minute after each test when the pitch and roll amplitudes were set to zero. These recordings of forces acting on a stationary foil in flowing water were used to calibrate the zero level, which is then used to compensate for drifts in the strain gauge amplifier.

The measurement systems for the experiment record time, positions in pitch, roll and yaw, as well as forces parallel and perpendicular to the foil chord. The channel flow speed was measured manually in Chilworth using the timed transit method and automatically in Newcastle using the control console. All other analysis parameters were calculated from these variables, including Strouhal number, foil inflow velocity, foil inflow angle, and angle of attack.

The Strouhal number of each test is calculated by multiplying the oscillation frequency with double roll amplitude at 0.7span and then dividing by flow speed. The amplitude of the flapping motion is the amplitude of the vertical motion in the Y axis. The Strouhal numbers of the tests were calculated using equation (6-1).

$$St_{0.7} = \frac{2((r_{0.7} + r_0)sin\phi_0)f}{U} \qquad (6\text{-}1)$$

The calculation of the foil's angle of attack requires knowledge of the inflow angle, β. The inflow velocities and inflow angles change depending on the distance from the roll axis. However, since angle of attack and Strouhal number were both defined at 0.7 foil span, only the inflow angle at 0.7 span needs to be considered. Unlike the Strouhal number, which was defined using the linear coordinate system centred on the actuator/vehicle, the inflow angle was calculated using a polar coordinate system based around the axis of rotation. The foil position was described by r, θ, ϕ, ψ, which represented the radius from the centre of rotation, pitch angle, roll angle and yaw angle, respectively. The formula used for calculating the inflow angle at 0.7 span is shown in equation (6-2).

$$\beta_{0.7} = arctan\left(\frac{-(r_{0.7} + r_0)}{U + (r_{0.7} + r_0)\dot{\psi}_{0.7}(t)}\right) \qquad (6\text{-}2)$$

Once the inflow angle was found, the angle of attack can be calculated by subtracting the inflow angle with the pitch angle (6-3).

$$\alpha_{0.7} = \beta_{0.7} - \theta \qquad (6\text{-}3)$$

Since the angle of attack varies throughout the actuation cycle, the angle of attack stated in the analysis would be the angle of attack at mid-stroke (quarter period).

6.2 Result Analysis

The aquatic flight experiments were conducted over a range of Strouhal numbers between 0.2 and 1.6, and angles of attack between 15° and 60°, and fixed roll amplitude of 20°. The experiment examined three different symmetrical actuation paths – one two-axis path (0° yaw) and two three-axis figure-of-eight paths (3° and 6° yaw).

The test for the two-axis cycle examined 105 cycles. It covered the range of Strouhal number and angle of attack by carrying out the tests at four different water flow speeds (0.1, 0.12, 0.2 and 0.3ms^{-1}), five different pitch amplitudes (20°, 25°, 30°, 35°, 40°) and five different flapping frequencies (0.20, 0.25, 0.30, 0.35, 0.40Hz). The Strouhal numbers and angles of attack examined are plotted in Figure 6-1.

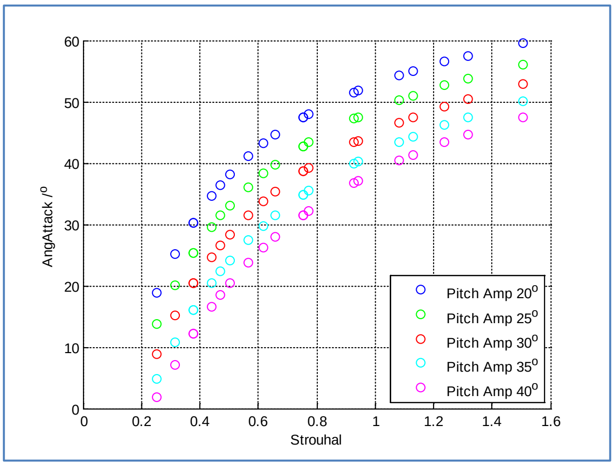

Figure 6-1 - Strouhal number and angle of attack covered by the experiment (with corresponding pitch angle input)

The two-axis cycle is very important in verifying the BET model so much of the effort was spent on it to make sure enough results were gathered for this task. However, due to facility scheduling and time limitations, this leaves only enough time for examining one type of three axis path, so the figure-of-eight path was chosen as the target for the three-axis investigation.

The experiment examined figure-of-eight flapping cycles with 3° and 6° yaw. These paths are illustrated in Figure 6-2. The experiment were first carried out at the Newcastle WWC tank and then supplemented by additional data from a second test in the Chilworth Internal Flume. The initial 3° cycle experiments were tested at a flow speed of 0.1 and 0.2ms^{-1}, with pitch amplitudes of 20°, 30°, and 40°, and at flapping frequencies of 0.2, 0.3, and 0.4Hz. The 6° yaw cycles examined the same range of pitch amplitude and frequency at 0.1ms^{-1}. The second set of experiments tested the actuation cycle at a flow speed of 0.12ms^{-1}, and it examined the cycles with yaw amplitude of 3° and 6°, with pitch amplitudes of 20°, 25°, 30°, 35°, and 40°, and flapping frequencies of 0.2, 0.25, 0.3, 0.35, and 0.4Hz. In total, 42 tests were carried out for yaw amplitude of 3° and 34 were carried out for yaw amplitude of 6°. The angles of attack and Strouhal numbers resulted from the combinations of these parameters are illustrated in Figure 6-3.

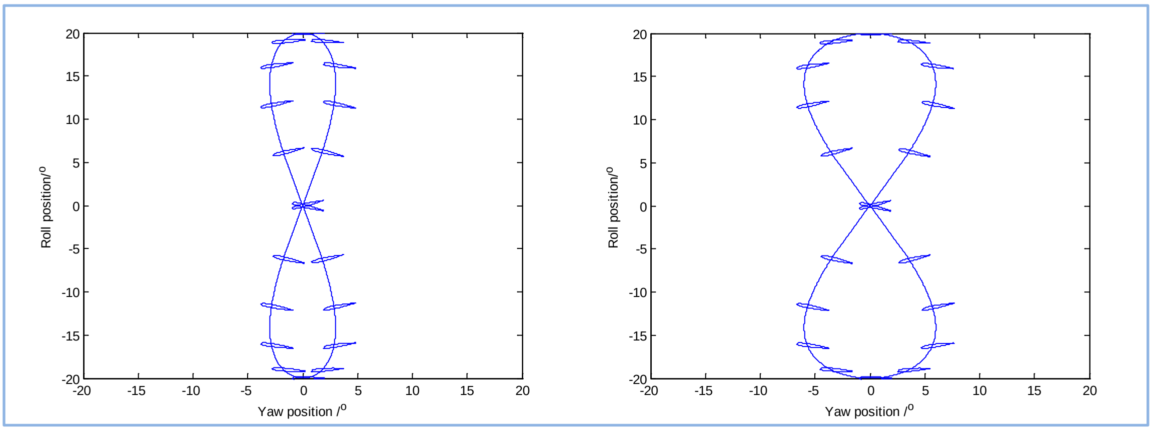

Figure 6-2 – Paths taken by the flapping foil during three-axis aquatic flight test

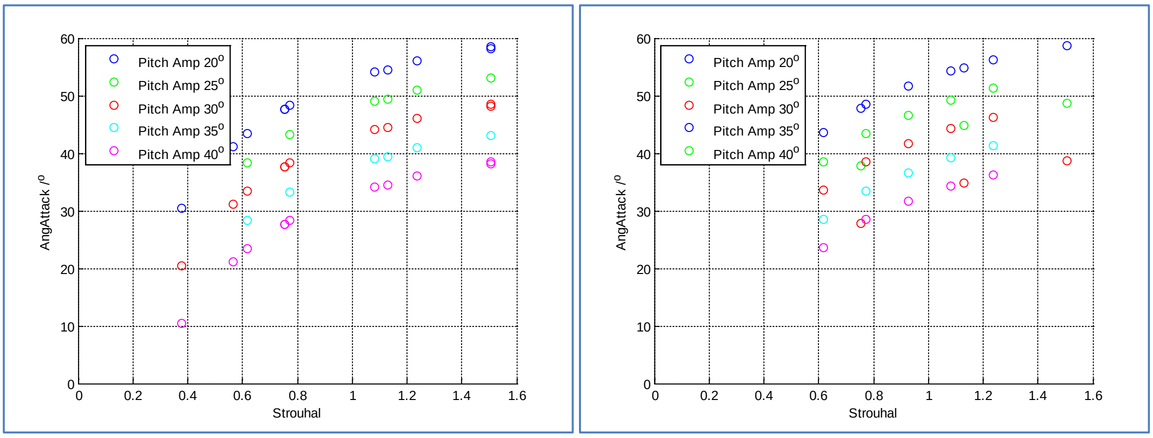

Figure 6-3 - Strouhal numbers and angle of attack covered by 3 axis experiment (Left) 3° figure-of-eight. (Right) 6° figure-of-eight

The experiment results analysis is separated into two parts. The first part analyses the foil forces from individual two axis cycles and compare them against the forces from the equivalent BET model results. This will verify the BET model and show whether the BET model can provide an accurate prediction of the forces involved in aquatic flight. It will also check for sign of added mass, Kramer effect and tip losses in the results. Once the investigation into the foil forces is completed, the investigation will proceed to investigate the thrust coefficients from the experimental results for both two and three axis aquatic flight and verify the three axis result.

6.2.1 Foil Force Analysis

The first part of the experimental results analysis looks at the force produced by the flapping foil aquatic flight using a two-axis stroke path (0° yaw). Different hydrodynamic phenomena produced different effects on the force responds of the foil. The hydrodynamics of aquatic flight following a simple sinusoidal motion should produce a wave form that resembles a sine-squared wave for horizontal forces in X and a sine wave for vertical forces in Y. Figure 6-4 shows extracts of the foil forces measured in the experiment. Figure 6-4 (Left) showed a cycle with 20° pitch amplitude while Figure 6-4 (Right) shows a plot with 40° pitch amplitude. The actuation frequencies for both cases were 0.3Hz.

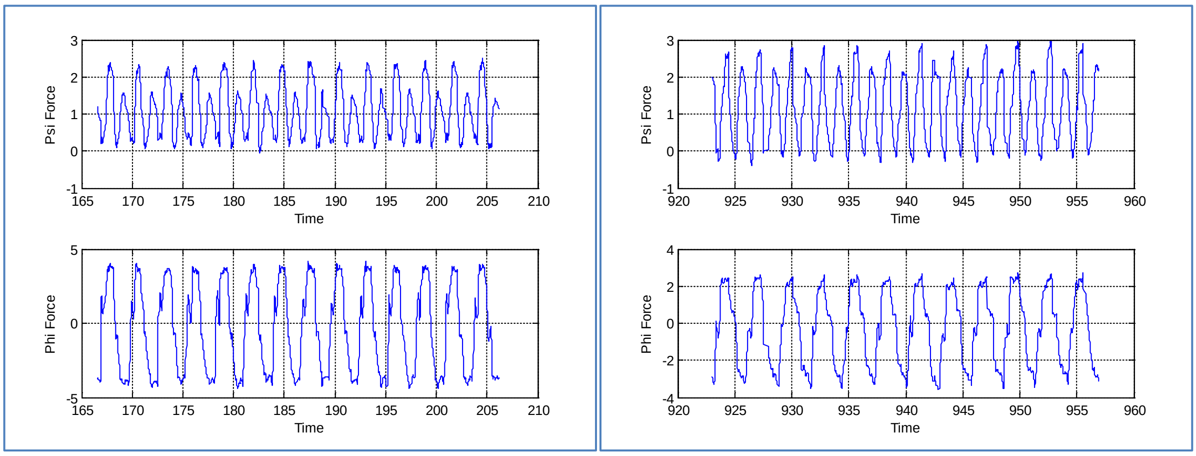

Figure 6-4 – Forces generated by a flapping cycle. (Left) – (0.3Hz, 20° pitch amplitude) (Right) – (0.3Hz, 40° pitch amplitude)

The cycle with 20° pitch amplitude is shown to have sinusoidal and symmetrical forces in the vertical Y direction and the horizontal thrust in X is produced at twice the frequency of the vertical forces in Y, just like the prediction from the BET model. This doubling of thrust frequency is caused by the aquatic flight propulsion producing thrust in both up and down strokes. In theory, the thrust peaks from both up and down strokes should be equal in magnitude, but some experimental results show the peak thrust in one stroke can be higher than the other. From the study of the BET model, three effects are known to the cause distortions in the shape of the force graph, namely added mass, Kramer effect, and asymmetric stroke. Each of these forces will be examined to see if any produce the distortion observed in the experimental results.

Added mass forces are produced by the acceleration of fluid around the hydrofoil. It has the effect of delaying the thrust respond, thereby shifting the peaks backwards. The effect of added mass force on the BET model’s thrust and vertical force is illustrated in Figure 6-5 (Left). The shift in peak position force is quite subtle, and the experimental result is too distorted from noise (despite the noise reduction) for a conclusion to be drawn on whether added mass force is present. However, it can be concluded that added mass forces is not the main cause for the uneven peaks observed in the experimental results

Kramer effect is produced by the viscous forces attempting to restore the Kutta condition in a rotating foil. Figure 6-5 (Right) shows its effect on the thrust and vertical force from the BET model. Kramer effect is a function of the pitch rotational velocity and it can also cause a shift in the peaks positions. The shift is a combination of pitch angular position, pitch velocity and roll velocity. However, the thrust peaks from both strokes are still equal in size so it can be concluded that Kramer effect is not the cause of the uneven peaks.

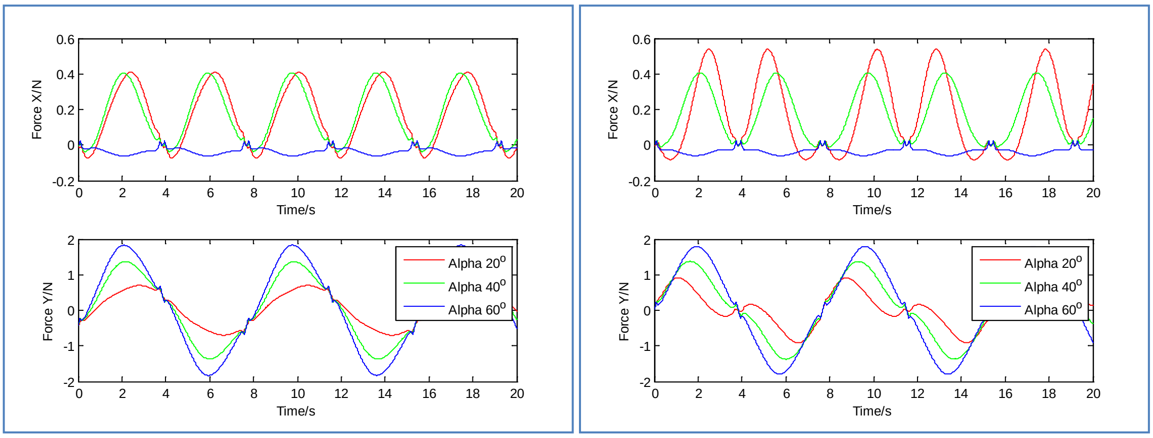

Figure 6-5 – Distortion to the shape of propulsive force cycle caused by: (left) Added mass, (right) Kramer Effect

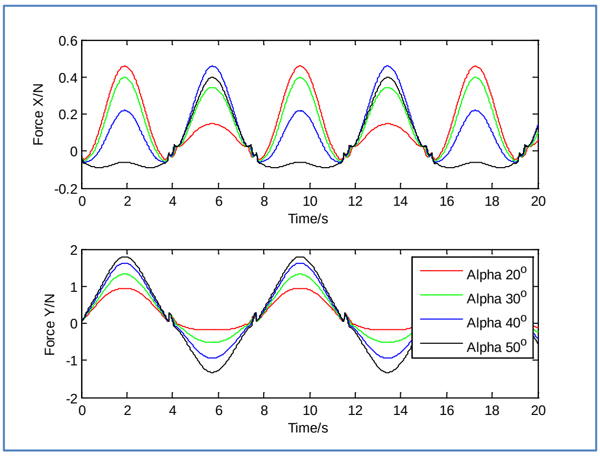

Figure 6-6 – Distortion to the shape of the propulsive force cycle caused by a 10° pitch angle bias. The most distinctive characteristic of angle bias is the unequal peak thrust between up and down strokes and a shift in the forces in Y

This mean the most likely cause for the High-Low double peak is stroke asymmetry. The most distinctive characteristic of a flapping cycle with pitch angle bias is the unequal peaks in X (Thrust) and vertically stretched peaks in Y (vertical force). This is caused by pitch angle bias which created differences in the angles of attack between both strokes. The fact that experimental results for the cycle with 40° pitch amplitude has less uneven peaks that the cycle with 20° pitch amplitude also supported this hypothesis. This because the maximum allowable pitch bias is constant, so the fractional error it causes on a cycle with larger amplitude will be lower than a cycle with smaller amplitude. Figure 6-6 show an example of a cycle with pitch bias of 10°. A 10° biased cycle can reduce C_T by around 20% at $St_{0.7} = 0.6$, while a 5° pitch bias can results in a reduction in thrust coefficient of up to 10% at $St_{0.7} = 0.5$.

In all three possible causes examined, asymmetric stroke is the most probable cause for the uneven peaks observed. Cases with significant pitch bias were discarded but small amount of pitch bias is unavoidable. Whilst pitch bias can affect thrust coefficient, the effect is relatively small if the bias angle is small, so the analysis can continue to analyse these data as long as the bias is not too high.

6.3 Thrust Coefficient Analysis

6.3.1 Two axis cycle thrust coefficient

After examining the results within the individual cycles, the second part of the analysis examines the non-dimension thrust coefficient. The thrust coefficients are calculated from the average thrust of the propulsion cycle and they enable comparison between systems with different configurations. Whilst idealised BET models only need to calculate thrust coefficient using the average force within one completed propulsion cycle because all cycles are identical, every experimental propulsion cycle contains random variation, so every cycle is different. In order to reduce the error caused by these random variations, the foil forces were averaged over multiple cycles.

Figure 6-7 shows the scatter plot of the results from the experiment using two-axis cycle. The left diagram shows the Strouhal number and angle of attack for the various points, and the right diagram shows the corresponding thrust coefficient. It can be seen, aside from a few outliners, most of the results appears to follow an upwards sweeping curve in which the thrust coefficient increase as the Strouhal number increases. This is similar to the pattern predicted by the BET model.

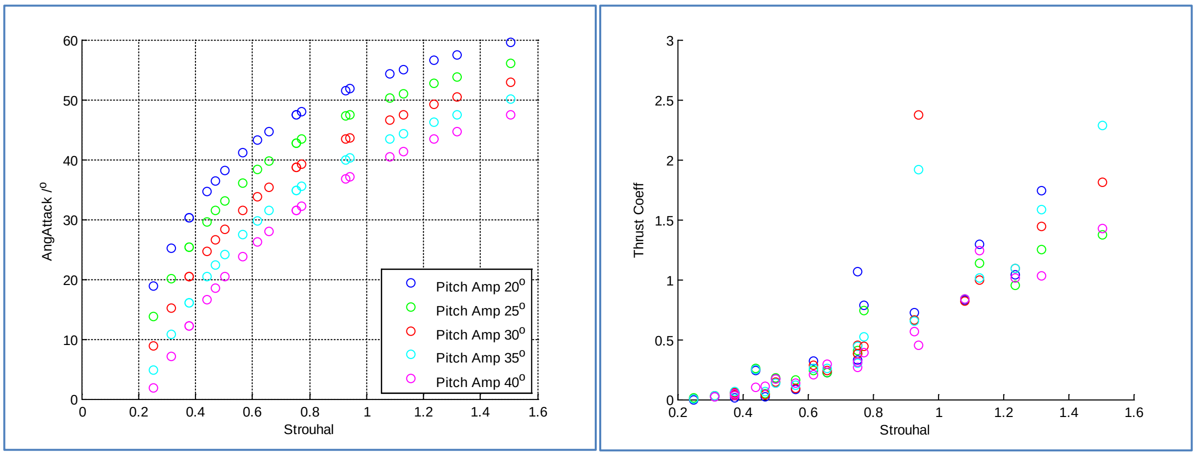

Figure 6-7 – Scatter plot of the thrust coefficient from the two axis experiment.

The two-axis cycle results were interpolated using Matlab Curve Fitting Toolbox with a second order polynomial fit, and the result is shown in Figure 6-8. The resulting surface resembles that of the BET model’s, where thrust coefficient increases as angle of attack and Strouhal number increase. However, the interpolated surface did not exhibit the reduction in thrust coefficient at higher angle of attack that is observed in the BET model, but this may be caused by the narrow range of the angles of attack examined at each Strouhal number.

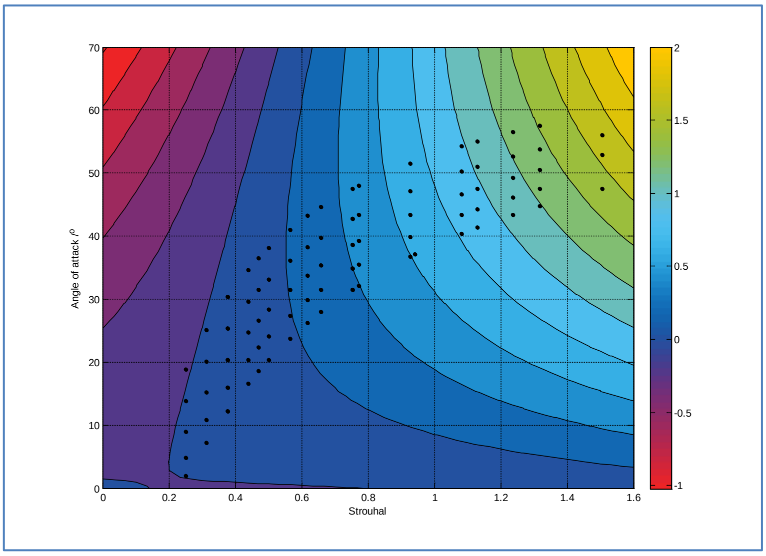

Figure 6-8 – Interpolation of experimental data (solid mesh). The scatter dots indicated the location of the experimental data point.

More importantly, Figure 6-8 shows the thrust coefficients from the experimental results are lower than that predicted by the BET model. Previously in Chapter 3, it was found the BET model predicted lower thrust coefficient than the single element SQS model, which in turn predicted lower thrust coefficient than experimental results reported in the literature. Due to this apparent ‘underestimate’ compared to the literature, the analysis originally came to the conclusion that tip loss may not be affecting a flapping foil. However, NIMBLE’s experimental results suggest otherwise, because the thrust coefficient were less than 1.0 when Strouhal number was less than 1. This is much smaller than the standard BET model results which can achieve a thrust coefficient of 1.6 at Strouhal number of 0.8. This suggests flapping foil may be experiencing tip loss, so a comparison between the experimental results, the BET model, and the BET models with tip loss will be made.

6.3.1.1 *Comparison between experiment and models with different tip loss models*

The first part of the analysis compares the experimental thrust coefficients with the base BET model with no tip loss. A scatter plot of the experimental results superimposed on a thrust coefficient surface plot generated by the BET model is shown in Figure 6-9. The plot shows most of the data points from the experiment had lower thrust coefficient than that of the two-axis BET model without tip loss, but they followed the same trend as the base-BET model, which suggests a thrust reducing phenomenon (e.g. tip loss) may be at work.

The 3D plots shown in Figure 6-9 give a general indication of the differences between the experimental results and the model, but it can be difficult to read in detail, so it is re-plotted as 2D contour plots. Figure 6-10 shows the thrust coefficient contour plots for the for the models results along with the absolute discrepancy between the modelling and experiment results. The models shown in the plots include the results from the BET only model without tip loss, the model with elliptical lift distribution and the model with Prandtl tip loss model. It can be seen from the plots that the BET only model overestimated the thrust coefficient throughout the analysis range, sometime by more than coefficient of 4 higher than the experiment at higher Strouhal numbers. The discrepancy also increases as the Strouhal number increased, so the cause of the error cannot be explain by random experimental errors alone. This is evidence that other factors are causing the large discrepancy.

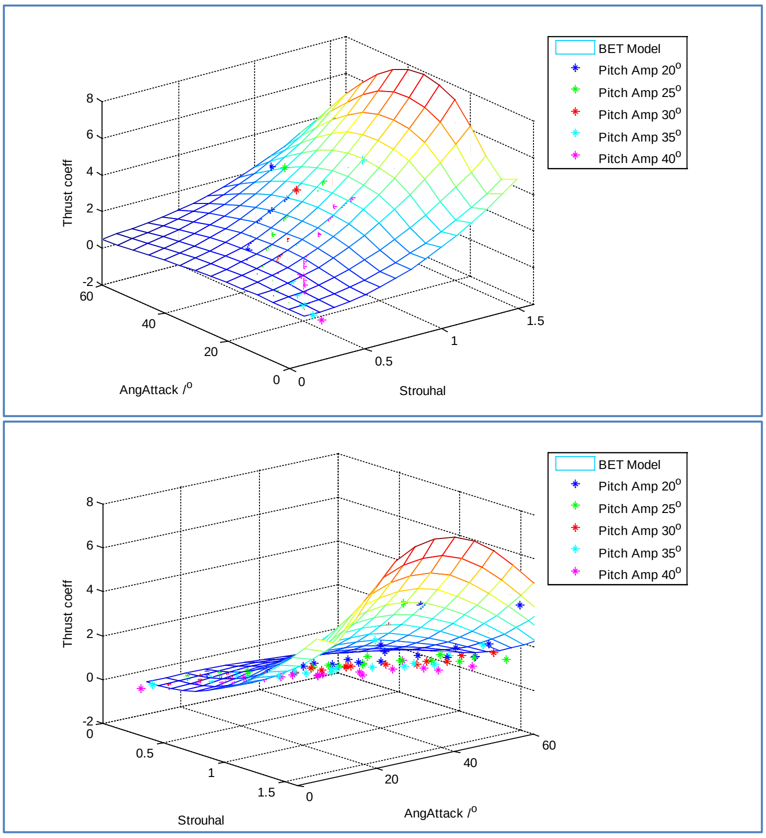

Figure 6-9 – Comparison of the BET model without tip loss and the experimental results. (Bottom diagram is a rotation of the top)

The main candidate for the cause of the discrepancy between the experiment and the BET model is tip loss. It can be seen from the discrepancy is greatly reduced when the tip loss models are enabled. Rather than overestimating the results throughout the analysis range, the absolute discrepancy has become a mix of over- and under-estimates, which suggest the flapping foil do experience tip loss during propulsion.

In addition to the dependency on Strouhal number, the absolute error plots also show the error increases as the pitch amplitude increases. The discrepancy is highest for the cycles with 40° pitch amplitude, which produces the most negative absolute errors. The magnitudes of the error reduce as pitch amplitude decreases. However, in many cases the cycles with 20° pitch amplitude also show higher absolute errors than the cycles with intermediate pitch amplitudes, and often underestimate the experimental results for models with tip loss calculation. Random mechanical error affects the cycles with smaller pitch amplitudes than cycles with larger amplitudes, which could explain why the errors for the cycles with 20° pitch amplitude appear higher than those from cycles with intermediate pitch amplitudes.

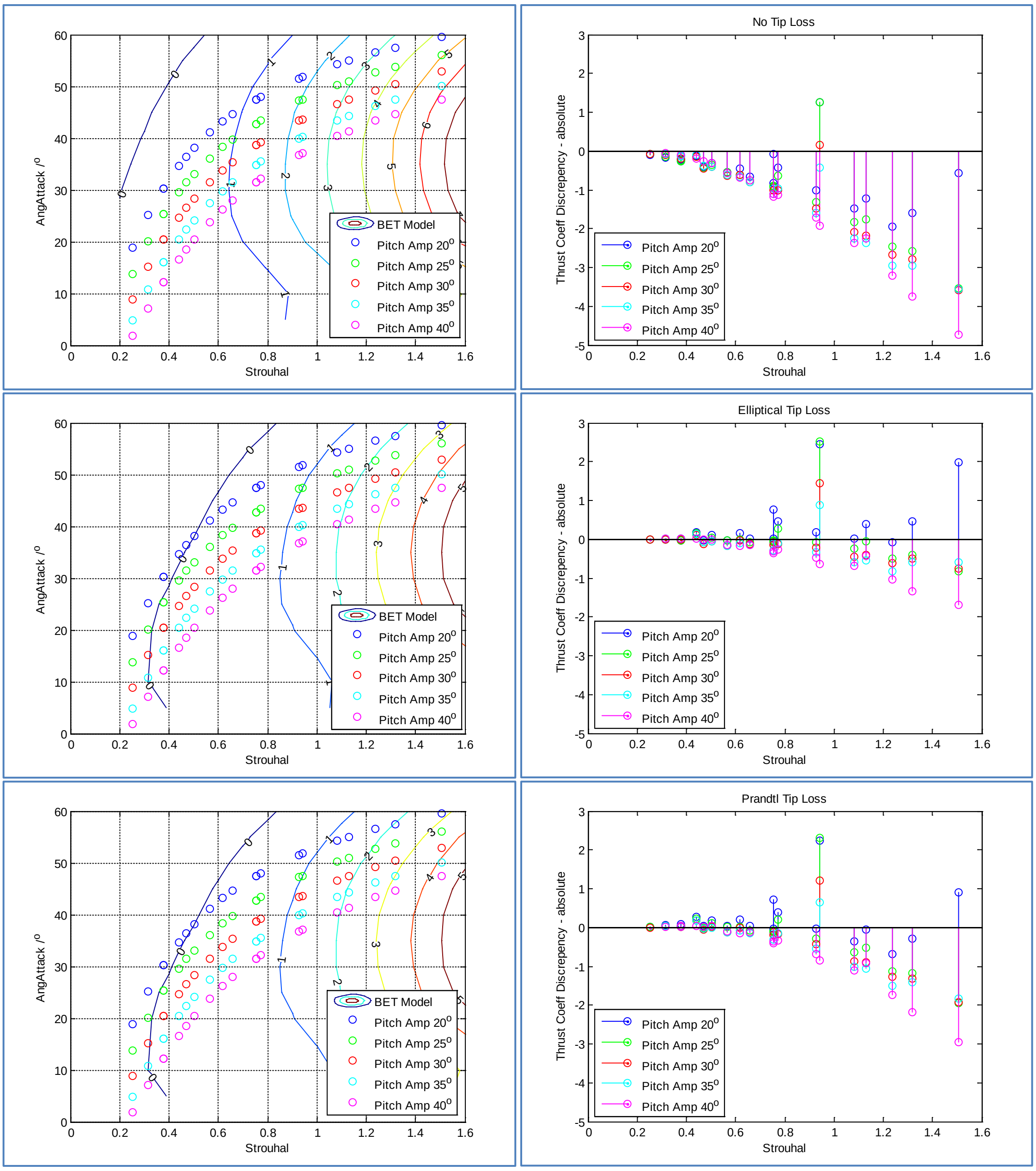

Figure 6-10 – (Left column) Contour plot of the BET model results and scatter plot of the experiment data points. (Right column) Differences between the modelling and experimental results.

6.3.1.2 *Fractional Error*

Since the absolute errors between the model and the experiment appear to be Strouhal number dependent, it would be useful to calculate the fractional error between the two to account for this discrepancy. The function for calculating the fraction error is listed in equation (6-4).

$$\delta C_{T,F} = \frac{C_{T,Exp} - C_{T,Model}}{C_{T,Model}} \tag{6-4}$$

Figure 6-11 shows the factional error between the experiment and the model. The left column shows the full range of the fractional error, while the right column shows a close up with Y-axis restricted to between -1 and +1. The plot for the BET only model shows the model overestimated the thrust coefficient across the range by around 70%. If the absolute error plot was examined, the cycles with pitch amplitude of 40° would appear to have the highest discrepancy, but when the fraction error plot was examined, the errors of the 40° cycles appear to be consistent with those from the other cycles.

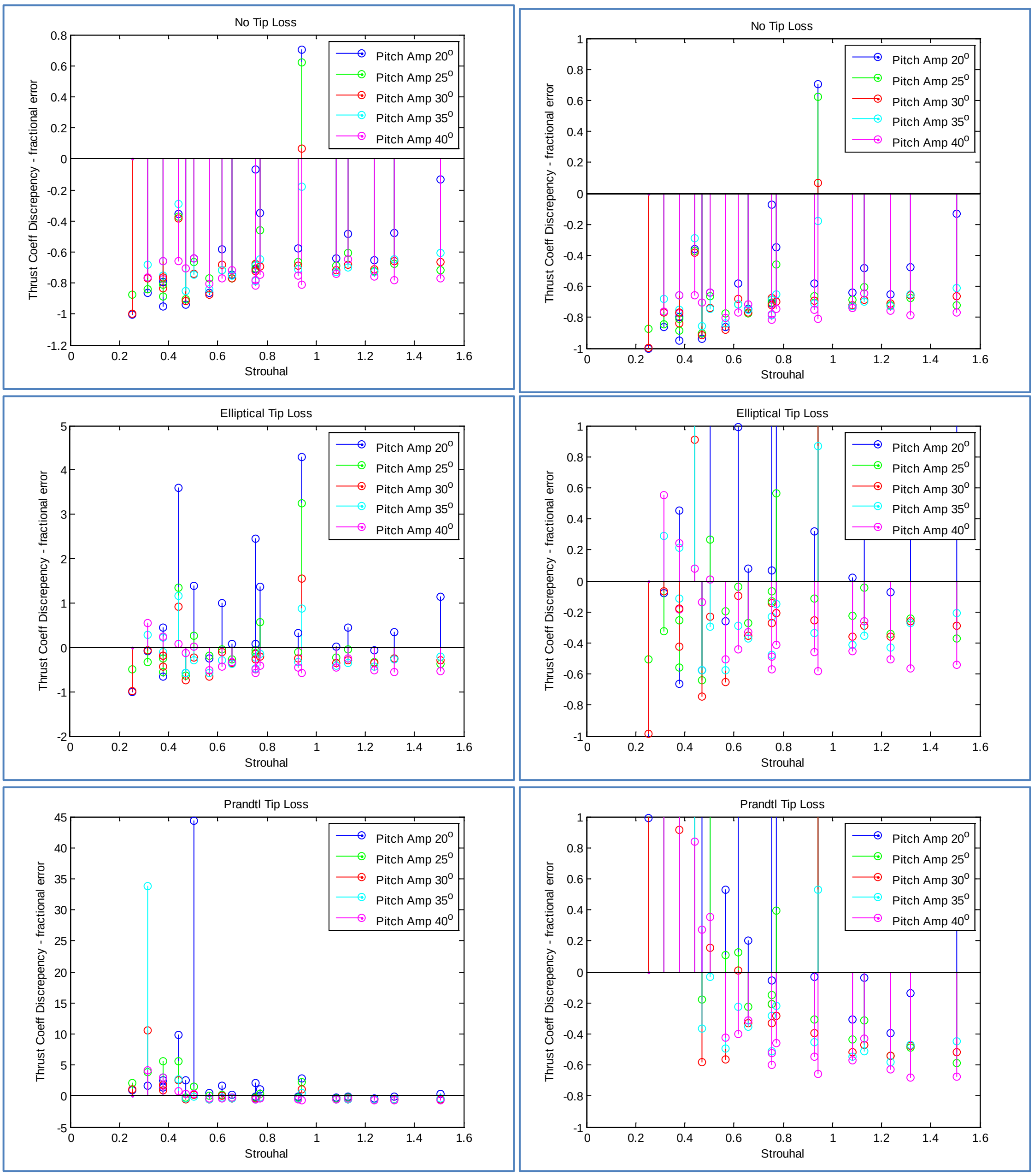

Figure 6-11 – Fractional error between modelling and experimental results. (Right column) – Full Range, (Left column) Y-axis restricted to between -1 and 1.

When elliptical lift force distribution was enabled, the absolute discrepancy between the experiment and modelling results decreased. The results also changed from a general overestimate to a mix of over- and under-estimates. This is reflected in the plot for fractional error. The model with elliptical lift distribution over estimates the experimental results by approximately 30%, which is much smaller than the average fractional error from the model without tip loss.

Whilst the absolute error for cycles with 40° pitch amplitude was quite large, it was reduced significantly when the error is converted into fractional error. The fractional error shown by the cycles with 40° pitch amplitude is comparable to those with smaller pitch amplitude. By contrast, the cycles with 20° pitch amplitude show much higher fractional errors between the model and experimental results than cycles with other pitch amplitude. Whilst the absolute error for the cycles with 20° pitch amplitude is comparable to those for cycles with 40° pitch amplitude, the thrust coefficient at higher angles of attack, as represented by the 20° cycles, was lower, which increase the fractional error of the 20° cycle.

The fractional errors produced by the model utilising Prandtl tip loss model is slightly higher than that using the elliptical tip loss model, at around 40% at higher Strouhal number. The fractional error at lower Strouhal numbers are very high because the model predicted thrust coefficient closed to zero at low Strouhal number, which significantly reduce the denominators in the calculation. In particular, Figure 6-10 shows experimental results from Strouhal numbers of 0.3 and the results from cycles with pitch amplitudes of 20° and 25° at Strouhal number up to 0.6, were positioned almost directly on top of the contour line which represent a thrust coefficient of zero. Division by these small denominators can exaggerate any small random errors and lead to very high fractional error. This is supported by the fact that the absolute errors observed at those points were very small. The problem stabilised at Strouhal number above 0.6 and the error settles at around 40% overestimate. Fractional errors from Strouhal numbers below 0.6 can be ignored due to their proximity to the zero contour.

The plots with Y-axis limited to between -1 and +1 show the fractional errors for the model with Prandtl tip loss is very similar to that from the model with elliptical tip loss, with a mix of over and under estimate. The error from the model with elliptical tip loss is smaller, but it not enough to rule out the viability of the Prandtl tip loss model at this stage.

6.3.1.3 *Mean and median of fractional error*

The plots in Figure 6-11 show the fractional error for every data points in the experiment, and it can be difficult to read due to the amount of information it contains. Figure 6-12 shows the plots for the averages of the fractional errors taken at each Strouhal number. This will give a better indication on how the errors are affected by changes in the Strouhal number. The plots included the median and mean error. The former is less affected by outliner, whilst the latter gives an indication of the mean error at each angles of attack tested at each Strouhal number.

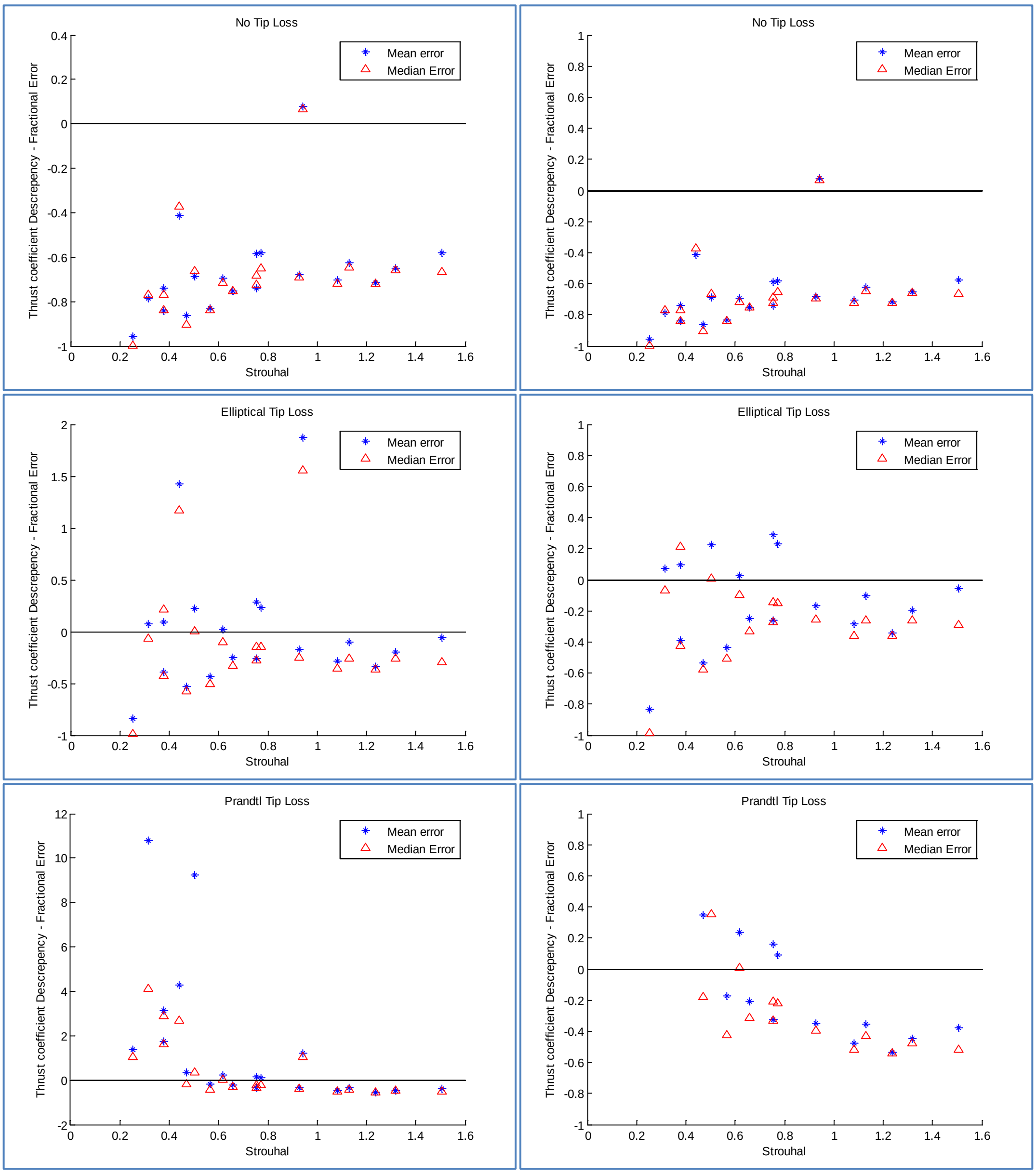

Figure 6-12 – Mean and Median of the fractional error between experiment and modelling results. (Right Column) – Full range, (Left column) – Y-Axis limited from -1 to +1

Like the plots in Figure 6-11, there are significant differences in the ranges of error covered by each of the three models, especially in the case of the Prandtl tip loss model, where division by denominators close to zero at smaller Strouhal number made the fractional error very large even though the absolute error is very small. As Strouhal number increases, the fractional error decreased and level out. The mean and median error settled at around -70% for the model without tip loss, and they were reduced to -40% when tip loss modelling was enabled.

6.3.1.4 *Error distribution at different pitch amplitudes*

In addition to looking at how errors are affected by Strouhal number, the investigation also looked at how the error is affected by different pitch amplitudes. Random mechanical errors have greater effects on the overall error when the pitch amplitude is small, so the deviation is expected to be greatest when the pitch amplitude is at its smallest. The errors will gradually decrease as the pitch amplitude increase. Figure 6-13 shows the averaged mean and median of the differences between the experiment and the model at the five pitch amplitudes examined.

In both cases the error is largest when the pitch angle is small. At a pitch amplitude of 20°, the mean error for the cases without tip loss is around -56%, whilst the differences between the Prandtl tip loss model and the experimental results are at its highest at over 300%. However there is a significant spread in the error for the model with Prandtl tip loss, and there are significant differences between the mean and median errors. The maximum median error for the Prandtl tip loss model is less than a third of the value of the mean error.

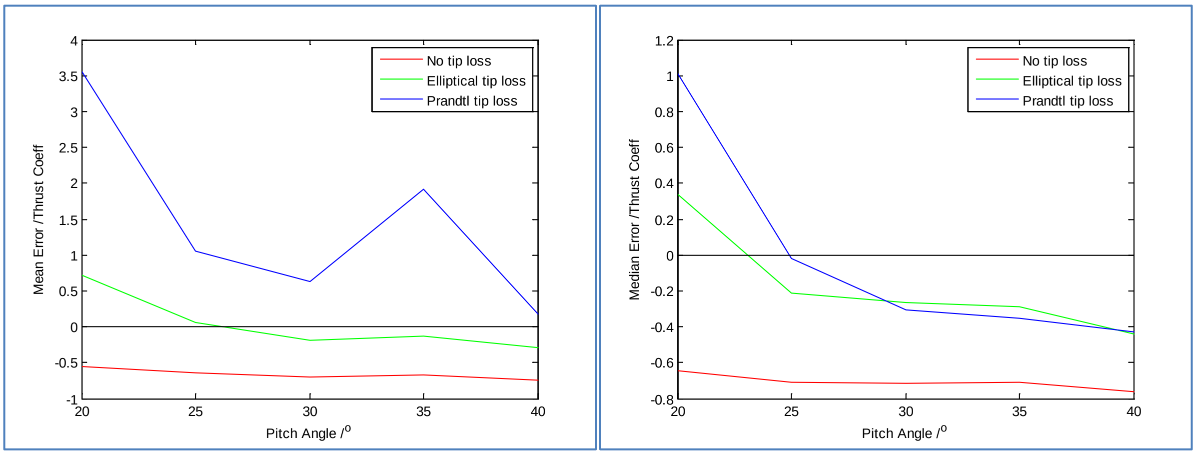

Figure 6-13 – Mean and median error between experimental and 2-axis modelling results.

As the pitch amplitude increases the error decreases, the mean and median errors for the model without tip loss is around -75% for the cycles with pitch amplitude of 40°. Results from the model with tip loss show smaller errors, with the median error for both elliptical and Prandtl tip loss settled at -45%.

The standard deviations of the errors are shown in Figure 6-14. The results from the model without tip loss show the lowest fluctuation. This is because that model's thrust coefficients are highest among all the models so the results is less affected by division with a small denominator which can bring out smaller random fluctuation. This is followed closely by the model with elliptical tip loss.

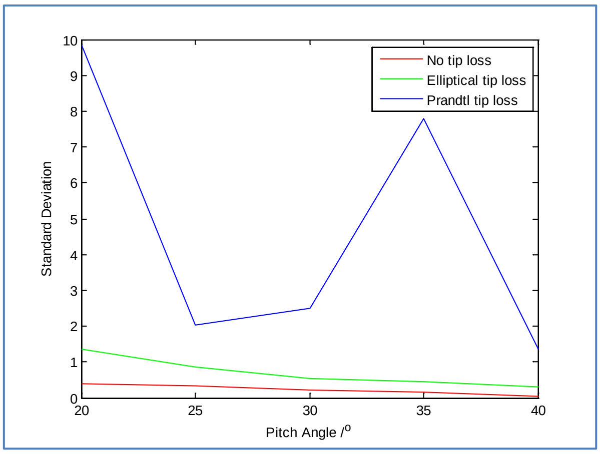

Figure 6-14 – Standard deviation of the error between experimental and the 2-axis modelling results

Overall, the model with elliptical lift distribution shows the best match to the experimental results when the result is analysed in terms of pitch amplitudes. The mean and median errors are consistently low and the standard deviation shows the results have a relatively low spread. The error and scatter is highest at low pitch amplitudes where random mechanical errors have the greatest effect. The pitch axis has up to 1° of mechanical play, which translates to 5% uncertainty for cycles with pitch amplitude of 20° and only 2.5% for cycles with pitch amplitudes of 40°.

6.3.1.5 *Summary of the two axis cycle's results analysis*

Examination of foil forces shows the experimental results exhibited similar pattern to the BET model's predictions. The horizontal thrust forces were mostly positive and it cycled at twice the frequency of the vertical forces in Y and the actuation frequency of the pitch and roll motion. Some experiment cycles deviated from the norm and produces different level of thrust for up and down stroke. This was attributed to the small residue pitch bias and should have minimal impact on the overall thrust.

After examination of forces within a cycle, the analysis compared the thrust coefficient from the experiment to that of the BET model. The experimental results show the BET model without tip loss overestimated the thrust coefficient. This is opposite to the other results reported in the literature which suggested the NIMBLE BET model should underestimate the thrust coefficient. In order to achieve a better fit, the tip loss sub-models for the BET aquatic flight model were enabled. It found the BET models with tip loss provided a better match for the experimental results, with average difference between the experiment and model reduced to around 25%.

Whilst the experimental results showed the thrust coefficient would increase if the Strouhal number increased, it did not show the reduction in thrust coefficient at higher angles of attack that was also shown by the BET model. This is thought to be a result of the quasi-steady approach failing to capture dynamic stall. However, the range of angles of attack and Strouhal numbers examined were distributed along a narrow band, so some behaviour may have been missed. Furthermore uncertainty caused by experimental error may also contribute to discrepancy.

6.3.2 3° Yaw Figure-of-Eight Path Thrust Coefficient

The second actuation path to be investigated is the three-axis figure-of-eight actuation paths with 3° of yaw. A total of 42 points were tested between a Strouhal number of 0.4 and 1.6. The experimental results’ thrust coefficients and the corresponding angle of attack and Strouhal numbers are shown in Figure 6-15.

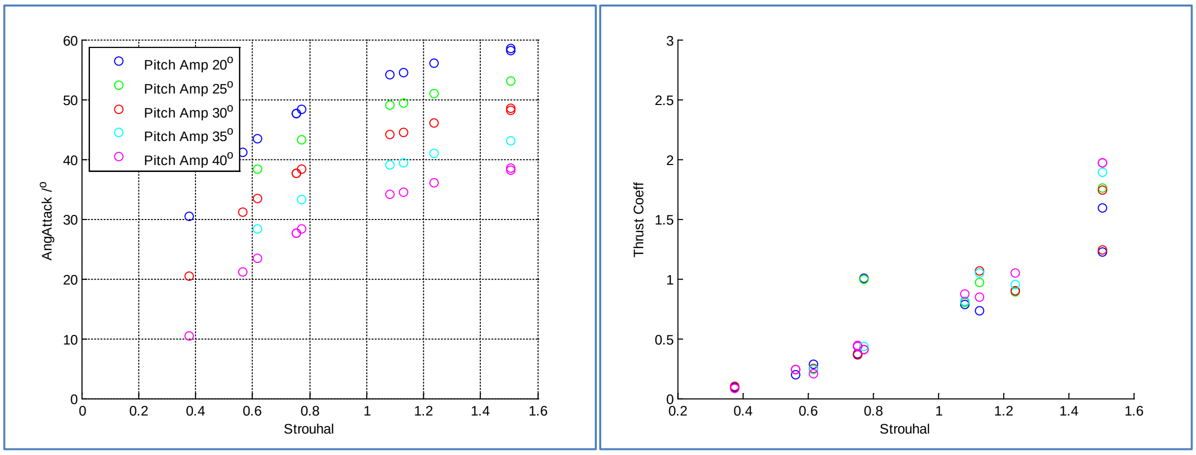

Figure 6-15 – Thrust coefficients and corresponding angles of attack and Strouhal numbers of the experimental results

6.3.2.1 *Comparison between experimental and modelling results*

The differences between the experimental and modelling results are shown in Figure 6-16. Similar to the results from the two-axis cycle, the absolute errors between model and experiment increase as Strouhal number increase.

Tip loss modelling was found to be very important again as the model without tip loss overestimated the thrust coefficients throughout the range of Strouhal number analysed, whilst the models with Elliptical or Prandtl tip loss contains a mix of over- and under-estimates at Strouhal numbers below 0.8. The absolute error is also smaller for both cases with tip loss. At Strouhal numbers above 0.8, the model with Prandtl tip loss overestimated experimental results, while the model with elliptical tip loss still contains a mix of over- and under-estimations.

When the experimental results’ pitch amplitudes are considered, it was found the cycle with pitch amplitude of 20° produces the lowest absolute error. However, unlike results from the two-axis cycle, further increase in pitch amplitude do not necessary lead to higher discrepancies. Instead, the discrepancies depend on the relative positions of the experiment point compared to the modelling results. Generally, the differences in thrust coefficient predicted by model and measured in experiments are highest near the model’s maximum. This means a number of cycles with intermediate pitch amplitudes produce greater discrepancy than cycles with pitch amplitudes of 20° or 40°.

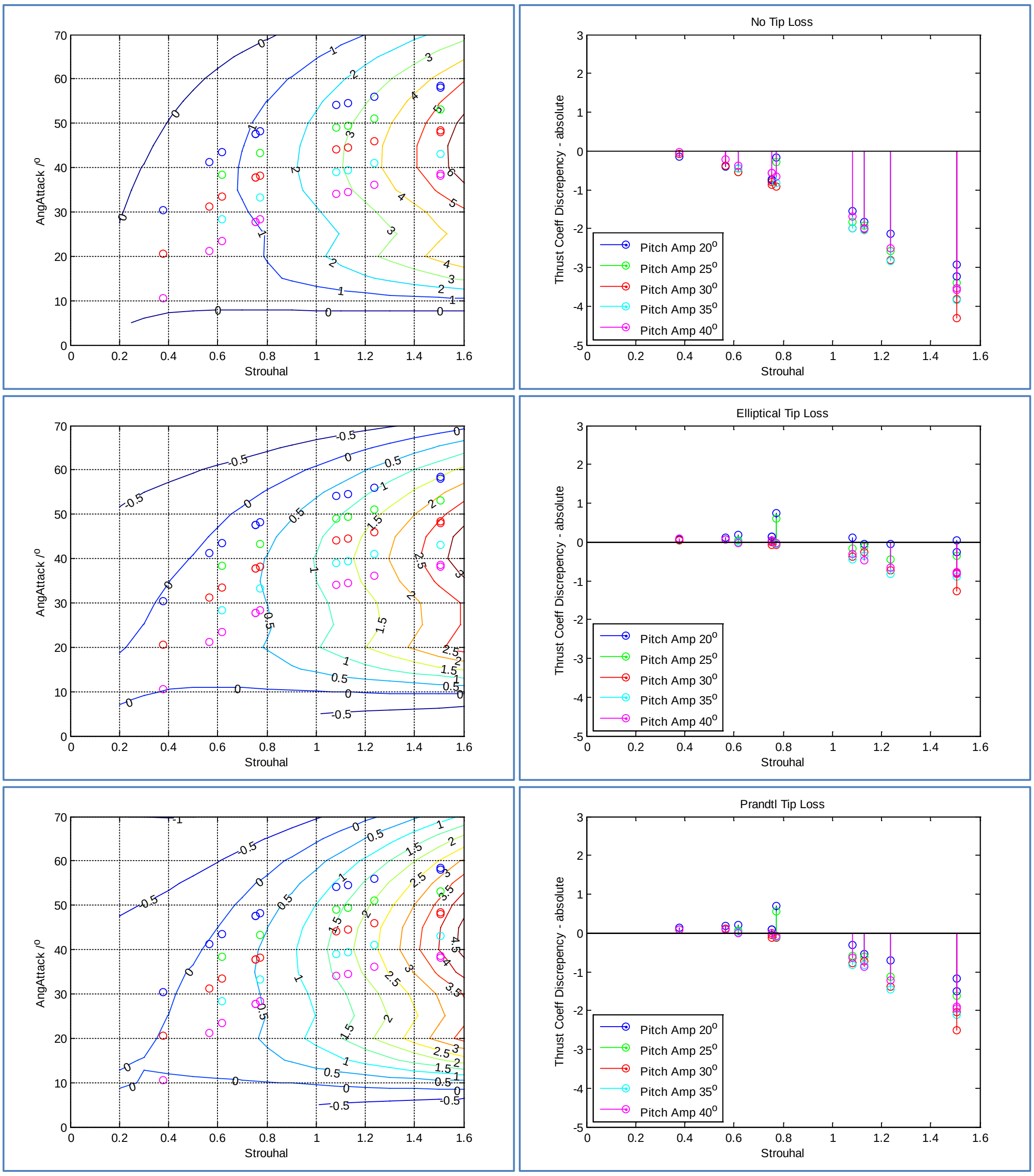

Figure 6-16 - (Left column) Contour plot of the BET model results and scatter plot of the experiment data points. (Right column) Differences between the modelling and experimental results.

6.3.2.2 *Fractional Error*

The absolute errors between the experiment and model are re-calculated into fractional error and plotted in Figure 6-17. The model without tip loss is shown to overestimate the experimental results by an average of 64%, and the differences gradually increase as Strouhal number increases. Unlike the examination of the absolute error, changes in the pitch amplitudes do not appear to have a significant effect on the magnitudes of the fractional error.

When the results from the models with tip loss are analysed, it was found both models with tip loss are shown to contain a mix of over- and under-estimates at Strouhal number less than 0.8. This shows the model predictions coincide with the experimental results. The large fractional errors in this region are caused by the very small thrust coefficient predicted by the model, which amplified the small random variations into large fractional errors. The absolute error plots in Figure 6-16 shows the actual errors in this range are very small.

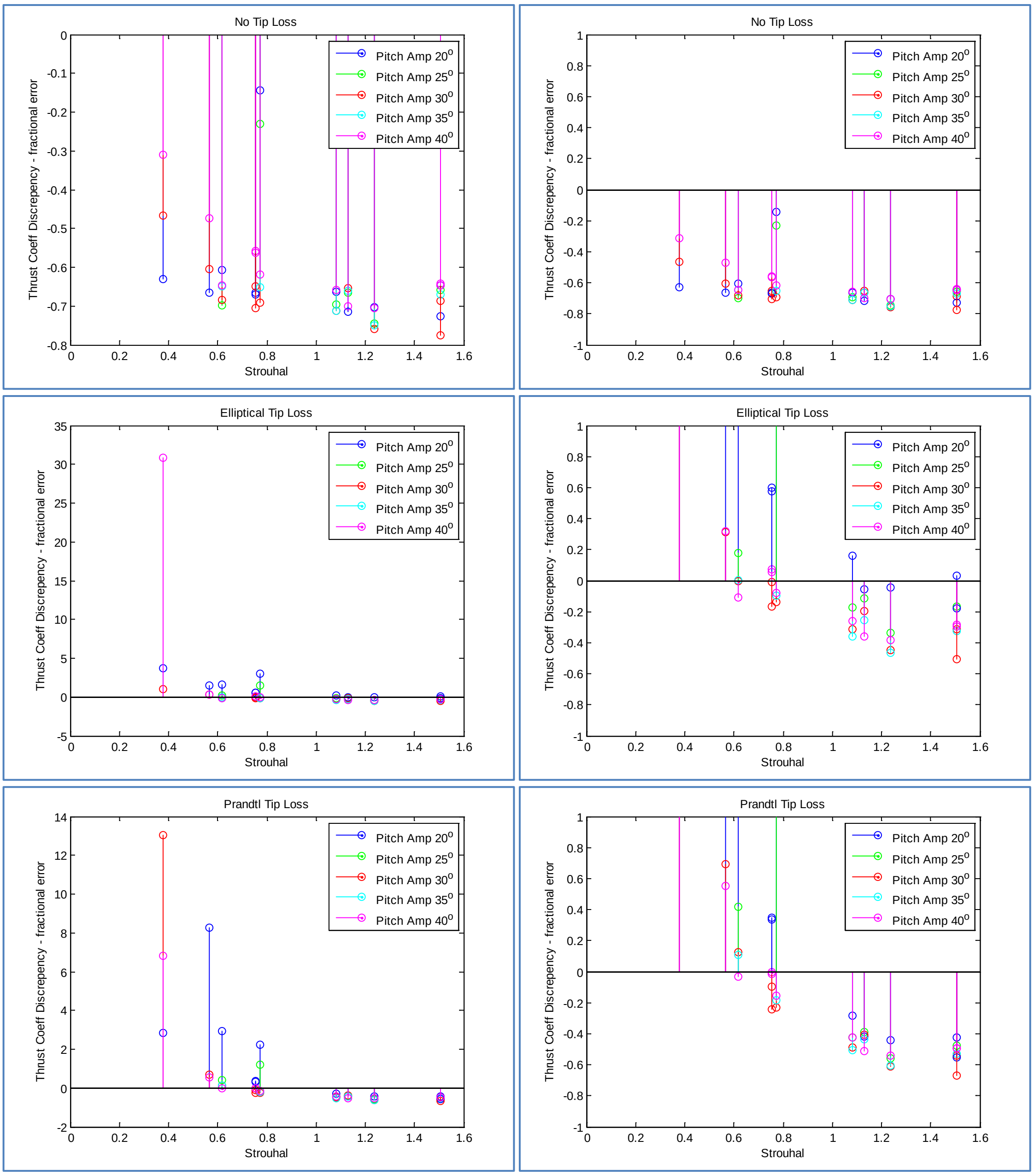

Figure 6-17 – Fractional error between modelling and experimental results (Left column) Full Range, (Right column) Y-axis limited to between -1 and 1.

When Strouhal number increases above 0.8, the models begin to over predict the thrust coefficient consistently by 20%-40%. The model utilising elliptical tip loss model shows less over predictions (20% overestimate) than the model utilising Prandtl tip loss (40% overestimate), and some experimental results remain higher than the results predicted by the elliptical tip loss model.

The mean and median errors of the models with tip losses were also examined and the two can be very different due to significant numbers of ‘outliners’. The fractional errors are very high at low Strouhal numbers due to the very small model thrust coefficients. In particular, small random errors are significantly amplified close to the zero thrust coefficient contour line.

6.3.2.3 *Error Distribution at different pitch amplitudes*

In addition to examining the effect of Strouhal number on the discrepancy between model and experiment, the investigation also analyse the effect of pitch amplitude. The pitch amplitude is one of several factors that determine the angles of attack which also include the Strouhal number. If the pitch amplitude remains constant, the angle of attack can increase if the Strouhal number was increased.

It can be seen from Figure 6-18 (Left, Centre) that the mean and median errors for the cycles without tip loss is very stable and level. On average the model show an overestimate of around 65%, and do not appear to show significant relationship between pitch amplitude and error. The standard deviations are also very small (approximately 0.1), which suggest there is very little spread in the results.

On the other hand, the models with tip losses show much greater variation with respect to pitch amplitudes. The mean errors of the models can be very large, but this is expected due to the large fractional errors and scatter previously observed at lower Strouhal numbers. Due to the significant spread in the results, the median will be a better average for analysing the average thrust coefficient error. The median errors of both models with tip loss are highest at pitch amplitude of 20°, but they are reduced as the pitch amplitude increase. The model with elliptical tip loss produces results that are less than 20% higher than the experimental results. The model with Prandtl tip loss performed worst and overestimated the results by an average of 30%. Nevertheless, despite showing higher variation in the fractional error, the magnitudes of fractional error for the two models with tip loss are smaller than the model without tip loss, which means these two models are better candidates for studying aquatic flight.

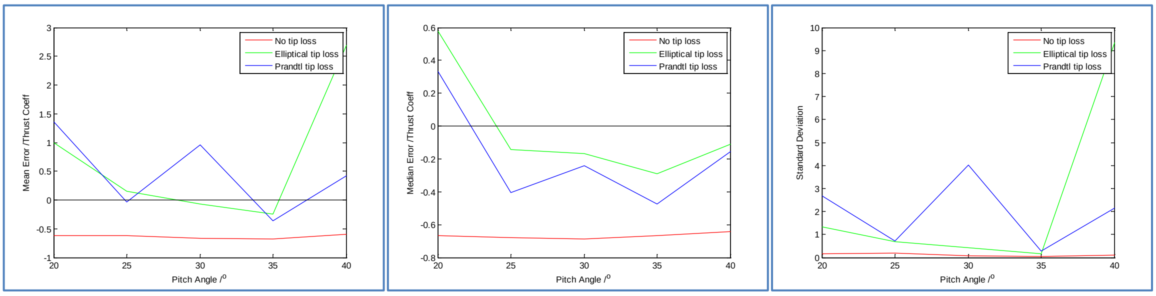

Figure 6-18 – Mean, median, and standard deviation of the fractional error of the three axis aquatic flight propulsion with 3° yaw amplitude

The standard deviation of the fractional error is shown in Figure 6-18 (Right). The plot shows the spread from the model without tip loss is lowest among the three tested. Meanwhile the models with tip loss show much higher standard deviations, suggesting a more significant spread. This is expected as the low modelling thrust coefficients at low Strouhal numbers significantly amplify the effects of small random variations that existed in the experimental dataset. The standard deviations of fractional error gradually decrease as the pitch amplitude increased. This can be explained by the reduced uncertainty from small mechanical errors. The pitch axis have mechanical play up to 1°, which represents 5% uncertainty in the pitch position for cycles with pitch amplitude of 20°. This uncertainty is reduced to 2.5% when the pitch amplitude increased to 40°, and as such the error caused by mechanical play is reduced as the pitch amplitude increase, which in turn reduces the error's standard deviation.

6.3.2.4 *Summary of figure of eight path with 3° yaw*

The investigation of the three-axis figure-of-eight actuation path with 3° yaw examined 42 combinations of pitch amplitudes and flapping frequencies. Like the two axis cycle, it is necessary to include tip loss modelling in the calculation, or else the model would significantly overestimate the thrust coefficient. Adding the tip loss model would reduce the thrust coefficient overestimate from 64% down to around 20% (Elliptical tip loss).

Results from the pitch amplitude analysis shows the error generally decrease as the pitch amplitude increase. This suggests mechanical play is a factor that contributes to the error, as the significant of the 1° uncertainty from mechanical play increases as the pitch amplitude decreases.

6.3.3 6° Yaw Figure-of-Eight Path Thrust Coefficient

The second figure-eight-actuation path examined by the experiment has a yaw amplitude of 6°. In total 34 combinations of flapping frequencies and pitch amplitudes were examined at flow speeds of 0.1 and 0.12ms^{-1}. The resulting thrust coefficients and their corresponding angles of attack and Strouhal numbers are shown in Figure 6-19. The plot shows a general trend where the thrust coefficient increases as the Strouhal number increased, but the relationships between the thrust coefficients and angles of attack or pitch amplitudes are less straight forward. The thrust coefficient is expected to first increase then decrease as the angle of attack increase, the optimum angle of attack can increase as the Strouhal number increase. A further complication is added in that the experiment was performed in terms of pitch amplitude, and the resultant angles of attack from this also increases as the Strouhal number increased. Analysis of the effects of pitch angle and angle of attack will have to be made by comparing the experimental results against the prediction from the BET model.

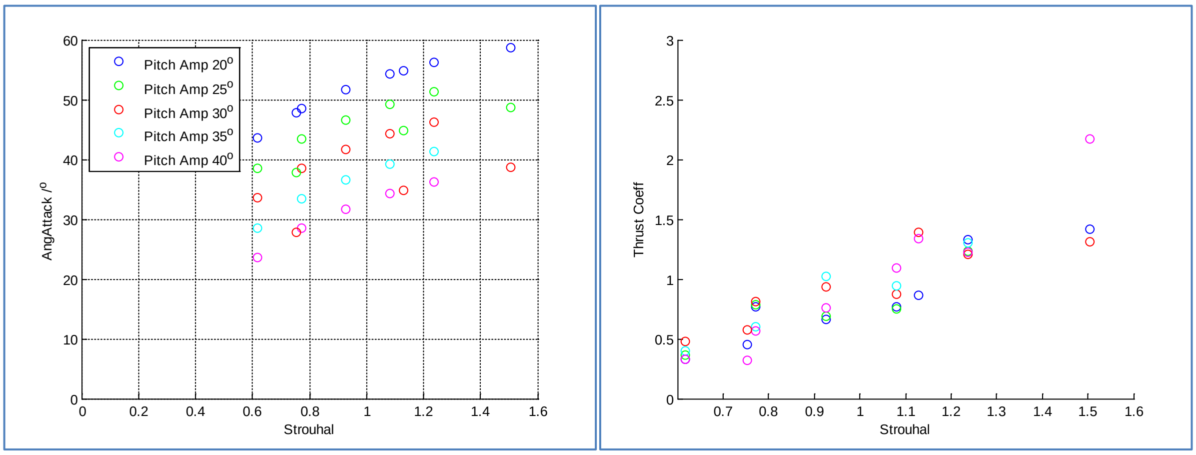

Figure 6-19 - Thrust coefficients and corresponding angles of attack and Strouhal numbers of the experimental results

6.3.3.1 *Comparison between Model and Experimental Results*

Like the results from the two-axis cycle and three-axis cycle with yaw amplitudes of 3°, the BET model without tip loss correction overestimates the thrust coefficients. The modelling results are found to be higher than the experimental results and the differences between the two increase as the Strouhal number increase. Therefore, it will be necessary to examine the results with the tip loss model enabled. Figure 6-20 shows the discrepancy (absolute error) between the experimental and modelling results, and their corresponding Strouhal numbers and angles of attack.

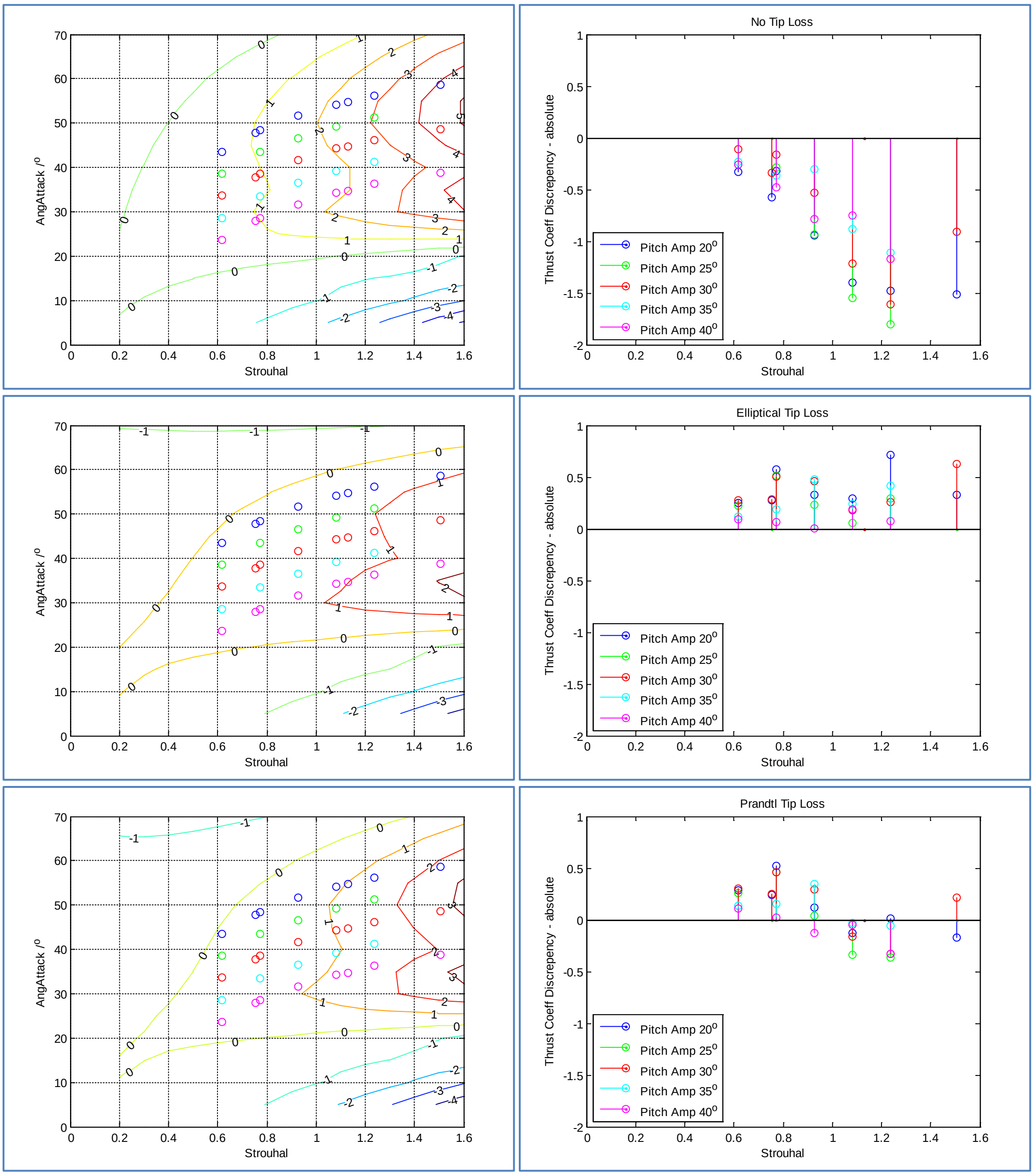
No Tip Loss

Elliptical Tip Loss

Prandtl Tip Loss

Figure 6-20 – (Left column) Contour plot of the BET model results and scatter plot of the experiment data points. (Right column) Differences between the modelling and experimental results.

When the tip loss models are enabled, the model thrust coefficients are reduced which leads to a reduction in the discrepancies between the modelling and experimental thrust coefficients. The model that utilised elliptical tip loss distribution sees a significant reduction in the thrust coefficient and the model underestimate the thrust coefficient across the analysis range. The model utilising Prandtl tip loss function produces thrust coefficients that are closer to the experimental results, where the surface representing the modelling prediction from the model with Prandtl tip loss passes through the scatter of data points produced by the experiment. The model underestimates the thrust coefficient at low Strouhal numbers before transitioning to slight overestimate at higher Strouhal numbers. However, both tip loss model produce results that are much closer to the experimental result than the model without tip loss.

6.3.3.2 *Fractional error*

The fractional errors between the modelling and experimental results are calculated by dividing the differences between the two set of results by the corresponding thrust coefficient from the modelling results. The results are plotted in Figure 6-21. The plot shows the model without tip loss overestimates the experimental results by an average 46%. In comparison, the model utilising elliptical lift distribution underestimates the results by around 60%. The magnitude of the fractional error also increased and the model could underestimate the thrust coefficient by over 320% at lower Strouhal number. Likewise the model utilising Prandtl tip loss function also produced very high fractional error, with the mean error at 50% underestimate, but a significant proportion of this is caused by the outliners at low Strouhal numbers. The median error, which is less affected by outliners, of the Prandtl tip loss model is only 15% underestimate, which is one of the smallest seen so far. As the Strouhal number increased, the errors from the model with Prandtl tip loss settle at around 20% from the model prediction, which is one of the closest observed.

The reason for the very high fractional error at Strouhal numbers below 0.8 can be found in Figure 6-20, which shows the model thrust coefficient are closed to zero at these Strouhal numbers. Since fractional error is calculated by dividing the differences between the two sets of results by the model thrust coefficient, any small random errors can be significantly amplified. In fact the cycle with pitch amplitude of 20° and Strouhal number of 0.62 sits almost directly on top of the zero contour line in the model with Prandtl tip loss, and this results in one of the highest fractional error observed (650%), despite having an average absolute error (~0.3 thrust coefficient).

In fact, the upper zero thrust coefficient contour line in the two models with tip loss run almost parallel to the experimental data points produced by cycles with pitch amplitude of

20°. This is reflected in the fractional error plots where the fraction errors from these cycles (denoted in blue) are found to be higher than other cycles that are further from this zero contour line.

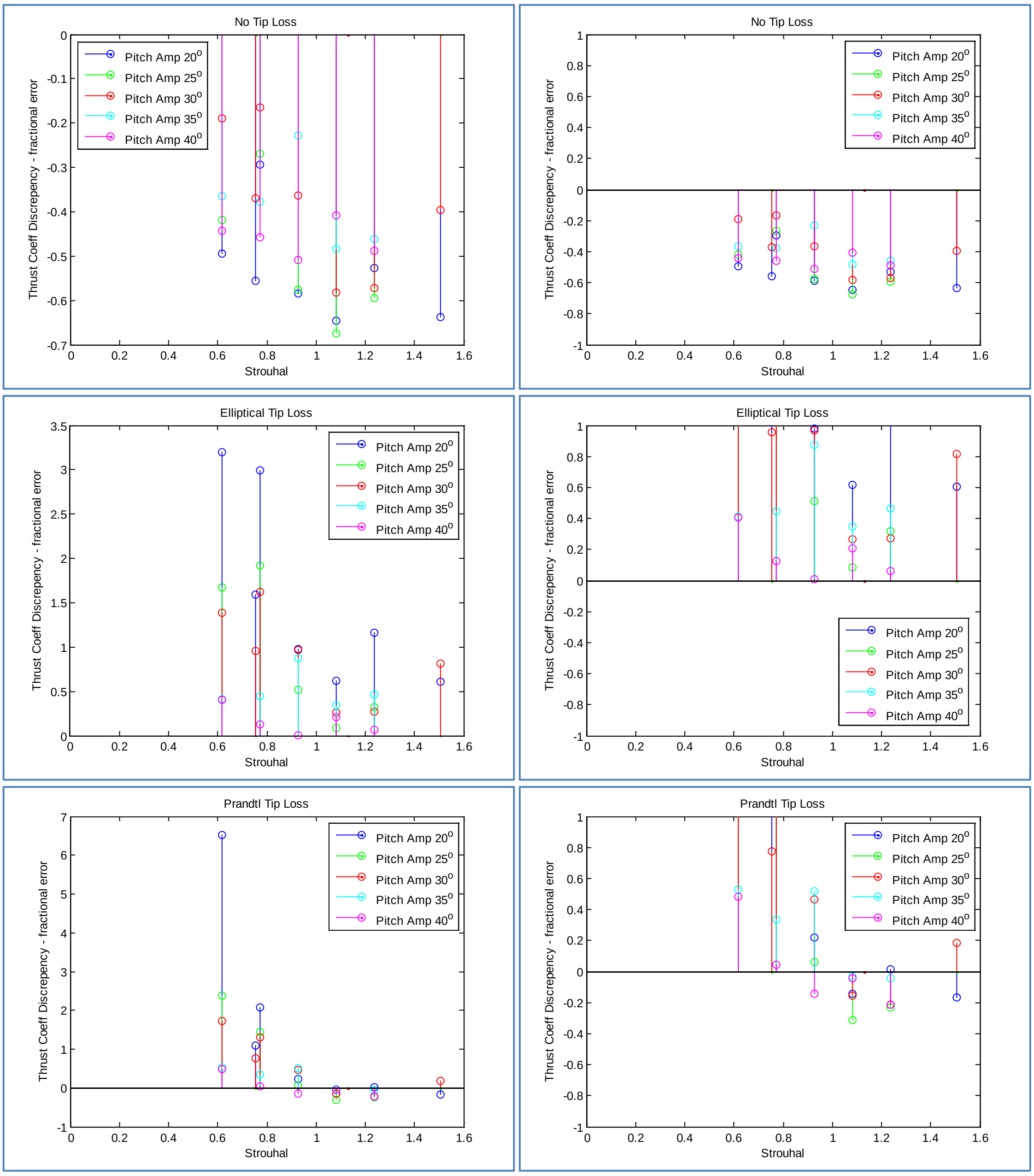

Figure 6-21– Fractional error between modelling and experimental results (Left column) Full Range, (Right column) Y-axis limited to between -1 and 1.

6.3.3.3 *Error distribution at different pitch amplitudes*

In addition to examining the effect of Strouhal number on the thrust coefficient error, the effects of pitch amplitude were also examined. The mean and median errors for each pitch angle are plotted in Figure 6-22. The plots show the fractional errors for the model without tip loss is relatively levelled (~0.5), which suggest the fractional errors are not significantly affected by the pitch amplitude. However, the situation is different for models with tip loss, which display very high discrepancy at lower pitch amplitudes. The mean error at pitch amplitudes of 20° are 1.5 and 1.2 for model with Elliptical and Prandtl tip loss respectively. The magnitude of the mean and median fractional error decreases quickly as pitch amplitude increased, in the case of the Prandtl tip loss model the fractional error is almost zero at the maximum pitch amplitude of 40°.

There are two mechanisms that can produce this effect. The first source of error is small mechanical play in the transmission system. The pitch axis have tolerance up to 1°, which amounts to a 5% uncertainty in a cycle with 20° pitch amplitude and 2.5% uncertainty in the cycle with amplitude of 40°. The second source of error is related to proximity of points to the zero thrust coefficient contour line as seen in Figure 6-12. In the two models with tip loss, the results from cycles with pitch amplitudes of 20° are found almost directly on top of the zero contour line, and as the Strouhal number increased the shift in the corresponding angle of attack kept the points very close to the zero contour line. The very small modelling thrust coefficients at these points amplify any random errors, and this lead to much higher fractional errors than other cycles with larger pitch amplitudes.

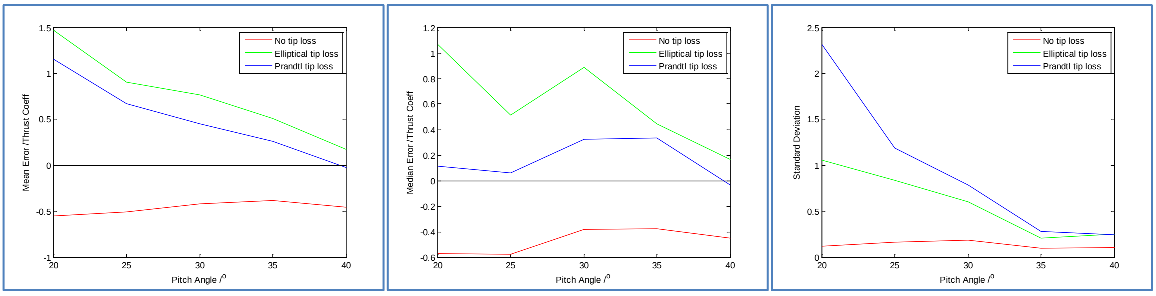

Figure 6-22 – Mean, median and standard deviation of the fractional error between modelling and experimental results

Like the mean and median errors, the standard deviations for the model without tip loss are also relatively small and constant (~13%). By contrast the two models with tip loss display significant spread at low pitch amplitudes which decreases as the pitch amplitudes decrease. The cause of this is mechanical error and proximity to the zero thrust coefficient contour line that was previously explained.

6.3.3.4 *Summary of figure of eight path with 6° yaw*

The analysis of the figure-of-eight path with 6° yaw examined 34 combinations of pitch amplitude, frequency and flow speed. Similar to the results of the two axis experiments, the standard three-axis BET model was found to be inadequate as it overestimated the foil thrust coefficients across the analysis range. Therefore it was necessary to enable the sub-models for tip losses in order to bring the model predictions closer to the experimental results.

Once the tip loss sub-models were enabled the thrust coefficient predicted by the model become much closer to the experimental results, but unlike previous cases, the elliptical tip loss model start to greatly underestimate the forces involved. Instead, the Prandtl tip loss model's prediction is much closer to the experimental result (~20%). Since the elliptical tip loss model performed better for the two axis cycle and the 3° figure-of-eight, and the Prandtl tip loss model performed better for the 6° cycle, further investigation will be required before a conclusion can be made about which tip loss model are better for modelling three-axis aquatic flight.

6.4 Comparison between different actuation paths

One of the key predictions for figure-of-eight actuation path is the reduction of thrust coefficient as the yaw amplitude increases. Due to the way the experimental data points were acquired, it could not cover the entire range of Strouhal numbers and angles of attack. Therefore it will be difficult to make comparison similar to ones found in Chapter 3.

Instead, all of the thrust coefficients from the experimental results are plotted in a scatter plot against Strouhal number (Figure 6-23). The different shapes denotes the thrust coefficient from different actuation paths (circle – two-axis, asterisk – three-axis 3° yaw, triangle – 6° yaw). Whilst the initial expectation was the thrust coefficients from each actuation path will form distinct and readily identifiable clusters, the reality is the result from all three actuation paths coincide with each other. If there are any reductions in thrust coefficient as a result of three axis actuation, the penalties would appear to be less than the spread of the experimental results. The BET model predicted differences only around 30% between the two axis and three axis results (6°), so it is understandable why the results did not form any distinct clusters.

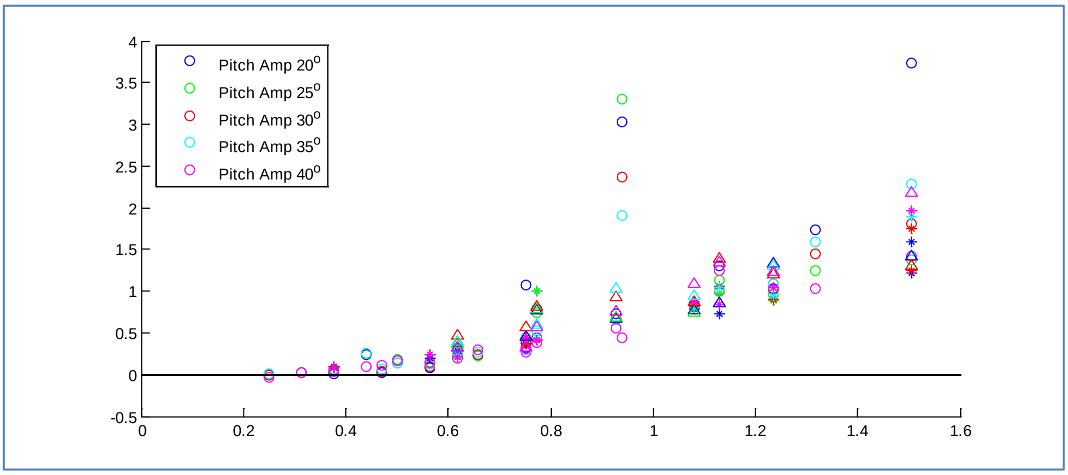

Figure 6-23 – A plot of the thrust coefficient from the experiments. Circle denotes data points from two-axis actuation, Asterisk denotes results from three axis cycles with 3° yaw and triangle denotes cases with 6° yaw.

However, it is immediately apparent from the scatter plot that the experiment's thrust coefficient is closer to that of the BET model with tip loss than the model without. Whilst the BET model without tip loss can achieve a maximum thrust coefficient of 1.6 at an angle of attack of 40° and Strouhal number of 0.8, the thrust coefficients from the experiment were all clearly less than 1.0. At Strouhal numbers of 0.8, the cycles with angle of attack closest to 40° are the ones with pitch amplitude of 30° (see Figure 6-24). Among the experiment data points, there are two cycles with pitch amplitude of 30° and Strouhal numbers close to 0.8. The cycles with Strouhal number of 0.75 reported a thrust coefficient of 0.38 and the cycle with Strouhal number of 0.77 reported a thrust coefficient of 0.44. These are much smaller than the thrust coefficient of 1.6 predicted by the BET model without tip loss but they are much closer to the 0.62 predicted by the model with elliptical tip loss.

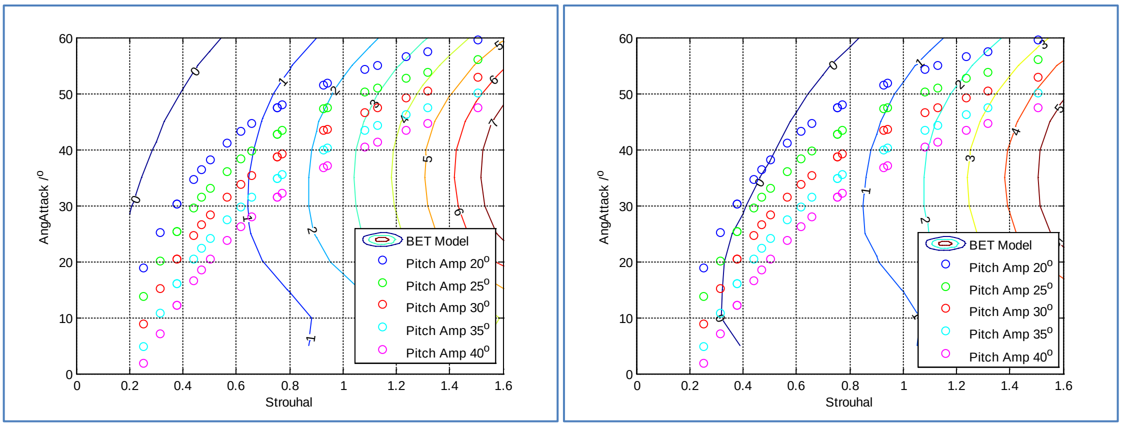

Figure 6-24 – The experiment data points and their position within the two-axis BET thrust coefficient contour plots. (Left) Model without tip loss. (Right) Model with Prandtl tip loss.

At lower Strouhal numbers (0.2 – 0.4) the experimental results shows the thrust coefficient were very small and close to zero. This is consistent with the BET model with tip loss where the zero thrust coefficient contour line can be seen to intercept the experimental results at Strouhal number of 0.3 (Figure 6-24).

The zero intercept at a Strouhal number of 0.3 is also consistent with the thrust coefficient predicted by the three-axis BET model with tip loss and yaw amplitude of 3° (Figure 6-16). The zero intercept of the 6° cycle occurs at higher Strouhal numbers, but the experiment did not test the 6° actuation cycle below 0.6 so it is unable to determine whether the experimental results reach a thrust coefficient of zero at the position predicted by the model.

While there may not be sufficient evidence to prove or disproves whether the yaw motion in the figure-of-eight reduces thrust coefficient. The examination of the experimental data points provides more evidence that a tip loss model is necessary for modelling aquatic flight propulsion, because the thrust coefficients produced by models with tip loss provided a closer match to the experimental results than the model without.

6.5 Summary

The NIMBLE experiment has successfully completed the examination of two-axis aquatic flight actuation path and three-axis aquatic flight figure-of-eight actuation path. The experiments examined 181 combinations of pitch amplitude, flapping frequencies and flow speed, which covers a range of Strouhal numbers from 0.2 to 1.6 and a range of angles of attack from 10° to 60°.

The foil forces from the experimental results were non-dimensionalised and converted into thrust coefficient to enable comparison between different cycles and BET model results. When the thrust coefficients from the experiment were compared against those from the standard BET model, the BET model was found to overestimate the thrust coefficient by around 70%. As such the tip loss models were enabled and these brought the BET model's thrust coefficients closer to the results from the experiment (20-30%). Whilst the model without tip loss overestimated the thrust coefficient across the range of the Strouhal numbers examined, the models with tip loss model consists of a series of under- and over- estimates.

Examination of the experimental results scatter plots also supported the models with tip loss, because the zero intercepts from the results matches that from the model, and the thrust coefficients at other points examined were also quite close to the predicted value.

Whilst thrust coefficients predicted by the BET models with tip loss were close to those from the experimental results, they weren't an exact match. This could be cause by other hydrodynamic effects that has not been modelled, or it may evidence that the quasi-steady BET model has reached its limits when used for modelling aquatic flight, due to hysteresis effects.

Potential enhancements to the experimental rig include: reducing the mechanical play in the actuator and improvement to the force measurement systems. Furthermore, it will be useful if the experiment can also examine the other foil actuation paths (e.g. oval, and reversed figure-of-eight), as well as the asymmetric actuation paths.

Nevertheless, the NIMBLE aquatic flight experiment showed the BET model with tip losses can provide a reasonable estimate of the thrust coefficient of the aquatic flight propulsion. This in turn allows calculation of the thrust produced by various aquatic flight foil propulsors. Once the forces produced by the foil propulsor are known, they can be used to calculate the thrust and torque acting on the propulsor and vehicle, which can then be used to create a model of the vehicles' propulsion and manoeuvring characteristics

Page intentionally left blank

Chapter 7: Conclusions and Future Work

7.1 Conclusion

The research into three-axis aquatic flight propulsion started as a part of the NEMO project research that aims to improve the performance of autonomous underwater vehicles through novel bio-inspired technology. During the preliminary stage of the research, manoeuvrability was identified as one of the major performance gap between manmade vehicles and animals, and aquatic flight propulsion was identified as one of the potential solution to this problem. Aquatic flight was found to be used by many highly manoeuvrable marine animals and many of these animals have relatively rigid body. The fact these animals can remain extremely manoeuvrable despite having relatively rigid bodies show the potential of adapting aquatic flight for AUVs, which require rigid pressure vessels to protect their systems from sea water.

There are still many unknown in aquatic flight propulsion and one of the biggest differences between exiting aquatic flight engineering research and observation made by biologist is the third axis in animal aquatic flight actuation. Most existing hydrodynamic research look at aquatic flight as a one (pitch only) or two-axis (pitch and dorsoventral yaw) problem, but animal aquatic flight shows a significant anteroposterior movement in yaw. In order to understand the significance of this third axis of actuation, the research investigation developed a three-axis blade element approach explore the transient forces on an aquatic flight flapping foil wing. The findings from the model are compared to experiments with a bespoke experimental rig. Whilst unable to capture all elements of the hydrodynamics, the model is able to predict key trends observed in the experiments. Both the experiments and model showed two-axis aquatic flight is better for producing propulsive thrust for most scenarios, but three axis aquatic flight are useful for producing additional off axis force. In particular, the three axis slanted foil actuation path can produce a sizeable vertical force with very little change to the horizontal thrust coefficient, which would be very useful for a positively buoyant AUV to control its depth.

7.1.1 Objective 1: Understanding Aquatic Flight

The first objective laid out in the research methodology was to review the literature to identify the performance gaps between AUV and animals and then find a solution that will close this gap.

A gap in manoeuvrability was identified through a database analysis of various kinematics data for over a hundred AUV and marine animals. An animal lift based paired fin propulsion strategy known as aquatic flight was identified as one of the most promising bio-inspired solution that can close this performance gap.

7.1.2 Objective 2: In depth literature analysis of aquatic flight

After aquatic flight was identified as the main focus of this research, extensive literature review was carried out for aquatic flight in both engineering and biological journals. It was found previous studies on aquatic flight studied one-axis (pitch only (Long et al., 2006)) and two-axis (Licht et al., 2004b; Techet, 2008) propulsion. However a number of papers in the literature, as well as a short video motion analysis carried out by this investigation, suggested there is a third actuation axis with a component in yaw. Three-axis flapping foil propulsion have been studied for aerial flight (Ansari et al., 2006; Liu and Kawachi, 1998; Sane, 2003), and drag based diodontiform motion (Kato, 2000), but not for lift based aquatic flight. As such the effect of yaw motion on aquatic flight was unknown and requires further investigation.

There is several ways to approach this problem of three axis aquatic flight. It can be investigated through CFD, experiment or both. Previous studies carried out by Long (2006) and Licht (2008) had been experimental. Aquatic flight is inherently a three axis transient problem which would be very computationally expensive to investigate. However, an experiment only approach also had its own limitations. Therefore, it was decided to investigate the problem of three-axis aquatic flight using a combination of modelling and experiment. A quasi-steady model would be built to help form an understanding of the mechanics of aquatic flight as well as identify specific cases of interest that will be further investigated experimentally. After that an experiment would be built to verify the model and then to examine the special cases experimentally.

7.1.3 Objective 3: Blade Element Model

After the research path was determined in Objective 2, the research proceeded to design and build a computer model for modelling aquatic flight. This started as a single element quasi-steady model using methods originally developed for studying propellers. Then this method was improved by incorporating blade element theory to take account for the span-wise variation in aquatic flight and numerous other techniques for studying aerial flight in animals. After that the model were further expanded to study three axis actuation.

Eventually this developed into the NIMBLE BET model for three-axis aquatic flight propulsion. At the centre of this model is a blade element theory lift and drag force model which has its origin in the study of propeller. This technique divides the foil into multiple elements to be analysed separately, and then recombined them to find the total force acting on the foil. This allows the model to account for flow speed variation along the foil span. The NIMBLE BET model used 50 foil elements, which offered a good balance between computation speed and accuracy.

The model extended to analyse the effect of tip loss, added mass and Kramer effects. It found added mass and Kramer effect only affected the performance of the flapping foil propulsor within a propulsion cycle and the changes cancel out over a complete propulsion cycle. Therefore, they have no effect on the overall thrust coefficient, but do influence the power consumption. These forces may also benefit or degrade transient manoeuvring, which may utilise strokes with incomplete propulsion cycle.

Tip losses reduce foil thrust over a cycle and two tip loss models were tested. One model was based one elliptical lift force distribution and the other based on Prandtl tip loss function. Prandtl tip loss model produce higher reduction in thrust than the elliptical tip loss model for most of the analysis range, but both have comparable performance when compared against the experimental results.

The three-axis model introduced yaw motion into the actuation cycle to study three-axis aquatic flight. The additional third degree of freedom dramatically increased the number of possible actuation paths, or gaits, and the study carried out in depth analysis of three types of three-axis propulsion paths – the figure-of-eight, the oval, and the reversed figure-of-eight. The study found most three-axis gaits reduce the thrust coefficient rather than contributing to it.

Although common sense may suggests the backwards sweeping power phase of a figure-of-eight stroke path should produce more thrust, the results of the study contradicted this. Instead, the model found the backwards sweeping stroke suffer a reduction of thrust compared to the simple two-axis cycle due to reduction of inflow velocity. Meanwhile the forward advancing recovery phase at the apex of each strokes increased drag, and the combination of these two factors reduce the overall thrust output of the three axis figure-of-eight propulsion cycle. In particular, the three axis figure-of-eight path with 6° yaw was found to be very disruptive to the flow, and would cause a significant loss of thrust.

When the thrust reduction effect in the backwards sweeping stroke was discovered, the logic was reversed to create the forward sweeping reversed figure-of-eight stroke path. Reversed figure-of-eight path has not been observed in nature nor reported in literature, but it was found to produce higher thrust coefficient than to two axis propulsion. Of all the actuation paths tested, the reversed figure-of-eight path is the only one that was found to produce higher thrust coefficient than two-axis aquatic flight.

7.1.4 Objective 4: NIMBLE Experiments

The result from the NIMBLE BET aquatic flight model needs to be verified, and the forth objective of this thesis research is to design, create and carryout an experiment to verify the model. A bespoke experimental test rig was designed to actuate a 0.5m long NACA0012 foil in three axis (pitch, roll, and yaw) and have strain gauge sensors that will measure the forces inline and perpendicular to the foil chord. The test rig was designed to be installed on a supporting bridge and suspend over a recirculating water channel with the foil penetrating the water surface.

In total the experiment tested 181 different aquatic flight cycles, 105 of which were two-axis cycle and the remaining 76 were three-axis figure-of-eight cycle with two different yaw amplitudes. The experiment found tip loss model is necessary to produce a good fit between experimental and modelling result. Results involving the two-axis cycles were within 20-30% of the model prediction. This was an excellent match after considering the scatter and uncertainties caused by the uncertainty in the force measurement, turbulent nature of the recirculating water channel, as well as the surface losses associated with operating through the water surface and hysteresis effects such as dynamic stall. Therefore, it is safe to conclude the NIMBLE two-axis experiment has successfully validated the NIMBLE BET model.

The three-axis cycles are a more complicated and the discrepancies between the model and the experiment increased. The increased uncertainty and scatter in the experimental results is partly caused by the increased degree of freedom and the proximity of the analysis point to the zero thrust coefficient contour line. These factors can combine and cause large fractional error at lower Strouhal numbers when the thrust is small. Nevertheless, the model predictions are mostly within 30% of the experimental results at higher Strouhal numbers. The two tip loss model also show a difference, with the Elliptical tip loss model performing better for the cycles with yaw amplitude of 3° and Prandtl tip loss model performing better for cycles with 6° yaw.

Although the model’s averaged errors suggest the model over predicts the forces produced by the three axis foil actuator undergoing aquatic flight, the errors often consist of a mix of under and over predictions. This means the modelling result intersect the experimental result, which means the experiment validated the BET model with tip loss. There is certainty room for improvement in both the model and the experiment to reduce the discrepancy, but the experiment has shown the BET model can be used for predicting the forces produced by aquatic flight.

7.1.5 Objective 5: New Insights into Three Axis Aquatic Flight Propulsion

Most studies into aquatic flight focuses on idealised symmetric strokes where the up and down stokes are symmetrical. This means the vertical forces would cancel out over each propulsion cycle. However, this investigation took a step further and carried out a study in asymmetric stroke aquatic flight where asymmetry is introduced into the propulsion cycle such that the up and down strokes ceased being symmetrical. This stroke asymmetry produces an imbalance between the vertical forces from the up and down strokes, which would results in a net vertical force. The net vertical force can be used for depth control, pitch control, or roll control depending on how the foil actuators on a vehicle work together.

The asymmetric stroke study analysed a number of two and three axis asymmetric strokes. The study found two axis aquatic flights with a pitch angle bias can produce significant amount of vertical lift/down force, but the corresponding thrust coefficient is also reduced. Three axis tilted actuation paths with no pitch angle bias on the other hand can produce a small amount of vertical thrust (up to 20% of horizontal) with almost no loss to its horizontal thrust coefficient. Also, the analysis found the direction of the tilt (tilt forward or tilt back) do not indicate the direction of the vertical thrust, as the forward tilted actuation path was able to produce both net upward and net downward force depending on the angle of attack and Strouhal number of the propulsion cycle. Finally a fully rotated path, with a pitch angle bias that cause the foil chord to be perpendicular to the actuation path at the end of each stroke, showed it can generate a significant amount of vertical thrust but with a significant reduction of the horizontal thrust coefficient. In fact the thrust coefficients can become negative in many cases, and care must be taken during the design of the control system to ensure flow reversal do not happen.

In generals the two-axis aquatic flight cycle was found to be better for producing propulsive thrust for most scenarios, but three axis aquatic flight are useful for producing additional off axis force for manoeuvring. In particular, the three-axis slanted foil actuation path can produce a sizeable vertical force with very little change to the horizontal thrust coefficient, which would be very useful for a positively buoyant AUV to control its depth.

7.2 Thesis Contribution

The main novelty of this thesis is the development of a numerical and experimental model of three-axis aquatic flight. As discussed in the literature review there are a number of pre-existing models that looked at two-axis motion. The work presented here includes the third axis which is a new development.

The NIMBLE BET model allowed rapid analysis of three axis aquatic flight motion. Aquatic flight is a three dimensional transient problem, so accurate modelling using traditional RANS based methods can be very computationally expensive and time consuming. The quasi-steady NIMBLE BET model allowed analysis to be performed on hundreds of cases, with different combinations of pitch, roll, and yaw amplitudes, frequencies and offsets, as well as different foil shape, in relatively short amount of time. In addition, a number of innovative ideas were produced including studying the effects of different gaits and using three-axis aquatic flight to generate manoeuvring forces via asymmetric stroke.

The development of the NIMBLE experiment provides data vital for the verification of the results of the analytical model of three axis aquatic flight. Such an experimental facility is unique and will form the basis of future research into the mechanisms and forces that can be generated by controlled movements of a hydrofoil in three-axis. The use of the NIMBLE experiment within the context of this research has been shown to provide verification data to assess the validity of the 3-axis BET analytical model.

7.3 Future work

This thesis research is part of a larger research project that aims to improve the performance of AUVs through bio-inspiration. Whilst the NIMBLE BET model for aquatic flight was successfully verified by the NIMBLE experiment, it is merely the first step towards creating an aquatic flight propelled AUV that is manoeuvrable at all speed. This thesis research built up the theoretical background information that will aid future researcher and engineer in designing the aquatic flight propulsor.

In addition to the greater objective of creating an aquatic flight AUV, there are also many rooms for incremental improvement for both the model and the experiment. Some of which has been identified. This section will provide a summary for the improvement that will need to be done.

7.3.1 Improvements to the Aquatic Flight Model

The current lift and drag coefficients were sourced from tabulated data for a NACA0012 foil section operating at Reynolds number of 160000. The working Reynolds number for NIMBLE is around 40000, which is a factor of four smaller than the Reynolds number of the tabulated data. Although the literatures suggest the lift and drag coefficients between these two Reynolds numbers are very close (within a few percent), there are still room for improvement. Furthermore, the foil cross section changes when yaw motion is introduced. The change in cross section is relatively small when the yaw amplitude is small, but the change increases as the yaw amplitude increases. As such additional models will be needed to model the change in foil cross section during the yaw cycle and calculate the corresponding lift and drag coefficients.

In addition to a more advanced lift and drag coefficient model, another area for improvement is the modelling of energy expenditure. NIMBLE studied how to maximise manoeuvring forces rather than minimising energy expenditure. This is because literature review and subsequent analysis shown bio-inspired locomotion is unlikely to be more efficient than conventional motor and propeller due to actuator limitations. However, it will still be useful to know the energy expenditure of aquatic flight, so it can be used for gait optimisation and mission planning.

The three degrees of freedom allowed the flapping foil to follow different actuation paths. The investigation only analysed three types of paths, namely figure-of-eight, oval, and reverse figure-of-eight. The investigation found all but one of these three-axis actuation paths produced less forward thrust than two-axis aquatic flight, and the only exception was the reversed figure-of-eight path. However, the normal figure-of-eight and oval gaits are used by many aerial flyers and marine animals, so there may be other unforeseen benefits or limitations that have yet to be identified by the model and experiments. These include energy efficiency, manoeuvring force and physiological limitations. Therefore further investigation of these strokes will be needed to identify benefits and limitations that may have been missed.

It must be noted that the current model and experiment only examined the idealised strokes, while all animals’ three-axis aquatic flights stroke paths have more complex asymmetrical shape. The asymmetric stroke analysis showed certain asymmetric path can produce vertical forces that can be used for manoeuvring and depth control, so this may be the reason behind the more complicated stroke path used by the animals.

So far, the asymmetric stroke investigation only analysed tilted and rotated actuation path based on introducing yaw motion to the two-axis cycle, such that the up and down strokes followed the same path. The first logical extension will be to examine the performance of tilted oval, figure-of-eight, and other tilted three-axis paths. Then hybrid gaits such as the D-shaped actuation path used by seals and plesiosaurs, which contains a mix of lift based flapping and drag based paddling, should also be examined.

As the complexity of the actuation paths increased, a more advanced path following algorithm will be needed to enable simulation of the complex animal aquatic flight stroke instead of the simple idealised stroke currently studied by the model. The analysis should extend to thrust vectoring in the XZ plane to see whether a three-axis aquatic flight propelled vehicle can perform sway.

There are many improvements that can be made to the current three-axis NIMBLE model, from improvements to the lift and drag model to more complex path following models. In summary, the lift and drag force model will need to be improved, and the model should analyse more gaits. The model will also need to extension to enable analyse of complex non-idealised stroke path, model forces in the XZ plane and model energy expenditures.

7.3.2 Whole Vehicle Manoeuvring Model

The investigation so far has focused on the aquatic flight propulsor, and ignored its interaction with the vehicle or interaction with other propulsors on the vehicle. A dynamic model for an aquatic flight propelled AUV can form the next stage of study into an aquatic flight propelled AUV.

Although the original aim of NIMBLE is to improve the manoeuvrability of AUV through adapting the bio-inspire aquatic flight for use in a manmade vehicle. The study thus far only analysed the aquatic flight foil propulsor. Vehicle's manoeuvrability is a function of the propulsion and control forces, relative placement of the control surfaces, thrusters and propulsors, hull hydrodynamics, vehicle mass and moment of inertia, vehicle's centre of mass and centre of buoyancy etc…. Since these other factors have yet to be model and analysed, the investigation cannot determine the level of improvement aquatic flight brought to vehicle manoeuvrability as a whole. A whole vehicle manoeuver model can potentially provide an answer to this, and determine whether an aquatic flight propelled AUV can achieve manoeuvrability and agility closed to its biological counterpart such as seals, penguins and turtles.

The whole vehicle investigation should also study the interaction between the two propulsive foils. It was noted in the literature review that penguins and sea turtles normally swim using left-right symmetrical flapping (i.e. both flippers do the same thing), but they both switch to anti-symmetrical flapping at very low speed. As such it is important to study how these foils interact. The investigation of the foil-hull and foil-foil interactions is likely to be very complicated and it is questionable whether the BET model can capture the resulting effects. Therefore a feasibility study will be needed to determine whether quasi-steady methods are sufficient, or whether this type of study can only be done with RANS based CFD or experimentation.

7.3.3 Experiment Actuator

Whilst the NIMBLE Experiment has verified the NIMBLE BET aquatic flight model, there are a lot of room for improvements**.** The results of the experiments have a fairly high uncertainty due to a number of different factors, such as flow speed errors, angular position errors, and force measurement errors.

Turbulence in the recirculating water channel is the main contributor to flow speed error, which not only affected the water flow over the flapping foil, but it affected the flow speed measurement as well. Flow speed in the Chilworth recirculating water channel was measured by timing transit time of floats in the water. The floats did not travel in a straight line or at a constant speed, but instead move around the channel and often get caught in eddies. The experiment overcome this by calculating the average transit time of the float from a dozen measurement, but the fluctuation in flow speed is a problem that can only be solved by modifying the recirculating water channel. In future experiments, a honey comb filter screen should be installed upstream of the experiment to reduce channel turbulence and create a more laminar flow.

The angular position errors are caused by mechanical play in the gearboxes and transmission. Currently, the angular positions are measured by the motor encoders, but despite the use of anti-backlash gearboxes, the mechanical play for each actuation axis was around 1°. Therefore there can be up to 1° of angular position error between the position reported by the motor encoder and the actual position of the output shaft. Whist 1° of uncertainty may be insignificant for the pitch and roll axis which has very high motion amplitude, it can be a serious problem for the yaw axis whose oscillation amplitude is much smaller. The mechanical transmission error cause by play in the drivetrain cannot be fixed without upgrading the entire drive train which would be expensive. However, if absolute position encoders are installed directly on the output shafts, they can measure the axis position directly and eliminate the mechanical play induced uncertainty between the actuation axis's positon and the motor's position.

The force measurement error is minor compared to the recirculating water channel problem and the angular position problem. Electrical interference can mask small details in the experimental results. A good example of this is the Kramer effect and added mass. These effects cause changes to foil forces within the flapping cycle but the experimental results were too distorted by noise to determine whether these effects are present. As such, the actuator's electromagnetic shielding needs to be upgraded to further reduce noise from electrical interference before more detailed study can be carried out.

In addition to EM shielding upgrades, the force measurement strain gauge should also be modified to improve force measurement. Currently the strain gauges on the pitch shaft measures the bending moment on the shaft, but it does not indicate the flapping foil's centre of force, so the actual thrust was calculated from a theoretical centre of pressure. The theoretical centre of pressure can be another source of error, so it needs to be replaced. One solution is to install a second set of strain gauge on another location along the span so the difference in moment between the current sets of strain gauge and the new gauges can provide an indication of the location of the centre of pressure. Apart of linear bending moment measurement, the load cell was also fitted with torque measurement strain gauges. These torque measurement gauges were not used during the current experiment, but they can be very useful for future investigations.

Apart from hardware upgrades, the software also needs to be modified for the next stage of the experiment. Like the current BET model, the paths investigated by the experiment were idealised path. Although the current control software can also be made to investigate oval, reversed-figure-of-eight and tilted asymmetric paths, the control software will need to be upgraded with a new path following algorithm if the actuator is to be used for investigating the more complex stroke paths used by marine animals (e.g. seals' D-shape hybrid stroke path).

7.3.4 Gait and Optimisation

After the hardware upgrades, the next stage of the experiment should carry out further investigation of different gaits as well as finding the optimum gaits for different situations. The experiment only analysed symmetrical two-axis stroke and three-axis figure-of-eight strokes. Oval, reversed-figure-of-eight and the various asymmetric strokes that were studied by the model were not tested by the experiment, so the immediate next stage of the experiments would be to test these gaits.

After testing the idealised stroke, the next step would be to examine the non-idealised stroke paths used by animals. Most animal aquatic flight stroke paths are asymmetric and skewed, and many are believed to have different actuation force between the up and down strokes. Whilst the model concluded the asymmetric stroke path can be used to produce vertical force, it is unknown if this is the only reason why animal stroke paths have such complex shape or whether there are other reasons yet to be determined advantages.

The goal of testing various gaits is to find the optimum stroke for different situations. As the modelling results points out, the two axis symmetrical stroke path is best for propulsive thrust, but if the vehicle is positively buoyant and need a constant down force, then a tilted three axis stroke path will be better. As the final stage of the recirculating water channel experiment, the actuator control system should be modified to enable unsupervised autonomous operation to test different gaits, and to modify the gaits to find the optimum gait for various scenarios. The results of the gait optimisation will lay the ground work for future experiment with flapping foil actuator on an AUV.

7.3.5 Aquatic flight propelled AUV

Finally after the various research branches in ‘Future Works’ are completed, the next step would be to create an aquatic flight propelled AUV technology demonstrator. One of the advantages of choosing aquatic flight propulsion over other bio-inspired propulsion strategy is its compatibility with conventional AUV design in that it does not require a significant tail and caudal fins, which enable the vehicle to have a larger pressure vessel for more sensitive equipment. This means the main challenge of producing an aquatic flight AUV is the aquatic flight actuator itself. Whilst this thesis research side stepped the issue with sealing by designing a rig that will operate out of water, waterproofing will become a major concern for underwater operation. In addition, may structural component will need to be designed to counteract the water pressure.

Once the technology demonstrator vehicle is completed, it will need to be tested in controlled environment. The control algorithm will require further development and refinement to take into account the wake interaction with hull and other complications. The envisioned role of the aquatic flight propelled AUV is high speed, high manoeuvrability mission, e.g. wild life filming, and the time span of various manoeuver is likely too short for a conventional feedback-type control system. The time sensitivity will require a feed-forward type control, which means an accurate fluid-structure interaction model is more important than ever.

In the end, the goal of the aquatic flight propelled AUV is a general purpose small AUV that can undertake a wide range of missions that has several speed profile and manoeuvrability requirement, such as that of offshore asset inspection and wildlife documentary filming. These types of mission require good manoeuvrability at low speed as well as high speed, neither of which the current generation of AUV excels in. This improved manoeuvrability of an aquatic flight AUV is likely to enable missions that were previously exclusive for ROV and divers, as well as novel missions that have never been attempted due to limitation of existing technology.

VI: References

Abu Sharkh, S. M., Griffiths, G. & Webb, A. T. 2003. Power sources for unmanned underwater vehicles. In: Griffiths, G. (ed.) Technology and Application of Autonomous Underwater Vehicles. Taylor & Francis.

Aitken, J. P. & O'dor, R. K. 2004. Respirometry and swimming dynamics of the giant australian cuttlefish, *Sepia apama* (mollusca, cephalopoda). Marine and Freshwater Behaviour and Physiology, 37(4)**,** pp 217 - 234.

Anderson, J. M. & Chhabra, N. K. 2002. Maneuvering and Stability Performance of a Robotic Tuna. Integr. Comp. Biol., 42(1)**,** pp 118-126.

Anderson, J. M., Streitlien, K., Barrett, D. S. & Triantafyllou, M. S. 1998. Oscillating foils of high propulsive efficiency. Journal of Fluid Mechanics, 360(-1)**,** pp 41-72.

Ansari, S. A., Żbikowski, R. & Knowles, K. 2006. Aerodynamic modelling of insect-like flapping flight for micro air vehicles. Progress in Aerospace Sciences, 42(2)**,** pp 129-172.

Bangsbo, J., Krustrup, P., Gonzalez-Alonso, J. & Saltin, B. 2001. ATP production and efficiency of human skeletal muscle during intense exercise: effect of previous exercise. Am J Physiol Endocrinol Metab, 280(6)**,** pp E956-964.

Bannasch, R. 1994. Functional anatomy of 'flight' apparatus in penguins. In: Maddock, L., Bone, Q. & Rayner, J. M. V. (eds.) Mechanics and physiology of animal swimming. Cambridge University Press.

Blake, R. W. 1979. The Mechanics of Labriform Locomotion I. Labriform Locomotion in the Angelfish (Pterophyllum Eimekei): An Analysis of the Power Stroke. The Journal of Experimental Biology, 82(1)**,** pp 255-271.

Blake, R. W. 1981. Influence of pectoral fin shape on thrust and drag in labriform locomotion. Journal of Zoology, 194(1)**,** pp 53-66.

Clark, B. D. & Bemis, W. 1979. Kinematics of swimming of penguins at the Detroit Zoo. Journal of Zoology, 188(3)**,** pp 411-428.

Clark, R. P. & Smits, A. J. 2006. Thrust production and wake structure of a batoid-inspired oscillating fin. Journal of Fluid Mechanics, 562(-1)**,** pp 415-429.

Cody, S. E. 1992. An Experimental Study of the Response of Small Tunnel Thrusters to Triangular and Square Wave Inputs,

Danson, E. 2002. The Economics of Scale: Using Autonomous Underwater Vehicles (AUVs) for Wide-Area Hydrographic Survey and Ocean Data Acquisition. FIG XXII International Congress, TS4.4 Hydrographic Surveying. Washington, D.c., USA April 19-26 2002.

Davenport, J., Munks, S. A. & Oxford, P. J. 1984. A Comparison of the Swimming of Marine and Freshwater Turtles. Proceedings of the Royal Society of London. Series B, Biological Sciences, 220(1221)**,** pp 447-475.

Davis, R. E., Eriksen, C. C. & Jones, C. P. 2003. Autonomous buoyancy driven underwater gliders. In: Griffiths, G. (ed.) Technology and application of autonomous underwater vehicles. Taylor & Francis.

Dickinson, M. H., Lehmann, F.-O. & Sane, S. P. 1999. Wing Rotation and the Aerodynamic Basis of Insect Flight. Science, 284(5422)**,** pp 1954-1960.

Feldkamp, S. D. 1987a. Foreflipper propulsion in the California sea lion, Zalophus californianus. Journal of Zoology, 212(1)**,** pp 43-57.

Feldkamp, S. D. 1987b. Swimming in the California sea lion: morphometrics, drag and energetics. Journal of Experimental Biology, 131(1)**,** pp 117-135.

Ferguson, J. S. 2003. Semi submersible AUV. In: Griffiths, G. (ed.) Technology and application of autonomous underwater vehicles. Taylor and Francis.

Fish, F. E. 1993. Power output and propulsive efficiency of swimming bottlenose dolphins (*Tursiops truncates*). J Exp Biol, 185(1), pp 179-193.

Fish, F. E. 1996. Transitions from Drag-based to Lift-based Propulsion in Mammalian Swimming. American Zoologist, 36(6), pp 628-641.

Fish, F. E. 2004. Structure and mechanics of nonpiscine control surfaces. IEEE Journal of Oceanic Engineering, 29(3), pp 605-621.

Fish, F. E. & Hui, C. A. 1991. Dolphin swimming–a review. Mammal Review, 21(4), pp 181-195.

Fish, F. E. & Rohr, J. J. 1999. Review of Dolphin Hydrodynamics and Swimming Performance, Centre, D. I.

Flores, M. 2003. Flapping motion of a three-dimensional foil for propulsion and maneuvering of underwater vehicles. Master Master Thesis, MIT.

Forng-Chen, C., Chi-Kang, C. & Jenhwa, G. A practical method for simulating pectoral fin locomotion of a biomimetic autonomous underwater vehicle. International Symposium on Underwater Technology, 20-23 April 2004 2004. 323-329.

Griffiths, G. & Edwards, I. 2003. AUVs: designing and operating next generation vehicles. In: H. Dahlin, N. C. F. K. N. & Petersson, S. E. (eds.) Elsevier Oceanography Series. Elsevier.

Healey, A. J., Rock, S. M., Cody, S., Miles, D. & Brown, J. P. Toward an improved understanding of thruster dynamics for underwater vehicles. Proceedings of the 1994 Symposium on Autonomous Underwater Vehicle Technology, 1994. 340-352.

Hover, F. S., Haugsdal, Ø. & Triantafyllou, M. S. 2004. Effect of angle of attack profiles in flapping foil propulsion. Journal of Fluids and Structures, 19(1), pp 37-47.

Jun, G., Shusheng, B., Yicun, X. & Cong, L. Development and design of a robotic manta ray featuring flexible pectoral fins. Robotics and Biomimetics, 2007. ROBIO 2007. IEEE International Conference on, 15-18 Dec. 2007 2007. 519-523.

Kato, N. 2000. Control performance in the horizontal plane of a fish robot with mechanical pectoral fins. Oceanic Engineering, IEEE Journal of, 25(1), pp 121-129.

Kato, N. & Furushima, M. Pectoral fin model for maneuver of underwater vehicles. Proceedings of the 1996 Symposium on Autonomous Underwater Vehicle Technology, 1996. 49-56.

Kim, J. & Chung, W. K. 2006. Accurate and practical thruster modeling for underwater vehicles. Ocean Engineering, 33(5), pp 566-586.

Lewis, E. V. (ed.) 1988. Principles of Naval Architecture: The Society of naval architects and marine engineers.

Licht, S. 2008. Biomimetic Oscillating Foil Propulsion to Enhance Vehicle Agility and Maneuverability. Doctor of Philosophy, Massachusetts Institute of Technology.

Licht, S., Hover, F. & Triantafyllou, M. S. Design of a flapping foil underwater vehicle. Underwater Technology, 2004. UT '04. 2004 International Symposium on, 20-23 April 2004 2004a. 311-316.

Licht, S., Polidoro, V., Flores, M., Hover, F. S. & Triantafyllou, M. S. 2004b. Design and Projected Performance of a Flapping Foil AUV. Institute of Electrical and Electronic Engineers.

Lighthill, M. J. 1969. Hydromechanics of Aquatic Animal Propulsion. Annual Review of Fluid Mechanics, 1(1), pp 413-446.

Lighthill, M. J. 1970. Aquatic animal propulsion of high hydromechanical efficiency. Journal of Fluid Mechanics, 44(02), pp 265-301.

Lighthill, M. J. 1971. Large-Amplitude Elongated-Body Theory of Fish Locomotion. Proceedings of the Royal Society of London. Series B, Biological Sciences, 179(1055)**,** pp 125-138.

Lindgren, J., Caldwell, M. W., Konishi, T. & Chiappe, L. M. 2010. Convergent Evolution in Aquatic Tetrapods: Insights from an Exceptional Fossil Mosasaur. PLoS ONE, 5(8)**,** pp e11998.

Lindsey, C. C. 1979. 1 Form, Function, and Locomotory Habits in Fish. In: Hoar, W. S. & Randall, D. J. (eds.) Fish Physiology. Academic Press.

Liu, H. & Kawachi, K. 1998. A Numerical Study of Insect Flight. Journal of Computational Physics, 146(1)**,** pp 124-156.

Long, J. H. J., Schumacher, J., Livingston, N. & Kemp, M. 2006. Four flippers or two? Tetrapodal swimming with an aquatic robot. Bioinspiration & Biomimetics, 1(1)**,** pp 20.

Man, S. G. K., Phillips, A. B., Boyd, S. W., Blake, J. I. R. & Griffiths, G. Bio-inspired aquatic flight propulsion system for agile and manoeuverable underwater vehicles. OCEANS, 2012 - Yeosu, 21-24 May 2012 2012. 1-10.

Massare, J. A. 1994. Swimming capabilities of Mesozoic marine reptiles: a review. In: Maddock, L., Bone, Q. & Rayner, J. M. V. (eds.) Mechanics and physiology of animal swimming. Cambridge University Press.

Mclean, M. B. 1991. Dynamic performance of small diameter tunnel thrusters,

Mcphail, S. 2007. AutoSub 6000, a leap forward in capabilities: a long range deep diving AUV.

Molland, A. F. & Turnock, S. R. 2007. Marine rudders and control surfaces: principles, data, design and applications: Butterworth-Heinemann.

Nahon, M. A simplified dynamics model for autonomous underwater vehicles. Proceedings of the 1996 Symposium on Autonomous Underwater Vehicle Technoloy, 2-6 Jun 1996 1996. 373-379.

Newman, P. Unmanned vehicles for shallow and costal water. 2010. Douglas Westwood limited.

Palmer, A., Hearn, G. E. & Stevenson, P. Modelling tunnel thrusters for autonomous underwater vehicles. Navigation, Guidance and Control of Underwater Vehicles (NGCUV'08), 2008.

Palmer, A. R. 2009. Analysis of the propulsion and manoeuvring characteristics of survey-style AUVs and the development of a multi-purpose AUV. Doctoral, University of Southampton.

Phillips, A. B., Steenson, L. V., Rogers, E., Turnock, S. R., Harris, C. A. & Furlong, M. 2013. Delphin2: an over actuated autonomous underwater vehicle for manoeuvring research. Transactions of the Royal Institution of Naval Architects, Part A – International Journal of Maritime Engineering, A4(171-180.

Prandtl, L. & Betz, A. 1927. Vier Abhandlungen Zur Hydrodynamik und Aerodynamik: Gottingen.

Read, D. A., Hover, F. S. & Triantafyllou, M. S. 2003. Forces on oscillating foils for propulsion and maneuvering. Journal of Fluids and Structures, 17(1)**,** pp 163-183.

Rivera, A. R. V., Rivera, G. & Blob, R. W. 2013. Forelimb kinematics during swimming in the pig-nosed turtle, Carettochelys insculpta, compared with other turtle taxa: rowing versus flapping, convergence versus intermediacy. The Journal of Experimental Biology, 216(4)**,** pp 668-680.

Rivera, A. R. V., Wyneken, J. & Blob, R. W. 2011. Forelimb kinematics and motor patterns of swimming loggerhead sea turtles (Caretta caretta): are motor patterns conserved in the evolution of new locomotor strategies? The Journal of Experimental Biology, 214(19), pp 3314-3323.

Rosenberger, L. & Westneat, M. 1999. Functional morphology of undulatory pectoral fin locomotion in the stingray taeniura lymma (Chondrichthyes: dasyatidae). J Exp Biol, 202(24), pp 3523-3539.

Sane, S. P. 2003. The aerodynamics of insect flight. Journal of Experimental Biology, 206(23), pp 4191-4208.

Sane, S. P. & Dickinson, M. H. 2002. The aerodynamic effects of wing rotation and a revised quasi-steady model of flapping flight. Journal of Experimental Biology, 205(8), pp 1087-1096.

Saunders, A. & Nahon, M. The effect of forward vehicle velocity on through-body AUV tunnel thruster performance. OCEANS '02 MTS/IEEE, 2002. 250-259 vol.1.

Seddon, J. 1990. Basic Helicopter Aerodynamics, Oxford: BSP Professional books.

Sfakiotakis, M., Lane, D. M. & Davies, J. B. C. 1999. Review of fish swimming modes for aquatic locomotion. Oceanic Engineering, IEEE Journal of, 24(2), pp 237-252.

Sheldahl, R. E. & Klimas, P. C. 1981. Aerodynamic characteristics of seven symmetrical airfoil sections through 180-degree angle of attack for use in aerodynamic analysis of vertical axis wind turbines. Sandia National Laboratories - Energy report, SAND-80-2114), pp.

Shen, W. Z., Mikkelsen, R., Sørensen, J. N. & Bak, C. 2005. Tip loss corrections for wind turbine computations. Wind Energy, 8(4), pp 457-475.

Techet, A. H. 2008. Propulsive performance of biologically inspired flapping foils at high Reynolds numbers. Journal of Experimental Biology, 211(2), pp 274-279.

Triantafyllou, M. S. & Triantafyllou, G. S. 1995. An efficient swimming machine. Scientific American, 272(3), pp 7.

Truong, Q. T., Nguyen, Q. V., Truong, V. T., Park, H. C., Byun, D. Y. & Goo, N. S. 2011. Aerodynamic Characteristics of a Three-Dimensional Wing in Heave Oscillation. Journal of the Korean Society for Aeronautical & Space Sciences, 39(10), pp 905.

Van Humbeeck, J. 2001. Shape Memory Alloys: A Material and a Technology. Advanced Engineering Materials, 3(11), pp 837-850.

Walker, J. & Westneat, M. 1997. Labriform propulsion in fishes: kinematics of flapping aquatic flight in the bird wrasse Gomphosus varius (Labridae). J Exp Biol, 200(11), pp 1549-1569.

Walker, J. A. 2002. Rotational lift: something different or more of the same? Journal of Experimental Biology, 205(24), pp 3783-3792.

Walker, J. A. & Westneat, M. W. 2002. Performance limits of labriform propulsion and correlates with fin shape and motion. J Exp Biol, 205(2), pp 177-187.

Walker, W. F., Jr. 1971. Swimming in Sea Turtles of the Family Cheloniidae. Copeia, 1971(2), pp 229-233.

Watanuki, Y., Wanless, S., Harris, M., Lovvorn, J. R., Miyazaki, M., Tanaka, H. & Sato, K. 2006. Swim speeds and stroke patterns in wing-propelled divers: a comparison among alcids and a penguin. J Exp Biol, 209(7), pp 1217-1230.

Webb, P. W. 1994. The biology of fish swimming. In: Maddock, L., Bone, Q. & Rayner, J. M. V. (eds.) Mechanics and physiology of animal swimming. Cambridge university press.

Westwood, J. 2010. The AUV market place. Oceanology 2010, 2010 Excel Centre, London.

Worasinchai, S., Ingram, G. & Dominy, R. 2011. A low-Reynolds-number, high-angle-of-attack investigation of wind turbine aerofoils. Proceedings of the Institution of Mechanical Engineers, Part A: Journal of Power and Energy, 225(6), pp 748-763.

Wu, T. Y.-T. 1961. Swimming of a waving plate. Journal of Fluid Mechanics, 10(03), pp 321-344.